MONTAN
UNIVERSITÄT
LEOBEN

Chair of Reservoir Engineering

Master's Thesis

Alkali-Polymer Flooding, from Core Flood Tests to Field Scale Simulation

Ulla Sabine Wagentristl, BSc

November2018

I dedicate this thesis to:

My husband, for his constant support,

Our children, for their infinite patience and indulgence,

My parents for enabling me an academic career

And my father, who encouraged me to become an engineer.

Declaration

I hereby declare that except where specific reference is made to the work of others, the contents of this dissertation are original and have not been published elsewhere. This dissertation is the outcome of my own work using only cited literature.

Erklärung

Hiermit erkläre ich, dass der Inhalt dieser Dissertation, sofern nicht ausdrücklich auf die Arbeit Dritter Bezug genommen wird, ursprünglich ist und nicht an anderer Stelle veröffentlicht wurde. Diese Dissertation ist das Ergebnis meiner eigenen Arbeit mit nur zitierter Literatur.

Ulla Wagentristl, 27 November 2018

Acknowledgements

First, I want to thank Prof. Holger Ott for his advice and supervision.

I also want to thank OMV Exploration & Production GmbH for the permission to use their data and for the guidance I received through Dr. Torsten Clemens, DI Bettina Schumi and DI Markus Lüftenegger. I also would like to take the opportunity to thank each and every colleague for their cooperation.

Last, I want to thank DI Kata Kurgyis for her annotations and her practical support.

Abstract

OMV Exploration & Production GmbH is attempting a rejuvenation of the mature 16th TH reservoir in the Matzen Field in Austria. As one of the largest reservoirs in Middle Europe, the 16th TH still has a high potential regarding unrecovered hydrocarbons. To further exploit the potential of the 16th TH, it was decided to undertake an alkali-polymer flood. Preoperational tests include single-phase tracer and alkali core flood tests and two-phase polymer and alkali-polymer core flood tests. By means of the tracer experiments, the concept of numerical dispersivity replacing physical dispersivity and its meaning concerning the determination of the optimum grid cell size were investigated. The results were applied on the polymer and alkali-polymer experiments to be validated. Within the scope of the simulation of the polymer and alkali-polymer core flood experiments, the capability of a black oil simulator to reproduce EOR treatments was examined. The perceptions of these simulations were applied on field scale. The simulation results prove, that black oil simulations are essentially applicable on EOR simulations and that dispersivity can be used to determine the optimum grid cell size, although it leaves space for upscaling without significant loss of accuracy.

Zusammenfassung

OMV Exploration & Production GmbH ist bestrebt, die Produktion der Lagerstätte 16. TH des Matzenfeldes in Österreich deutlich zu erhöhen. Als eine der größten Lagerstätten Mitteleuropas hat der 16. TH weiterhin ein großes Potential bezüglich ungeförderter Kohlenwasserstoffe. Um das Potential des 16. TH weiter auszuschöpfen wurde entschieden, eine Alkali-Polymer-Flutung durchzuführen. Präoperative Kernflutexperimente beinhalten Einphasen-Tracer- und Alkali-Kernflutversuche und Zweiphasen-Polymer- und Alkali-Polymer-Kernflutversuche. Anhand der Tracerexperimente wurden das Konzept des Ersetzens von physikalischer Dispersivität durch numerische Dispersivität und seine Bedeutung für die Bestimmung der optimalen Gitterzellengröße untersucht. Zur Bestätigung wurden die Ergebnisse auf die Polymer- und Alkali-Polymer-Experimente angewandt. Im Rahmen der Simulation der Polymer- und Alkali-Polymer-Kernflutversuche wurde die Fähigkeit eines Black Oil Simulators, EOR-Behandlungen zu reproduzieren, untersucht. Die Erkenntnisse dieser Simulationen wurden auf die Größenordnung eines Feldes angewandt. Die Ergebnisse der Simulationen beweisen, dass Black Oil Simulatoren grundsätzlich für EOR Simulationen benutzt warden können und dass es mit Hilfe der Dispersivität möglich ist, die optimale Gitterzellengröße zu bestimmen, auch wenn Raum für Upscaling ohne signifikanten Genauigkeitsverlust bleibt.

Table of Contents

List of Figures

List of Tables

Nomenclature

F_{kr}	permeability reduction factor	[-]
F_{krr}	residual permeability reduction factor	[-]
HA	pseudo-acid component	[-]
k	permeability	[mD]
k_o	oil effective permeability	[mD]
k_p	effective aqueous polymer solution permeability	[mD]
k_{ro}	oil relative permeability	[-]
k_{rw}	water relative permeability	[-]
k_w	water effective permeability	[mD]
n_o	oil Corey parameter	[-]
n_w	water Corey parameter	[-]
S_w	water saturation	[-]
wt	weight	[N]
μ	viscosity	[cP]
$_o$	oleic phase	[-]
$_w$	aqueous phase	[-]

Abbreviations

AP	alkali-polymer
API	American Petroleum Institute
EOR	enhanced oil recovery
HPAM	partially hydrolyzed polyacrylamide
IFT	interfacial tension
IPV	iInaccessible pore volume
KBr	potassium bromide
MB	megabyte
NaCl	sodium chloride
Na_2CO_3	sodium carbonate
$NaHCO_3$	sodium bicarbonate
PAM	polyacrylamide
PV	pore volume
RF	recovery factor
RRF	residual resistance factor
SS	sub sea
TAN	total acid number
TH	Tortonian horizon
TU	Technische Universität
TW	Testwasser
WF	water flood

Chapter 1

Introduction

OMV Exploration & Production GmbH is looking into a rejuvenation of the mature 16th TH reservoir in the Matzen Field in Austria. Since production has been conducted for almost 70 years, the hydrocarbon production rate is naturally very low to the limit of becoming uneconomical, but as one of the largest reservoirs in Middle Europe, the 16th TH still has a high potential in terms of unrecovered hydrocarbons.

The field development strategy includes water injection (since 1968) and natural gas injection (since 1995). To further exploit the potential of the 16th TH, it was decided to take EOR measures. Since OMV Exploration & Production GmbH executed a successful polymer injection pilot in the 8th TH, another reservoir in the Matzen Field, this option was investigated. Related core flood experiments and simulations depicted, that the increase in production due to polymer injection would be too low to justify it. Due to the high TAN (>2) of the oil present in the 16th TH, an alkali-polymer flood might lead to substantial increase in oil production and was therefore chosen. The high acid content in the oil and presence of alkali ensure sufficient spontaneous in-situ surfactant generation, which makes alkali-polymer injection into the 16th TH even more attractive, since no, comparably costly, surfactants have to be purchased. The 16th TH contains two major production units (PU 216-10 and PU 216-20). The whole PU 216-20 and the most western part of PU 216-10 will be chemically flooded, so the targeted project can be described as a field rollout with pilot character.

The preceding core flood experiments include single-phase tracer and alkali core floods and two-phase polymer and alkali-polymer core floods. Aim of this study is to investigate the effects of dispersion and dispersivity on the results of history match simulations of these tests and to examine, how accurate core flood data can be utilized for field scale simulations. To potentially improve the simulation efficiency, the suitability of the dispersivity as a measure of the optimum grid cell size and the consequences of up- and downscaling are investigated. Simulation of the executed core floods and investigation of dispersivity effects will improve the understanding of the processes involved with alkali-polymer injection, and can contribute to an improvement of operating conditions of an alkali-polymer flood.

Within the scope of this thesis, not only methodologies for upscaling of core flood data to field scale simulations are investigated, but also the capability of a black oil simulator to accurately simulate EOR treatments. Use of a black oil simulator instead of a compositional simulator might be a valid option because of the more economical mode of operation in terms of simulation time, required memory or data management.

Chapter 2

Literature Review

The rejuvenation of mature fields with EOR methods plays a vital part in supplying the global energy demand. Compositional simulators play an important role in this task, although economic requirements may promote the use of phase-behavior based simulators to simulate chemical EOR methods. An important factor regarding flow through porous media is dispersion. Since dispersion and dispersivity are not implemented in common black oil simulators, reproducing physical dispersivity by numerical dispersivity might be an option. This effect may be achieved by optimizing the grid cell size.

2.1 Optimum Grid Size

The chosen grid size has a big influence on the results of a chemical flood simulation. Therefore, the determination of the optimum grid size is of great importance. Main problem is that an increase in grid cell size leads to a dilution of the injected chemicals, which causes the executed simulation to falsify the effectiveness of the process and therefore to deliver incorrect results. The complexity of a chemical EOR process indicates the application of a fine grid rather than a coarse grid. Since a fine grid is very computationally intensive, choosing a grid cell size smaller than necessary can induce severe consequences. Designing an economic optimization study might even become unfeasible. Therefore, it is essential to create a reliable upscaling method (Veedu, Delshad and Pope, 2010).

Different stimulation treatments react with dissimilar sensitivity to upscaling. Studies show that polymer flood simulations are less sensitive than water flood simulations. Apparent reason for that is the comparable long injection time typical for a polymer flood. As a result, polymer rheology and operation conditions influence the simulated recoveries to a much greater extent than variations in grid cell size (Yuan, Delshad and Wheeler, 2010).

2.2 Dispersion

Dispersion is defined as an increase in mixing caused by variations in velocity due to uneven fluid flow or concentration gradients originating in fluid flow. Together with diffusion and convection, it contributes to the spread of a propagation front and is therefore an important parameter concerning EOR processes, but due to its scale dependency, it is hard to be quantified properly. Two types of dispersion are differentiated, the dispersion in the direction of gross fluid movement (longitudinal dispersion) and the dispersion normal to the direction of gross fluid movement (transverse dispersion). They are represented by the longitudinal dispersion coefficient D_L and the transverse dispersion coefficient, D_T. The dispersion coefficients cannot be determined by fundamental principles, but must be experimentally estimated, individually for every flow setting. The longitudinal dispersion coefficient is the sum of molecular diffusion and convective dispersion. Depending on the setting, the dispersion coefficient can be diffusion dominated, convection dominated or balanced, as it is the most frequent case regarding flow in porous media (Sheng, 2011).

During a simulation, numerical dispersion is added to the physical dispersion, artificially increasing the apparent level of mixing (Solano, Johns and Lake, 2000), (Parakh and Johns, 2004). It increases with increasing grid block size and can be reasonably larger than physical dispersion (Haajizadeh et al, 1999), (Lantz, 1971), (Fanchi, 1983). Opposite to the numerical dispersion, velocity variations are reduced due to an increase in grid block size, which results in less mixing and a decrease of the dispersion (Garmeh,Johns and Lake, 2007), which tempers the extent of the numerical dispersion. In a homogeneous reservoir model, the observed dispersion is purely a matter of numerical dispersion and, if applied, input dispersivity.

2.3 Dispersivity

Dispersivity is a specific of a porous medium and includes the typical grain size and the inhomogeneity of reservoir rock. It is an important parameter r the efficiency of an EOR process and can be determined using conservative tracers. Opposite of dispersion, dispersivity is independent of the flow velocity. It is scale dependent in a directly proportional way and this dependency makes it difficult to include it in simulations. Simulations including fine grids use smaller dispersivities, simulations with coarse grids require larger dispersivities (Sheng, 2011). Usually longitudinal dispersivity is assumed to be larger, and as a result, transverse dispersivity is neglected. However, it becomes important when reservoir heterogeneities cause changes in the flow direction. In rare occasions, it can even become larger than longitudinal dispersivity. Associated with dispersion, longitudinal, transverse and numerical dispersivity exist.

The numerical dispersion can be defined as in **eq.1** (Adepoju and Lake, 2012).

$$\alpha_{num} = \frac{\Delta x}{2} + \frac{v\Delta t}{2} \qquad (1)$$

α_{num}	numerical dispersivity [m]
Δx	grid cell length [m]
v	interstitial velocity [m/s]
Δt	time step [s]

Investigations on the optimum grid cell size found that for small time steps, the numerical disperisvity is approximately half as large as the grid cell size. Simulation models with optimum grid cell size have a numerical dispersion equal the total dispersion of a fine scale model (Adepoju and Lake, 2012).

2.4 Mode of Action of Polymer Injection

Regarding displacement of one fluid by another fluid, displacement stability is directly related to displacement efficiency. Displacement stability is determined by the mobilities of the involved fluids. If the mobility of the displacing fluid is lower than the mobility of the displaced fluid, stable displacement takes place. Since changing oil mobility is often not achievable without using thermal EOR methods, the water mobility is often changed by injection of chemicals, mainly polymers. Polymers reduce viscous fingering thus improve volumetric sweep efficiency, reduce channeling and delay breakthrough by increasing the viscosity of the displacing water. How effectively polymer injection increases ultimate incremental oil recovery primarily depends on the amount of polymer injected though the allowable injection pressure limits polymer concentration. Polymers are only soluble in water but not in oil, and fluid flow stays immiscible because of polymer injection. They are able to form a hydrogen bond with water molecules which leads to rock surfaces becoming more water-wet due to the improved affinity between the polymer-bond water molecules and the adsorption layer.

2.5 Polymer Characteristics

The effectiveness of a polymer injection is mainly determined by certain polymer characteristics. The main parameters affecting polymer performance are the polymer viscosity, polymer retention, pore volume inaccessible to polymers and pore plugging.

2.5.1 Polymer Viscosity

As discussed earlier, viscosity is the most important parameter of a polymer solution. The higher the viscosity of the displacing fluid, the more favorable is the mobility ratio and therefore the displacement efficiency. Main factors influencing the viscosity of a polymer solution are: polymer concentration, brine salinity, shear rate, pH of the fluid, temperature and molecular weight, where a higher molecular weight has a higher viscosifying power. Since with Flopaam™ 3630 S a synthetic polymer was used, possible divergent effects on biopolymers are not discussed within the extent of this thesis. Additional information about Flopaam™ 3630 S are provided in Appendix A.

- ### Concentration Effect on Polymer Viscosity

The polymer viscosity increases in a non-linear way with increasing polymer concentration as illustrated in Figure 2-1.

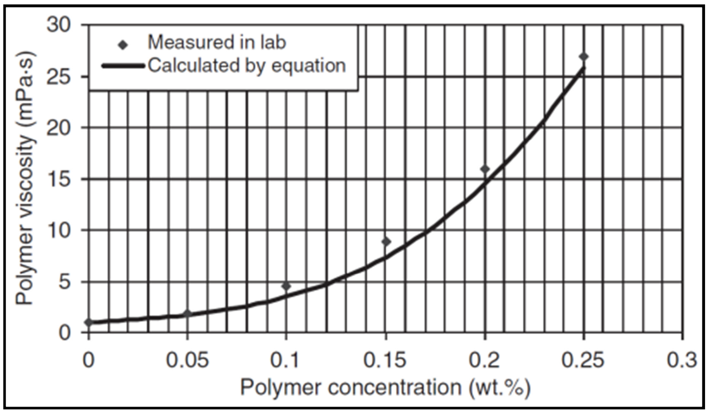

Figure 2-1: Effect of polymer concentration on viscosity (Sheng, 2011)

- ### Salinity Effect on Polymer Viscosity

The effect of salinity on polymer viscosity depends on the type of polymer used. The viscosity of a PAM solution increases with increasing monovalent salt concentration as well as increasing divalent salt concentration. In contrast, the viscosity of a HPAM solution decreases with increasing monovalent salt concentration. The effect of divalent salts on HPAM solution viscosity is complex. If hydrolysis is low, the solution viscosity first decreases until reaching a minimum after which it increases. If hydrolysis is high, the solution viscosity decreases sharply until precipitation occurs.

- ### Shear Rate Effect on Polymer Viscosity

The viscosity of polymer solutions is strongly shear dependent and decreases with increasing shear rate. They can be seen as pseudo plastic fluids and their behavior can be described by a power-law model.

- ### pH Effect on Polymer Viscosity

The pH of a polymer solution influences polymer viscosity by affecting hydrolysis, therefore it acts only on HPAM. An increase in pH leads to a decrease of HPAM solution viscosity. Such a rise is typically caused by adding alkali.

- ### Temperature Effect on Polymer Viscosity

At low shear rates, the shear viscosity of a polymer solution decreases with increasing temperature due to reduced friction between the molecules present in the solution. This effect varies for different polymers; HPAM tends to be insensitive to temperature effects.

2.5.2 Polymer Retention

Talking about polymers, retention combines adsorption, mechanical trapping and hydrodynamic retention. It depends on polymer type, salinity of the solvent and the rock surface. Mechanical trapping and hydrodynamic retention are linked and only appear in flow-through porous media. Polymer retention causes the polymer molecules to run slower through the formation and consequently leads to a delayed polymer breakthrough.

- ### Polymer Adsorption

Adsorption describes the binding of the injected polymer to the rock surface and is a fundamental property of the polymer-rock surface-system and the most important retention mechanism. It occurs due to mainly physical adsorption, van der Waals forces and hydrogen bonding and depends on the area of the rock surface exposed to polymers. Polymer adsorption is considered being an irreversible process in most cases although small amounts of polymer can be removed from the rock surface by prolonged exposure to water. It depends on the mineralogy of the reservoir rock, salinity of the injected brine, polymer concentration, hydrolysis, permeability and temperature. The adsorption of HPAM is much higher on calcium carbonate than on silica due to strong interactions between Ca^{2+} ions from the rock surface and the carboxylate groups on the polymer molecules and it increases with increasing salinity. Polymer concentration has a weak impact on adsorption because the concentration curve quickly levels as illustrated in Figure 2-2.

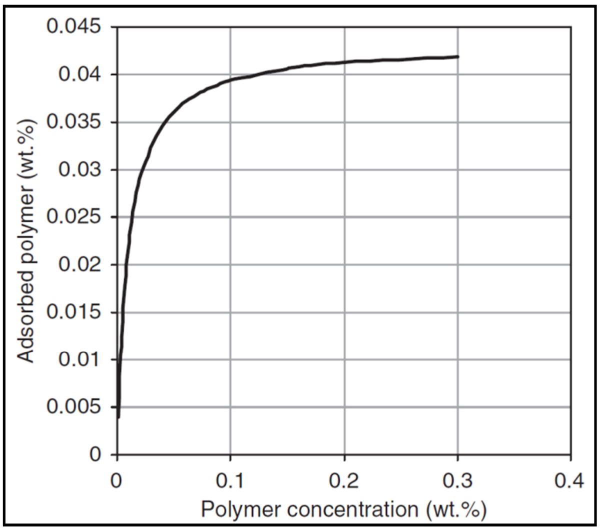

Figure 2-2: Effect of polymer concentration on adsorption (Sheng, 2011)

The effect of hydrolysis on polymer adsorption is similar to the effect on polymer solution viscosity. Adsorption decreases with increasing hydrolysis until a minimum is reached, after which it starts to increase. Lowering permeability leads to higher polymer adsorption, either due to increased likelihood of mechanical trapping or due to clay that is found more often in low permeability formations.

- **Mechanical Trapping of Polymers**

Mechanical trapping describes the wedging of polymer molecules in flow channels. The probability for molecules being tapped rises with increasing molecule size and decreasing permeability and depends on pore size distribution. If polymers are lodged in pores with average pore size, a build-up near the injection well will develop and the formation will be plugged. Therefore polymer injection should preferably take place in high permeability formations or be preceded by hydraulic fracturing. Mechanical trapping can also be avoided by pre filtering the polymer to ensure the use of molecules of appropriate size.

- **Hydrodynamic Retention of Polymers**

Hydrodynamic retention describes the trapping of polymer molecules due to abruptly increased flow rates and is a reversible process.

2.5.3 Inaccessible Pore Volume

Inaccessible pore volume describes the part of the pores that is smaller than the polymer molecules and therefore cannot be entered by them but is bypassed. It is consistently observed during polymer flow through porous media and is seen as a general characteristic. The IPV causes the polymer solution to run faster through the formation and therefore leads to an accelerated polymer breakthrough.

2.5.4 Pore Plugging

The term pore plugging refers to a permeability reduction due to polymer adsorption. The rock shows to be less permeable to a polymer solution than to water. This effect is called permeability reduction factor and defined as shown in **eq.2** (Sheng, 2011).

$$F_{kr} = \frac{k_w}{k_p} \qquad (2)$$

F_{kr}	permeability reduction factor [ ]
k_w	rock permeability when water flows [mD]
k_p	rock permeability when aqueous polymer solution flows [mD]

Since polymer adsorption is considered an irreversible process, the rock permeability is permanently altered as result of a polymer flood. It is quantified by the residual permeability reduction factor as is defined in **eq.3** (Sheng, 2011).

$$F_{krr} = \frac{Rock\ perm.to\ water\ before\ polymer\ floow}{Rock\ perm.to\ water\ after\ polymer\ flow} \qquad (3)$$

F_{krr} residual permeability reduction factor [ ]

The residual permeability reduction factor is usually represented by the residual resistance factor as described in **eq.4** (Sheng, 2011).

$$RRF = \frac{water\ mobility\ before\ polymer\ flow}{water\ mobility\ after\ polymer\ flow} \qquad (4)$$

RRF residual resistance factor [ ]

Resistance includes the effects of both permeability and viscosity change. In the case of water flooding preceding and succeeding a polymer flood, the water viscosity is constant and resistance only depends on the permeability change. The residual resistance factor is higher for polymers with a higher molecular weight and for polymer solutions with a wide molecular weight distribution. Even though a high residual resistance factor is favorable because it leads to a higher oil recovery factor, the polymer molecular weight is limited by the formation permeability; a high molecular weight is related to large molecules and encourages as a result pore plugging. Next to a possible wettability change, the residual resistance factor is the only manner in which relative permeability is altered due to polymer injection (Sheng, 2011).

2.6 Mode of Action of Alkaline Injection

As already discussed, the increase in recovery factor due to polymer injection is based on alteration of the mobility ratio. Another possibility is to mobilize trapped oil. In the case of alkali injection (caustic flooding), alkali agents react with organic acids present in crude oil and produce surfactants, which lower the interfacial tension. This reduction allows for emulsification of crude oil and its potential movement. Additionally, the wettability of the reservoir might be changed due to an alkaline flooding, where a change from oil-wet to water-wet will increase oil production. Alkalis typically used include sodium hydroxide, sodium carbonate, sodium orthosilicate, sodium tripolyphosphate, sodium metaborate, ammonium hydoxide and ammonium carbonate, which all lead to a similar reduction of IFT. Dissociation of alkalis results in high pH, where the pH values vary with salt content. For chemical treatments, alkaline is often combined with polymer. One reason is that alkali only improves sweep efficiency, not displacement efficiency. Added polymers improve mobility control by stabilizing flow to prohibit viscous fingering and early water breakthrough. Additionally, alkaline concentrations, which are required to obtain low interfacial tensions, are not capable of propagation through the reservoir due to consumption by ion exchange and dissolution.

2.6.1 In Situ Soap Generation

During an alkali or an AP flooding, alkali is injected into a reservoir where it reacts with the saponifiable organic acids (naphtenic acids) of the present crude oil, mainly carboxylic acids. The composition of these acids is individual for each crude oil. To cover the included processes fundamentally, a pseudo-acid component (HA) is used instead of a particular acid. The overall process of acid reacting with alkali to form surfactant and water is described by **eq.5** (Sheng, 2011) and the involved sub processes are illustrated in Figure 2-3.

$$HA_o + NaOH \leftrightarrow NaA + H_2O \qquad (5)$$

The involved sub processes are partitioning of the HA between the oleic and the aqueous phases (**eq.6**) (Sheng, 2011) and hydrolysis of the aqueous pseudo-acid component (**eq.7**) (Sheng, 2011), leading to the production of a soluble anionic surfactant A^- with a long organic chain.

$$HA_o \leftrightarrow HA_w \qquad (6)$$

$$HA_w \leftrightarrow H^+ + A^- \qquad (7)$$

The extent of the hydrolysis highly depends on the pH of the aqueous solution and it takes place at the water/oil interface. Only a part of the acids in the oil become ionized in the presence of alkali and the forming hydrogen bonds between the ionized and neutral acids leads to the formation of acid soaps. Water concentration remains unchanged due to the described processes since an increase in OH^- ions leads to a decrease in H^+ ions.

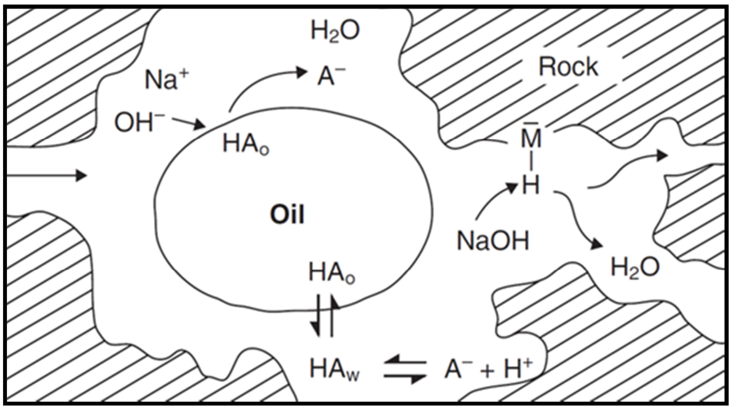

Figure 2-3: Oil recovery by in situ soap generation (Sheng, 2011)

2.6.2 Interfacial Tension

The dynamic minimum IFT generally is an important parameter in enhanced oil recovery. A low IFT has the capability to mobilize residual oil by breaking it into small droplets. A minimum IFT exists only over a narrow range of alkaline concentrations. At lower and higher concentrations, the IFT increases quickly and a too high concentration leads to a significant cut in IFT reduction, as illustrated in Figure 2-4.

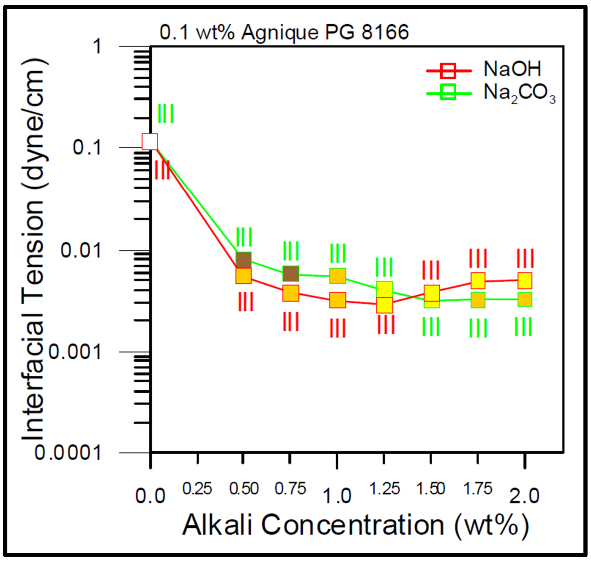

Figure 2-4: Interfacial tension behavior (OMV Exploration & Production GmbH, 2018)

Different alkalis lead to different interfacial tensions at equal alkaline concentration. Although the pH of an alkaline solution is one of the main parameters affecting the IFT, other active compounds can contribute to its reduction.

2.6.3 Emulsification

An eventual emulsification of the crude oil in the reservoir and its subsequent mobilization and coalescence with each other may lead to an increased sweep efficiency and promote the formation of a continuous oil bank. The extent of emulsification is mainly determined by the interfacial tension of the water and oil, where a low IFT facilitates the generation of an emulsion. Certain components of crude oils influence emulsification. Acidic components encourage emulsification due to their capability of reducing interfacial tension and asphaltene surfactants enhance the stability of an emulsion. Generation of an emulsion is not completely reversible and in an alkaline flooding, it is an instant process and the generated emulsions are very stable.

2.6.4 Total Acid Number

The total acid number or TAN number quantifies the potential of a crude oil to generate surfactants in the presence of alkali. It is defined as the mass of potassium hydroxide in mg necessary to neutralize one gram of crude oil. Acid numbers are graded as either low (0.1 to 0.25), intermediate (0.3 to 1) or high (>1), where most crude oils have an acid number lower than 5.0. Even though the acid number of a crude oil can be determined easily, no predictions about the extent to which surfactants will be converted into soap can be made.

2.7 Alkali Interactions with Rock

The complex mineralogy of a reservoir rock enables a large amount of possible reactions with the injected alkali, which are difficult to be captured. Especially present clays have a big impact on the displacement of an alkaline solution. Contact with alkali leads to an ion exchange between the rock surfaces and to the chemical solution of rock minerals into the alkaline solution in a fast and reversible manner. The triggered chemical reaction causes the consumption of the base present in the alkaline solution as it propagates through the reservoir. Additionally, certain rock minerals containing divalent ions (Ca^{2+}, Mg^{2+}) can react directly with the injected alkali in a slow and irreversible manner, and potentially causing plugging.

2.8 Alkaline Effects on Polymer Viscosity

The polymer viscosity is potentially altered by two different effects, the increased cation electric shield effect (salt effect) and the increased hydrolysis effect. The electric shield effect is referred to as the alkaline concentration effect, causing a decrease in polymer viscosity and the increased hydrolysis effect is referred to as the alkaline dynamic effect, causing an increase in polymer viscosity. The absolute effect on the viscosity depends on the fact which effect dominates. Usually the salt effect is bigger.

2.8.1 Alkaline Dynamic Effect

A reaction between polymer and alkali leads to hydrolysis of the polymer and consumption of the alkali. The hydrolyzed polymer exhibits increased viscosity. Due to the decreased alkali concentration, the pH also decreases, lowering the potential of the chemical solution to generate soap and reduce interfacial tension. A potential solution to this problem can be the application of buffer alkalis to maintain a constant pH over a wide range of alkali concentrations.

2.8.2 Alkaline Concentration Effect

Addition of alkali only increases the viscosity of hydrolyzed polymers. With other polymers, the salt effect reduces the stretch of polymer molecules in solution when alkali concentration increases. This leads to a decrease of the polymer viscosity.

2.9 Alkaline Adsorption in Alkali-Polymer Systems

In an alkali-polymer system, both alkaline and polymer adsorption are reduced compared to a one-component slug. Alkaline adsorption decreases because the present polymer limits alkali-rock contact. Polymer adsorption decreases because the present alkali reacts with a part of the available cations, leaving the rock surface more negatively charged.

2.10 Synergy between Alkali and Polymer

In an alkali-polymer flooding, the benefits of both components are combined. The alkali contributes soap generation, emulsification and wettability change, and the polymer provides the necessary mobility control. As a result, it has a better displacement potential compared to the individual treatments. Three different modes of injection are available: alkali followed by polymer, polymer followed by alkali and alkali and polymer co-injection, where the latter generates the highest recovery factors. Additionally to the polymer, possible precipitation caused by alkali can help to increase sweep efficiency. These precipitations can reduce water and oil relative permeability but compared to polymer, they can easier flow through pores without blocking them. Another positive effect occurs in the case of low-injectivity wells, where the reduction of the polymer viscosity caused by the alkali is beneficial. The low viscosity at the beginning of the treatment improves the chemical slug injection. As the alkali is consumed while propagating through the reservoir, the viscosity of the polymer solution increases. Again, the final effect depends on the fact which type of adsorption dominates (Sheng, 2011).

2.11 Simulator

The simulations were all executed with the ECLIPSE 100 simulator from Schlumberger. It is a fully-implicit black oil simulator. It provides free format input, simulation of one-, two- or three-phase systems and corner-point and block-center geometry. Main advantage of the fully-implicit method is that it provides stability over long time steps and that it is well suited for small cell sizes typical for core flood simulations (Schlumberger, 2017). Within the scope of the present Master Thesis, one-phase systems (water), two-phase systems (water and oil), tracer tracking, the polymer model and the surfactant model were used. In ECLIPSE 100, the effects of alkali injection cannot be simulated independently, but only coupled with surfactant injection. To execute an alkali-polymer simulation, not the alkali parameters but the parameters of the in situ generated surfactants have to be matched and therefore the surfactant model has to be used. The equations mentioned in this chapter are summarized in Appendix A.

2.11.1 The ECLIPSE 100 Polymer Model

The ECLIPSE 100 Polymer Model is a fully implicit model that allows simulating polymer floods. It is able to account for the viscosity change of the injected brine induced by the added polymers, viscosity degradation caused by non-Newtonian shear effects at high velocities, polymer adsorption and reduction of the relative water permeability and inaccessible pore volume, which is assumed constant for each rock type. Properties affected by the polymer concentration are water viscosity and polymer adsorption. Properties remaining unaffected are water density and formation volume factor. The following parameters were utilized during the polymer flood simulations executed within the scope of this thesis.

- ### Relative Permeabilities

Hydrocarbon permeabilities are assumed to be unaffected by polymers and the hydrocarbon phases are treated using the usual black-oil formulations and interpolating PVT properties as a function of pressure and temperature. Since the aqueous phase is affected by polymers, the standard black-oil equation had to be modified and additional equations had to be added to describe polymer flow properly (**eq.15** to **eq.17**).

- ### Viscosities

Beside polymer concentration, the water viscosity depends on the degree of mixing of the polymer slug and water and is covered by the viscosity parameters. Physical dispersion at the leading edge and fingering at the rear edge of the slug are treated with the Todd-Longstaff technique (**eq.18**). It quantifies the degree of segregation between the water and polymer solution where a Todd-Longstaff parameter of 1.0 represents complete mixing and a Todd-Longstaff parameter of 0.0 represents complete segregation.

- ### Polymer Adsorption

  Adsorption is treated as an instantaneous effect and can be set as irreversible. It may either be specified as a function of polymer concentration or as an analytical model depending on rock permeability. Both options offer to model salinity dependence.

- ### Permeability Reduction and Inaccessible Pore Volume

The permeability reduction is computed from the residual resistance factor and the maximum adsorbed polymer concentration (**eq.19**), which have to be specified for each rock type and must not be zero. If necessary, the RRF can also be defined on a cell-by-cell basis. The inaccessible pore volume has also to be defined for each rock type and is applied to each individual cell (Schlumberger, 2017).

2.11.2 The ECLIPSE 100 Surfactant Model

The ECLIPSE 100 Surfactant Model is a fully implicit model that allows simulating enhanced floods, where surfactants reduce the capillary pressure between the water and the oil phases and therefore the interfacial tension. It is able to account for the reduction in the residual saturation and the modification of the relative permeability curves. Properties affected by the surfactant concentration are water viscosity and surfactant adsorption. With the ECLIPSE surfactant model, it is not possible to model the chemical processes related to surfactants but the important features can be covered on field scale. Beside the parameters used during the polymer flood simulations, the following parameters were utilized during the executed alkali-polymer simulations:

Relative Permeability Model

The transition from immiscible relative permeability curves to miscible relative permeability curves can be simulated with the Surfactant Relative Permeability Model. A parameter for interpolation between these curves is defined as a function of the logarithm (base 10) of the capillary number. To calculate the used relative permeability at a given value of the miscibility function, first the saturation endpoints of the curves are interpolated and both relative permeability curves are scaled to meet the new saturation endpoints. Second, the relative permeability of the current saturation is looked up at the scaled curves and interpolated accordingly to the weighting function F (**eq.20**). The course of action is illustrated in Figure 2-5.

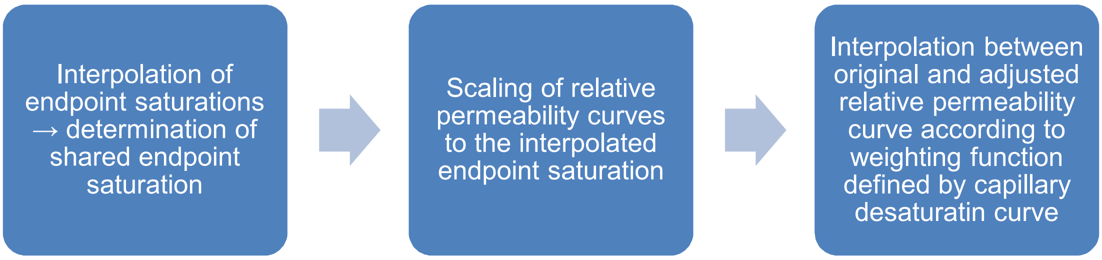

Figure 2-5: Determination of miscible flow relative permeability

Capillary Pressure

With increasing surfactant concentration, the capillary pressure will decrease. This process and the related decrease in interfacial tension lead to the reduction in residual oil saturation (**eq.21 and eq.22**).

Water Viscosity

The alteration of the viscosity by the surfactants is modeled as a function of surfactant concentration (**eq.23**).

Surfactant Adsorption

The surfactant adsorption is a function of the surrounding surfactant concentration. It is modeled as an instantaneous process using an adsorption isotherm defined as a function of surfactant concentration (**eq.24**). Optionally, de-adsorption can be implemented (Schlumberger, 2017).

Chapter 3

Data and Methodology

3.1 Core Flood Experiments

Within the scope of this thesis, the outcomes of five core flood experiments were investigated. They were executed at Technische Universität Clausthal with a HOT cEOR flooding rig. In total, three single-phase experiments and two two-phase experiments were carried out. Figure 3-1 shows a schematic of the experimental setup.

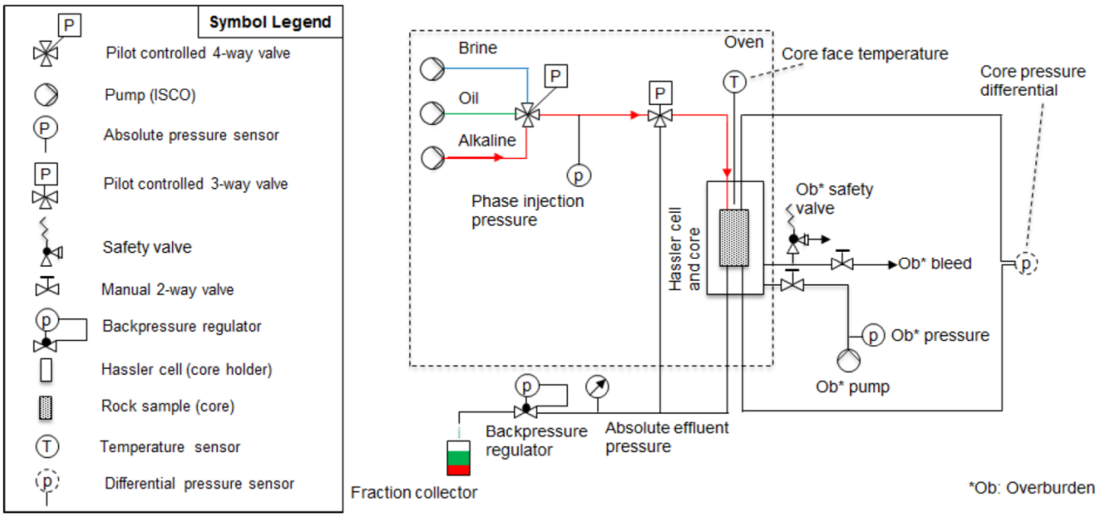

Figure 3-1: Schematic of the experimental core flooding setup (HOT Microfluidics GmbH, 2017)

3.1.1 Single-phase Experiments

Two tracer tests (‘Tracer Test 1’ and ‘Tracer Test 2’) using potassium bromide (KBr) and one alkaline injection test (‘Alkaline Test’) using sodium carbonate (Na_2CO_3) were performed. First, the cores were initialized. They were vacuum saturated with the synthetic formation brine ‘Testwasser 1’ (TW1) and aged for one week. Table 3-1 shows the parameters of the aging process.

Table 3-1: Parameters of the aging process (single-phase)

Parameter	Value	Unit
Temperature	60	°C
Radial pressure	70	bar
Pore pressure	2	bar

The core initialization was succeeded by following injection sequence: Synthetic formation brine injection – tracer/alkaline injection – synthetic formation brine injection, where the effluent of respective first brine injection was collected as one sample. Table 3-2 and Table 3-3 show the respective setups.

Table 3-2: General setup (single-phase)

Parameter	Value	Unit
Experiment temperature	60	°C
Radial confining pressure	70	bar
Pore pressure	2	bar
Initial saturation	100	%
Core length	29.1	cm
Core diameter	2.93	cm
Core mass (dry)	400.76	g
Brine density (TW1) at 22.5 °C	1	g/cm³
Porosity	21.83	%
Brine permeability (average)	1513	mD

Table 3-3: Specific parameters (single-phase)

Test	Agent	Doping [g/l]	Injection rate [ml/hour]	Injected volumes (brine – agent – tracer) [ml]	Sample Size [ml]
Tracer Test 1	KBr	1	50	50 – 150 – 150	2
Tracer Test 2	KBr	1	2	50 – 150 – 150	2
Alkaline Test	Na_2CO_3	7	1.9	25 – 129.2 – 133	1.9

Records include the elapsed time, differential pressure and core temperature. Additionally, the ion concentrations and the pH of each sample were measured. Further measurements included viscosity, shear rate and electrical conductivity. Additional information on the experimental setup is provided in Appendix B.

3.1.2 Two-phase Experiments

One polymer injection test and one alkali-polymer injection test were performed. First, the cores were cleaned and routine core analysis took place. Hydrocarbons were removed by toluene injection and salts were leached out by methanol injection. Afterwards it was flow-through saturated with the synthetic formation brine TW1 and aged for one week. Table 3-4 shows the parameters of the aging process.

Table 3-4: Parameters of the aging process (two-phase)

Parameter	Value	Unit
Temperature	60	°C
Radial pressure	30	bar
Pore pressure	3	bar

Afterwards, the cores were initialized with a mixture of crude oil from the 16th TH and 15 vol.% cyclohexane until the target oil saturation of approximately 20% was reached. The oil from the reservoir was mixed with cyclohexane to achieve the in-situ viscosity at 60 °C (6 mPa s). Initialization was succeeded by following injection sequence: Synthetic formation brine injection – chemical slug injection (both two-phase floods). Within the Polymer core flood experiment, the chemical slug injection was followed by synthetic formation brine injection and synthetic formation brine injection doped with KBr (as a tracer). Table 3-5 to Table 3-7 show the respective setups.

Table 3-5: General setup (two-phase)

Experiment	Polymer injection	AP injection	
Parameter	**Value**	**Value**	**Unit**
Experiment temperature	60	60	°C
Radial confining pressure	30	30	bar
Pore pressure	3	3	bar
Average initial water saturation	20.12	19.85	%
Core length	29.55	29.5	cm
Core diameter	2.93	2.93	cm
Core mass (brine saturated)	451.58	449.39	g
Brine density (TW1) at 22 °C	1.01	1.01	g/cm³
Oil density at 22 °C	0.89	0.89	g/cm³
Porosity	23.19	25.39	%
Brine permeability (average)	1489	1331	mD

Table 3-6: Specific parameters (Polymer flood)

Agent	Doping [g/l]	Injection rate [ml/hour]	Injected volumes (brine – chem. slug - brine – [ml]	Sample size [ml]
Flopaam™ 3630 S	2	1.986	143 – 43 – 85 – 78	1.986

Table 3-7: Specific parameters (AP flood)

Agent	**Doping [g/l]**	**Injection rate [ml/hour]**	**Injected volumes (brine – chem. slug) [ml]**	**Sample size [ml]**
Flopaam™ 3630 S	2	2.178	141 – 153	2.178
Na_2CO_3	7			

Records include the elapsed time, differential pressure and core temperature. Additionally, the phase volumes (oleic, emulsion and aqueous) of each sample were measured. In the effluent, no emulsion could be verified. Further measurements included viscosity, shear rate and electrical conductivity. Additional Data are provided in Appendix B.

3.2 Selection of Core Material

For the core floods, Bentheimer sandstone was used as core material. Main reason is simply that no sufficient core material from the reservoir horizon exists. Additionally, the gained experience will improve the outcome of eventual future core flood test executed with reservoir rock.

3.2.1 Characteristics of Bentheimer Sandstone

Bentheimer sandstone is easily available since mined from outcrops and its lateral continuity and block scale homogeneity makes it ideal for laboratory use. It forms a shallow marine sedimentary deposition. Reasons for being an ideal sedimentary rock for laboratory tests are the consistency regarding mineralogy, grain size distribution, porosity, permeability and dielectrical values and limited amount of minerals. Porosity is in the range of 21% to 27% and permeability in the range of 520 to 3020 mD. Average pore body diameter is 0.014 mm and average pore throat diameter is 0.012 mm. Figure 3-2 shows a representative Bentheimer sandstone sample.

Figure 3-2: Representative Bentheimer Sandstone (OMV Exploration & Production GmbH, 2018)

Bentheimer sandstone consists mainly of monocrystalline quartz with polycrystalline feldspars, authigenic clay (weathering product of feldspars) and iron-(hydr)oxides. The high quartz content results in a high mechanically stability which makes handling easier. Table 3-8 summarizes the distribution of the predominant minerals (Peksa, Wolf and Pacelli, 2015).

Table 3-8: Mineral distribution in Bentheimer sandstone (Peksa, Wolf and Pacelli, 2015)

Mineral	**wt%**
Quartz	91.7
Feldspars	4.86
Clay minerals	2.68
Pyrite and iron (hydro)oxides	0.17

3.3 Geological Background

3.3.1 The Matzen Field

The Matzen Field is located approximately 25 km northeast of Vienna in the central part of the Vienna Basin and is one of the largest multi-pool oil and gas field onshore Europe (Kienberger and Fuchs, 2006). It is approximately 10 km long and 5 km wide and consists of 36 hydrocarbon bearing horizons and is part of the Tertiary pull-apart structure of the Vienna Basin (Kienberger and Fuchs, 2006), (Arzmüller et.al, 2006).

3.3.2 The 16th Tortonian Horizon

The 16th Tortonian horizon (also 16th Badenian horizon or ‘Matzen Sand’) was discovered in 1949 and is one of the most important zones in the Vienna Basin according to production (Arzmüller, et al. 2006), and the most crucial part of the Matzen Field. It has a pore volume of 112 million m³ (94.56 in the oil zone and 17.64 in the gas zone) (Kienberger and Fuchs, 2006). Figure 3-3 shows the location in the Vienna Basin.

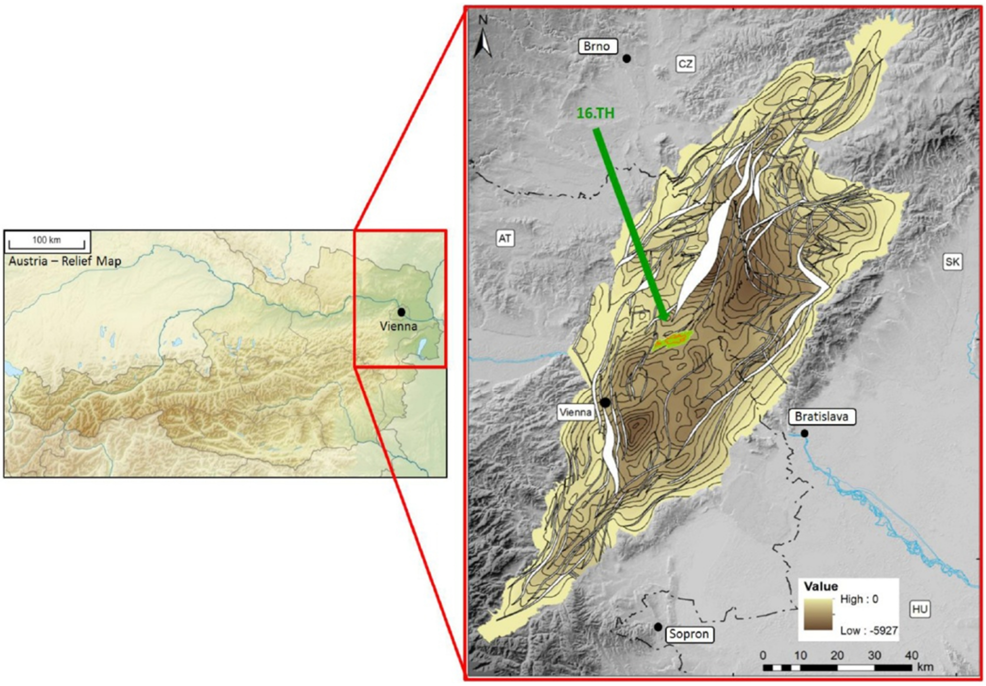

Figure 3-3: Location of the 16th TH in the Vienna Basin (Giden et al, 2016)

The pay thickness varies strongly from 1 m to 70 m. It is built from a relatively homogeneous blocky transgressive sand with excellent reservoir characteristics and subdivided into seven onlapping layers by discontinuous, hard, low permeable, calcite layers as illustrated in Figure 3-4. These vertical barriers are 0.1 to 1 m thick and reduce sweep efficiency, leaving certain areas completely unswept and are therefore critical for production (Kienberger and Fuchs, 2006), (Giden et al, 2016). Material was deposited into an erosional relief, which explains the fast changes in net pay thickness over short distances.

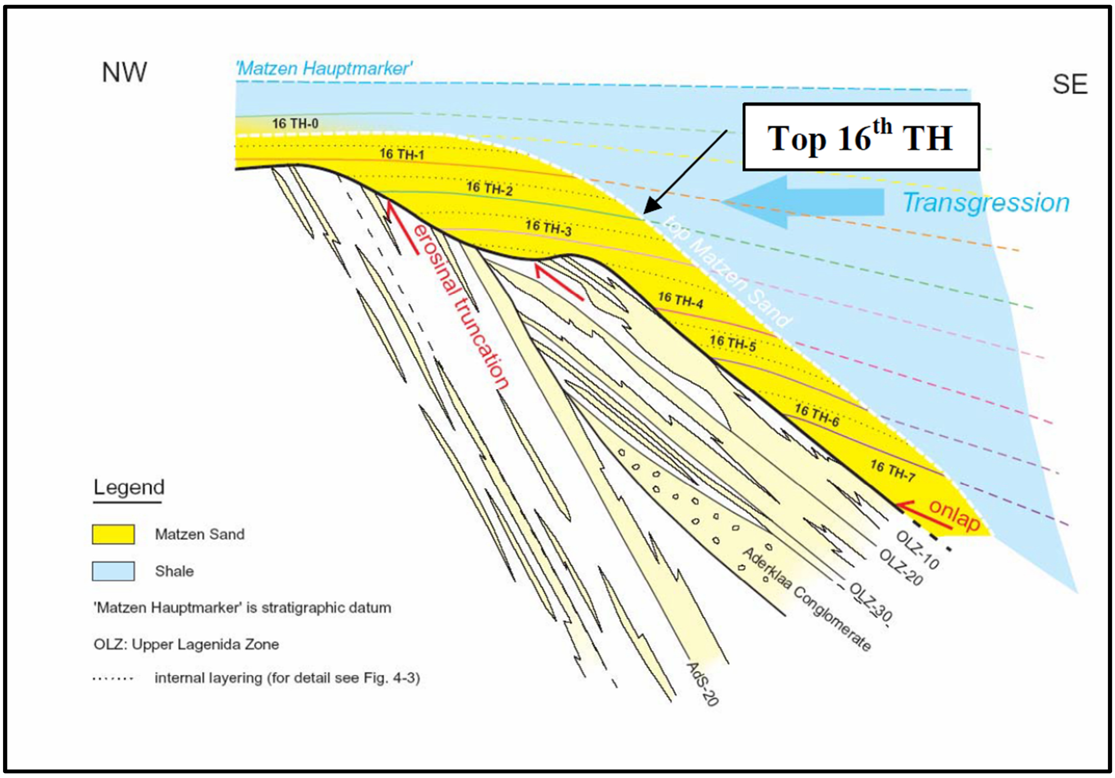

Figure 3-4: Layer Structure of the 16th TH (Kienberger and Fuchs, 2008)

Figure 3-5 shows the top structure of the 16th TH and displays the locations of the existing production units.

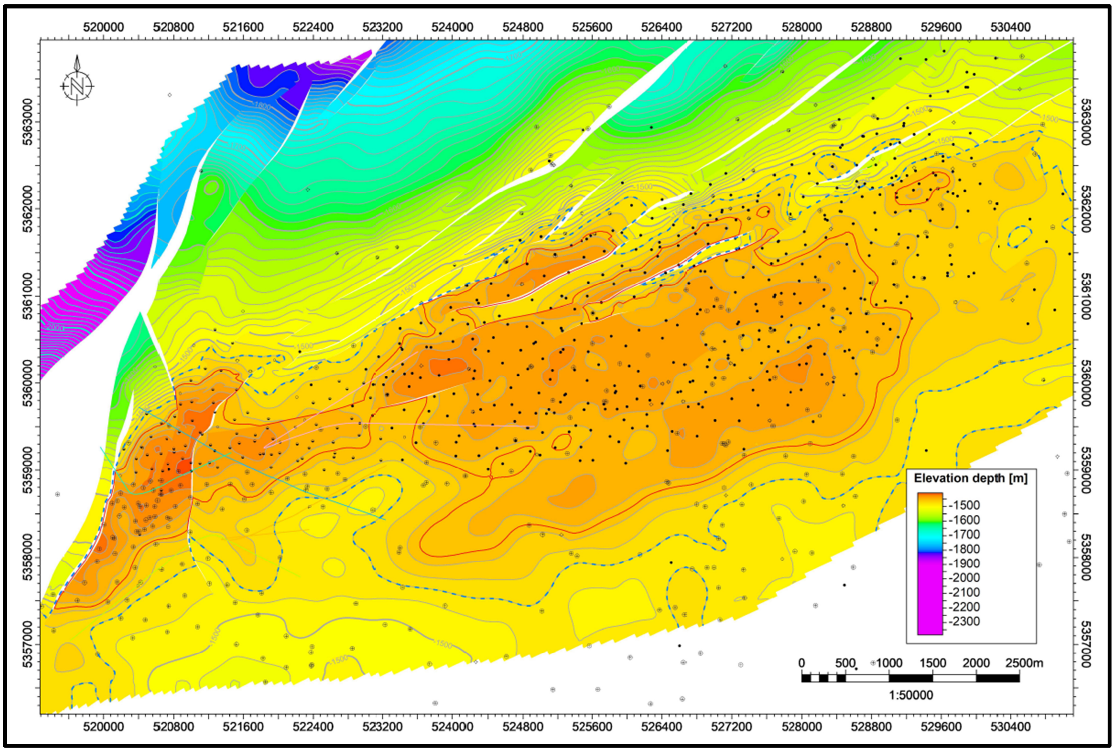

Figure 3-5: Top structure map of the 16th TH along the Matzen Field (OMV Exploration & Production GmbH, 2018)

The sand shows excellent porosity and permeability. Under initial conditions, a gas cap was present in all reservoir compartments. Driving mechanisms are water drive (81%), provided by a strong aquifer and water injection, gas cap drive (9.4%) and solution gas drive (9.6%) (Kienberger and Fuchs, 2006). Table 3-9 summarizes the most important reservoir parameters.

Table 3-9: Reservoir properties of the 16.TH (Kienberger and Fuchs, 2006)

Property	**Value**	**Unit**
Average permeability	1190	mD
Permeability range	17.8 - 20,4000	mD
Average Porosity	27	%
Porosity range	17 - 42	%
Specific oil gravity	25	°API
Viscosity at initial conditions	5.8	cP
Initial solution gas ratio	44.8	m^3/m^3
Initial reservoir pressure at volumetric center	163.6	bar
Initial reservoir temperature	60	°C
Average initial water saturation	18.6	%
Initial water saturation range	11.2 - 40.2	%
Average oil net sand thickness	17.1	m
Effective gas sand thickness	8.7	m
Initial oil-water-contact	1490	m SS
Initial gas-oil contact	1455	m SS
Estimated practical oil recovery factor	53.2	%

Production history includes water injection since 1968, which led to an annual production decline reduction from 8.3% to 4% as illustrated in Figure 3-6. From 1995 on, natural gas injection led to an annual production decline reduction from 4% to 2%. 85% of the current production are accountable to these measures. The production profile is typical with early peak production and extended tail production as illustrated in Figure 3-6 (Kienberger and Fuchs, 2006).

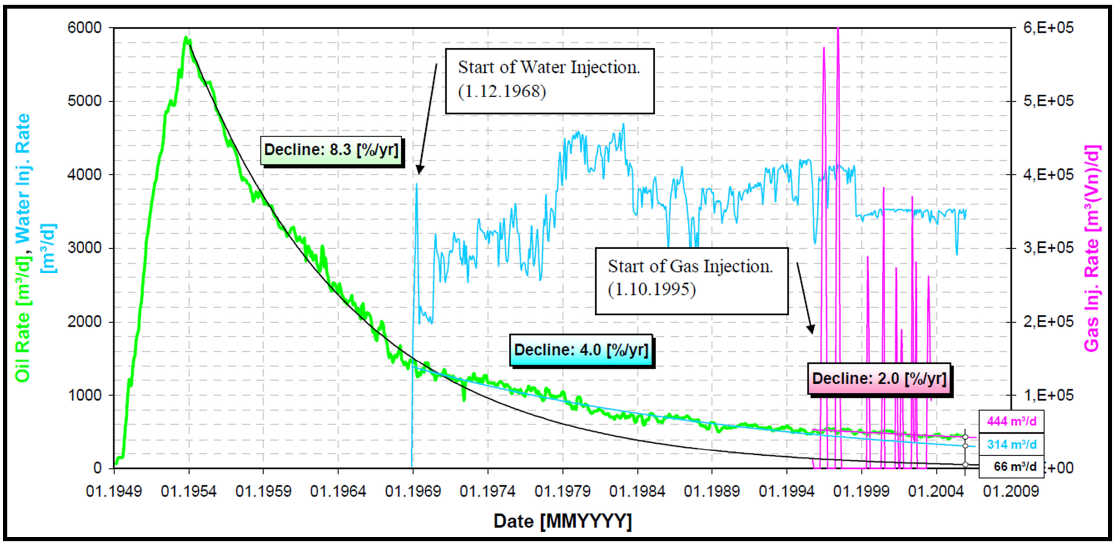

Figure 3-6: Production Profile of the 16th TH Main Pool PU 216-10 (Kienberger and Fuchs, 2006)

The recovery factors are 52.1 for the whole PU 216-10 and 62.2 for PU 216-20. The noticeable difference in recovery factors is mainly caused by the closer well spacing in PU 216-20. Figure 3-7 shows the production profile of the well that will be affected by the AP flooding.

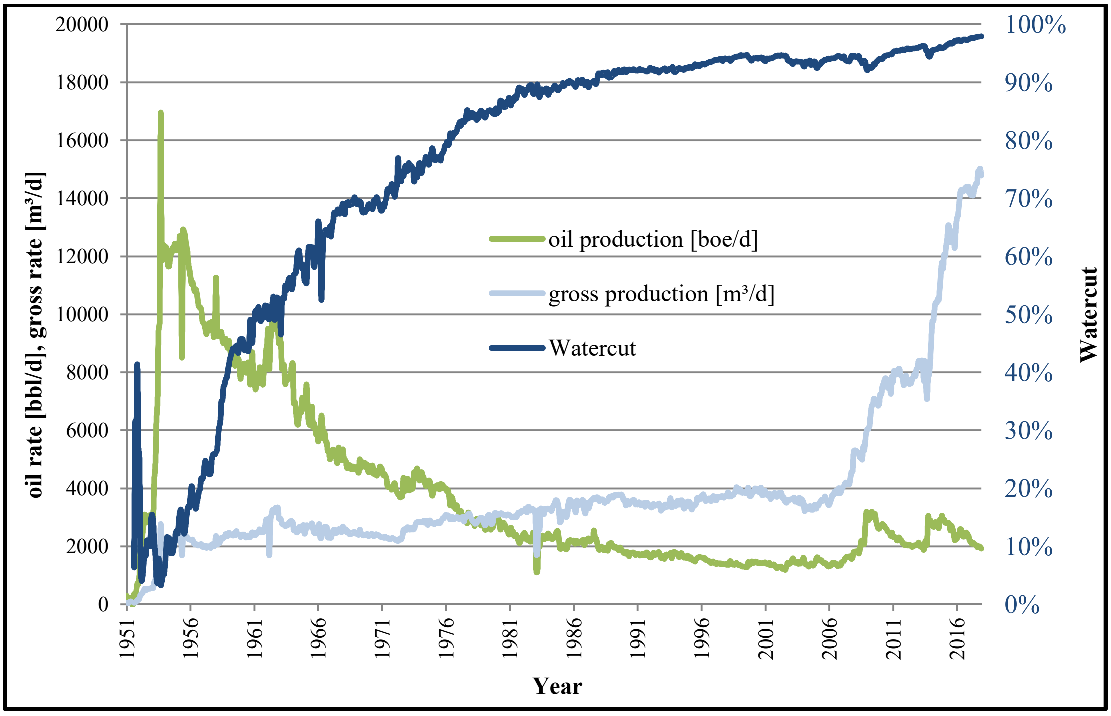

Figure 3-7: Production profile of area selected for AP flooding (OMV Exploration & Production GmbH, 2018)

3.4 Workflow

The course of action of the practical work for the present Master Thesis can be described as following:

1) Determination of the optimum grid cell size using the concept of replacing physical dispersivity by numerical dispersivity and verification through tracer core flood experiments.
2) History match of Polymer core flood experiment to review polymer parameters
3) History match of AP core flood experiment to review alkali parameters
4) Transfer of history matches to field scale.

3.5 History Match Models

Table 3-10 summarizes the history match models discussed in this thesis.

Table 3-10: Overview of discussed history match models

Type	Name	Description
Polymer core		
	Match 1	Water injection match based on laboratory measurements
	Match 2	Water injection match based on laboratory measurements
	RRF_best match	Best overall match, assumes an unexpectedly high RRF of 60
	expected RRF_unrealistic IPV	Match using the expected RRF of 30, IPV has the unrealistic value of 0.6
	expected RRF_matched peak	Match using the expected RRF of 30 and an IPV of 0.3, matches the pressure differential peak but not the tail
AP core flood		
	Match 1	Water injection match based on laboratory measurements
	Match 2	Water injection match based on laboratory measurements
	Match 3	Water injection match based on laboratory measurements
	Original	Match including polymer adsorption from the polymer core flood match
	Zero	Match including nearly zero polymer adsorption

Chapter 4

Core Flood Experiments

Core flood experiments are standard laboratory experiments with a large scope of application and play a vital part in evaluating possible reservoir treatments. Previous to the executed simulations, three single-phase tracer core flood experiments and two two-phase polymer and alkali-polymer core flood experiments were carried out. The data from the single-phase experiments were utilized to determine the optimum grid cell size and the result was applied to the two-phase experiments. Figure 4-1 to Figure 4-3 display the experimental data from the tracer core flood experiments.

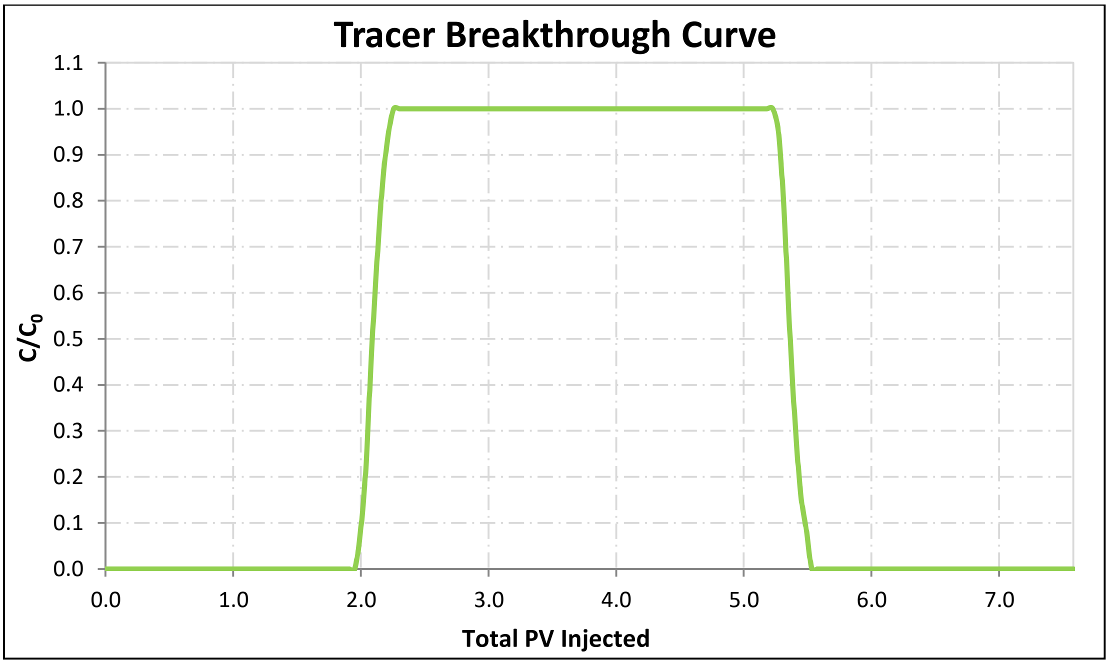

Figure 4-1: Data from tracer core flood experiment (Tracer Test 1)

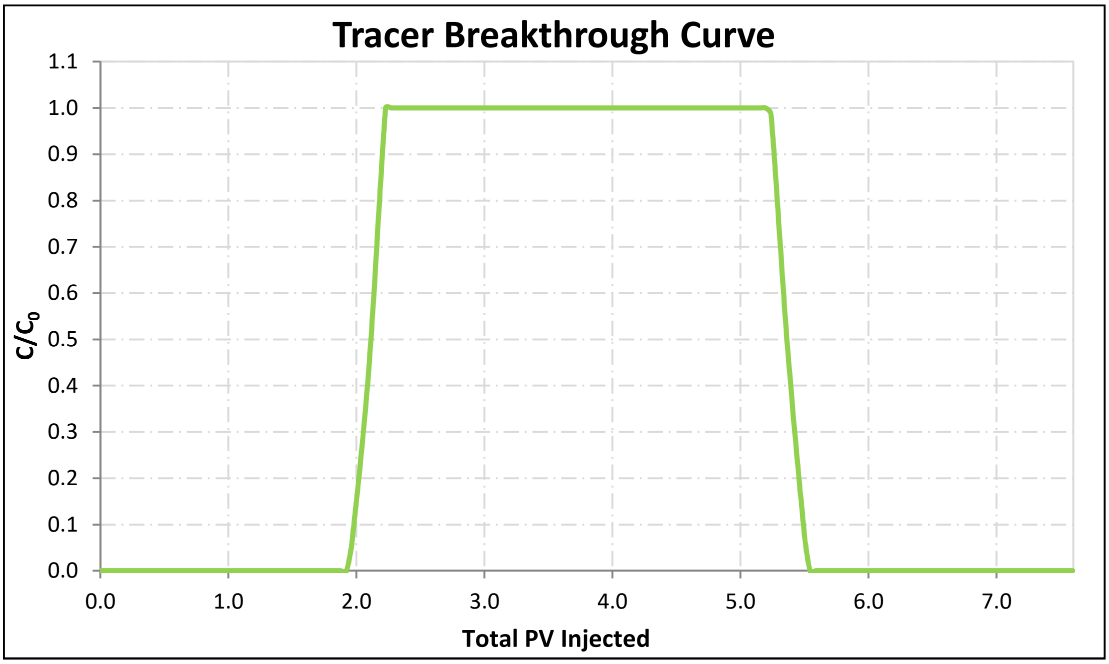

Figure 4-2: Data from tracer core flood experiment (Tracer Test 2)

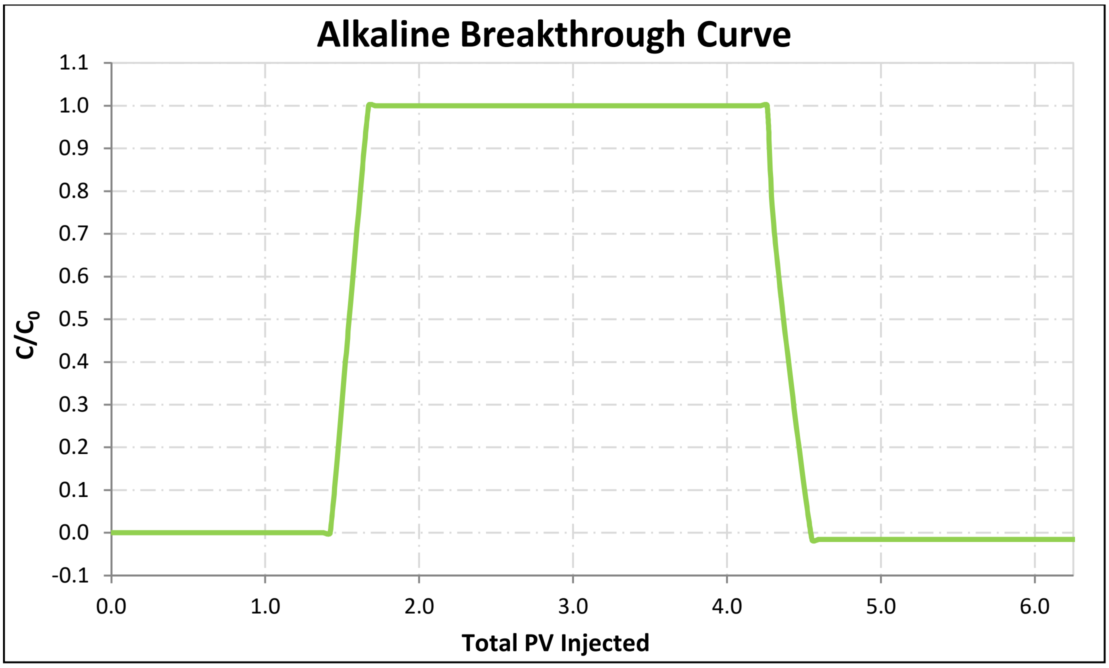

Figure 4-3: Data from tracer core flood experiment (Alkaline Test)

4.1 Analytical Solution of the Tracer Core Flood Experiment

Before the tracer core flood history match simulations, the experimental data were analytically investigated.

The dimensionless concentration is defined as in **eq.8** (Sheng, 2011).

$$C_D = \frac{1}{2}\left[1 - erf\left(\frac{x - vt}{2\sqrt{D_L t}}\right)\right] \qquad (8)$$

C_D	dimensionless concentration [ ]
erf(x)	error function [ ]
x	distance [m]
v	interstitial velocity [m/s]
t	time [s]
D_L	longitudinal dispersion coefficient [m²/s]

Figure 4-4 to Figure 4-6 illustrate the analytical solutions for the single-phase experiments. Table 4-1 summarizes the matched dispersion coefficients.

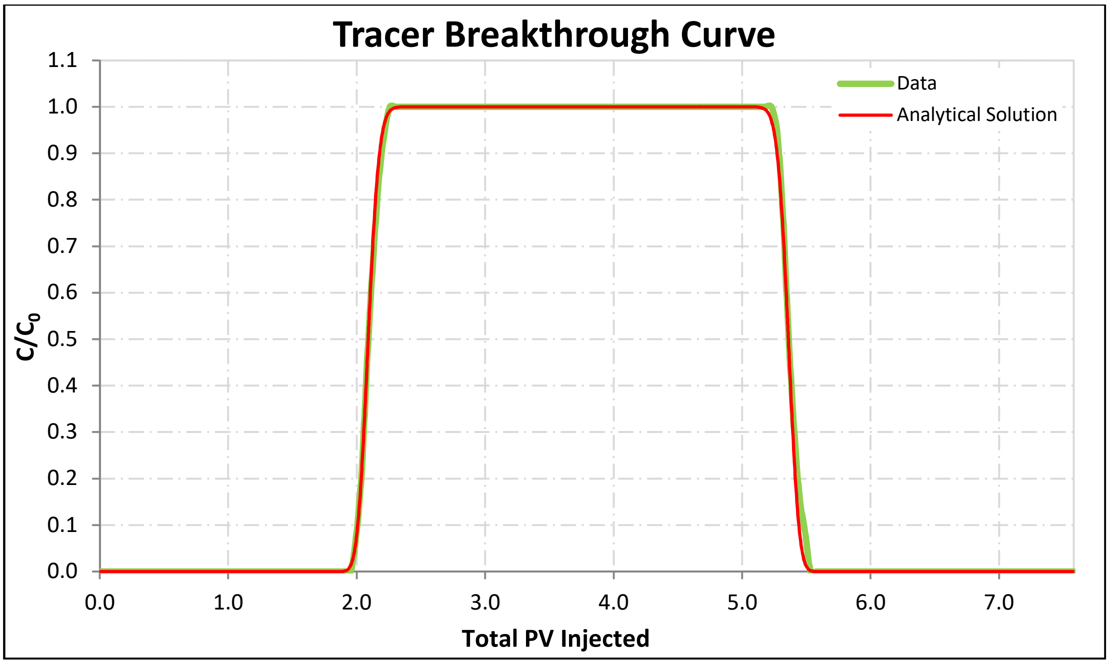

Figure 4-4: Analytical Solution (Tracer Test 1)

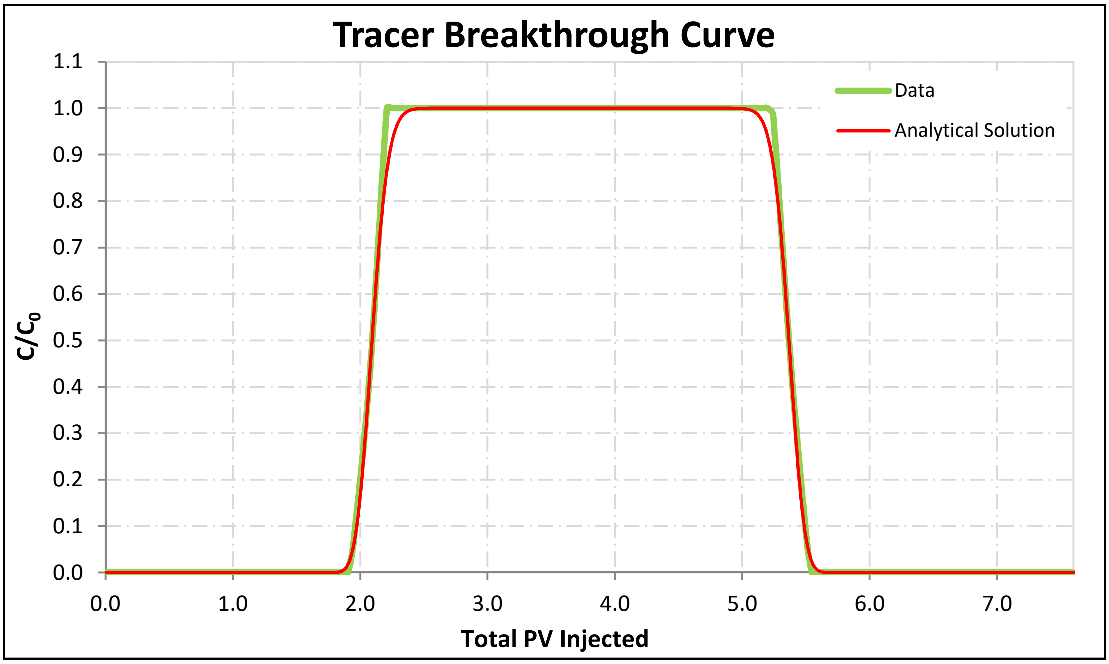

Figure 4-5: Analytical Solution (Tracer Test 2)

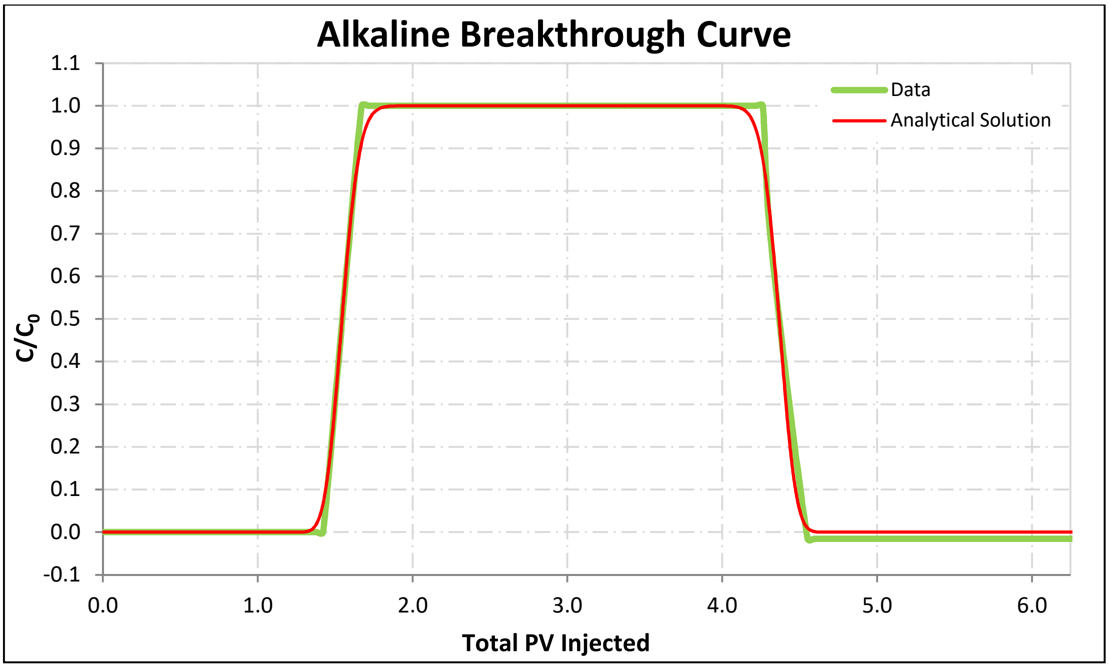

Figure 4-6: Analytical Solution (Alkaline Test)

Table 4-1: Matched longitudinal dispersion coefficients (single-phase experiments)

Test	D_L [m²/s]
Tracer Test 1	6.0e-8
Tracer Test 2	5.5e-9
Alkaline Test	4.0e-9

The used values for the longitudinal dispersion coefficients were compared with literature data (eg. Pereira et al., 1999, Li, Amador and Ding, 2016, Flury and Gimmi (2002, Ahl, J., 2004) and deemed reasonable.

4.2 Tracer Core Flood History Match

The longitudinal dispersion was matched utilizing the tracer breakthrough curve defined by the dimensionless concentration. For the tracer core flood history match and all subsequent core flood history matches, a homogeneous 1D core model was constructed. The first and the last grid cell are the same size for all models, with an injector placed in the first grid cell and a producer placed in the last grid cell. The number of cells was determined utilizing the concept of numerical dispersivity being proportional to the grid cell size to represent physical dispersivity, as defined in **eq.9 to eq.12** (Sheng, 2011), (Lüftenegger and Clemens, 2017).

$$\alpha_L = \frac{D_L}{v} \tag{9}$$

$$\alpha_L = \alpha_{num} \tag{10}$$

$$\alpha_{num} = \frac{\Delta x}{2} \tag{11}$$

$$\Delta x = 2\alpha_{num} = \frac{2D_L}{v} \tag{12}$$

α_L	longitudinal dispersivity [m]
D_L	longitudinal dispersion coefficient [m²/s]
v	interstitial velocity [m/s]
α_{num}	numerical dispersivity [m]
Δx	grid cell size [m]

The optimum grid cell size for the history matches of the single-phase core flood test was estimate to be approximately 0.21 cm. For the present models, this signifies and optimum cell numbers of 138. To increase the consistency of the grid cell size sensitivity analysis, this number was converged using 125 cells. Figure 4-7 to Figure 4-9 illustrate the executed history matches. The raw simulation results exhibit an accelerated ion breakthrough. It origins in the fact, that the simulator uses the calculated pore volume while during the experiment the pore volume corrected for dead volume and fraction size was used. Therefore, the history matches had to be corrected to that effect. Comparison of the experimental and numerical data shows, that utilizing the dispersivity to determine the optimum grid cell size produces sufficient result.

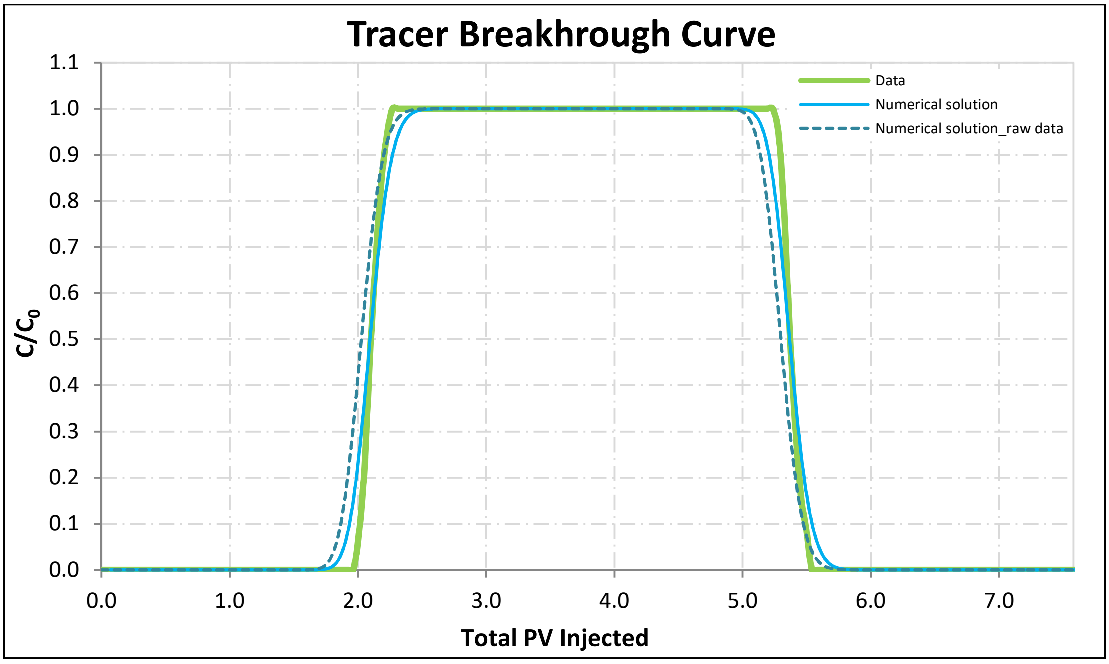

Figure 4-7: History match of the tracer breakthrough curve (Tracer Test 1)

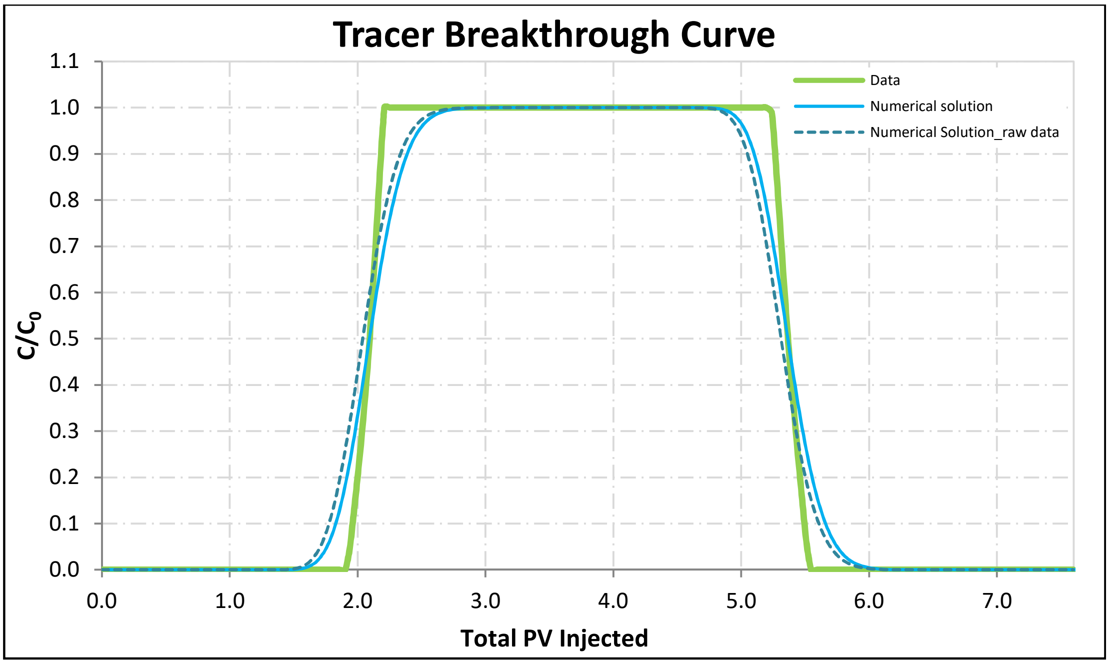

Figure 4-8: History match of the tracer breakthrough curve (Tracer Test 2)

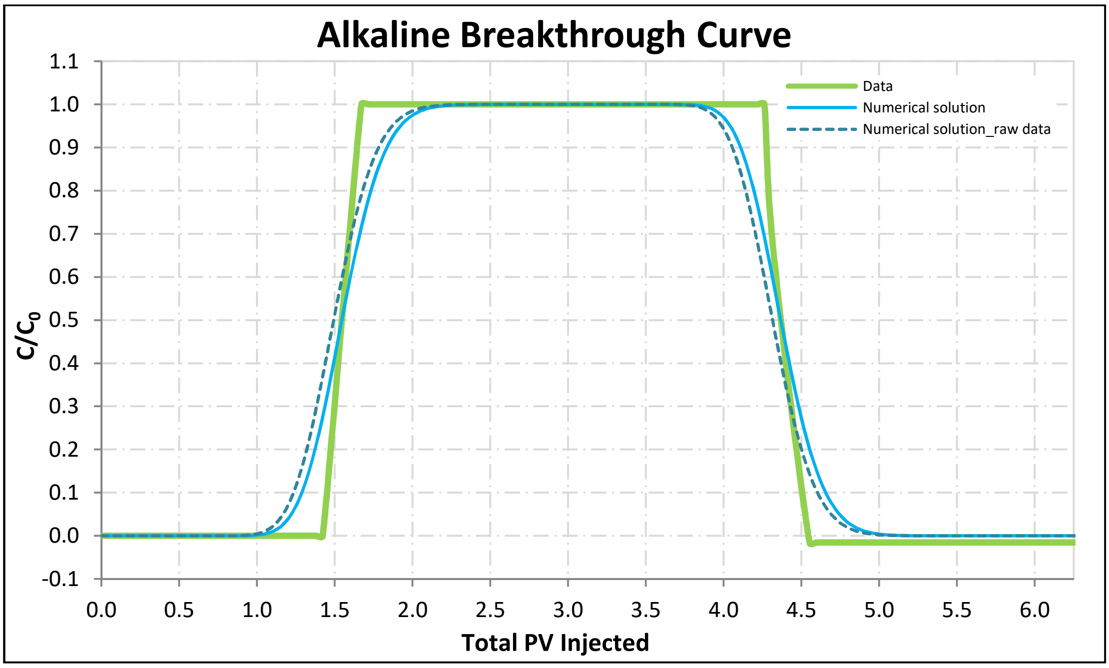

Figure 4-9: History match of the tracer breakthrough curve (Alkaline Test)

4.3 Polymer Core Flood History Match

The history match of the water saturation data gained from the polymer core flood experiment was executed in two steps. First, the preceding water flood was matched to define the permeability parameters. Afterwards, the actual polymer injection and the subsequent water injection were matched. Additionally, a grid size sensitivity analysis took place. Figure 4-10 displays the experimental data from the polymer core flood experiment.

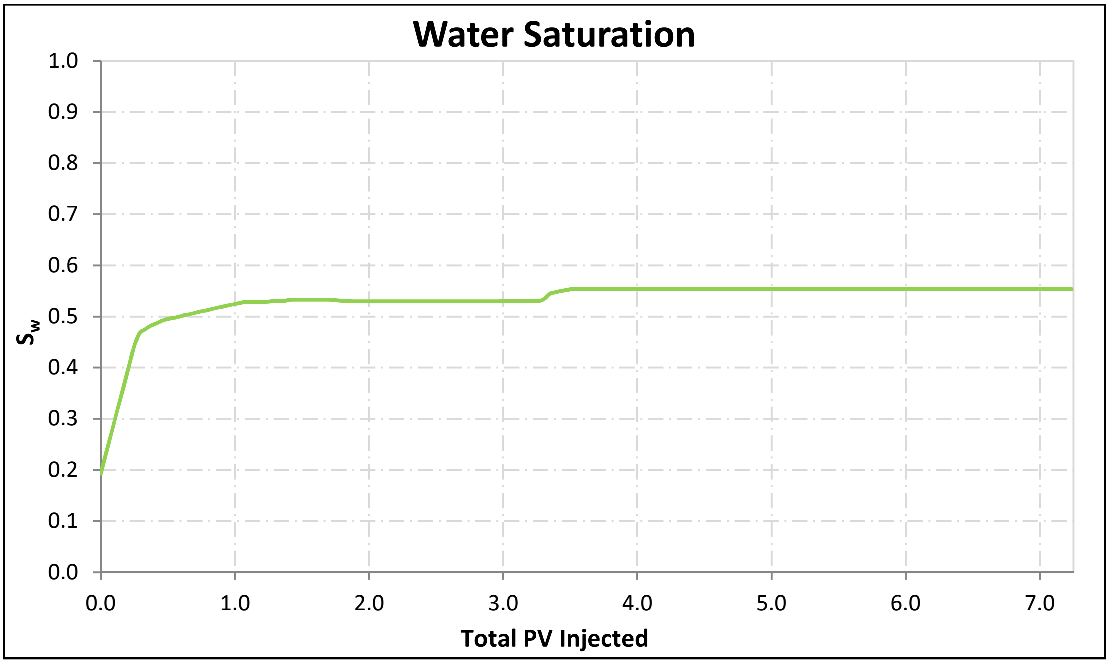

Figure 4-10: Data from polymer core flood experiment

4.3.1 Water Flood History Match

The purpose of an isolated water flood history match is the eased determination of the multiphase flow properties of the involved fluids, in this case oil and water. To describe the dependency of the relative permeability on water saturation, the modified Brooks-Corey model was used (**eq.25** and **eq.26**). The equations are provided in Appendix C.

Beside static properties, the experimental data include some information concerning dynamic properties. Effective permeability measurements at initial water saturation and remaining oil saturation narrow uncertainties significantly down, leaving only the Corey parameters completely unknown. The relative permeability range indicated by the core flood experiments was calculated using the measured average permeability of 1489 mD. This approach has the benefit of reducing the degree of freedom and was confirmed by sensitivity analyses that proved that variations in permeability do not benefit the results of the history match. Table 4-2 summarizes the measured permeability values and related statistical properties.

Table 4-2: Permeability measurements executed during the polymer core flood experiment

Fluid	**Effective permeability [mD]**	**S_w**	**Relative permeability**		
			minimum	**average**	**maximum**
water	122 ± 5	0.53	0.0786	0.0819	0.0853
oil	860 ± 51	0.2012	0.5433	0.5776	0.6118

To prevent a falsification of the results, the water flood match was executed ignoring the bump flood, which took place directly before the polymer flood. Since the bigger part of the parameters has a limited variability, only few valid combinations exist. Regarding the relative permeability, distinct trends can be observed. Within the range defined by the experimental measurements, very low water relative permeability values and quite high oil relative permeability values lead to the most favorable matching results. Figure 4-11 displays the relative permeability curves of the two matches.

Property	Match	
	Match 1	Match 2
$k_{rw,max}$	0.11	0.11
$k_{ro,max}$	0.6	0.6
S_{or}	0.42	0.42
n_w	2.7	2.2
n_o	2.0	1.9

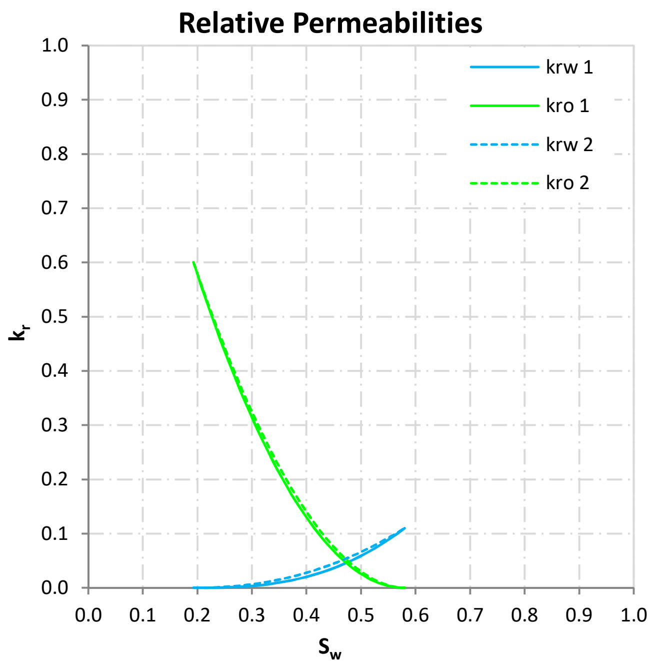

Figure 4-11: Relative permeability curves (water flood before polymer flood)

At all executed history matches, the pressure differential was used as a control parameter. Figure 4-12 illustrates the matched parameters. The apparently bad match of the pressure differential partly origins in the very small range of the ordinate.

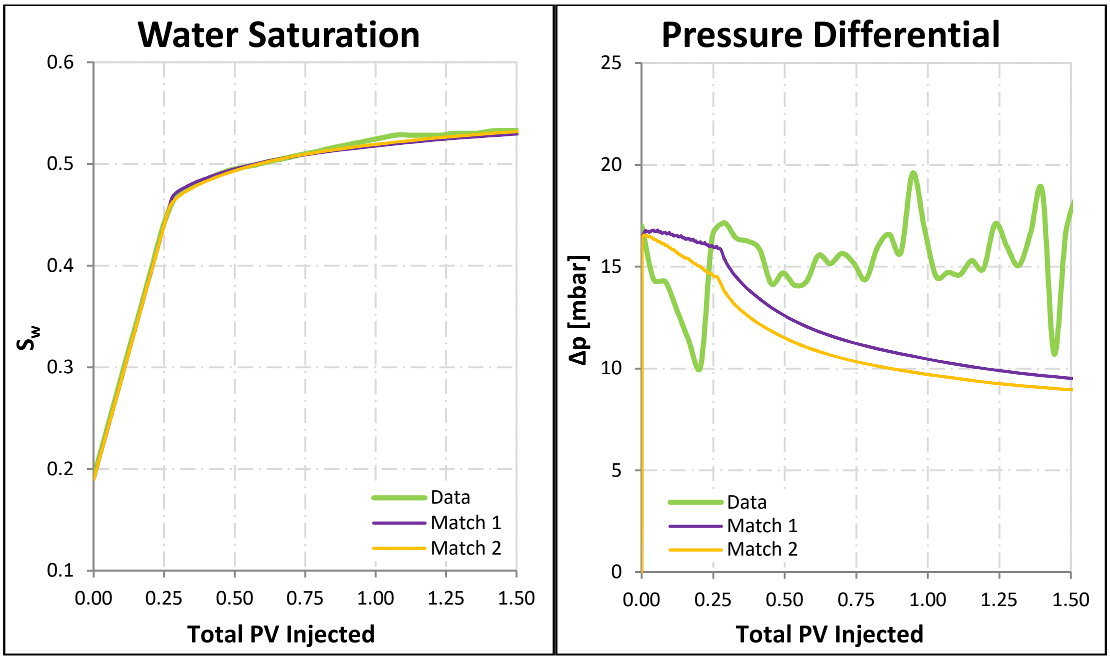

Figure 4-12: History match of the water flood (exclusive of bump flood, polymer flood

Figure 4-13 illustrates the water saturation match encompassing the whole water flood. It can be clearly observed that the bump flood alters the behavior of the propagation through the core and matching the long flat section would require unrealistically low Corey parameters (1.0 and closely above).

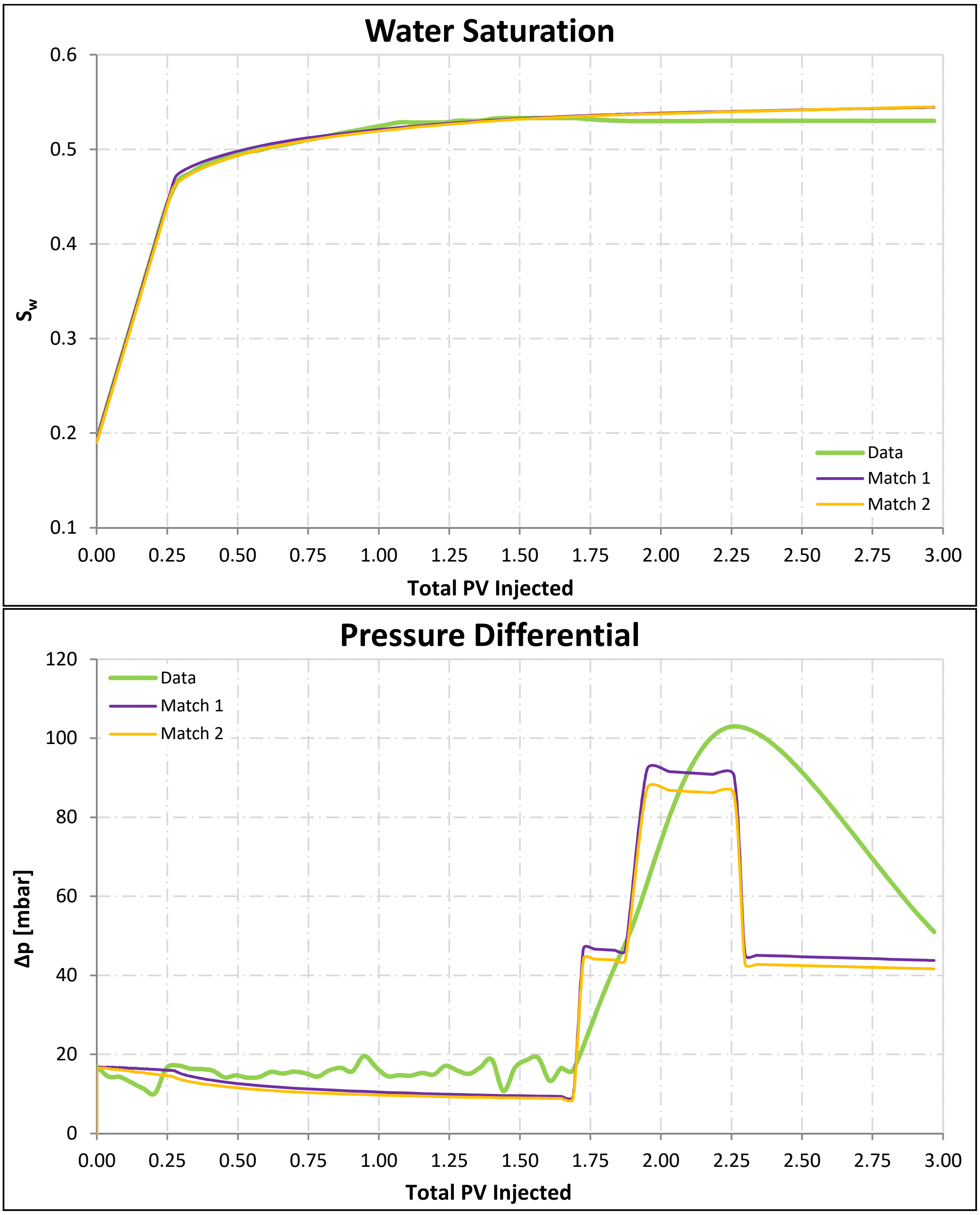

Figure 4-13: History match of the water flood (including bump flood, polymer flood)

4.3.2 Polymer Flood History Match

During a polymer history match, additional parameters have to be taken into account, the viscosity increase caused by the polymer, the polymer adsorption, the permeability reduction of the subsequent water and the inaccessible pore volume.

Polymer Viscosity

The effect of the injected polymer on the viscosity is implemented in ECLIPSE 100 in form of a multiplier. It is input in tabular form as function of polymer concentration. During the simulations, two polymer viscosity functions were matched and are displayed in Figure 4-14. Variations of the polymer viscosity have no noticeable impact on the water saturation curve, but a huge impact on the polymer injection ‘peak’ of the pressure differential curve, at which they exhibit a directly proportional behavior.

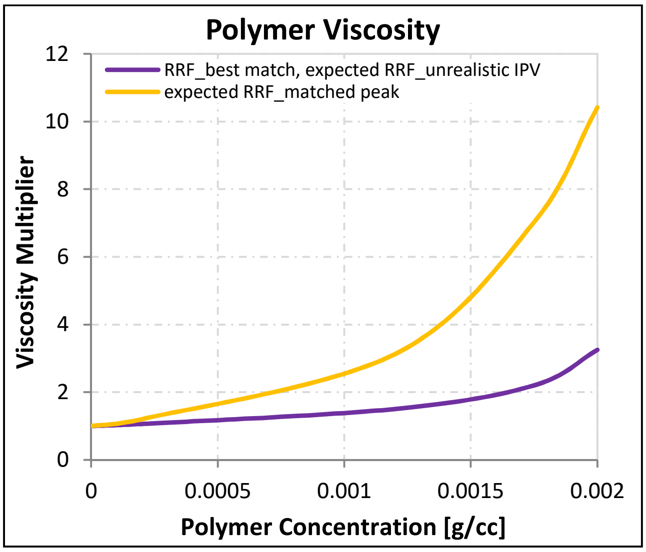

Figure 4-14: Polymer viscosity curves

Polymer Adsorption

Like the polymer viscosity, the polymer adsorption is also input in tabular form. It is specified as percentage of adsorbed polymer as a function of polymer concentration. During the simulations, three polymer adsorption functions were matched and are displayed in Figure 4-15. Variations of the polymer viscosity have a reasonable effect on the water saturation curve as well as on the pressure differential curve. An increase of the polymer adsorption leads to a delayed polymer breakthrough and to a rise of the water saturation. Additionally, it causes an increase of the ‘peak’ and the ‘water tail’ of the pressure differential.

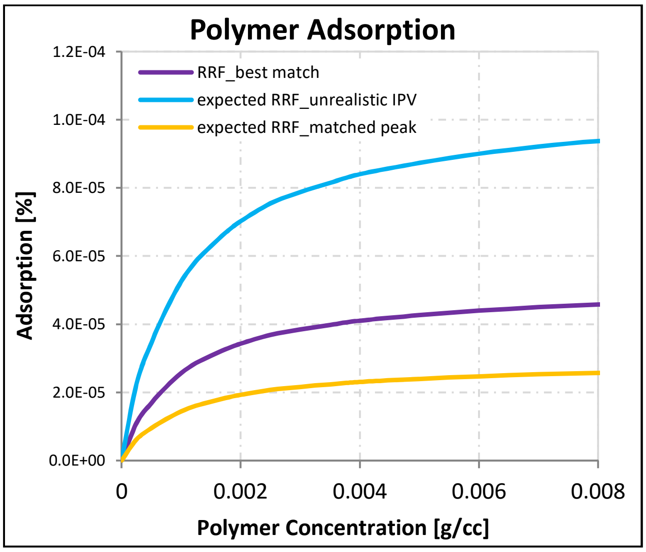

Figure 4-15: Polymer adsorption curves

Residual Resistivity Factor

Alterations of the RRF affect both water saturation and pressure differential. A reduction leads to a significant flattening of the polymer-induced rise on the water saturation curve and diminishes the peak and tail of the pressure differential.

Inaccessible Pore Volume

The inaccessible pore volume affects both water saturation and pressure differential. A decrease leads to a delayed and more gradual rise of the water saturation and it tilts the polymer peak to the right.

Additionally, the relative permeability has to be adjusted, since the bump flood led to a lowering of the final water saturation. Still, even an increase of the residual oil saturation from 0.42 to 0.43 does not catch the features of the polymer flood, as illustrated in Figure 4-16.

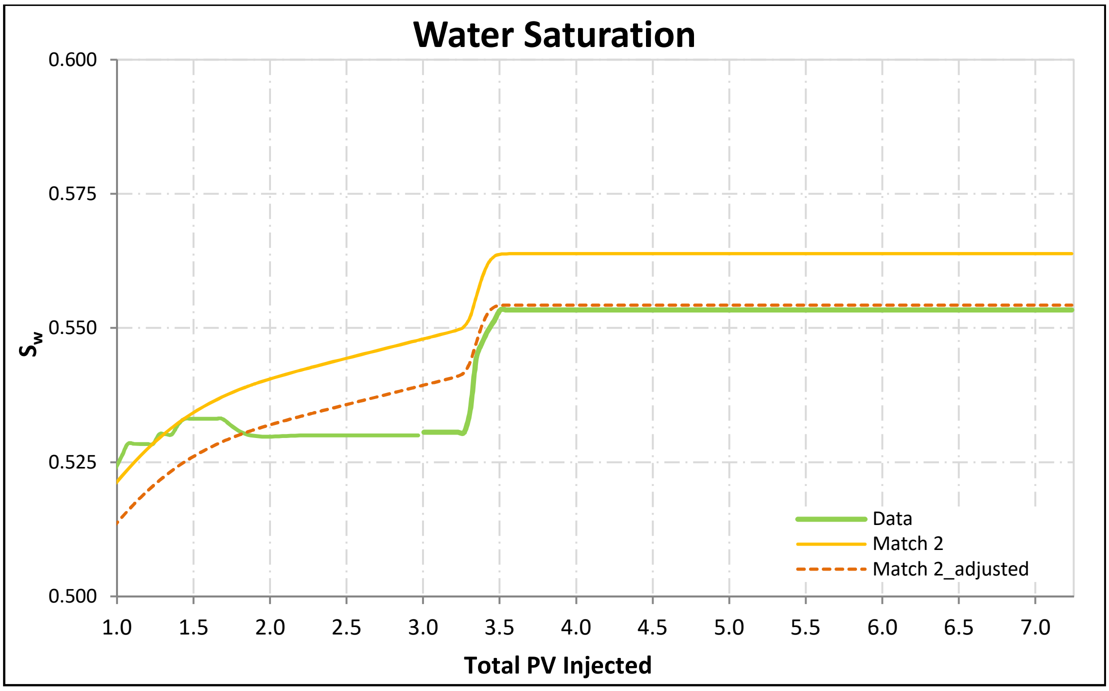

Figure 4-16: Polymer match using ‘Match 2’ from the water flood

Additionally to the residual oil saturation, the Corey parameters have to be adjusted as well. Figure 4-17 displays the relative permeability curves of the polymer flood.

Property	Value
$k_{rw,max}$	0.11
$k_{ro,max}$	0.6
S_{or}	0.43
n_w	3.0
n_o	2.2

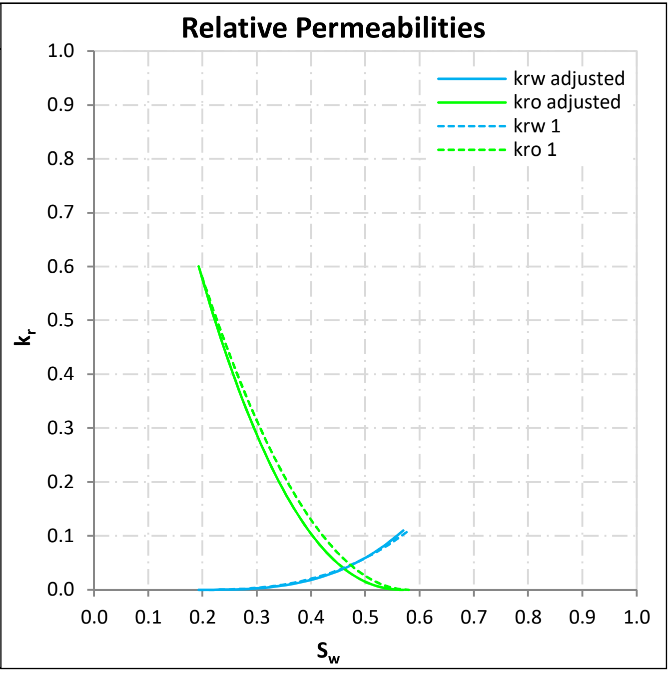

Figure 4-17: Relative permeability curves (polymer flood)

Increasing the oil Corey parameter leads to a match with the water saturation at the start of the polymer injection and an increase of the water Corey parameter leads to a match with the slope of the rise, as illustrated in the left hand side of Figure 4-18. The right hand side of Figure 4-18 displays the corresponding deterioration of the match along the water flood section.

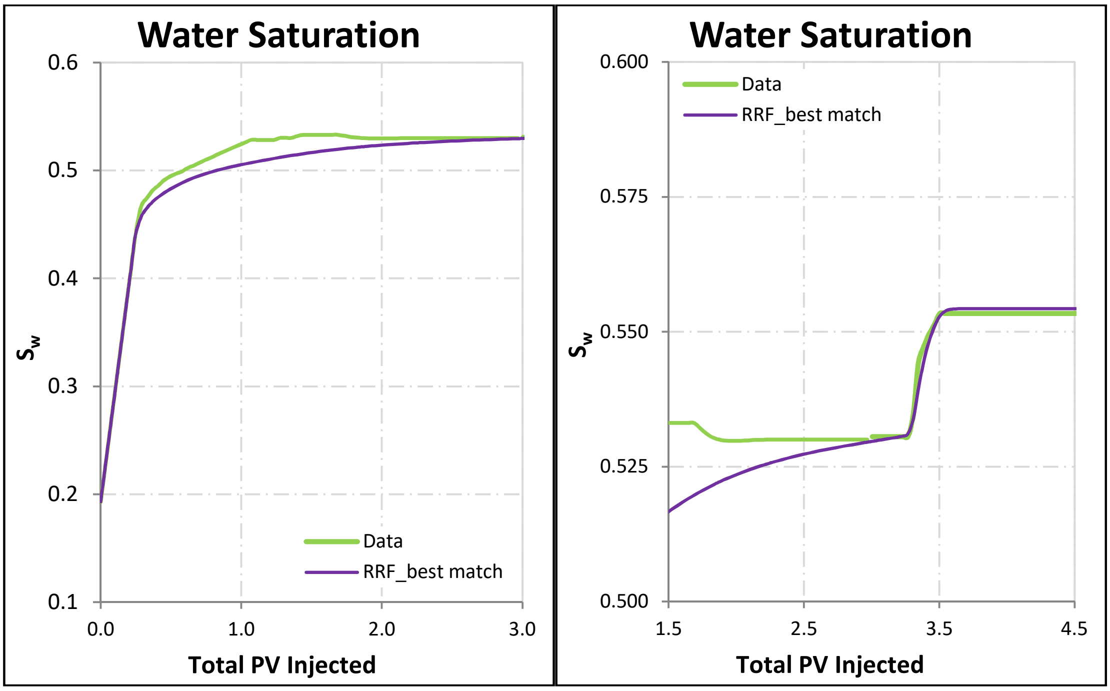

Figure 4-18: Polymer match with adjusted parameters

Further simulations varying the polymer-connected parameters were executed and their behavior and impact on the results were investigated. By variation of these parameters, the history match 'RRF_best match' was generated. This was achieved by expected values for the polymer viscosity and adsorption, and unexpected values for the RRF and IPV. 'RRF_best match' was realized assuming and RRF of 60, which stands in contrast with and expected value of 30, although it is still in a reasonable range. The used IPV of 0.3 is certainly more challengeable, although still possible. A reduction to 0.1 would lead to a distinctly better matched polymer peak, but it would drastically decrease the accordance with the water saturation curve, even combined with a polymer adsorption of almost zero. The results of 'RRF_best match' are illustrated in Figure 4-19.

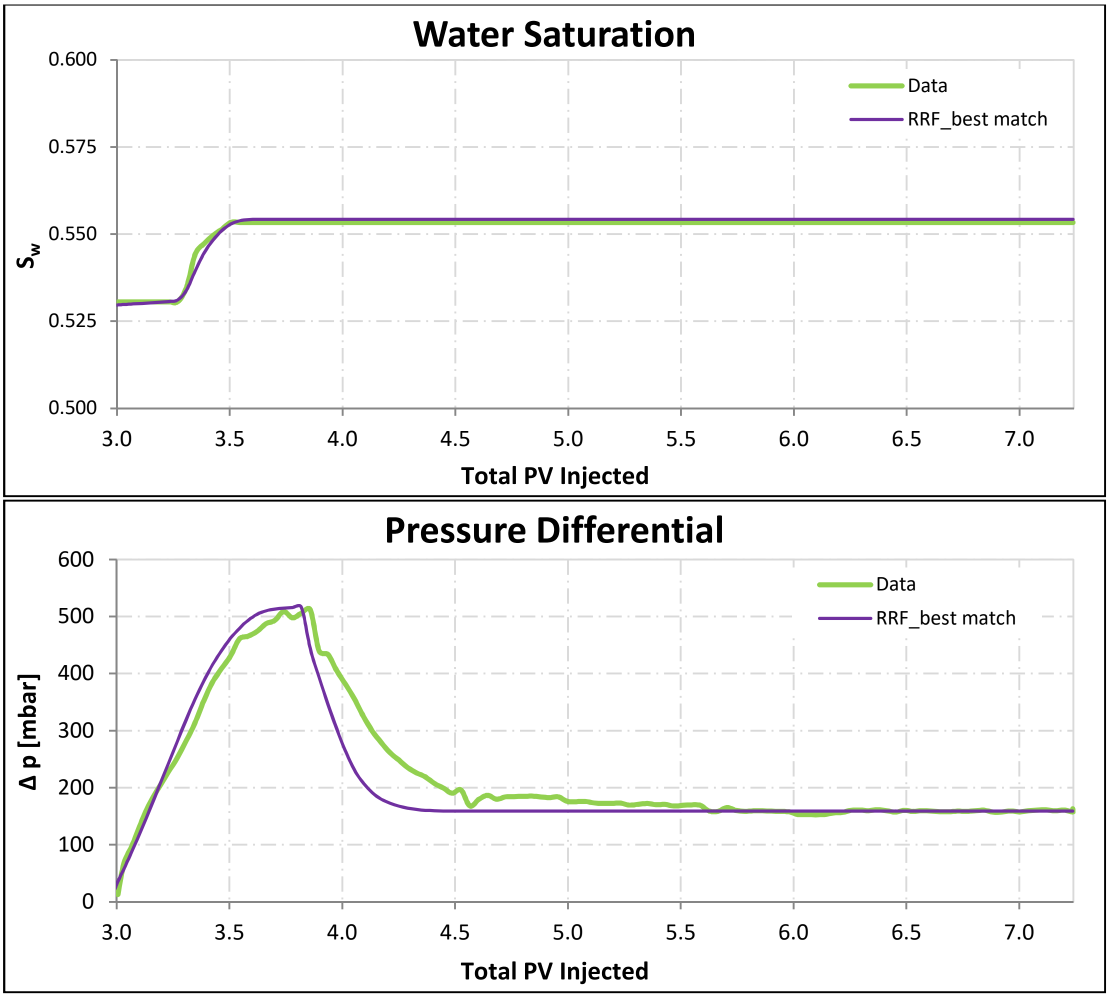

Figure 4-19: Polymer match 'RRF_best match'

Although a reduction of the RRF to the expected value of 30 leads to a sufficient water saturation match, it is either impossible to match the pressure differential over all injection phases, or a change of the inaccessible pore volume to an unrealistic value is necessary. An increase of the IPV to 0.6 and the polymer adsorption by a factor 2 delivers a false match ('expected RRF_unrealistic IPV'). The polymer peak can be matched by adjusting viscosity and adsorption but this leads to a mismatch of the water tail (‘expected RRF_matched peak’), as illustrated in Figure 4-20.

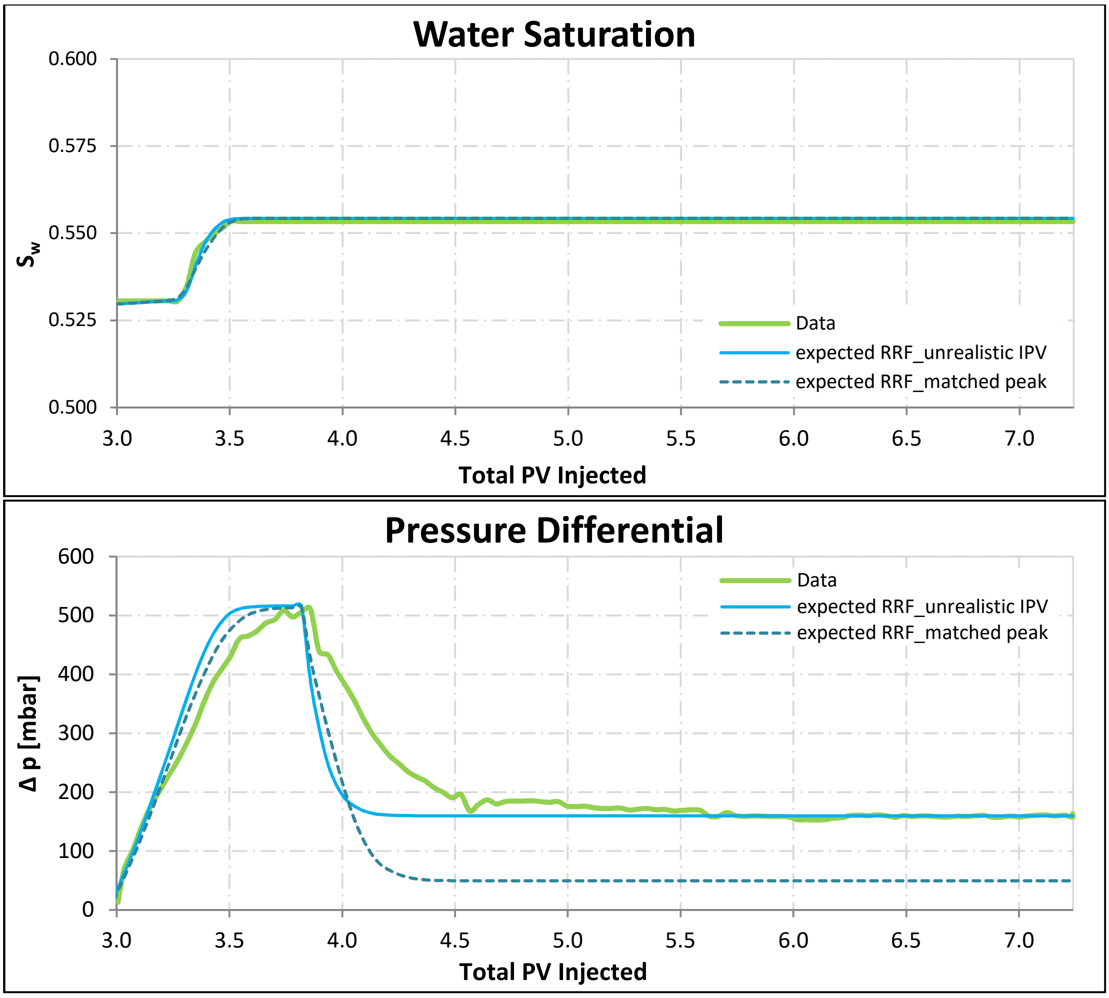

Figure 4-20: Polymer match implementing RRF=30

Table 4-3 summarizes the matching parameters of the polymer core flood simulation matches.

Table 4-3: Matching parameters (polymer flood)

Model	RRF	IPV
RRF_best match	60	0.3
expected RRF_unrealistic IPV	30	0.6
expected RRF_matched peak	30	0.3

In contrast to the reduction of the RRF, an increase by one third from 60 to 80 shows hardly any impact.

4.4 Alkali-Polymer Core Flood History Match

Like the polymer core flood history match, the match of the water saturation data gained from the AP core flood experiment was executed in two steps. Analogous, the preceding water flood was matched to define the permeability parameters. Afterwards, the actual AP injection was matched. Additionally, a grid size sensitivity analysis took place. Figure 4-21 displays the experimental data from the alkali-polymer core flood experiment.

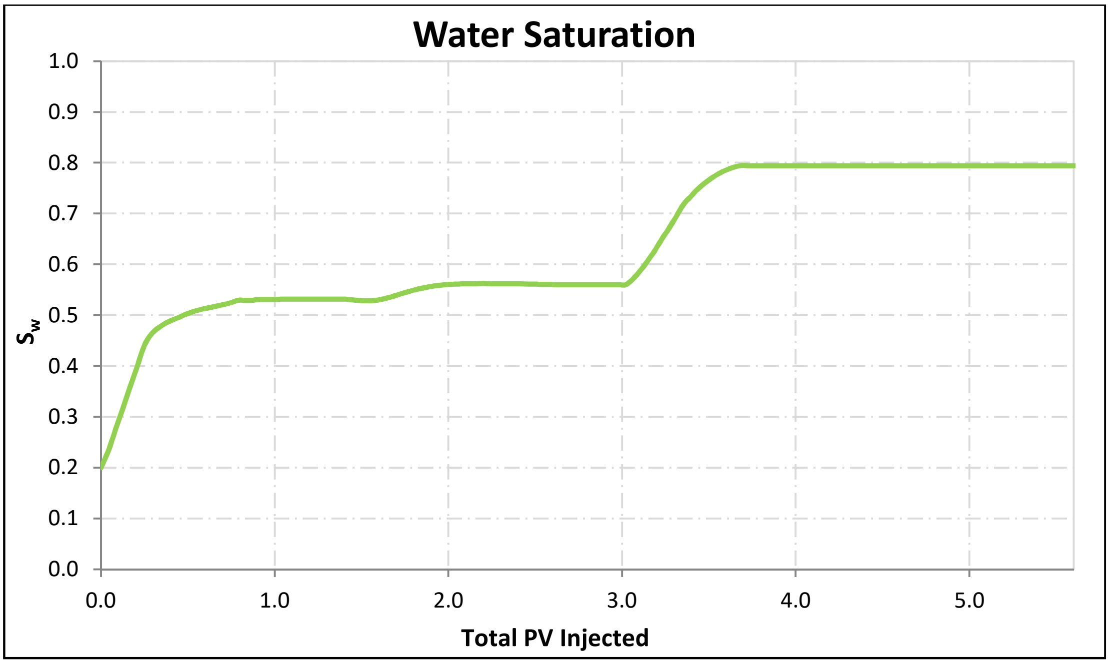

Figure 4-21: Data from alkali-polymer core flood experiment

4.4.1 Water Flood History Match

The water flood history match of the AP core flood was executed identically to the history match of the polymer core flood. In case of the AP experiment, the relative permeability has a larger range of uncertainty. The measured permeability and related properties are summarized in Table 4-4.

Table 4-4: Permeability measurements executed during the AP core flood experiment

Fluid	**Effective permeability [mD]**	**S_w**	**Relative permeability minimum**		
water	102 ± 7	0.56	0.0714	0.0766	0.0819
oil	796 ± 94	0.1985	0.5274	0.5980	0.6687

Regarding the water relative permeability, a trend can be observed. Within the range defined by the experimental measurements, comparably high and nearly identical water relative permeability values lead to the most favorable matching results. Regarding the oil relative permeability, values from the complete range of uncertainty were used to attain sufficient results. Figure 4-22 displays the relative permeability curves of the three matches.

Property	Match		
	Match 1	Match 2	Match 3
$k_{rw,max}$	0.098	0.1	0.1
$k_{ro,max}$	0.66	0.66	0.53
S_{or}	0.4	0.4	0.395
n_w	1.6	2.0	2.0
n_o	2.0	2.0	2.0

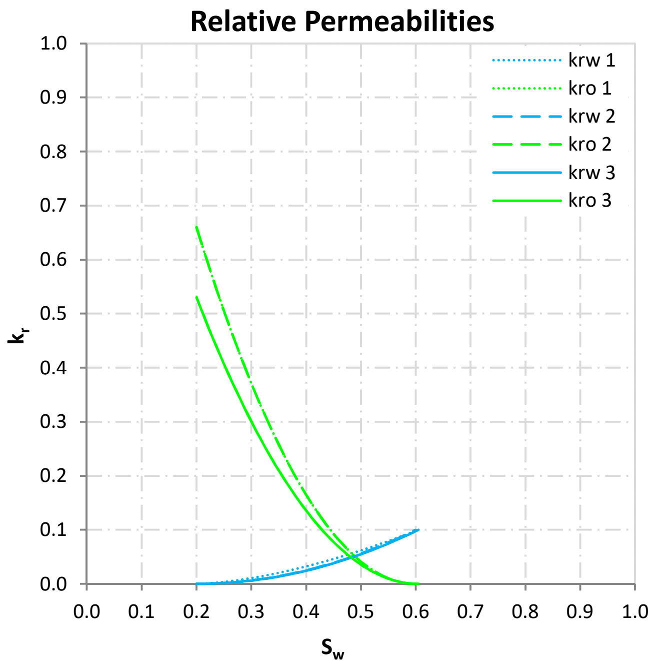

Figure 4-22: Relative permeability curves (water flood before AP flood)

Figure 4-23 shows the water saturation and pressure differential matches. Analogous to the polymer flood match, the seemingly bad match of the pressure differential partly origins in the very small range of the ordinate.

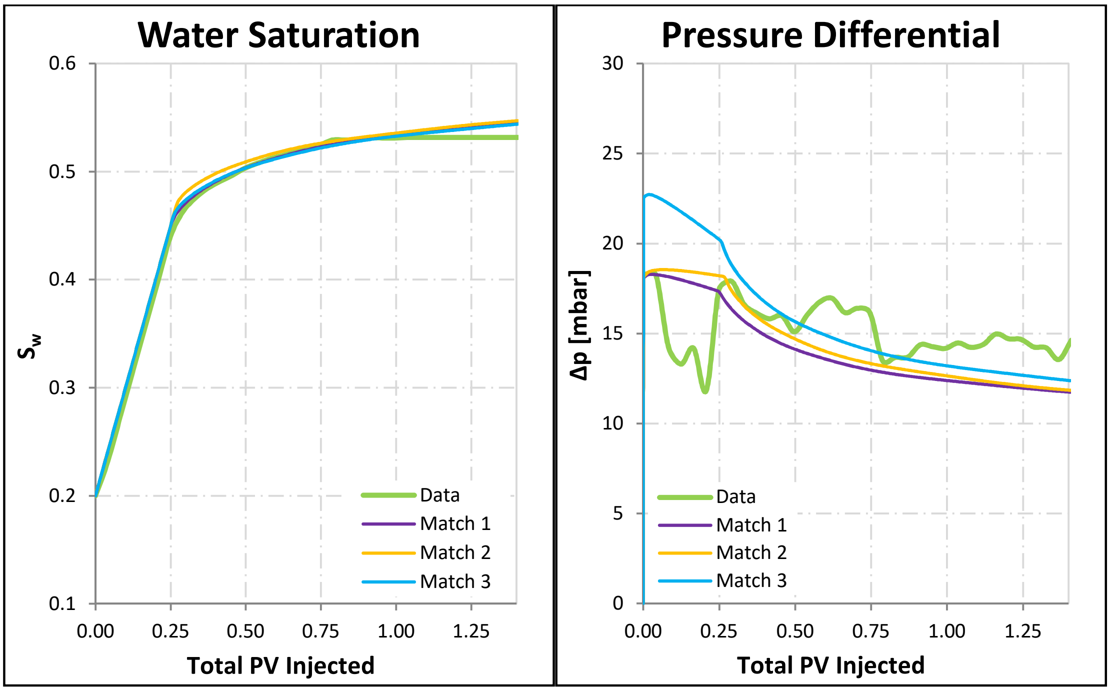

Figure 4-23: History match of the water flood (exclusive of bump flood. AP flood)

Figure 4-24 illustrates the water saturation match including the bump flood.

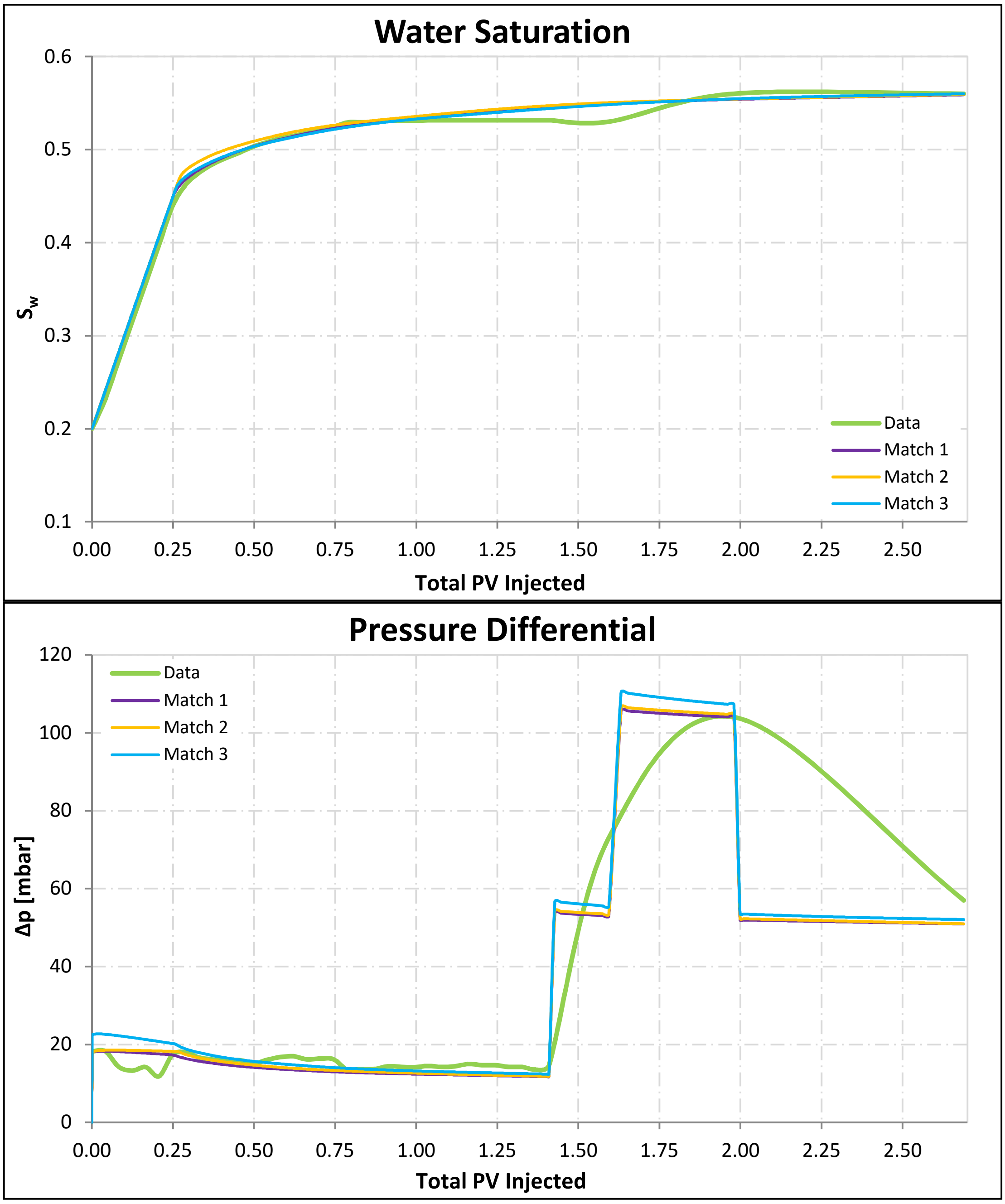

Figure 4-24: History match of the water flood (including bump flood, AP flood)

4.4.2 Alkali-Polymer History Match

During an AP history match, not only parameters connected with the injected polymer have to be taken into account, also the parameters connected with the injected alkaline and generated surfactants have to be investigated, viscosity increase, adsorption of the generated surfactants, surface tension reduction and shape of the capillary desaturation curve. Again, the relative permeability has to be adjusted, and relative permeability for miscible flow regions has to be defined. This second set of relative permeability curves was assumed to consist of straight lines, connoting Corey parameters of 1.0. Figure 4-25 displays the relative permeability curves of the three matches.

Property	Value	
	immiscible	miscible
$k_{rw,max}$	0.1	1.0
$k_{ro,max}$	0.53	1.0
S_{wi}	0.2	0.35
S_{or}	0.4	0.18
n_w	2.0	1.0
n_o	2.1	1.0

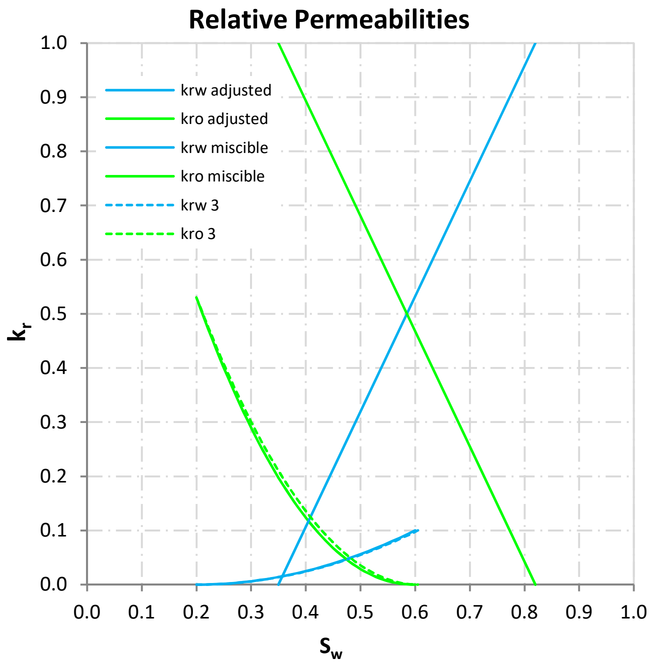

Figure 4-25: Relative permeability curves (AP flood)

Simulations varying the alkaline-connected parameters and some of the polymer-connected parameters were executed and their behavior and impact on the results were investigated.

Surfactant Viscosity

The increase of the viscosity caused by the generated surfactants is input in tabular form as a function of concentration. During the simulations, two polymer viscosity functions were matched as illustrated in Figure 4-26. Variations of the surfactant viscosity are hardly affecting the water saturation curve, only the curvature of the transition between the slant and the flat section is affected. In contrast, it has a large impact on the peak pressure differential, which is significantly increased by a comparably small increase of the inclination of the viscosity curve.

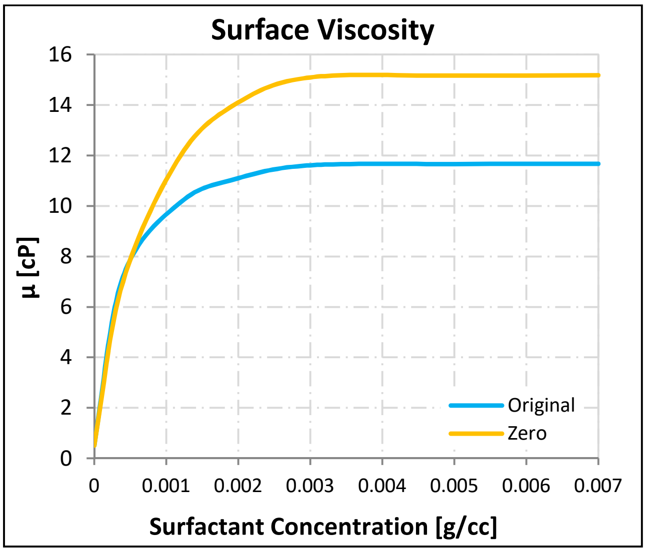

Figure 4-26: Surfactant viscosity curves

Surfactant Adsorption

Like the surfactant viscosity, the surfactant adsorption is also input in tabular form. It is specified as percentage of adsorbed surfactant as a function of surfactant concentration. During the simulations, two surfactant adsorption functions were matched as illustrated in Figure 4-27. Alterations of the surfactant adsorption have only a marginal effect on the water saturation curve and the pressure differential curve. A decrease of the surfactant adsorption causes an earlier surfactant breakthrough and therefore increases the inclination of the sharp water saturation rise. Additionally, it lowers and tilts the pressure differential peak.

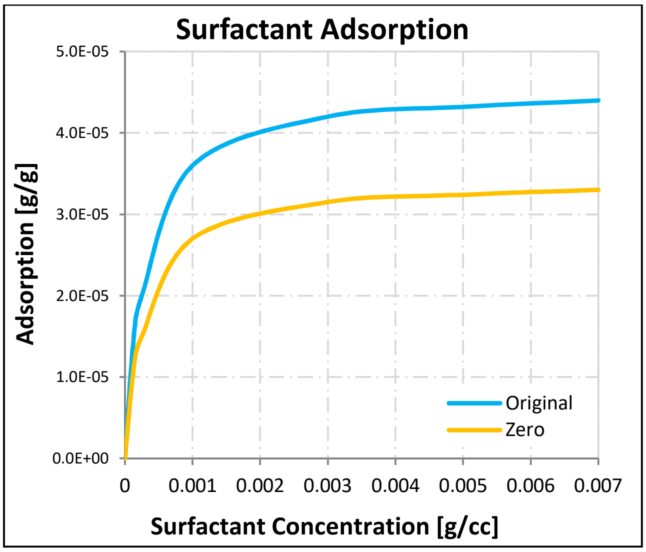

Figure 4-27: Surfactant adsorption curve

Surface Tension

The development of the water-oil-surface tension as a function of surface concentration is input in tabular form. During the simulations, a reduction of the surface tension by a factor 100 was assumed and delivered sufficient results. Alterations of the surface tension can have a large impact, which can create problems due to its high uncertainty range, which is mainly caused by the lack of knowledge about the amount of generated surfactants. A less effective surface tension reduction increases the slope of the rise of the water saturation, and reduces the peak of the pressure differential. Figure 4-28 displays the used surface tension curve.

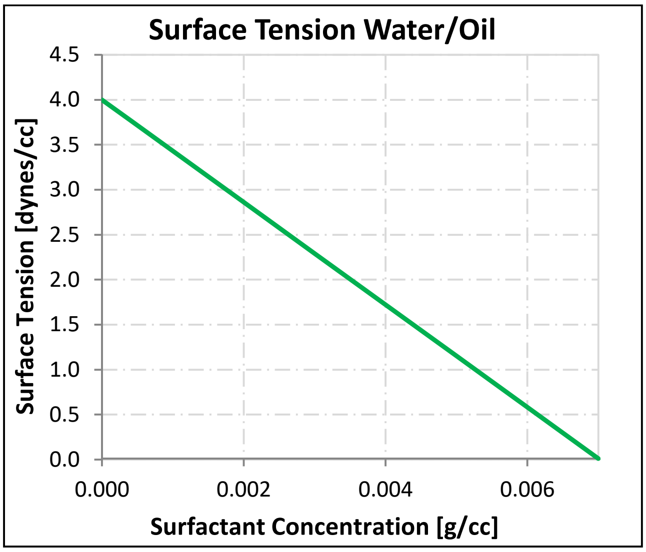

Figure 4-28: Surface tension curve

Capillary Desaturation Curve

The capillary desaturation curve defines the transition from immiscible flow to miscible flow. The capillary desaturation curve was calculated and not varied any further since appropriate results were achieved and smoothening of the curve showed no effect. Figure 4-29 shows the used capillary desaturation curves.

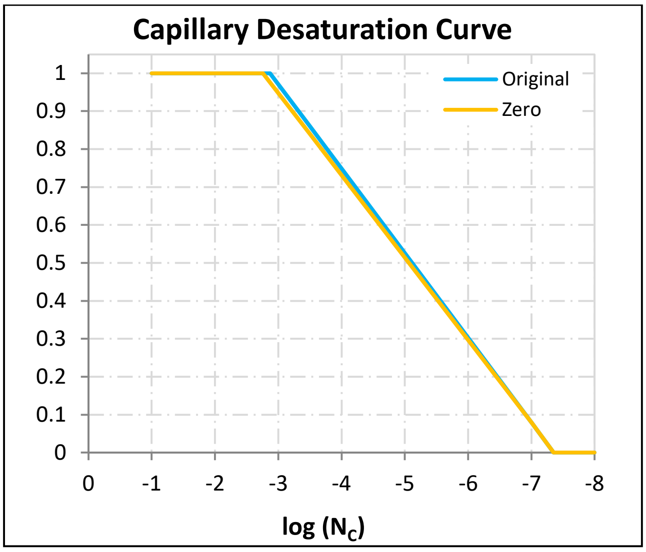

Figure 4-29: Capillary desaturation curve

Table 4-5 summarizes the matching parameters of the alkali-polymer core flood simulation matches.

Table 4-5: Matching parameters (AP flood)

Model	Polymer adsorption	RRF	IPV
Original	Polymer adsorption from polymer match	1.2	0.3
Zero	Polymer adsorption nearly zero	1.2	0.0

By variation of these parameters and retention of the fitting parameters gained from ‘RRF_best match’, the history match ‘Original’ was generated. Only the residual resistance factor had to be reduced from 60 to 1.2. The match ‘Original’ is illustrated in Figure 4-30.

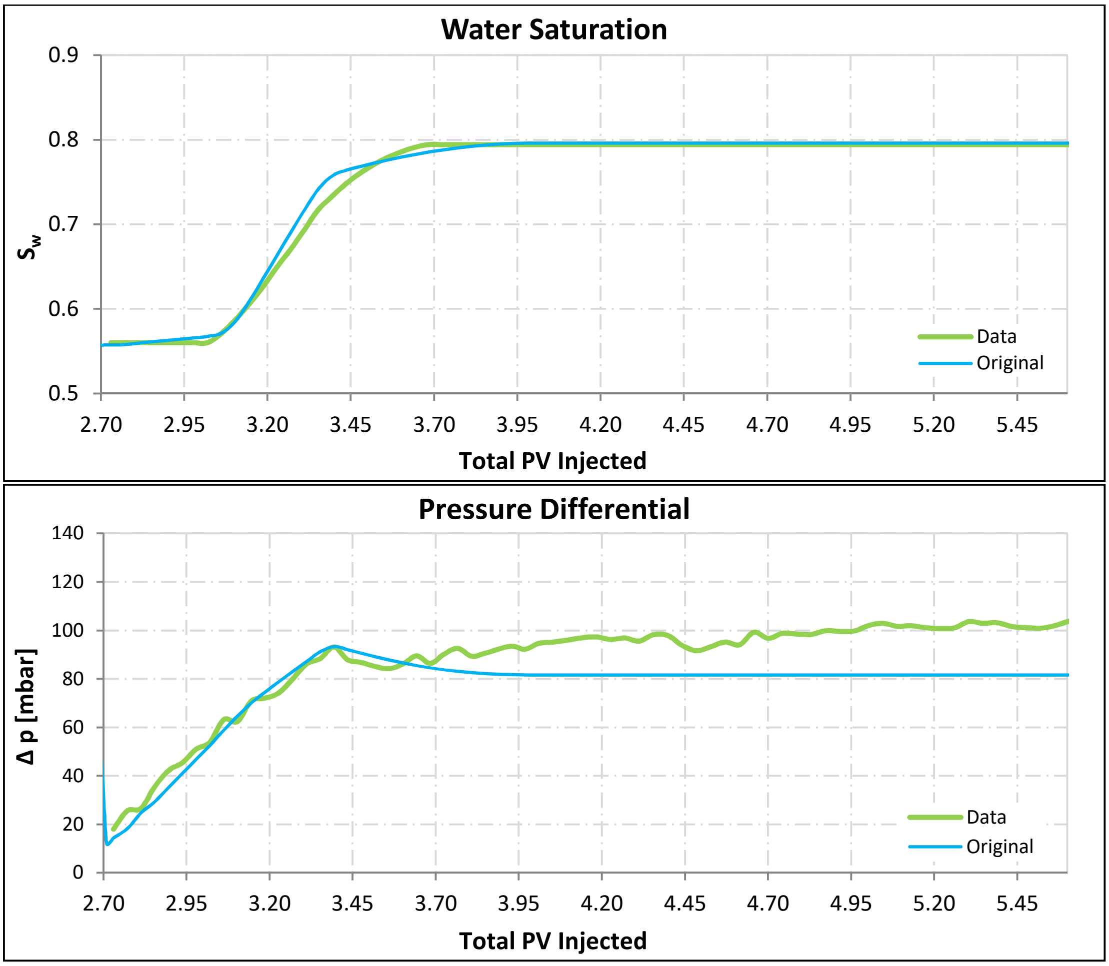

Figure 4-30: AP core flood simulation match ‘Original’

Further, the consequences of a reduction of the IPV to zero and the polymer adsorption to a value close to zero were investigated. Outcome of this task is AP flood simulation match ‘Zero’. The resulting water saturation curve is nearly congruent with the water saturation curve of ‘Original’. Investigation of the pressure differential curve shows distinct dissimilarities, although those might be ignored due to the general disability to match the events succeeding the pressure differential peak. The match ‘Zero’ is illustrated in Figure 4-31.

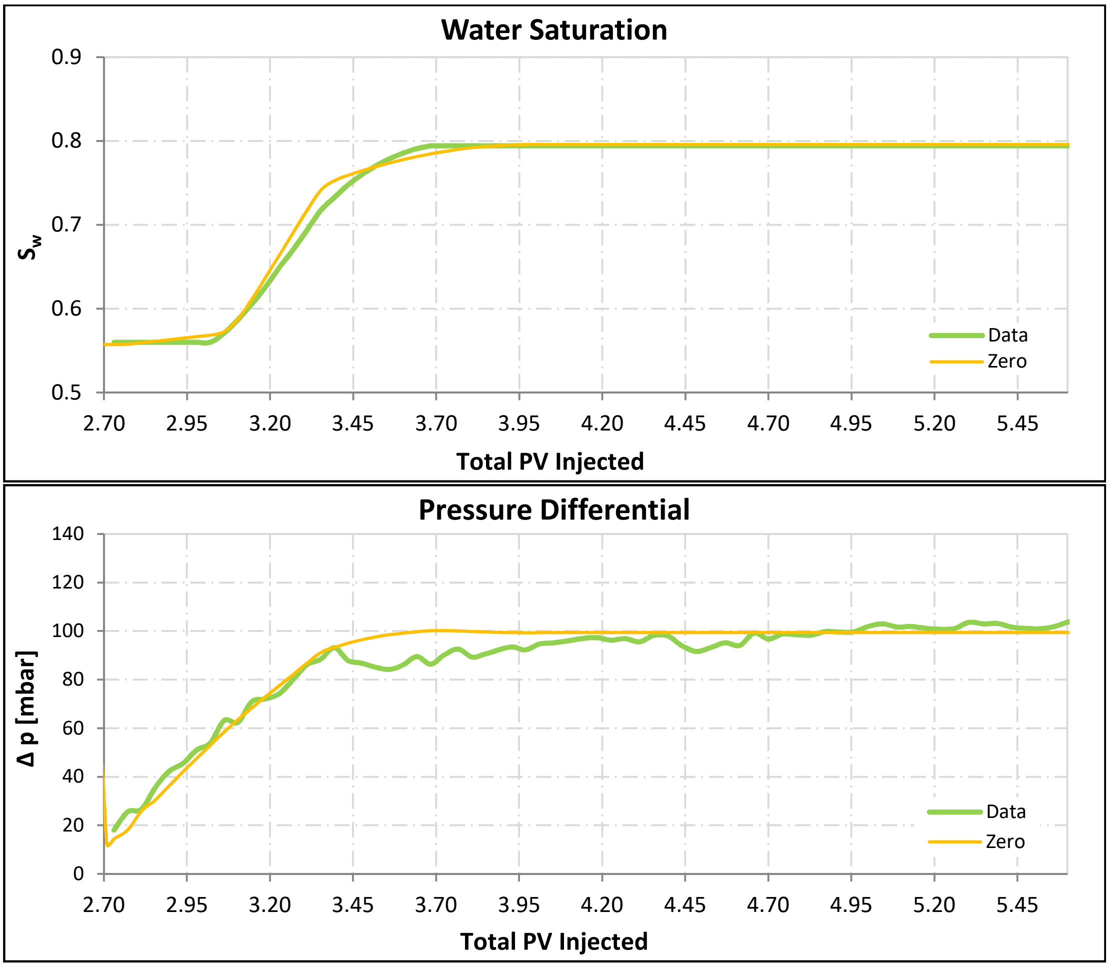

Figure 4-31: AP core flood simulation match 'Zero'

4.4.3 Miscible Flow Sensitivity

To account for the uncertainties within the endpoint relative permeability of the miscible flow type, a sensitivity analysis was executed. For both matches, four control setups were created by subdividing the distances between the actual endpoint relative permeability and an endpoint relative permeability of 1.0, to create five equal sections. For comparison, the endpoint relative permeability at the upper margin of each section was chosen, as illustrated in Figure 4-32.

Figure 4-33 and Figure 4-34 show clearly, that the water saturation curve and the pressure differential curve are distinctly affected by a reduction of the endpoint permeability. By means of the water saturation curve, it can be observed that the occurrence of the AP breakthrough is accelerated and the AP front is less blurred. The impact on the pressure differential curve is even higher, not only the magnitude is clearly altered, but also the shape of the curve changes significantly. Comparison of Figure 4-33 and Figure 4-34 demonstrates that the magnitude of the sensitivity to variations of the endpoint relative permeability is more or less independent of the respective match.

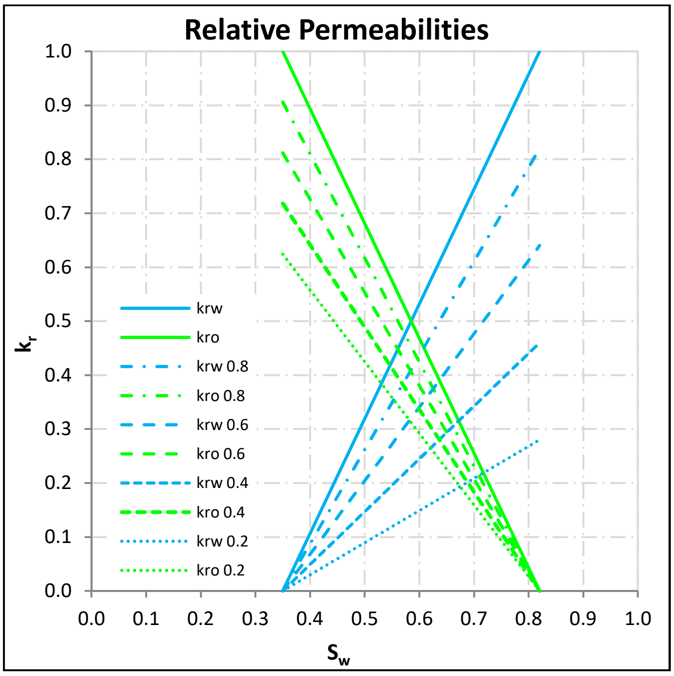

Figure 4-32: Miscible relative permeability

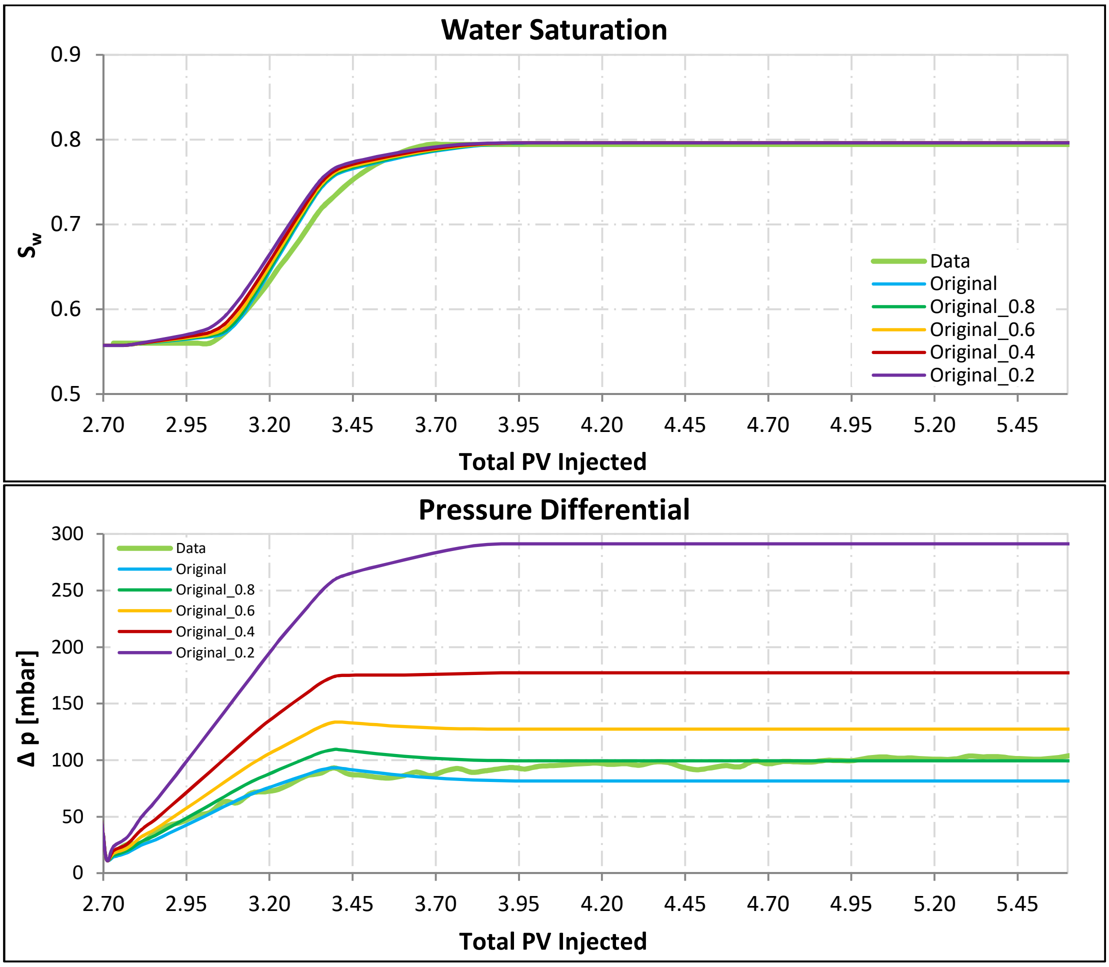

Figure 4-33: Miscible flow sensitivity analysis ('Original')

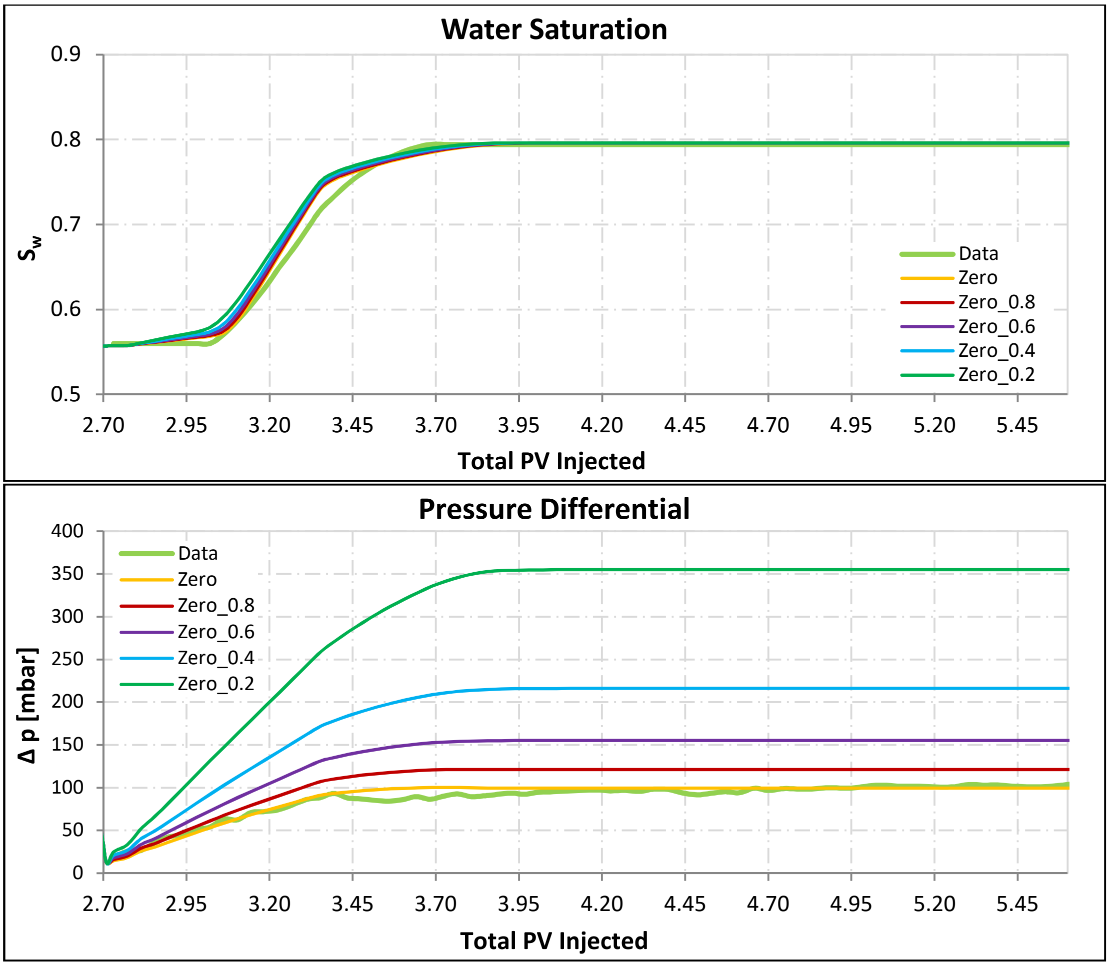

Figure 4-34: Miscible flow sensitivity analysis ('Zero')

Additionally, a sensitivity analysis regarding nearly miscible flow was executed. For this purpose, the Corey parameters of the second set of relative permeability curves were increased to 1.5, as displayed in Figure 4-35. The impact of not attaining completely miscible flow is comparable to the effect of varying endpoint relative permeability, although less in extent, as illustrated in Figure 4-36 and Figure 4-37.

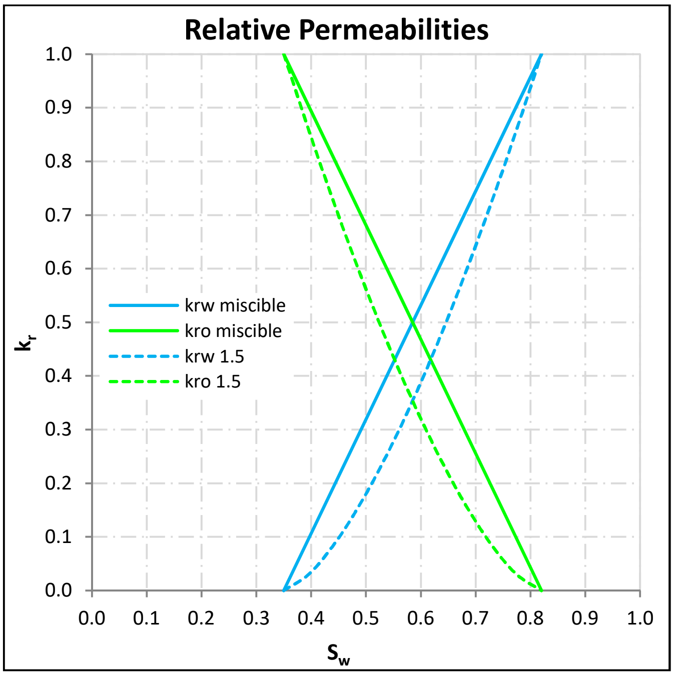

Figure 4-35: Relative permeability curves of nearly miscible flow

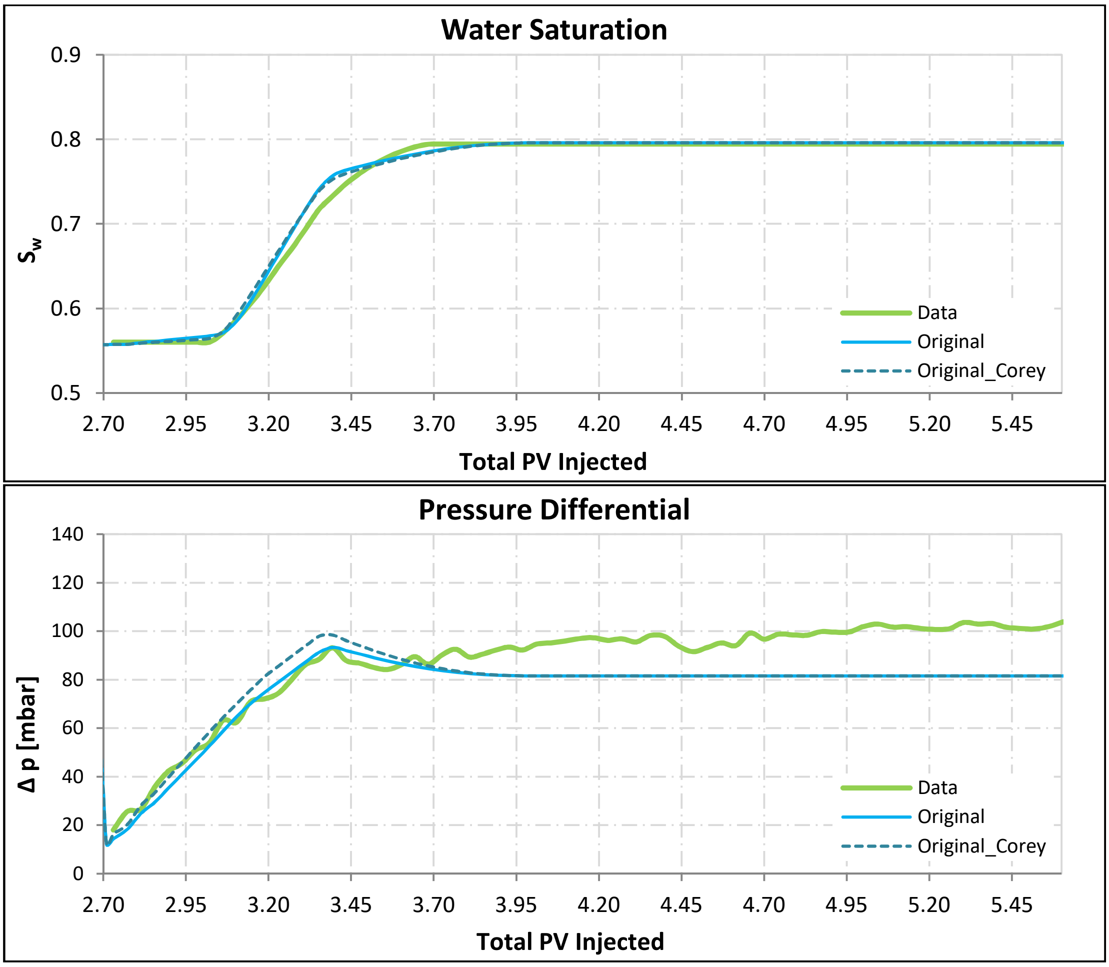

Figure 4-36: Nearly miscible flow sensitivity analysis (‘Original’)

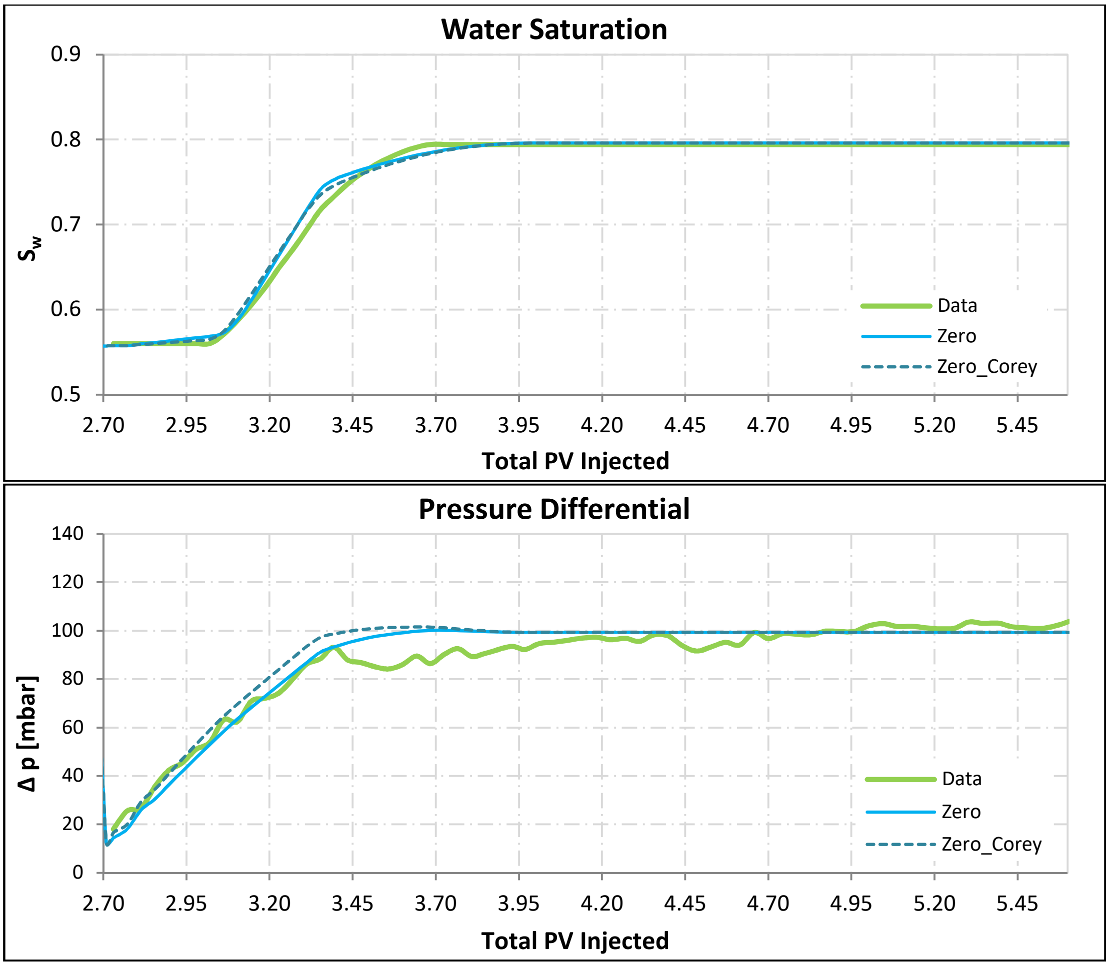

Figure 4-37: Nearly miscible flow sensitivity analysis ('Zero')

4.5 Matching Parameter Sensitivity

Regarding history matching, for quality improvement it is crucial to identify the parameters sensitive to variation. The matching parameters for every type of simulation were analyzed and investigated for sensitive behavior. Regarding the water flood, the sensitive parameters are oil relative permeability and the water Corey exponent. Table 4-6 summarizes the matching parameters for the water floods.

Table 4-6: Matching properties water flood

	Polymer Flood		**Alkali-Polymer Flood**		
Property	**Match 1**	**Match 2**	**Match 1**	**Match 2**	**Match 3**
$k_{rw,max}$	0.11	0.11	0.098	0.1	0.1
$k_{ro,max}$	0.6	0.6	0.66	0.66	0.53
S_{or}	0.42	0.42	0.4	0.4	0.395
n_w	2.7	2.2	1.6	2.0	2.0
n_o	2.0	1.9	2.0	2.0	2.0

Regarding the polymer flood, the most sensitive parameter is residual resistance factor. Regarding the alkali-polymer flood, the only sensitive parameter is the surface tension reduction.

4.6 Grid Size Sensitivity

Variations in grid size can have a tremendous effect on simulation results; therefore, the effects of grid coarsening have to be identified, so that an ideal balance between required accuracy and economic demands can be achieved.

4.6.1 Tracer Core Flood Grid Size Sensitivity

For the grid cell size sensitivity analysis, the numbers of cells were chosen to advance by a factor of 4.0. Figure 4-38 to Figure 4-40 and Fig. C.2-1 to Fig C.2-3 (Appendix C) display the results of the grid size sensitivity analysis of the single phase experiments. It is clearly displayed for all three experiments, that an increase from 125 to 5000 cells delivers hardly any improvement, while a reduction to 32 cells still produces sufficient results. A further decrease of grid cell numbers leads to tremendous inaccuracies, which increase exponentially with further reduction of the grid cell number.

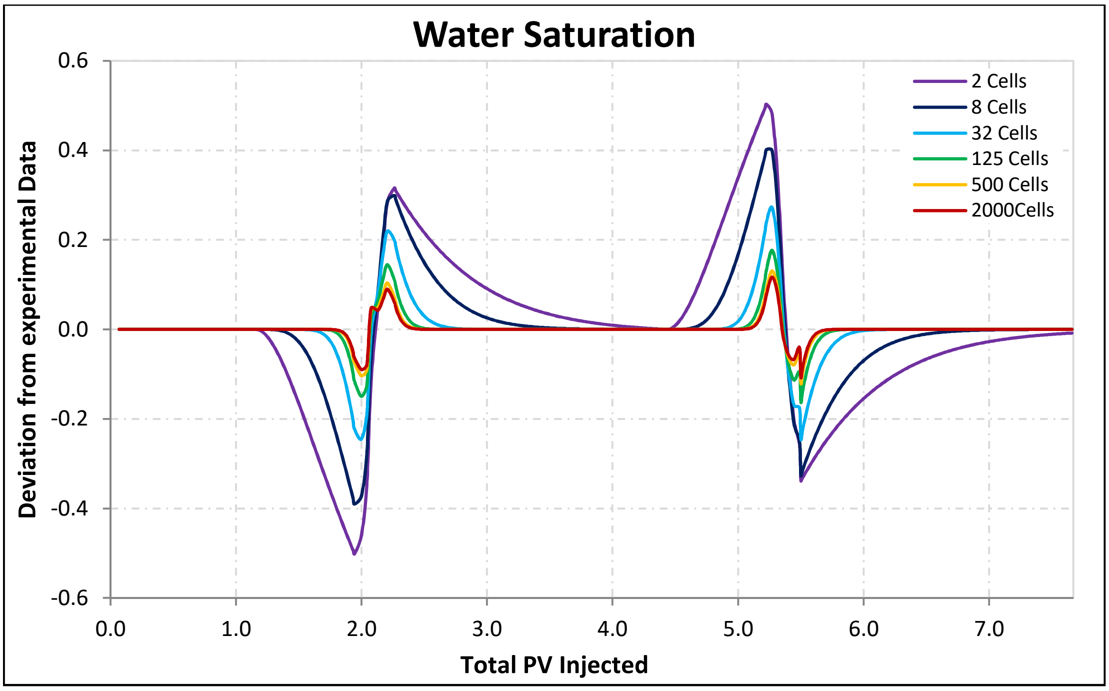

Figure 4-38: Tracer concentration difference plot (Tracer Test 1)

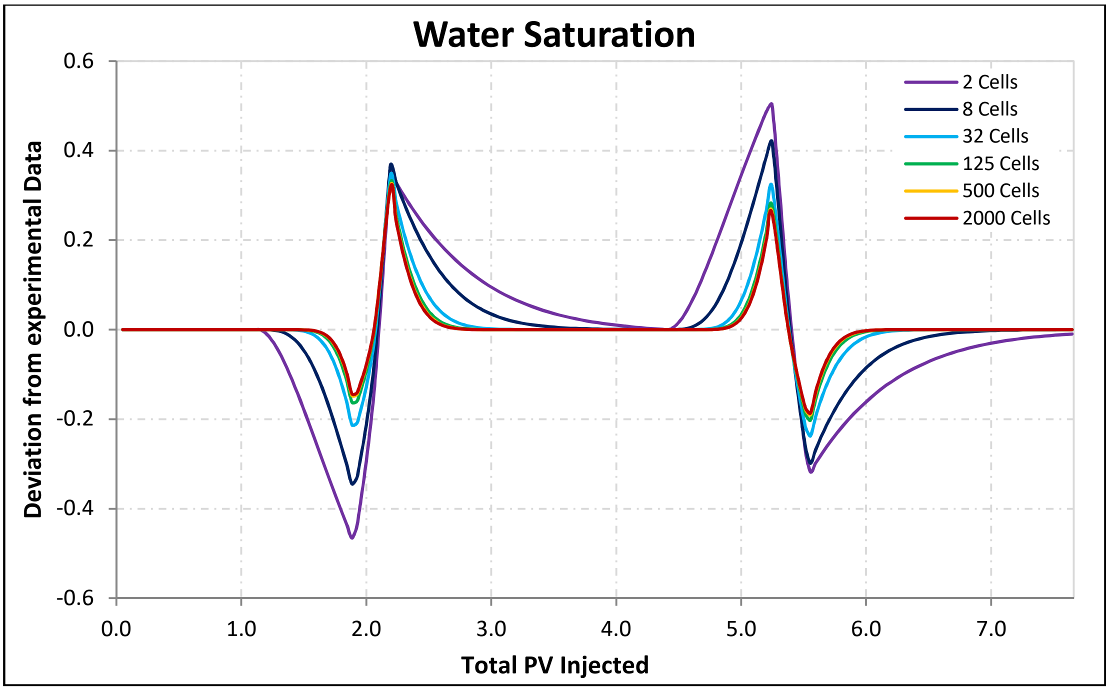

Figure 4-39: Tracer concentration difference plot (Tracer Test 2)

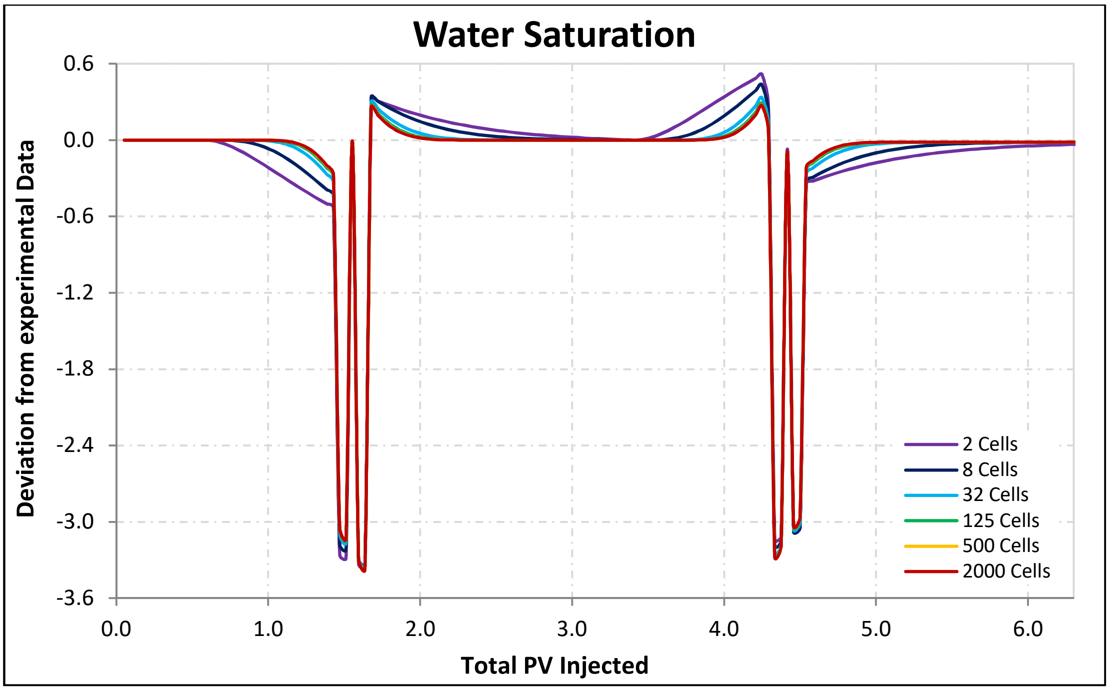

Figure 4-40: Tracer concentration difference plot (Alkaline Test)

4.6.2 Polymer Core Flood Grid Size Sensitivity

The grid size sensitivity analysis for ‘RRF_best match’ was executed analogous to the tracer core flood sensitivity analysis. In Figure 4-41 and Fig. C.2-4 (Appendix C), it is clearly illustrated, that analogous to the tracer core flood analysis, a further increase of the cells number from 125 to 500 or 2000 provides hardly any improvement. Again, a reduction to 32 cells might be an economical attractive option by requiring significantly fewer resources like simulation time, data management or required memory, and still deliver useful simulation results, depending on the circumstances. A further reduction generates tremendous inaccuracies, while the water saturation reacts more sensitive than the pressure differential.

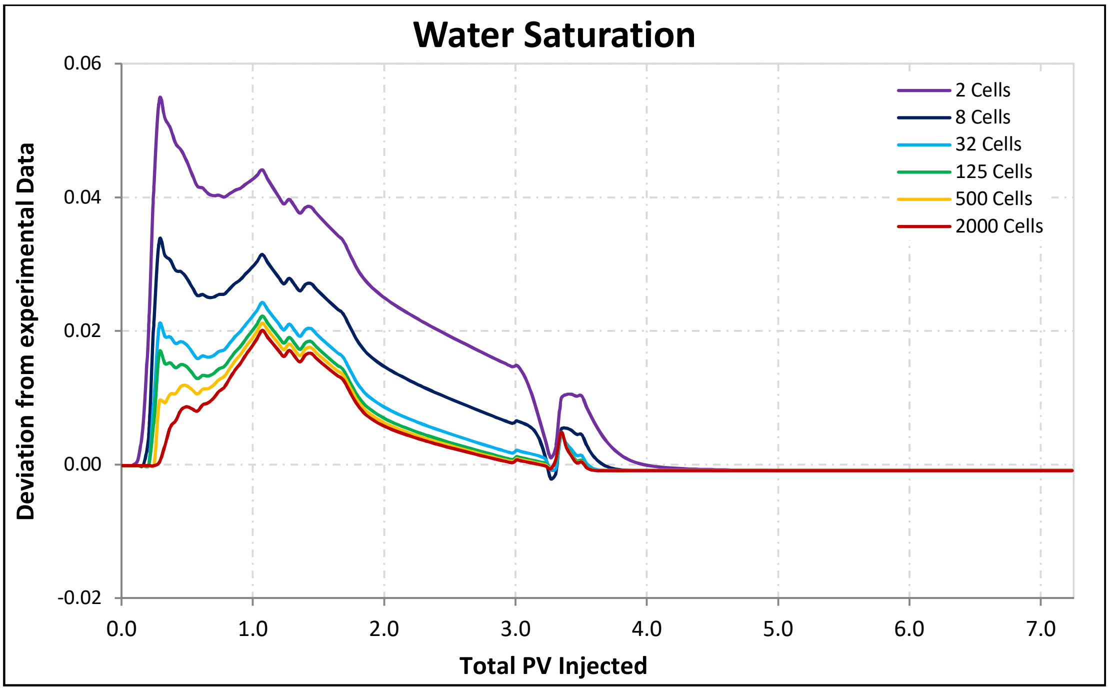

Figure 4-41: Water saturation difference plot (polymer flood)

4.6.3 AP Core Flood Grid Size Sensitivity

The grid size sensitivity analysis for ‘Original’ and ‘Zero’ was executed analogous to the tracer core flood and polymer core flood sensitivity analyses. Figure 4-42, Figure 4-43 and Fig. C.2-5 and Fig C.2-6 (Appendix C) clearly depict, that a further increase leads to effects similar to the ones observed within the tracer and polymer core flood simulations. Compared to the simulation of the polymer flood, the AP flood simulation generally reacts more sensitive to a reduction to 32 cells, although in the certain case the impression is given, that usage of the 32-cell model leads to a better coverage of certain features of the experimental data than usage of the 125-cell model. Analogous to the previously accomplished grid size sensitivity analyses, a further reduction generates tremendous inaccuracies, while the water saturation reacts more sensitive than the pressure differential. Again, the magnitude of the sensitivity to variations of the endpoint relative permeability is more or less independent of the respective match. Comparison of AP grid size sensitivity analysis and polymer grid size sensitivity analysis shows clearly, that the AP core flood reacts more sensitive to a reduction of the grid cell size than the polymer core flood. Figure 4-42 and Figure 4-43 show difference plot of 'Original' and 'Zero'.

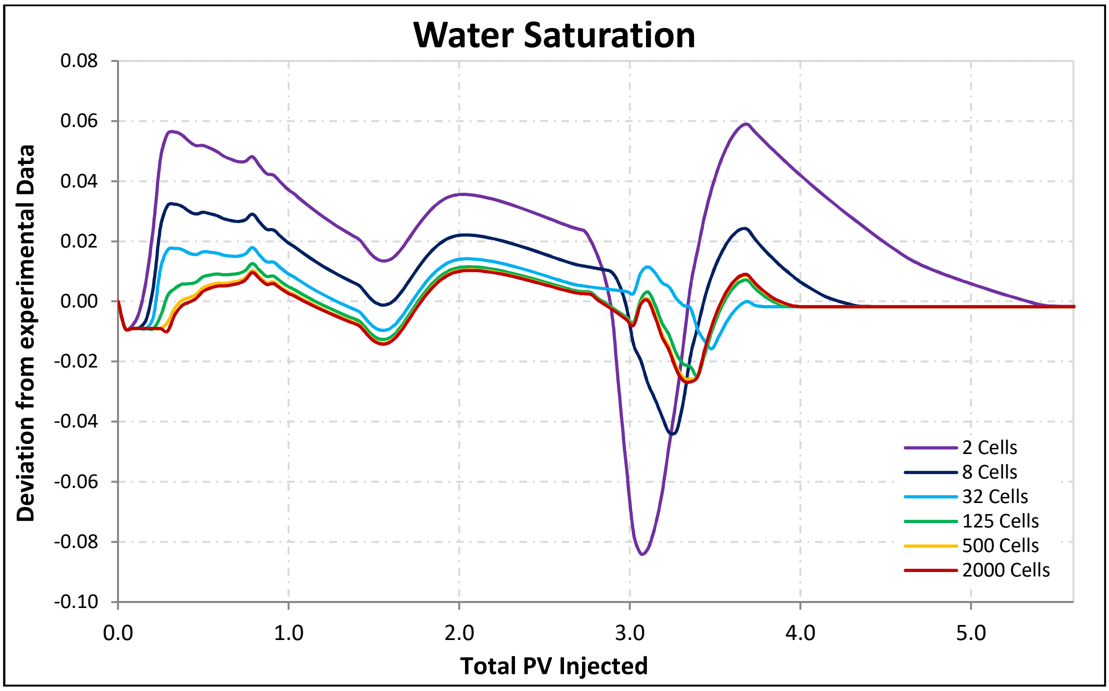

Figure 4-42: Water saturation difference plot (AP flood 'Original')

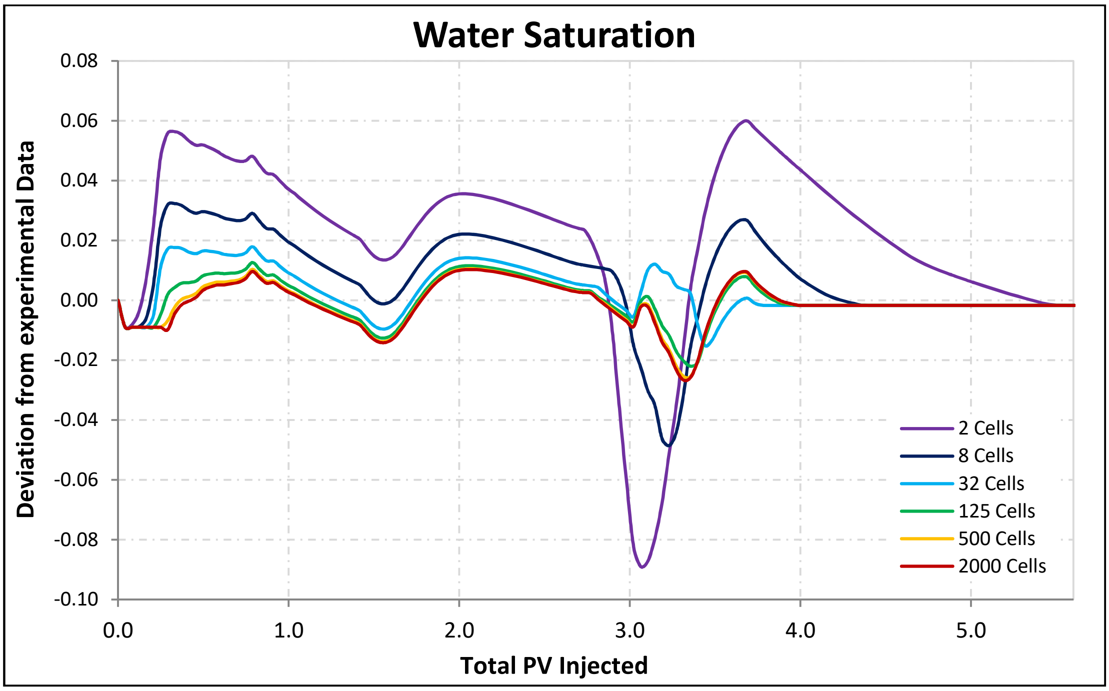

Figure 4-43: Water saturation difference plot (AP flood 'Zero')

Chapter 5

Field Scale Simulation

One aim of core flood simulations is to apply the gained knowledge on field scale. Investigation of the effects of variations in grid cell size and grid orientation is of great importance regarding the ability to predict at the best the occurring fluid propagation and its effects. These insights are crucial for decision making, treatment design and production optimization. For the executed field scale simulations, the polymer and alkali-polymer matches from the core flood simulations were used.

5.1 The Reservoir Model

The reservoir model is a typical five-spot pattern with one injection well in the center and four surrounding production wells. The dimensions of the model are 305 m x 305 m x 10 m and the distance between injector and producer is approximately 212.5 m. All used setups are vertically subdivided into 10 layers of 1 m thickness. Regarding boundary conditions, a box model with no-flow boundaries was chosen. A conventional color scheme is used, green representing high oil saturation and blue representing high water saturation. Figure 5-1 illustrates the geometry of the reservoir model.

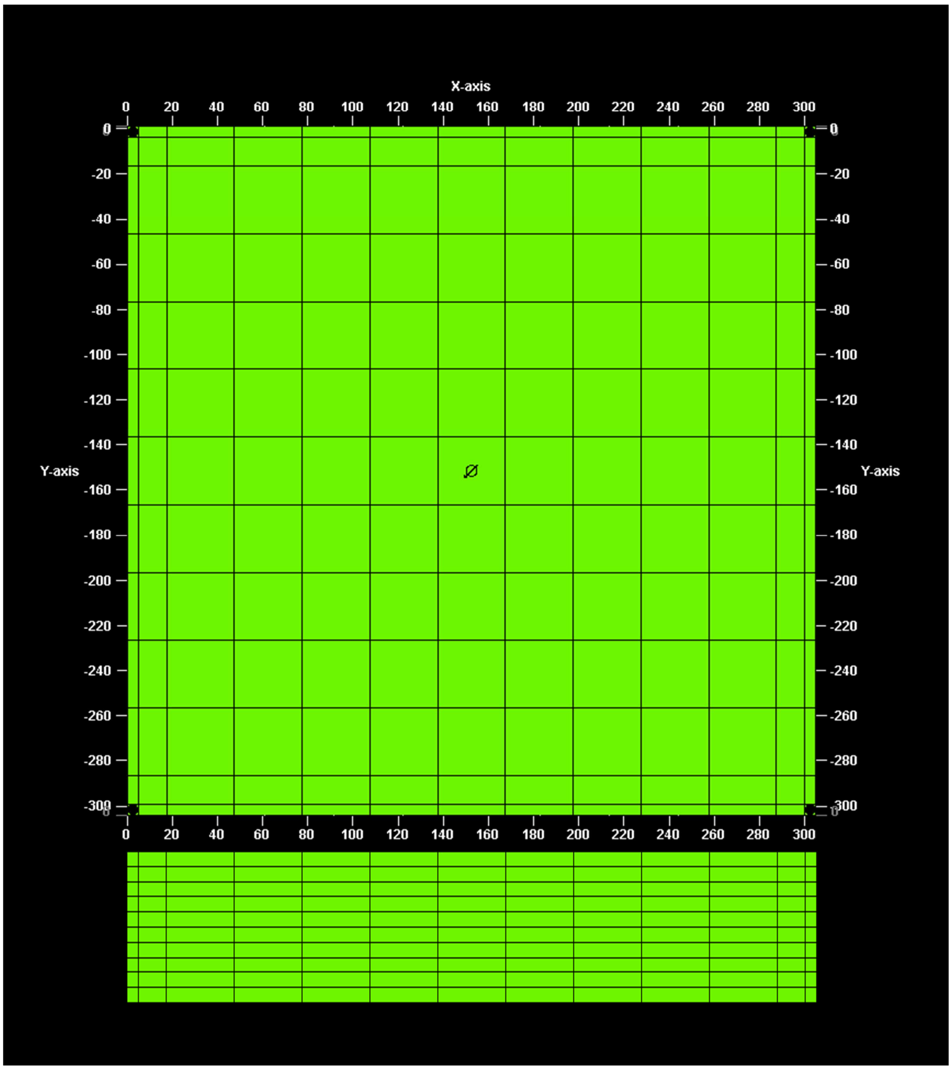

Figure 5-1: Top and side view of the reservoir model

The injection scheme was defined to be 1.5 PV water, followed by 0.6 PV chemical slug, followed by 1.5 PV water. Combination with an aspired injection rate of 1 PV/10 years leads to the schedule: 15 years water injection - 6 years chemical injection - 15 years water injection. The injection rate of 1 PV per 10 years is equivalent to an injection rate of 64.7 m³/d. Table 5-1 gives a summary of the most important parameters of the reservoir model.

Table 5-1: Reservoir model parameters

Parameter	**Value**	**Unit**
Dimensions	305x305x10	m
No of layers	10	
Distance injector-producer	~ 212.5	m
Permeability	1000	mD
Initial water saturation	0.2	
Porosity	25.39	%
Pore volume	236190	m³
Injection rate	64.7	m³/d

In order to study the effect of grid sizes and grid orientations, five different grid cell sizes (Model 1 - Model 5) and two different grid orientations (Model 1 and Model 1B) were set up. Table 5-2 summarizes the applied geometries.

Table 5-2: Applied grid cell sizes and grid orientations

Model	**i-direction [m]**	**j-direction [m]**	**k-direction [m]**	**orientation °**
Model 1	5	5	1	0.0
Model 1B	5	5	1	45
Model 2	10	10	1	0.0
Model 3	20	20	1	0.0
Model 4	30	30	1	0.0
Model 5	50	50	1	0.0

5.2 Flow Simulation Results

5.2.1 Flow Simulation Results of the Secondary Water Flood

Since the mechanisms of the pre-water flood are the same regardless the subsequent chemical injection, it is discussed separately. The results are of different magnitude although the processes, which take place, are the same. This actuality origins in the circumstance that for the field scale simulation a setup was created which alters from the core flood experiments (e.g. permeability). Figures and tables are created from the simulation results of the polymer flood simulation .

The water flood preceding the chemical flood exemplifies the fundamental displacement process in a porous medium and some involved phenomena like typical propagation patterns, boundary effects and velocity differences. The general water flood observations are discussed with the help of ‘Model 1’. First, a clearly radial pattern can be observed, as illustrated in Figure 5-2.

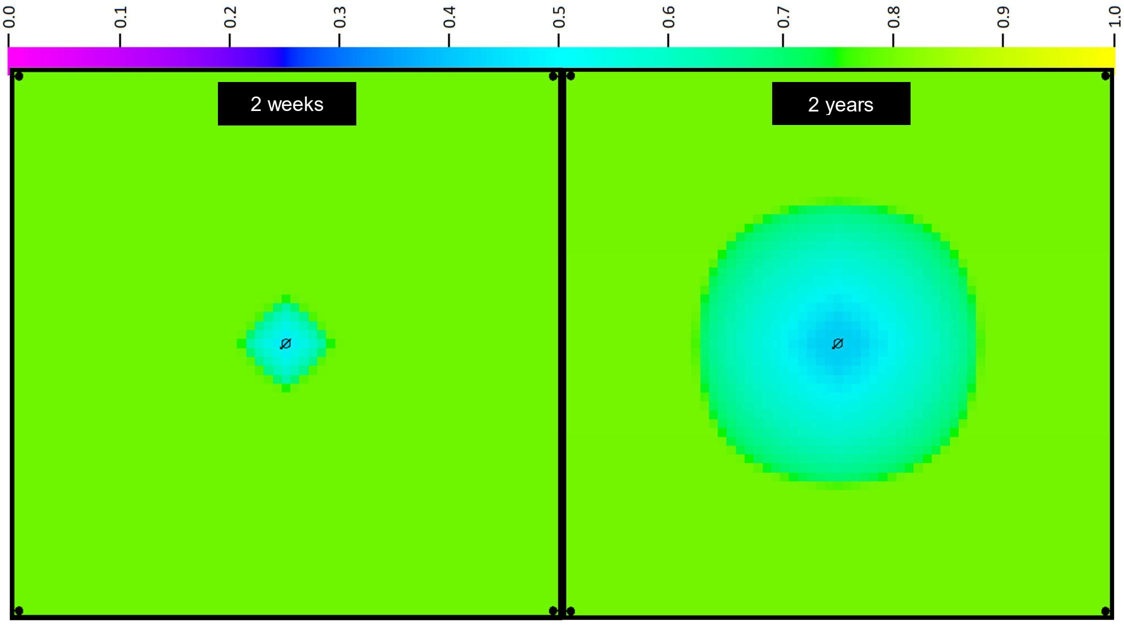

Figure 5-2: Radial water propagation

Once the waterfront reaches a certain proximity to the production wells, the driving force towards the well changes the radial propagation pattern into a star shaped one, as illustrated in Figure 5-3.

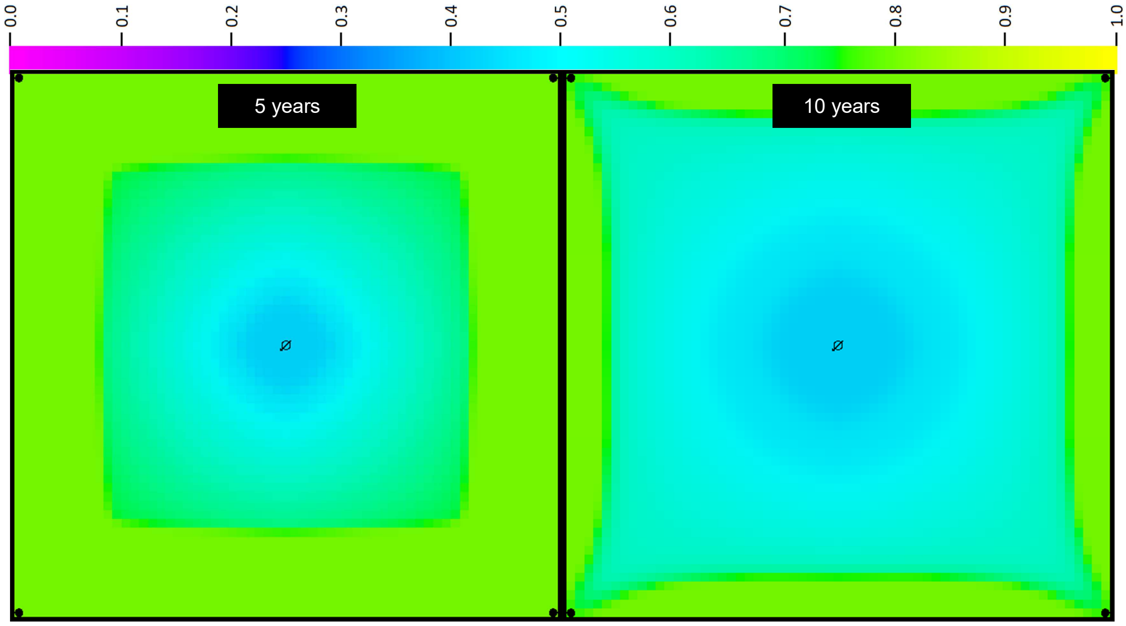

Figure 5-3: Star-shape water propagation

Comparing the water front propagation of the top layer and the bottom layer shows that the water is under running the oil according to the density differences of water and oil. As a result, the waterfront is propagating faster through the deeper layers and therefore arrives earlier at the bottom of a production well than at the top of the perforations. This process is illustrated in Figure 5-4 to Figure 5-6.

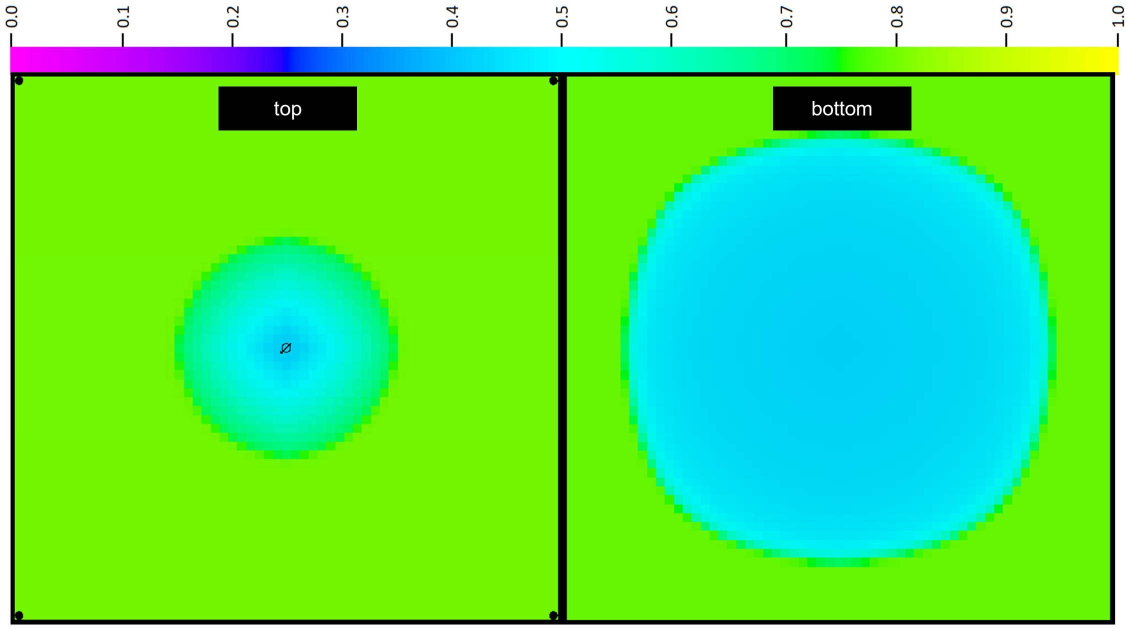

Figure 5-4: Comparison of water propagation after 1 year

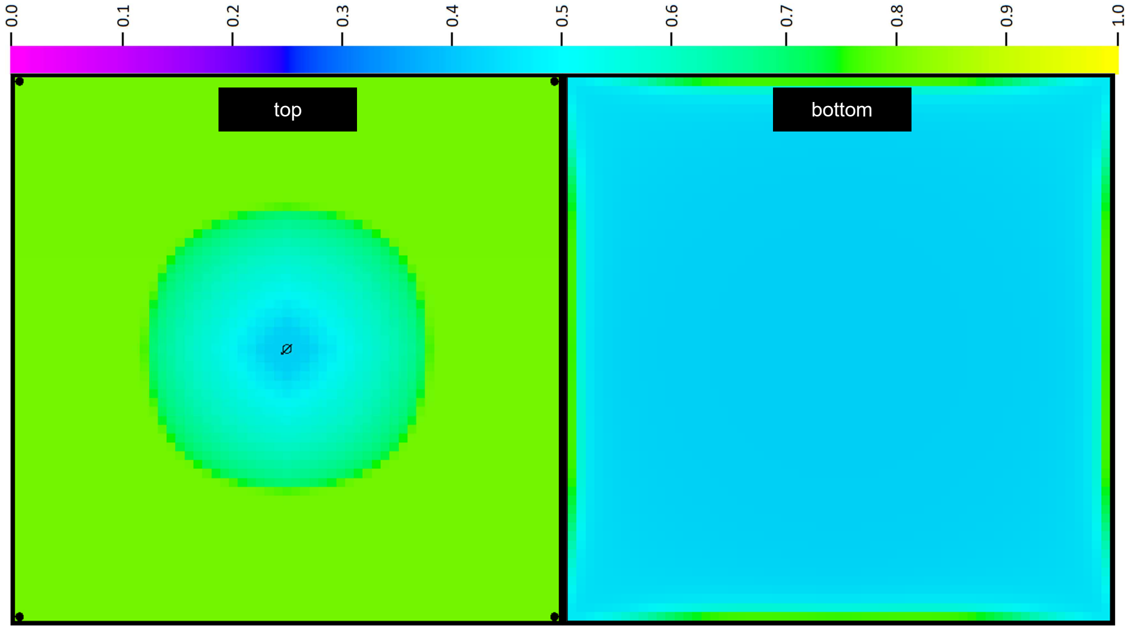

Figure 5-5: Comparison of water propagation after 2 years

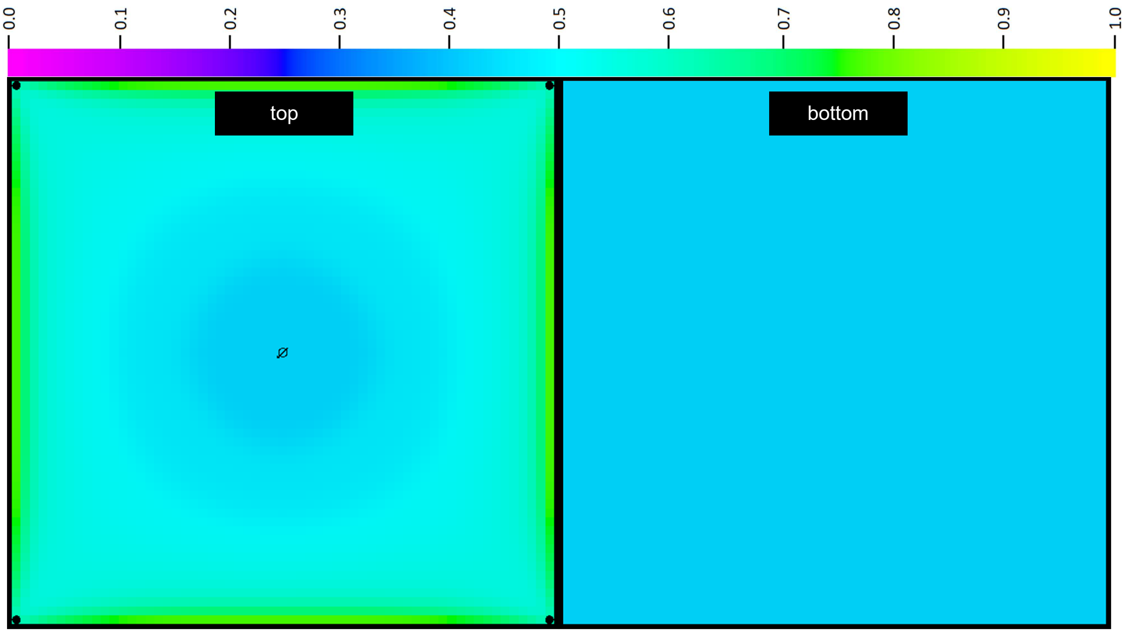

Figure 5-6: Comparison of water propagation at the end of the water flood

Additionally to the comparison of the top view and bottom view of the reservoir, the side view directly displays, that the waterfront is propagating faster through the deeper parts of the reservoir than through the shallower parts. This discrepancy increases with time, as illustrated in Figure 5-7. In the bottom layer, the waterfront arrives at the production wells after approximately 1.7 years while in the top layer it takes significantly longer.

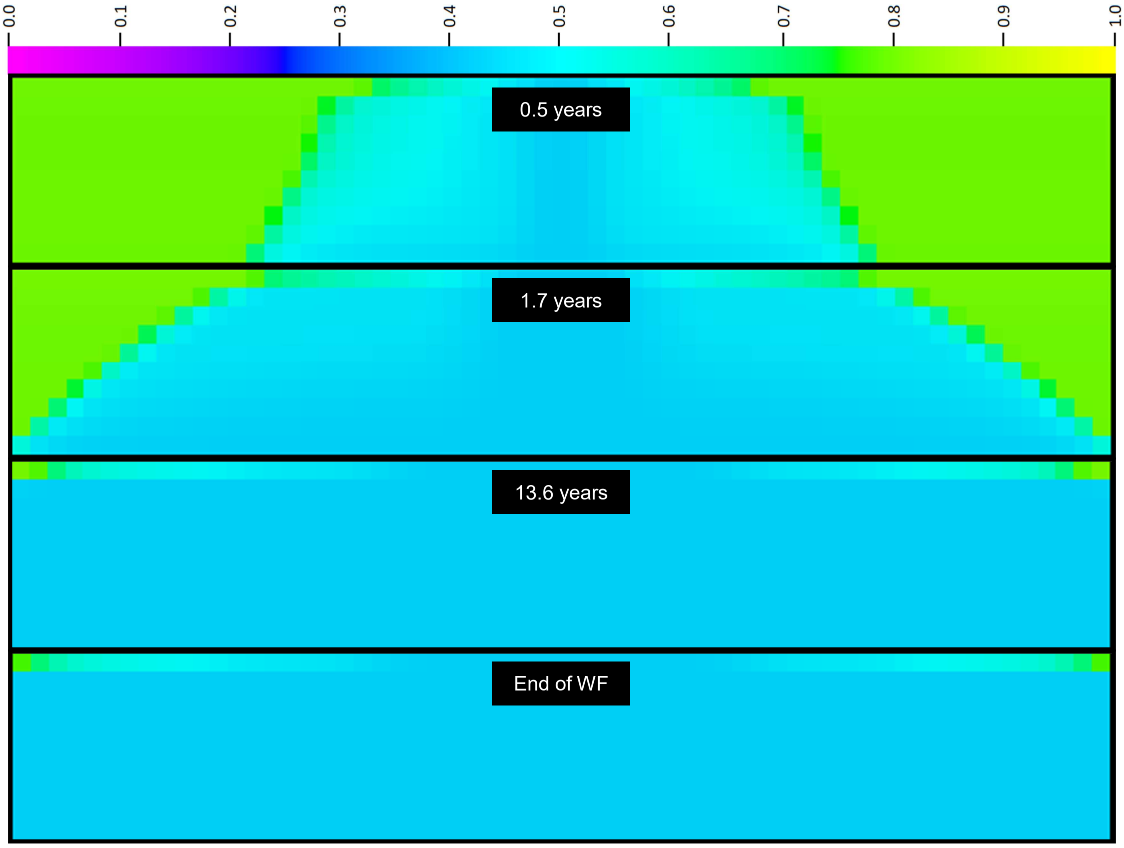

Figure 5-7: Waterfront arriving at production wells

Figure 5-8 and Figure 5-9 show the cumulative water production and the recovery factor of the water flood. The attained recovery factor after the water flood is 45.0%.

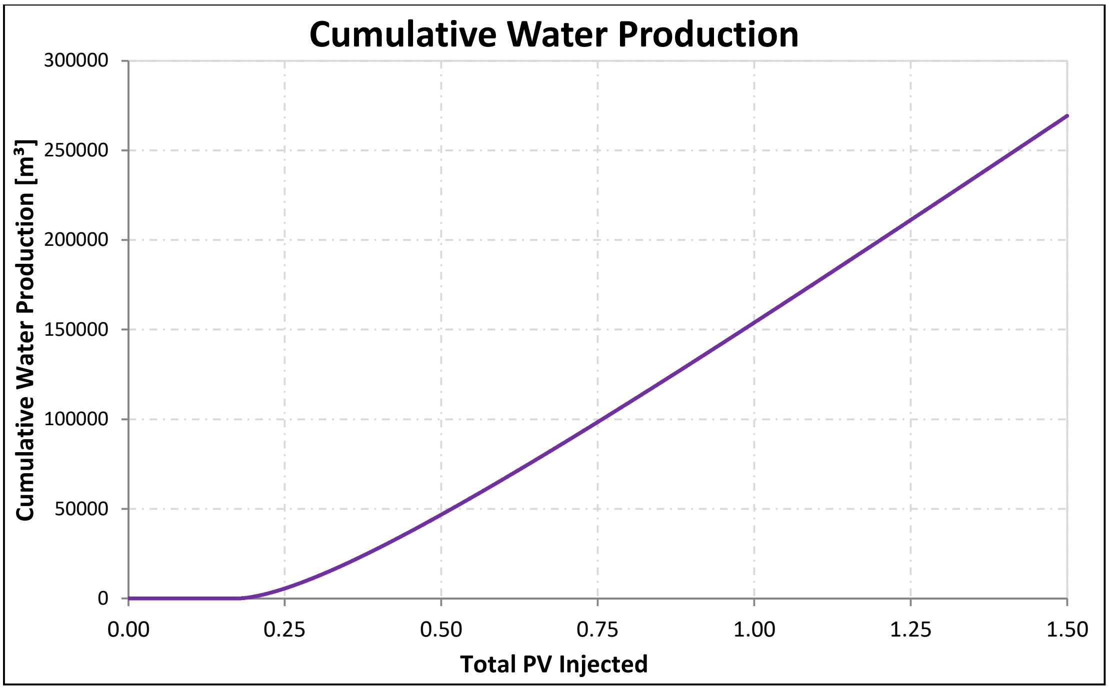

Figure 5-8: Cumulative water production (water flood)

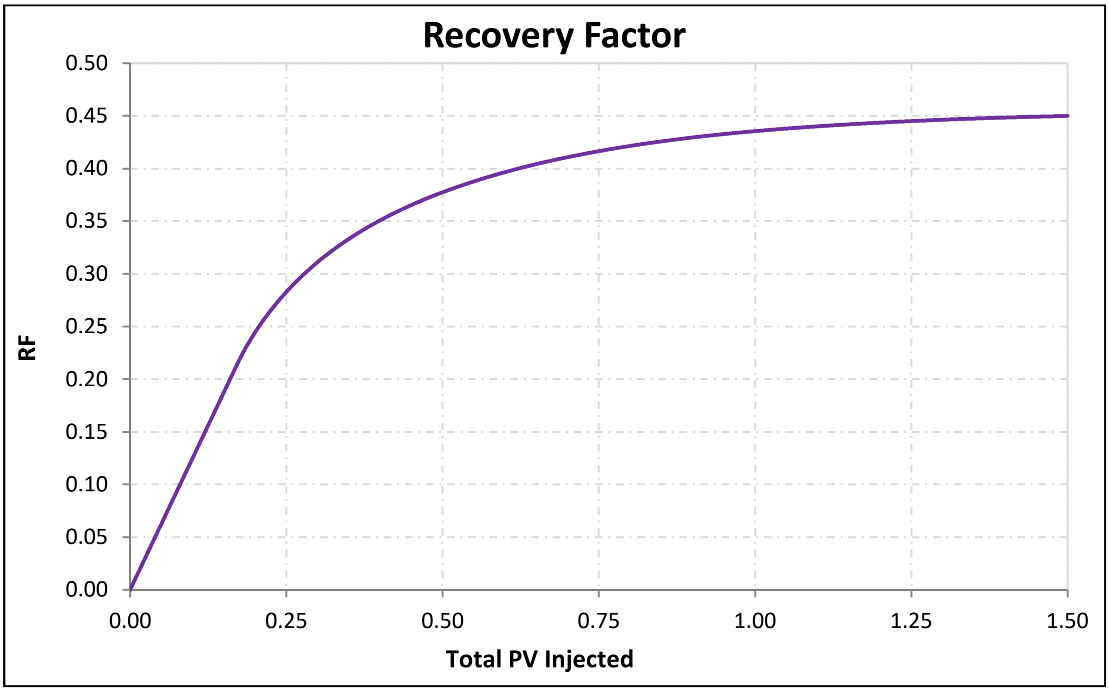

Figure 5-9: Recovery factor (water flood)

5.2.2 Flow Simulation Results of the Polymer Flood

For the field scale polymer flood, the parameters of match ‘RRF_best match’ from the polymer core flood experiment were used. Important input parameters are summarized in Table 5-3.

Table 5-3: Simulation input parameters (polymer flood)

Parameter	Value
$k_{rw,max}$	0.11
$k_{ro,max}$	0.6
S_{or}	0.42
n_w	2.7
n_o	2.0
RRF	60
IPV	0.3

As discussed previously, the main mechanism behind polymer flooding is the alteration of the mobility ratio via increase of the water viscosity. This results in a more effective oil displacement and the development of an oil bank ahead of the waterfront. Since this process is relatively slow and the achievements regarding oil recovery relatively low, the succeeding water flood evolves no visible effect, as illustrated in Figure 5-10 and Figure 5-11. Nevertheless, it is still essential to maintain the propagation of the oil ring towards the production wells.

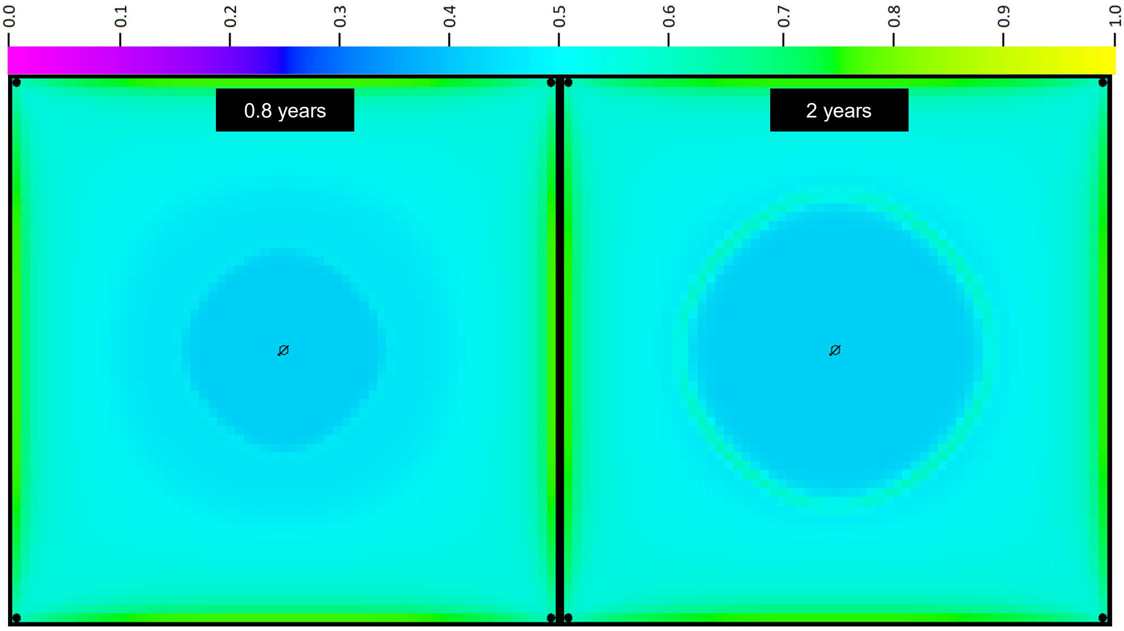

Figure 5-10: Effect of the polymer injection on the oil displacement

In contrast to a water flood, no star-shape propagation front develops during a polymer flood, which origins in the reduced mobility of the water and accordingly diminished driving force towards the production wells. Additionally, the extent of the oil ring grows over time. The triangle-shaped oil displacement exhibited on the left hand side of Figure 5-11 is a no-flow boundary effect of the simulation model and has no physical significance. After the end of the

EOR measures, the water saturation over the extent of the entire reservoir is nearly uniform, as illustrated on the right hand side of Figure 5-11.

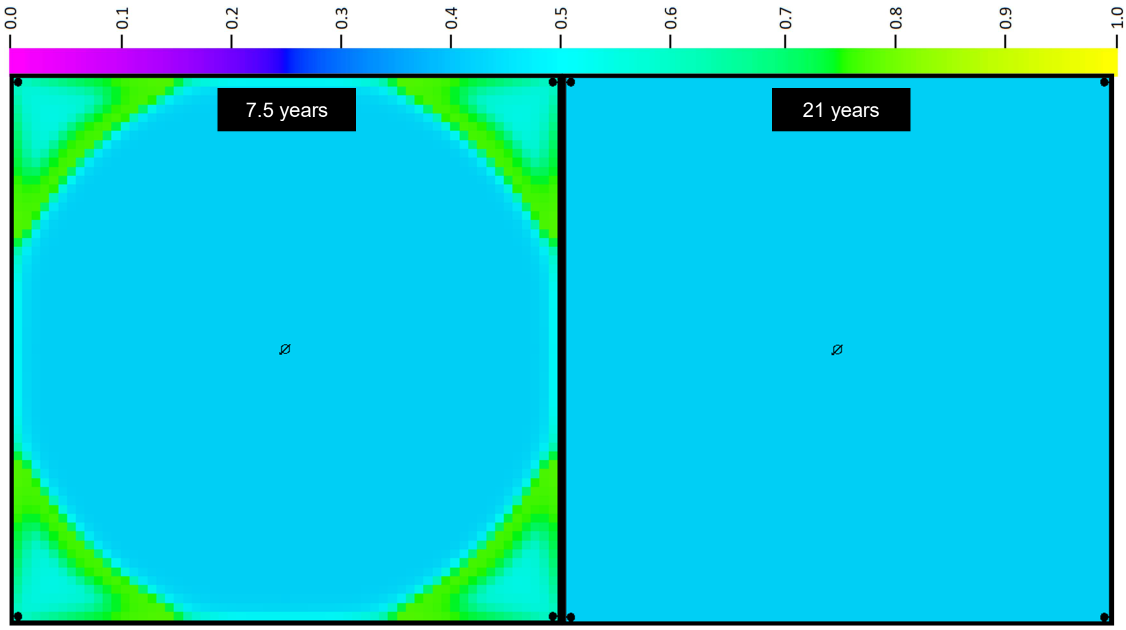

Figure 5-11: Effect of the post-polymer water injection on the oil displacement

Investigation of the events occurring along the bottom layer of the reservoir reveals that no significant developments take place. As already addressed, the vertical displacement leads to largely uniform water saturation in the deeper regions of the reservoir after the end of the preceding water flood. As a result, the processes visible on the top of the reservoir cannot be observed at the bottom of the reservoir, no ring appears and no noticeable change in water saturation occurs, as illustrated in Figure 5-12.

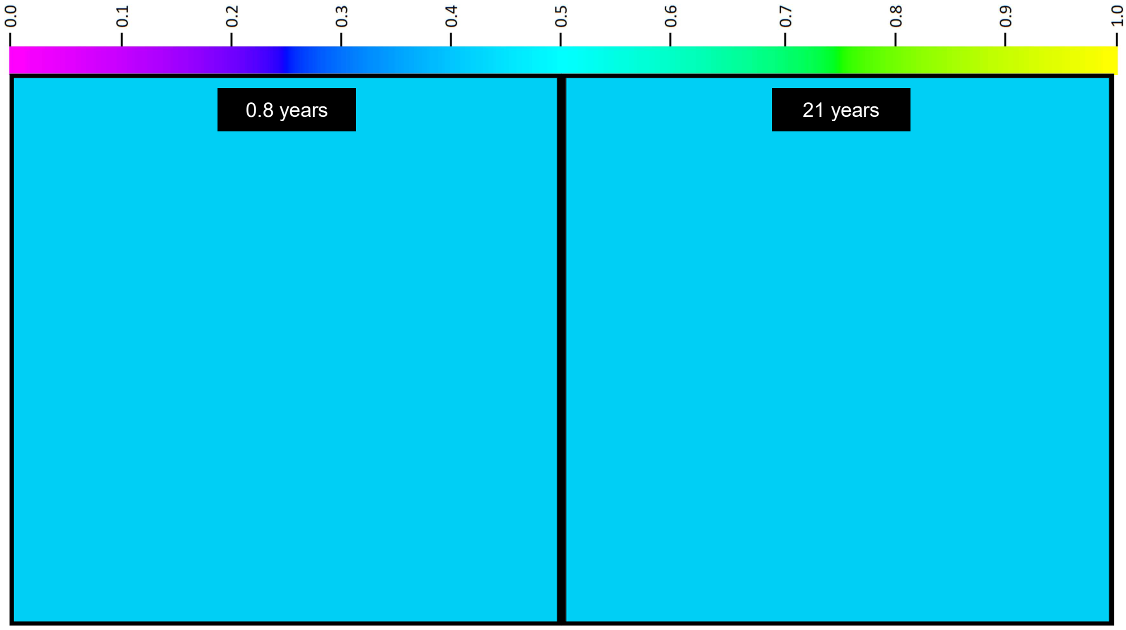

Figure 5-12: Effect of the polymer injection on the lower part of the reservoir

Figure 5-13 and Figure 5-14 show the cumulative water production and the recovery factor of the polymer flood. The attained recovery factor after the polymer flood is 46.3%.

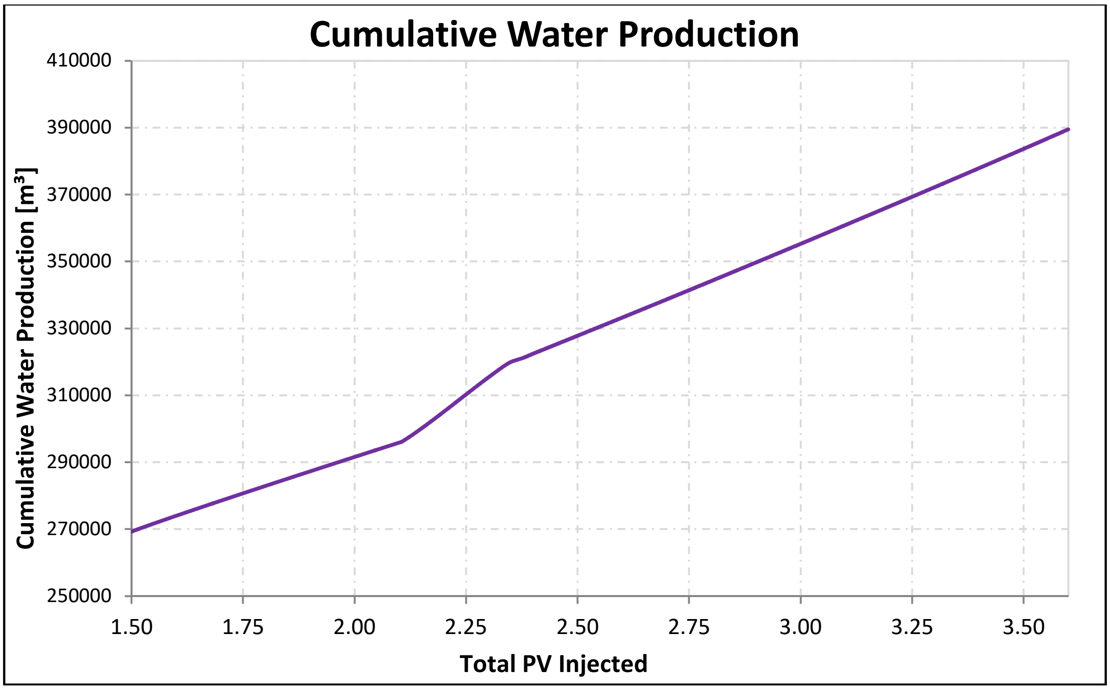

Figure 5-13: Cumulative water production (polymer flood)

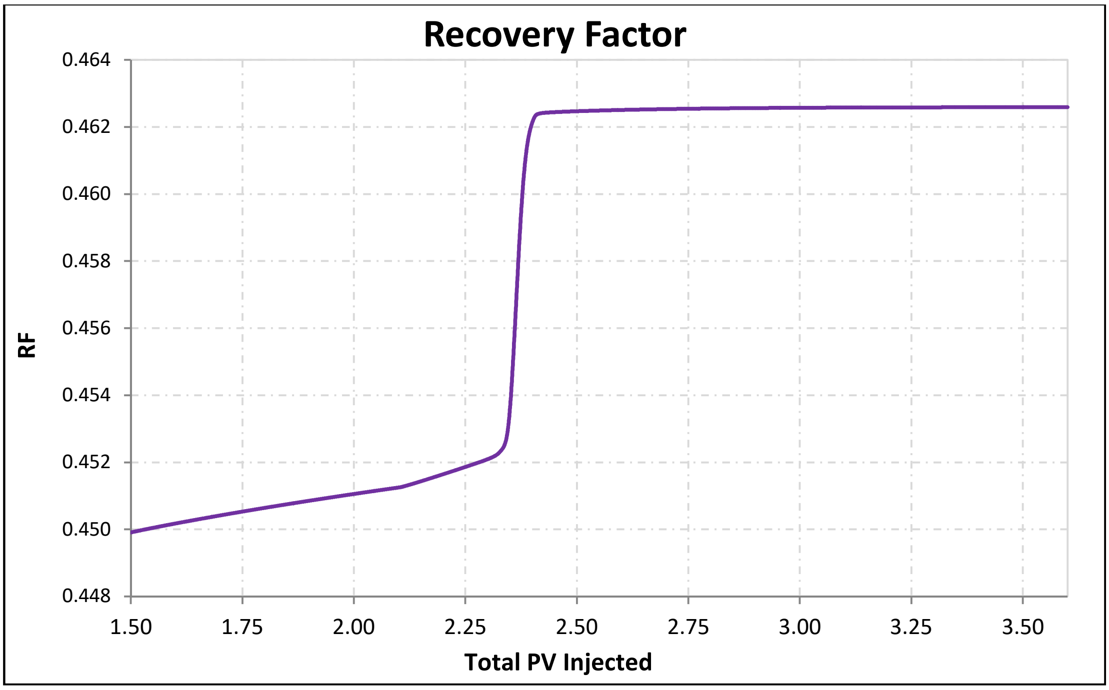

Figure 5-14: Recovery factor (polymer flood)

5.2.3 Simulation Results of the Alkali-Polymer Flood

Field scale alkali-polymer floods were performed using the parameters of AP matches ‘Original’ and ‘Zero’ from the AP core flood experiment and will be referred to as ‘Match 1’ and ‘Match 2’ within the field scale simulations. For the general interpretation and the investigation of varying grid cell sizes and grid orientation, the simulation results from ‘Match 1’ were used. Important input parameters are summarized in Table 5-4.

Table 5-4: Simulation input parameters (AP flood ‘Match 1’)

Parameter	Value
$k_{rw,max}$	0.11
$k_{ro,max}$	0.6
S_{or}	0.42
n_w	2.7
n_o	2.0
RRF	1.2
IPV	0.3

As discussed previously, the main mechanism behind alkali-polymer flooding is the mobilization of residual oil by lowering the interfacial tension. This mechanism is highly more effective than a water flood or a pure polymer treatment. Similar to the latter, a continuous oil bank develops ahead of the waterfront. It is a very fast process and results can be observed immediately after the start of the AP injection, as illustrated at the left hand side of Figure 5-15. The achievements regarding oil recovery are relatively high and the succeeding water flood evolves no visible effect, as illustrated in Figure 5-16. Analogous to a polymer flood, it is still essential to maintain the propagation of the oil ring towards the production wells.

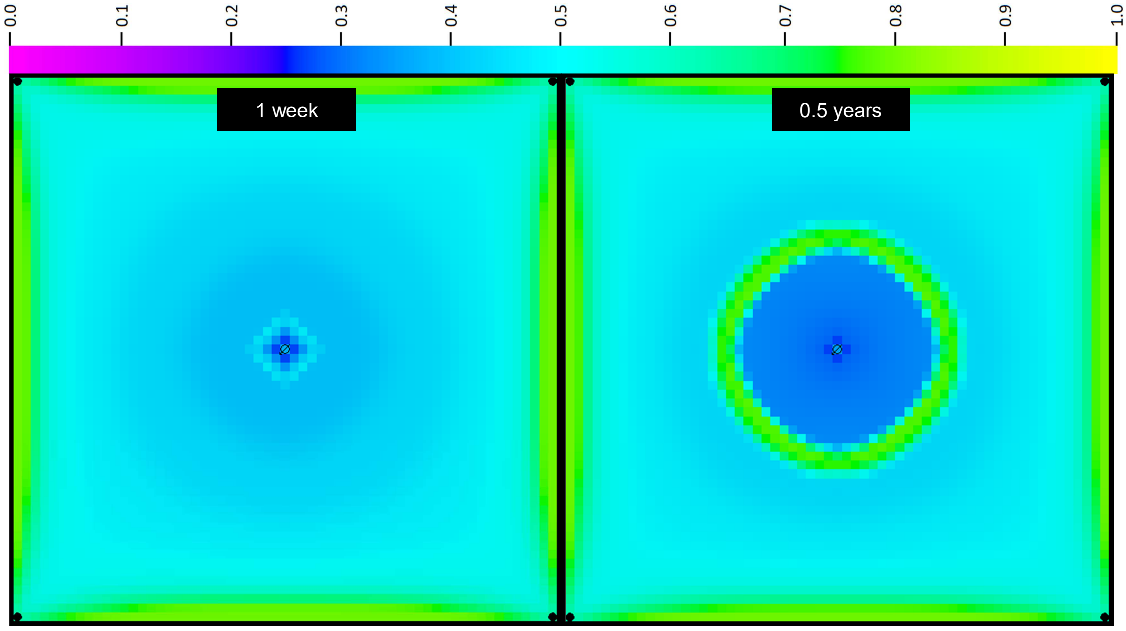

Figure 5-15: Effect of the AP injection on the oil displacement (AP flood ‘Match 1’)

Similar to the polymer flood, no star-shape propagation front develops during the AP flood, originating in the low mobility of the oil compared to the mobility of the water. The extent of the oil ring grows heavily over time, as shown in Figure 5-15 and Figure 5-16. After the end of the EOR measures, the water saturation over the extent of the entire reservoir is nearly uniform, although a slightly higher water saturation can be observed along the flow path from the injection well to the production wells, as illustrated on the right side of Figure 5-16.

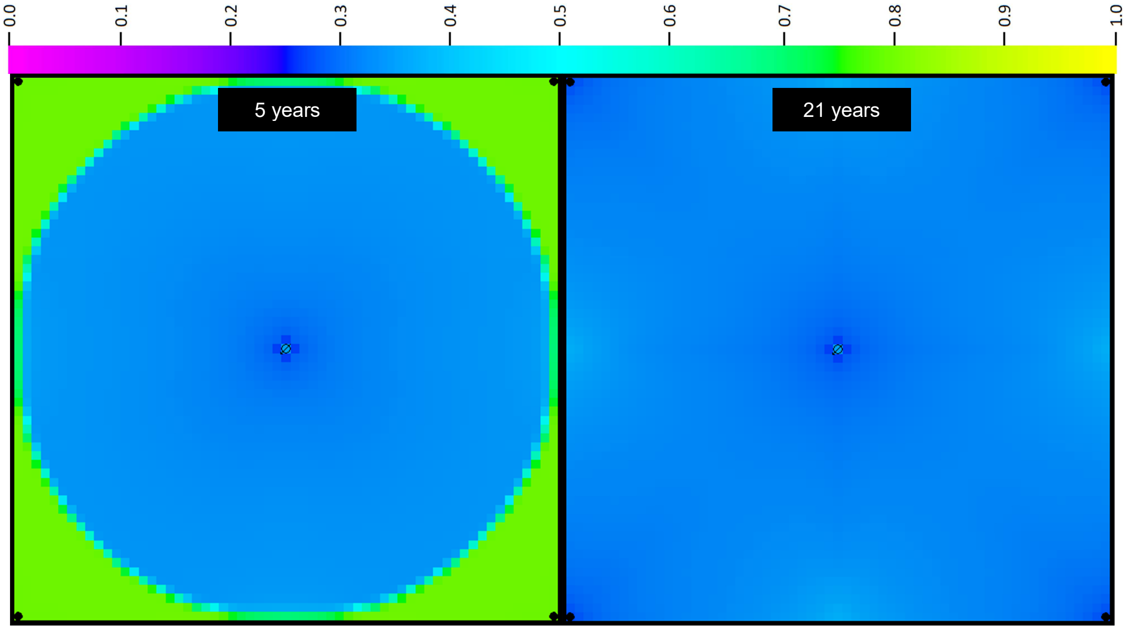

Figure 5-16: Effect of the post-AP water injection on the oil displacement (AP flood 'Match 1')

Investigation of the events occurring along the bottom layer of the reservoir reveals that in contrast to the polymer flood significant developments take place and that the residual water saturation is reasonably increased. A circular zone of increased oil saturation develops at the bottom layer, although of a significant lower oil saturation than in the top layer, caused by the higher water saturation in the bottom layer at the beginning of the AP flood. Opposite to the water flood, the propagation velocity of the AP slug is similar over the vertical extent of the reservoir. The portrayed developments are illustrated in Figure 5-17.

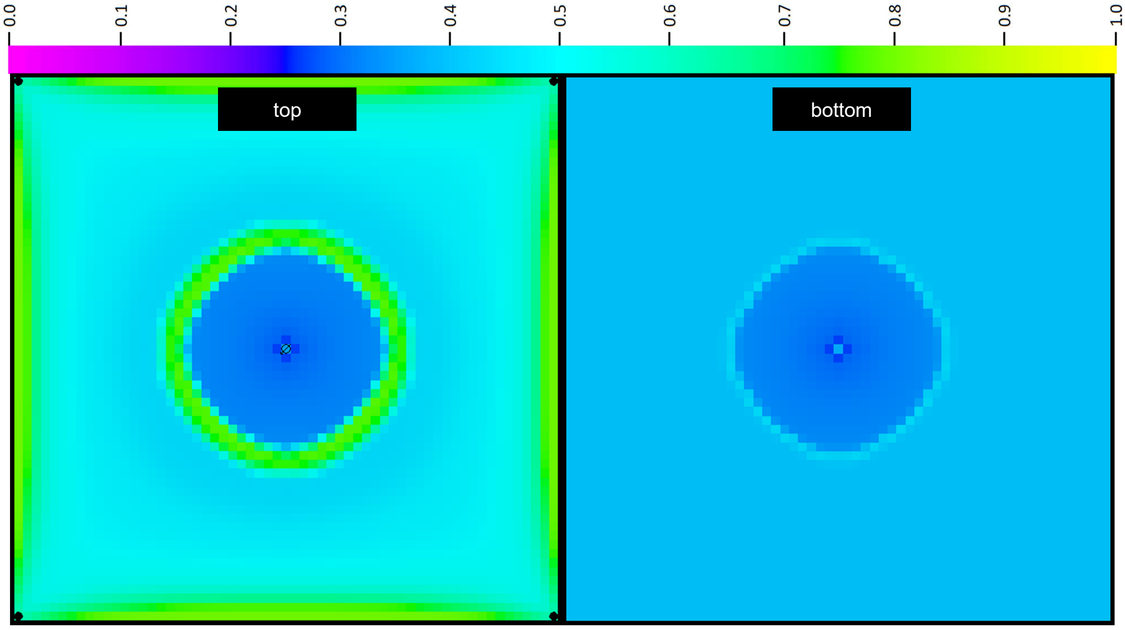

Figure 5-17: Comparison of the propagation velocities at different depths (AP flood 'Match 1')

During the simulation of an AP flood, severe boarder effects occur, as illustrated on the left hand side of Figure 5-18. At the End of the EOR measures, the spatial distribution of the water saturation in the bottom layer is comparable with the one in the top layer, but the magnitude is slightly higher, as illustrated on the right hand side of Figure 5-18.

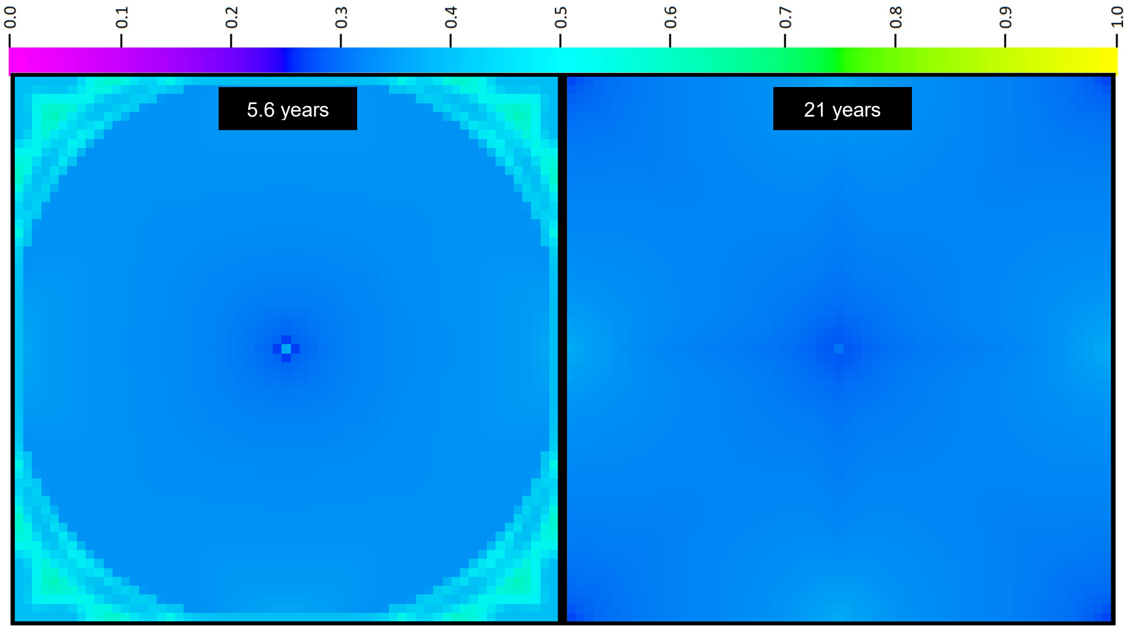

Figure 5-18: Effect of the AP injection on the lower part of the reservoir (AP flood 'Match 1')

Figure 5-19 and Figure 5-20 show the cumulative water production and the recovery factor of the alkali-polymer flood. The attained recovery factor after the end of the AP flood is 59.4%.

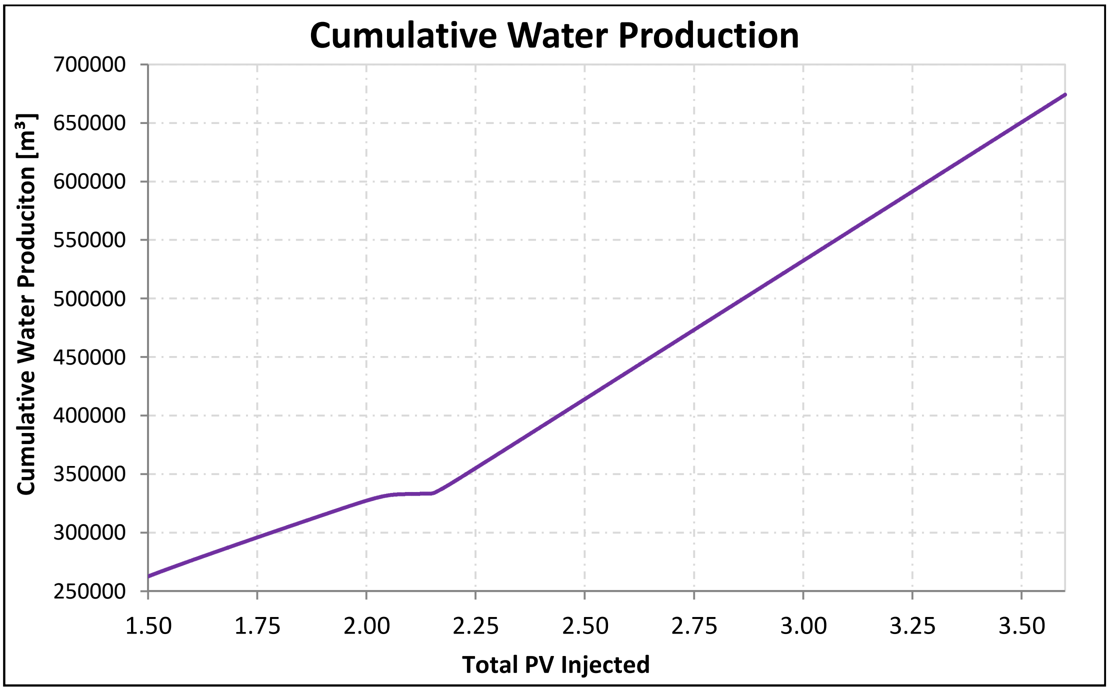

Figure 5-19: Cumulative water production (AP Match 1)

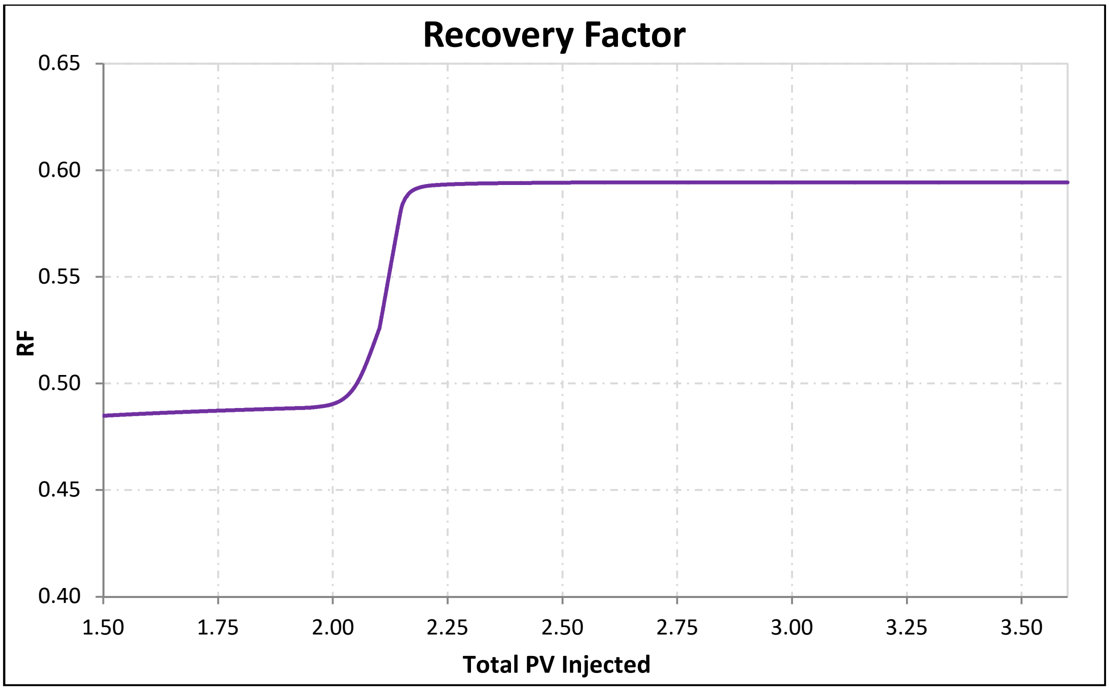

Figure 5-20: Recovery factor (AP flood 'Match 1')

- ### Differences between Alkali-Polymer Flood 'Match 1' and 'Match 2'

Although the difference between the AP core flood history matches seems negligible, its impact on field scale simulation has to be investigated. Important input parameters of AP flood 'Match 1' and 'Match 2' are summarized in Table 5-5.

Table 5-5: Comparison of simulation input parameters (AP flood 'Match 1' and 'Match 2')

Parameter	**Value**	
	Match 1	**Match 2**
$k_{rw,max}$	0.11	0.11
$k_{ro,max}$	0.6	0.6
S_{or}	0.42	0.42
n_w	2.7	2.7
n_o	2.0	2.0
RRF	1.2	1.2
IPV	0.3	0.0

A comparison of 'Match 1' and 'Match 2' shows that the simulation executed with the parameters of 'Match 1' exhibits a higher propagation velocity of the oil ring. Although this effect takes place from the beginning, it only becomes visible after a certain time. Figure 5-21 and Figure 5-22 illustrate how this development accelerates over time.

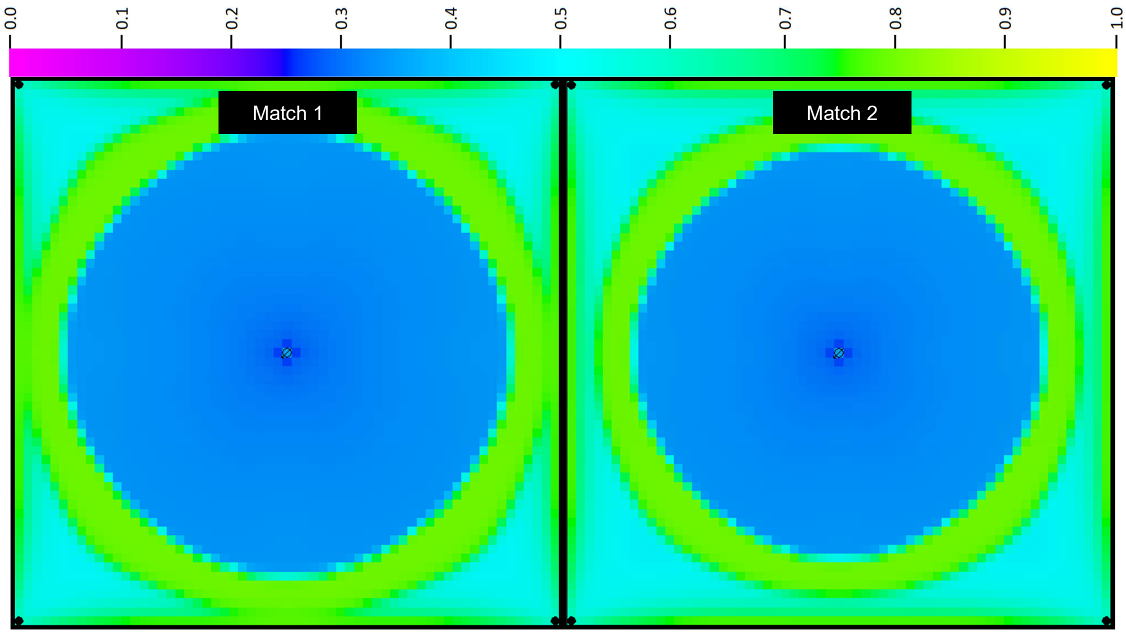

Figure 5-21: Comparison of the propagation velocities of AP flood 'Match 1' and 'Match 2' (3.25 years)

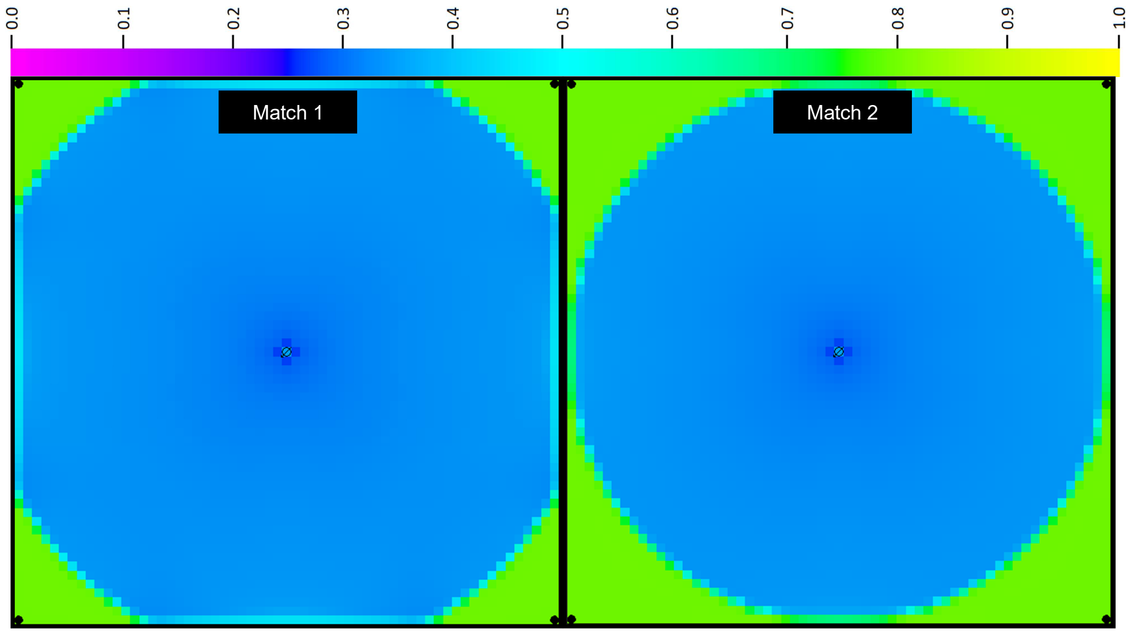

Figure 5-22: Comparison of the propagation velocities of AP flood 'Match 1' and 'Match 2' (6 years)

The different propagation velocities have no effect on the overall performance of the EOR treatment, and at the end of the stimulation measures, both simulations accomplish nearly the same S_w, as illustrated in Figure 5-23.

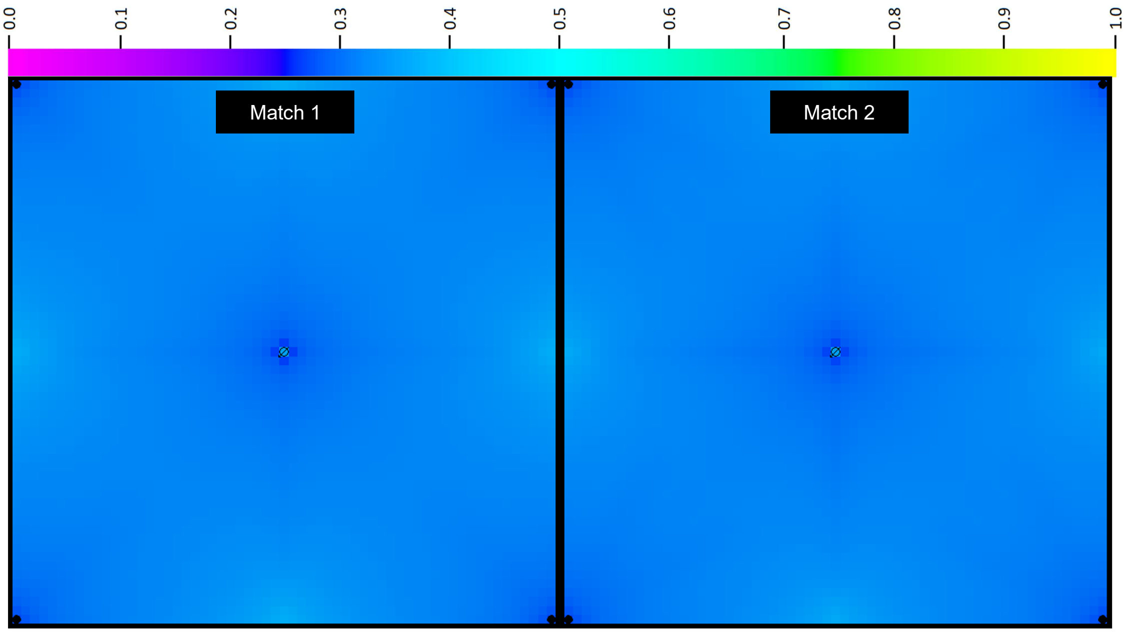

Figure 5-23: Comparison of S_w of AP flood ‘Match 1’ and ‘Match 2’ at the end of the AP flood

Comparing the boarder effects occurring to ‘Match 1’ and ‘Match 2’, it becomes visible that concerning local oil saturation they have a larger impact on ‘Match 2’ than on ‘Match 1’. Additionally the have a different spatial allocation, as illustrated in Figure 5-24.

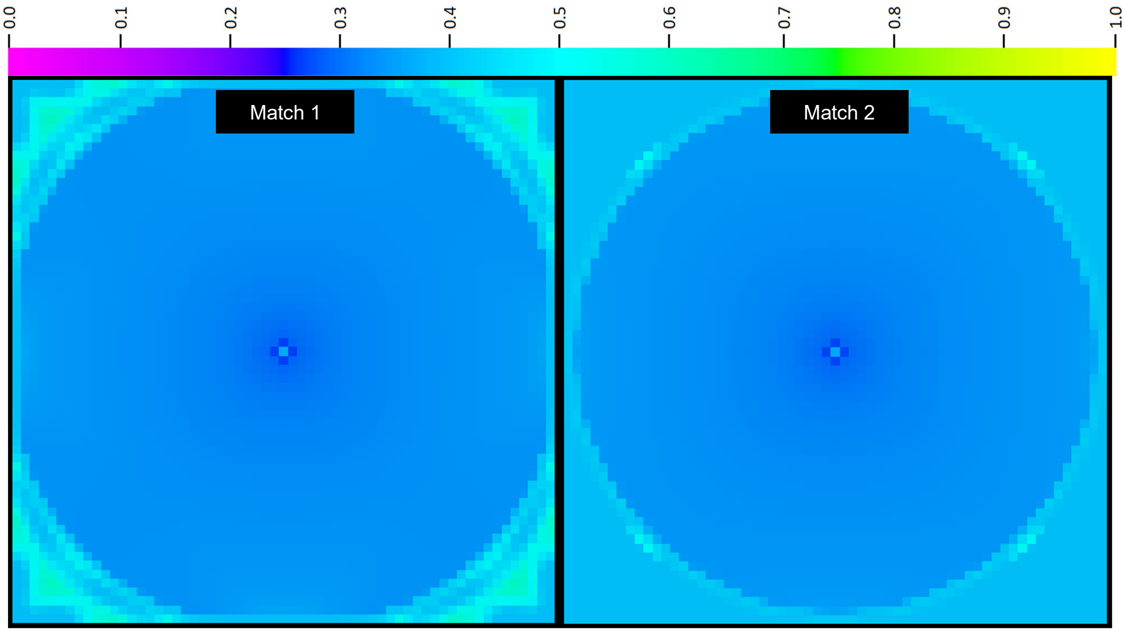

Figure 5-24: Comparison of boarder effects of AP flood ‘Match 1’ and ‘Match 2’

Comparison of the water saturation at the chosen points in time displays, that an examination of the reservoir as a total leads to a tremendously smaller deviation range (0.01% to 0.27%) than the examination of individual points (0.0% to 17.06%) for the investigated set. The difference in deviation between the saturation of the entire reservoir and of individual points has a similar range of 0.01% to 17.16% (Tbl. D.1-1 and Tbl. D.1-2, Appendix D).

Although the front of 'Match 1' propagates faster from the beginning, the difference becomes only visible shortly before the oil ring arrives at the production wells. The maximum deviation occurs after approximately 2.15 PV injected and has a magnitude 5.18%. Once the propagation front of 'Match 2' arrives at the production wells, the water saturation graphs become nearly identical and the final water saturation differs only by 0.27% with 'Match 2' leading to a higher S_w. 'Match 2' leads to an decrease in cumulative water production by 1.8% and a reduction of the recovery factor by 0.3% (Fig. D.1-1 to Fig. D.1-3, Appendix D). Figure 5-25 and Figure 5-26 show the difference plots of the cumulative water production and the recovery factor of the different alkali-polymer flood matches.

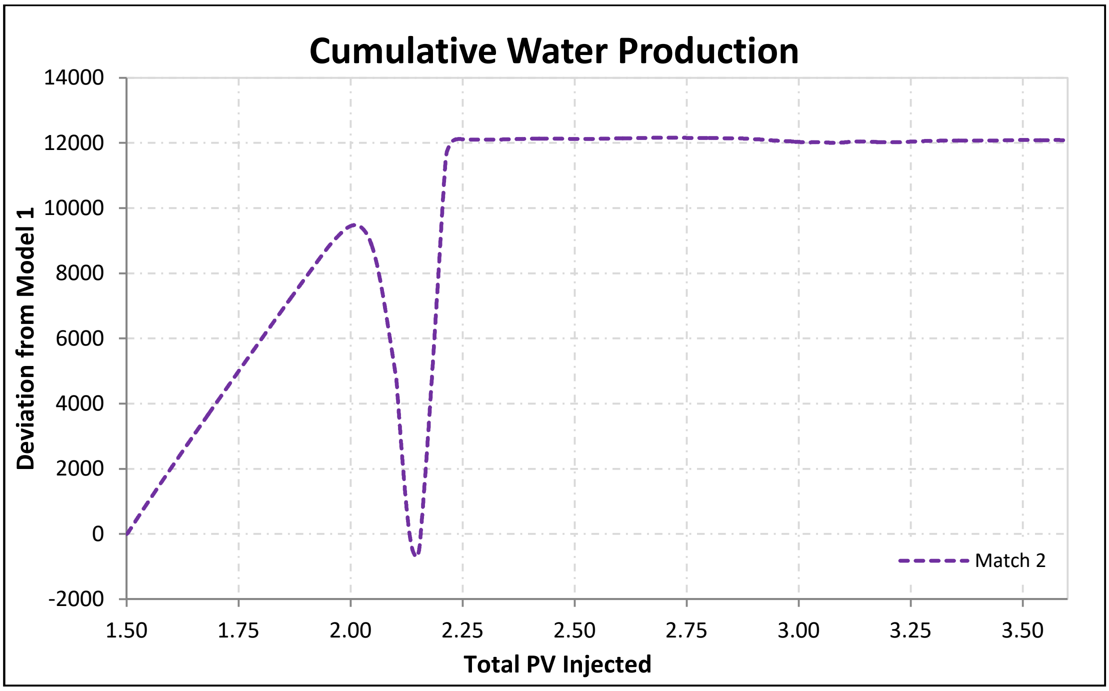

Figure 5-25: Cumulative water production difference plot (comparison AP flood 'Match 1' and 'Match 2')

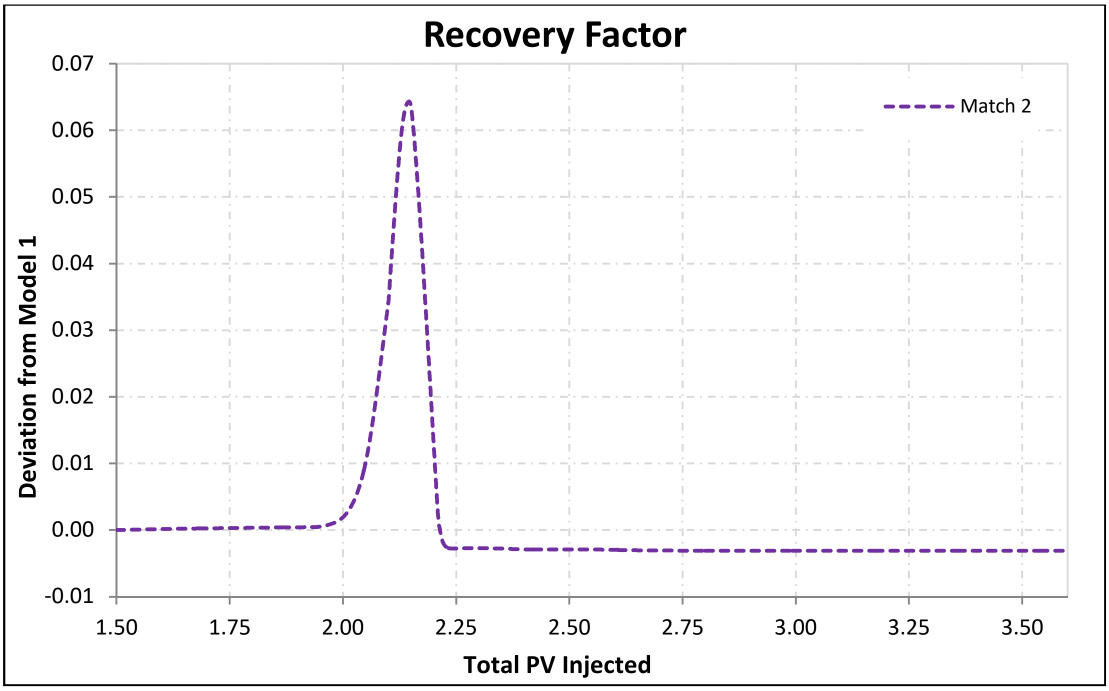

Figure 5-26: Recovery factor difference plot (comparison AP flood 'Match 1' and 'Match 2')

5.3 Grid Resolution Effects

Increasing grid cell size can have a dramatic effect on simulation accuracy; especially the increase in velocity associated with increasing grid cell size is noticeable. The dimension of this effect depends on the magnitude of the cell size enlargement and increases with growing time. Visualizations of the impact of the grid resolution are displayed in Appendix D.

5.3.1 Grid Resolution Effects on the Secondary Water Flood

A large difference in the range of the deviation between the observation of the reservoir as a total and the observation of individual points exists. Comparison of the water saturation at the chosen points in time displays, that an examination of the reservoir as a total leads to a significantly smaller deviation range for a certain point in time (0.0% to 0.92%) than the examination of individual points (0.0% to 22.84%). The difference in deviation between the saturation of the entire reservoir and of individual points has an equal range of 0.0% to 22.84% (Tbl. D.2-1 and Tbl. D.2-2, Appendix D).

The numerical values and the graphs both display that all models deliver the same results, until the water front arrives at the production wells, after approximately 0.13 to 0.17 PV were injected. From this point in time, Model 2 to Model 5 start deviating from Model 1, reaching a maximum after approximately 0.25 to 0.3 PV were injected. Time and magnitude depend on the model used, the latter ranging from ‰ to %. An increase in grid cell size leads to an earlier water break through and a larger and later maximum deviation from Model 1. Table 5-6 quantifies these observations for the models with increased grid size.

Table 5-6: Maximum deviation (S_w) of Model 2 and Model 5 from Model 1 (water flood)

Model	Grid cell enlargement	Max. deviation	Time of max. deviation [years]
Model 2	x 4	0.0017	2.2
Model 3	x 16	0.0046	2.7
Model 4	x 36	0.0073	2.8
Model 5	x 100	0.0122	3

After reaching the maximum, the deviation decreases until it becomes negligible at the end on the water flood. This shows that the magnitude of the impact of the grid cell size depends on the time span of the water flood and its simulation. The total water saturation at the end of the water flood is larger for models with smaller grid cells and it varies although a deviation of 0.18% due to a 100-fold grid cell size increase is negligible. The range of deviation regarding cumulative water production is in per mill range and the range of deviation regarding recovery factor ranges from per mill range to 0.3% (Fig. D.2-5 to Fig. D.2-7, Appendix D). Figure 5-27 and Figure 5-28 show the difference plots of the cumulative water production and the recovery factor of the water flood.

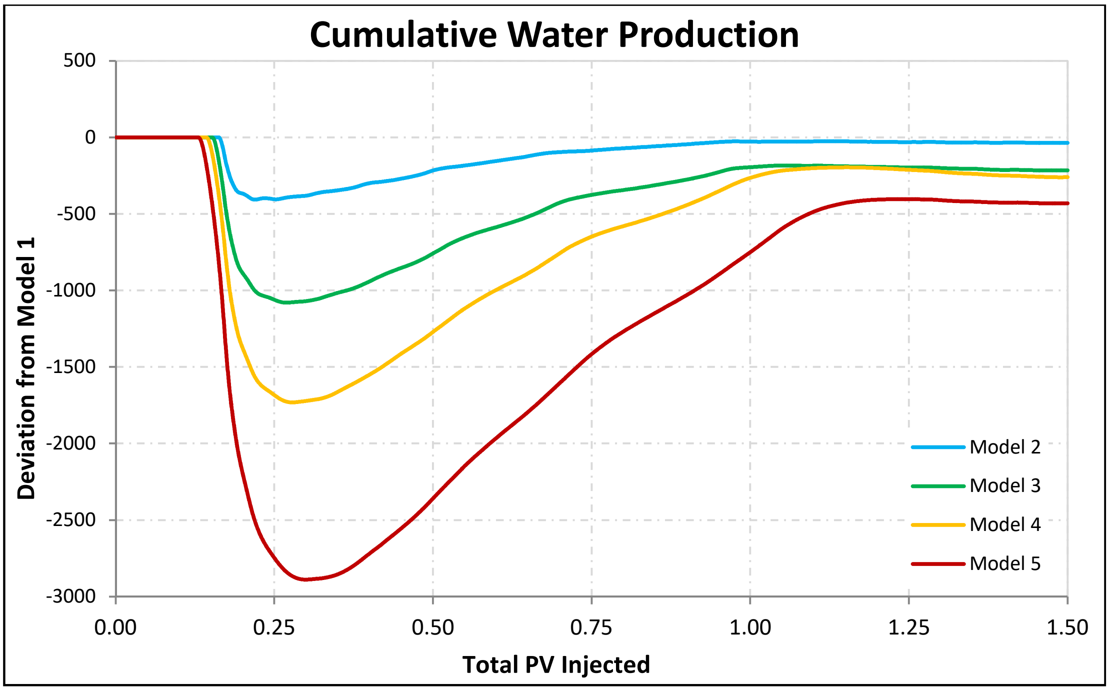

Figure 5-27: Effects of grid resolution on cumulative water production (water flood)

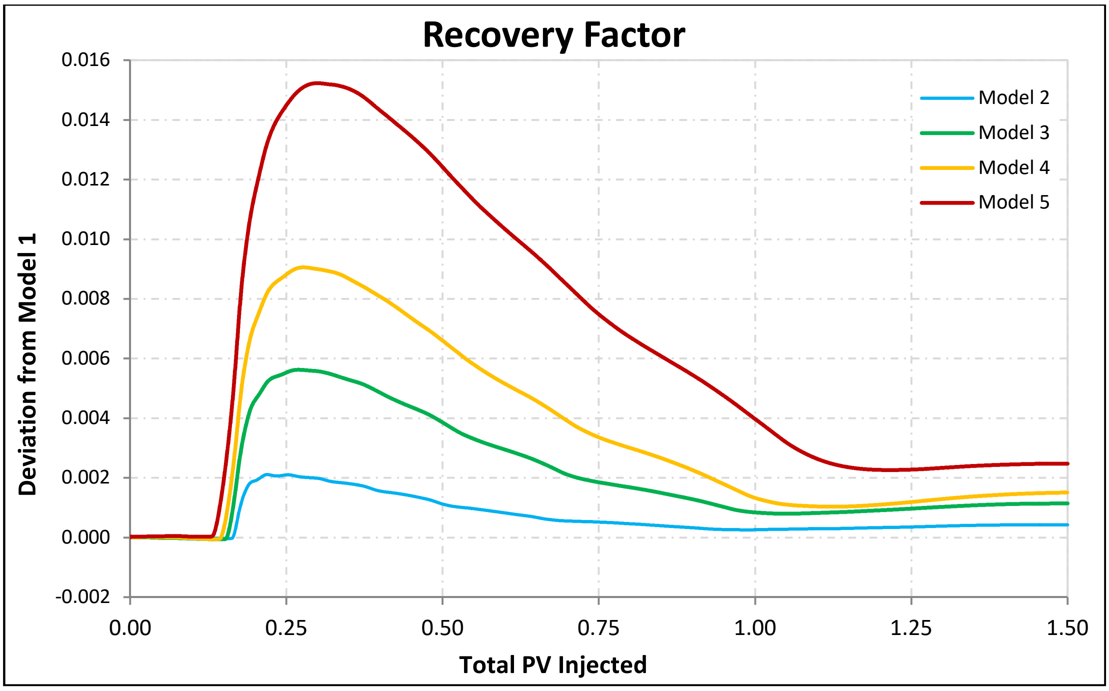

Figure 5-28: Effects of grid resolution on recovery factor (water flood)

5.3.2 Grid Resolution Effects on the Polymer Flood

Analogous to the water flood simulation, the accuracy of the polymer flood simulation decreases with increasing grid cell size. Due to the more complex propagation front, the effect of grid cell size observed at a polymer flood simulation is larger. Above a certain grid resolution, the early ring development cannot be observed any longer due to dilution of the polymer at larger grid cell sizes.

With increasing extent, the oil ring becomes also visible in models with larger grid size. However, larger grid blocks lead to a larger velocity and therefore to an earlier increase in water saturation.

Comparable to the water flood simulation, a large difference in the range of the deviation of the water saturation between the observation of the reservoir as a total and the observation of individual points exists. Comparison of the water saturation at the chosen points in time displays, that an examination of the reservoir as a total leads to a significantly smaller deviation range for a certain point in time (0.01% to 0.89%) than the examination of individual points 0.0% to 17.56%). The difference in deviation between the saturation of the entire reservoir and of individual points has a similar range of 0.0% to 17.7%. This outcome is comparable with the effects caused by using different AP flood matches (Tbl. D.2-3 and Tbl. D.2-4, Appendix D).

The numerical values and the graphs both display that for all models the deviation from Model 1 remains nearly constant until the first additional oil arrives at the production wells, after approximately 1.75 to 2.1 PV were injected. The small jumps observed at Model 1 and Model 2 display boundary effects, caused by the comparable sizes of the outer cells and the inner cells. From this point in time, a first gradual increase of the water saturation can be observed, depicting both boarder effects and the fact that the outline of the oil ring is blurred. This gradual increase lasts from less than 0.1 to more than 0.25 PV injected. Subsequently a sharp second increase of the water saturation can be observed. Time, inclination and abruptness of the rise depend on the model used. After attaining a certain water saturation, the slope flattens significantly and furthermore only small changes occur. The maximum deviation is practically the same for all models and has a magnitude of 0.84% to 0.89% and the bigger part of it represents the larger dispersion caused by larger grid cells, rather than the absolute difference in water saturation. Table 5-7 quantifies these observations for the models with increased grid size.

Table 5-7: Maximum deviation (S_w) of Model 2 and Model 5 from Model 1 (polymer flood)

Model	**Grid cell enlargement**	**Max. deviation**	**Time of max. deviation [years]**
Model 2	x 4	0.0089	23.3
Model 3	x 16	0.0089	22.7
Model 4	x 36	0.0083	22
Model 5	x 100	0.0084	21

Similar to the water flood simulation, an increase in grid cell size leads to an earlier arrival of the first additional oil and a closer succeeding oil ring at the production wells and consequently to an earlier and more sudden rise and a lower inclination of the sharp second rise but a higher inclination of the flattened interval. Additionally, Model 4 and Model 5 display a third, but less extended increase of the water saturation. This event originates in simulation effects caused by the larger cell sizes and has no physical meaning. The final water saturation increases with increasing grid cell size, although the difference is marginal. It is six times smaller than at the end of the water flood. The range of deviation regarding cumulative water production is 2.2% to 10.5% and the deviation regarding recovery factor is in per mill range (Fig. D.2-10 to Fig. D.2-12, Appendix D). Figure 5-29 and Figure 5-30 show the difference plots of the cumulative water production and the recovery factor of the water flood.

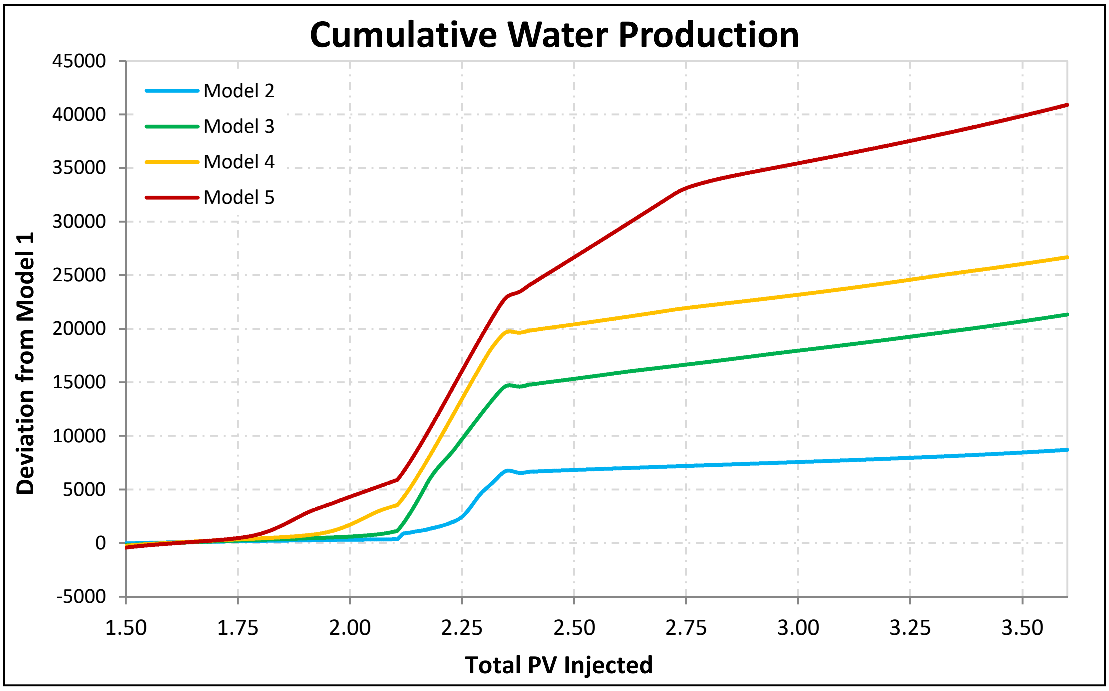

Figure 5-29: Grid resolution effects on cumulative water production (polymer flood)

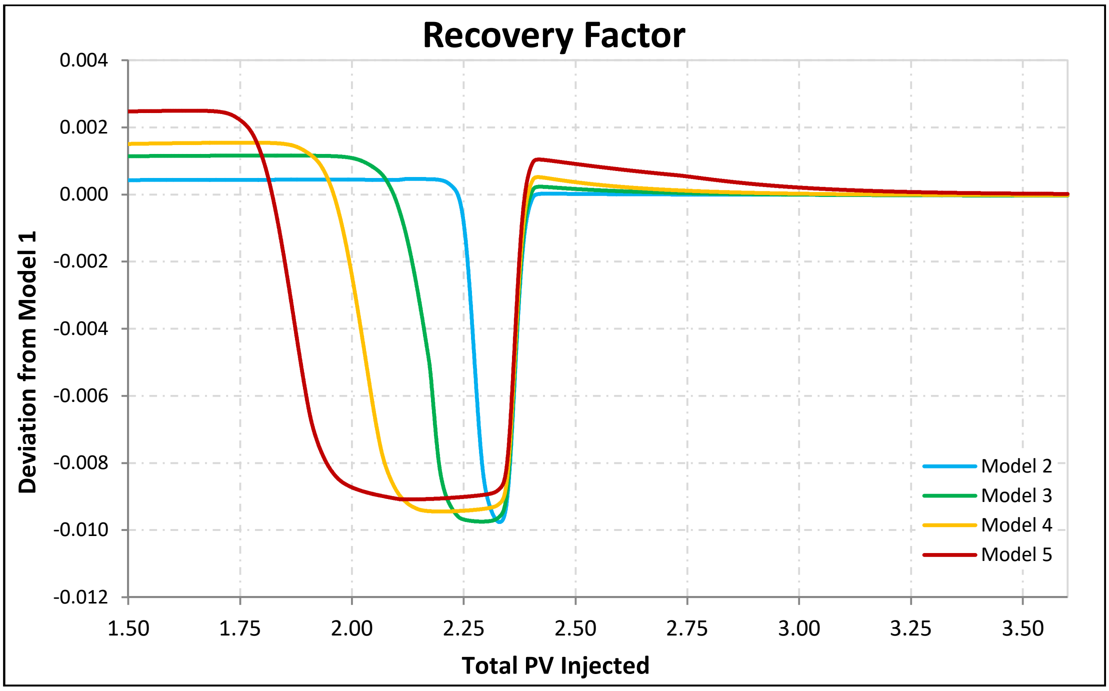

Figure 5-30: Grid resolution effects on recovery factor (polymer flood)

5.3.3 Grid Resolution Effects on the Alkali-Polymer Flood

In contrast to a polymer or a water flood simulation, the effect of grid cell size on an AP flood simulation is severe, first due to the more complex propagation front, second due to the general much higher recovery potential of an AP treatment. With increasing grid block size, the accuracy of the simulation decreases extremely. The oil ring becomes larger in extent and its oil saturation decreases due to dilution of the alkali-polymer caused by the increase in grid cell size. The velocity is increased and this results in a premature arrival of the oil ring at the production wells and therefore to an earlier increase in water saturation. The same behavior can be observed within the zone of increased water saturation adjacent to the injection well.

Investigation of the developments in the bottom layer shows a corresponding behavior. With increasing grid cell size, the previously discussed border effects become more severe.

Comparison of the water saturation at the chosen points in time displays, that an examination of the reservoir as a total leads to a significant smaller deviation range for a certain point in time (0.02% to 6.46%) than the examination of individual points (0.02% to 48.1%). The difference in deviation between the saturation of the entire reservoir and of individual points has a similar range of 0.0% to 41.64% (Tbl. D.2-5 and Tbl. D.2-6).

The numerical values and the graphs both display that for all models the deviation from Model 1 remains nearly constant until the oil ring arrives at the production wells, after approximately 1.75 to 1.95 PV were injected. From this point in time, a first gradual increase of the water saturation can be observed, depicting boarder effects. This gradual increase lasts from less than 0.03 to more than 0.06 PV injected and this short duration illustrates that the oil ring has a sharp outline. Subsequently a sharp second increase of the water saturation can be observed. Time, inclination and abruptness of the rise depend on the model used. After attaining a certain water saturation, the slope almost immediately becomes practically constant. The maximum deviation has a magnitude of 2.22% to 6.51% and represents the larger dispersion caused by larger grid cells. Table 5-8 quantifies these observations for the models with increased grid size.

Table 5-8: Maximum deviation (S_w) of Model 2 and Model 5 from Model 1 (AP flood 'Match 1')

Model	Grid cell enlargement	Max. deviation	Time of max. deviation [years]
Model 2	x 4	0.0222	21.3
Model 3	x 16	0.0348	20.7
Model 4	x 36	0.0609	20.4
Model 5	x 100	0.0651	19.8

The developing water saturation graph behaves similar to one from the polymer flood simulation. Again, an increase in grid cell size leads to an earlier arrival of the first additional oil from the boarder effects and a closer succeeding oil ring at the production wells and consequently to an earlier and more sudden first rise and a and a more gradual transmission to the nearly constant interval. The only exemption is Model 2, which exhibits a reverse behavior, which is caused by the small cells of 2.5 x 2.5 m dimension adjacent to the outer cells, which were necessary to attain the same geometry for all models. Additionally, Model 3, Model 4 and Model 5 display a third, but less extended increase of the water saturation. This event originates in simulation effects caused by the larger cell sizes and has no physical meaning. The final water saturation decreases with increasing grid cell size and is comparable with the one at the end of the water flood. Again, Model 2 is an exemption and leads to a higher final water saturation than Model 1. The range of deviation regarding cumulative water production is 2.8% to 11.5% and the deviation regarding recovery factor is per mill range to 0.3% (Fig. D.2-15 to Fig. D.2-17, Appendix D). Figure 5-31 and Figure 5-32 show the difference plots of the cumulative water production and the recovery factor of the water flood.

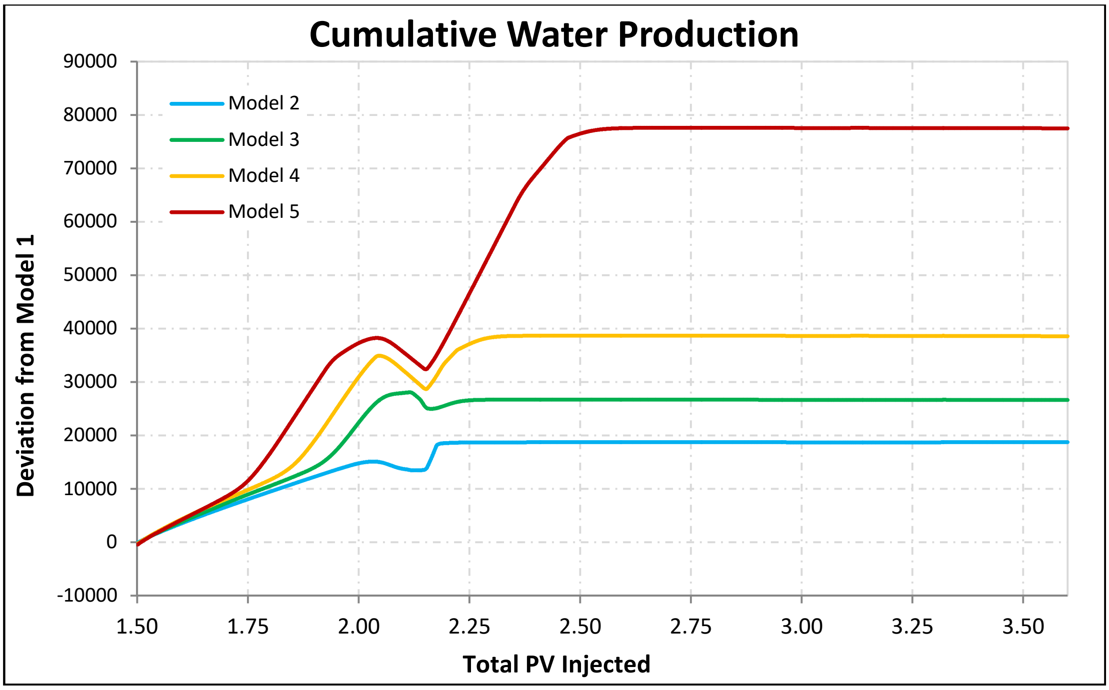

Figure 5-31: Effects of grid resolution on cumulative water production (AP flood 'Match 1')

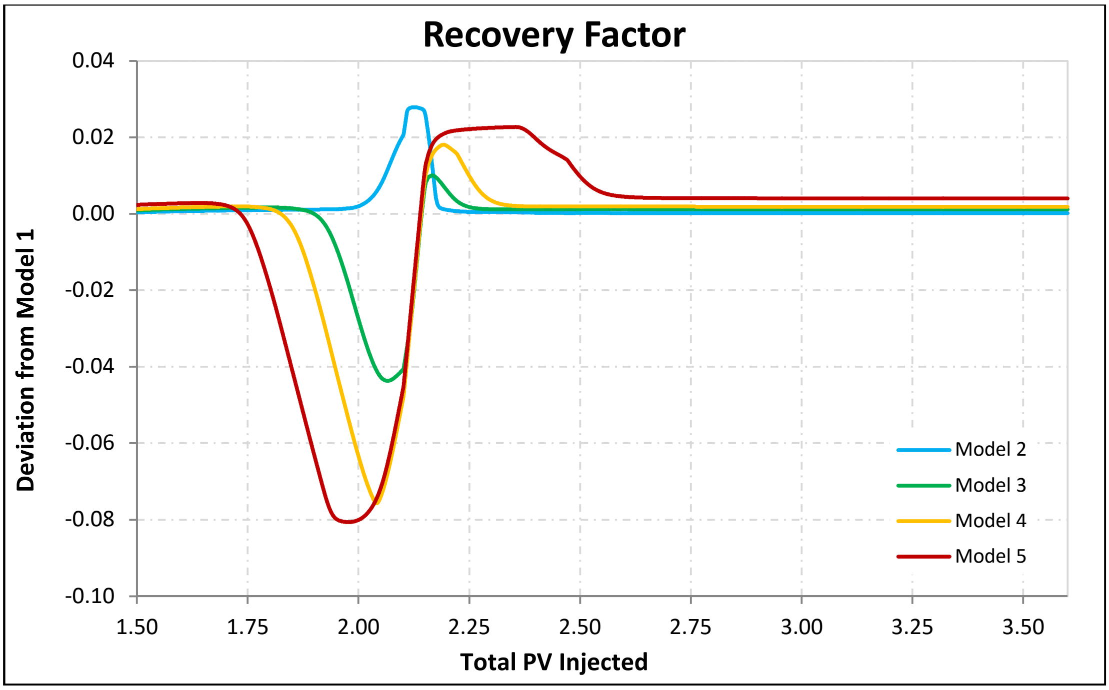

Figure 5-32: Effects of grid resolution on recovery factor (AP flood 'Match 1')

5.4 Effect of Grid Orientation

Because different grid orientations lead to differences in flow path length, it influences simulation results and the extent of the grid orientation effect has to be identified. Visualizations of the effect of grid orientation are displayed in Appendix D.

5.4.1 Effect of Grid Orientation on the Secondary Water Flood

A visible effect occurs immediately after the start of the water flood. At an early stage, the shape of the water front is identical but alters its orientation in accordance with the grid. The water is predominantly propagating along the grid.

As the displacement proceeds, it can be observed that a radial propagation front does not develop on principle, but only at certain grid orientation scenarios. It is a combination effect generated from the tendencies of the water to propagate along the grid as well as to move towards the production wells. The shorter flow path of a favorable grid orientation not only leads to an earlier arrival of the water front at the production wells, it also displays a stronger driving force towards the producer, resulting in a more defined star shape. According to the different grid cell sizes, different grid orientations vary the results of a water flood simulation only over a certain time period. At the end of the water flood, the effect of grid orientation is only marginal.

Comparison of the water saturation at the chosen points in time displays, that an examination of the reservoir as a total leads to a smaller deviation range (0.0% to 0.49%) for the investigated set than the examination of individual points 0.0% to 3.77%) over the time span of the water flood. The difference in deviation between the saturation of the entire reservoir and of individual points has a similar range of 0.0% to 2.35%. Comparison of this outcome with the results from the investigation of the effects of grid cell size demonstrates that regarding the chosen point of observation, variations in grid cell size have a significant larger impact on the simulation results than grid orientation (Tbl. D.3-1 and Tbl. D.3-2, Appendix D).

As for the various grid cell sizes, the numerical values and the graphs display that both models deliver the same results, until the water front arrives at the production wells, after approximately 0.15 PV were injected. From this point in time, the water saturation curve of Model 1B starts deviating from Model 1, reaching a maximum deviation of 0.79% after approximately 0.31 PV injected. The magnitude is in the ‰ range. The maximum deviation is comparable to the deviation caused by a 36-fold increase of the cell size (Model 4 with a maximum deviation of 0.0072) and the deviation at the end of the water flood is comparable to the deviation caused by and 100-fold increase of the cell size (Model 5). This demonstrates that the deviation caused by rotation of the grid does not deviate as much over time as an increase in grid cell size but the total impact is comparably high. The deviation regarding cumulative water production is 0.2% and the deviation regarding recovery factor is 0.3%

(Fig. D.3-5 to Fig. D.3-7, Appendix D). Figure 5-33 and Figure 5-34 show the difference plots of the cumulative water production and the recovery factor of the water flood.

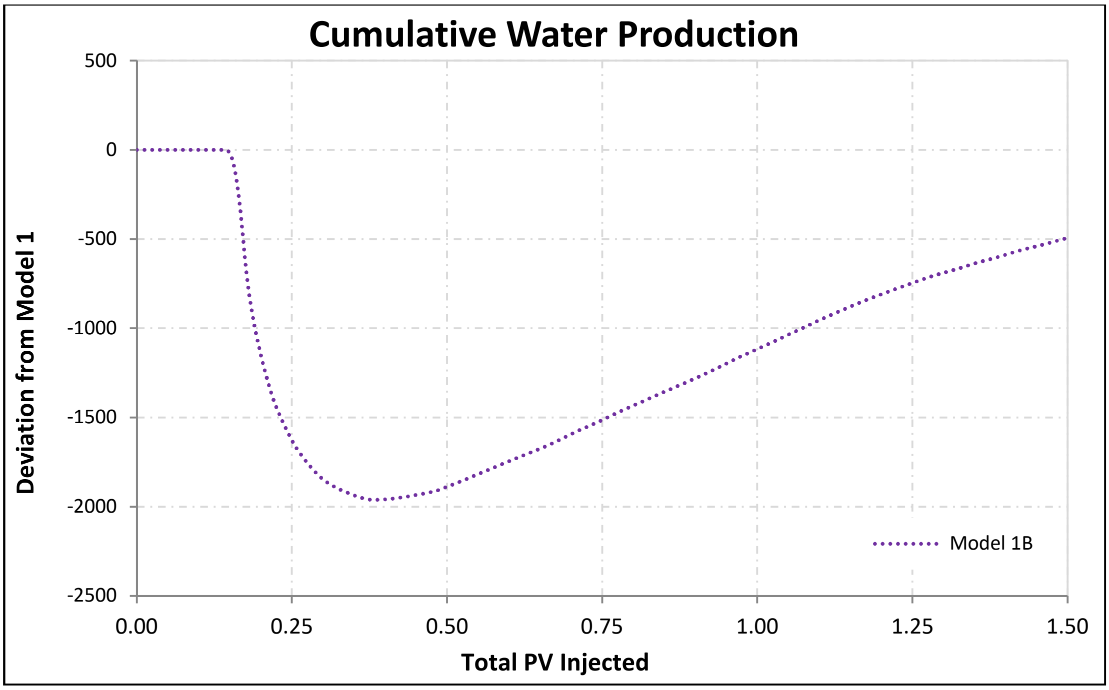

Figure 5-33: Effect of grid orientation on cumulative water production (water flood)

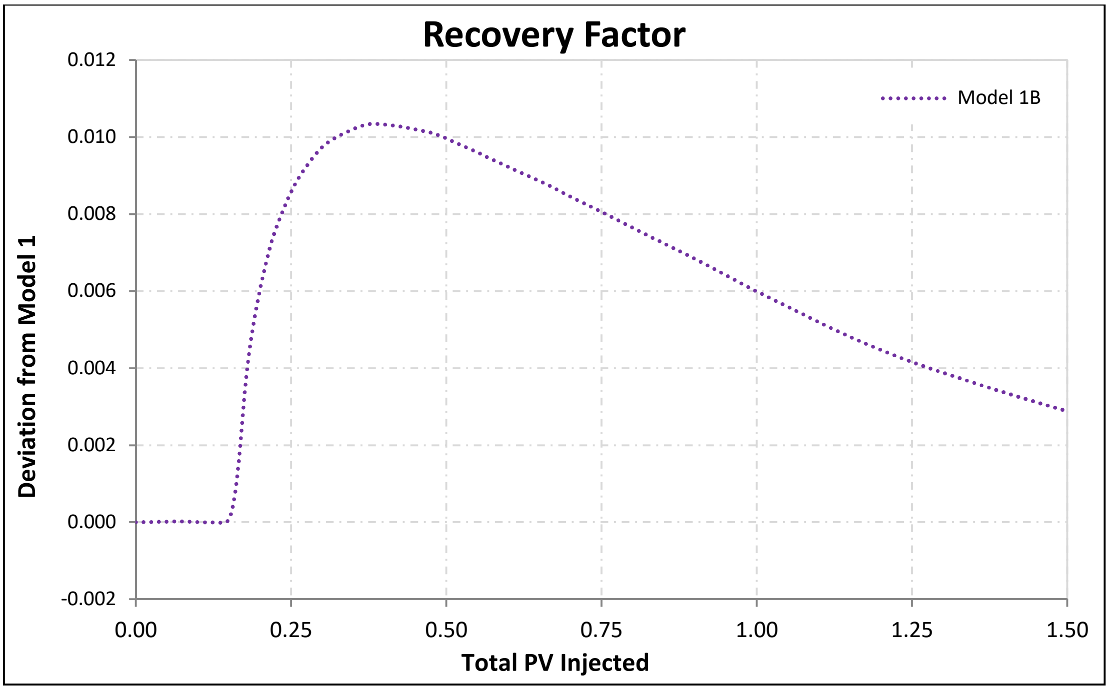

Figure 5-34: Effect of grid orientation on the recovery factor (water flood)

5.4.2 Effect of Grid Orientation on the Polymer Flood

Similar to the water flood, a visible effect occurs shortly after the start of the polymer flood. Initially the shape of the propagation front is identical but alters its orientation in accordance with the grid.

As the displacement proceeds, for the original grid orientation it can be observed, that the propagation front caused by a polymer flood is not as circular as the one developed during a water flood. This is caused by the increased viscosity, which reduces the effectiveness of the driving force towards the production wells and leads the front to propagate preferably along the grid. Rotation of the grid by 45° lessens this effect, but still no clearly radial propagation front is developed. Model 1B develops a slightly more radial pattern than Model 1.

The shorter flow path of the favorable grid orientation of Model 1B leads to a slightly earlier arrival of the oil ring at the production well, although boundary effects occurring at Model 1 cause an isochronal arrive of the first oil at the production wells, generating a premature moderate increase of the water saturation. Like the different grid cell sizes, different grid orientations vary the results of a polymer flood simulation only over a certain time period. At the End of the EOR treatment, the effect of grid orientation is only marginal.

Comparison of the water saturation at the chosen points in time displays, that an examination of the reservoir as a total leads to a significantly smaller deviation range (0.02% to 0.2%) for the investigated set than the examination of individual points (0.0% to 30.92%). The difference in deviation between the saturation of the entire reservoir and of individual points has a similar range of 0.02% to 30.77%. Comparison with the effects of grid cell size demonstrates, that regarding the chosen point of observation, variations in grid orientation have a larger impact on the simulation results than grid cell size, although the difference is not as significant as the one observed at the water flood simulation (factor 6 at the water flood compared with factor 1.8 for the polymer flood) (Tbl. D.3-3 and Tbl. D.3-4).

The deviation of the water saturation curve of Model 1B from Model 1 performs analogous to the deviation caused by increasing grid cell size. The first additional oil arrives at the production wells, after approximately 2.1 PV were injected. The maximum deviation occurs after approximately 2.35 PV injected and has a magnitude 0.6% and is the range of the maximum deviation caused by varying grid cell sizes. The final water saturation increases with changing grid orientation, although the difference is as marginal as due to an increase in grid cell size. The deviation regarding cumulative water production and recovery factor is in per mill range (Fig. D.3-12 to Fig. D.3-14, Appendix D). Figure 5-35 and Figure 5-36 show the difference plots of the cumulative water production and the recovery factor of the polymer flood.

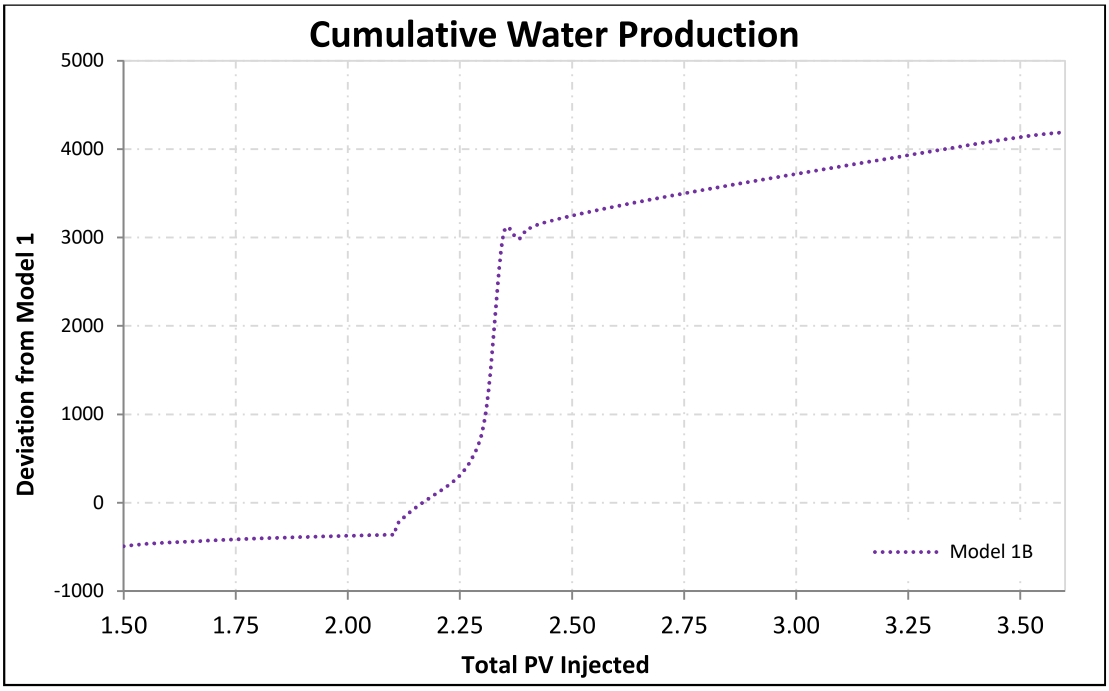

Figure 5-35: Effect of grid orientation on cumulative water production (polymer flood)

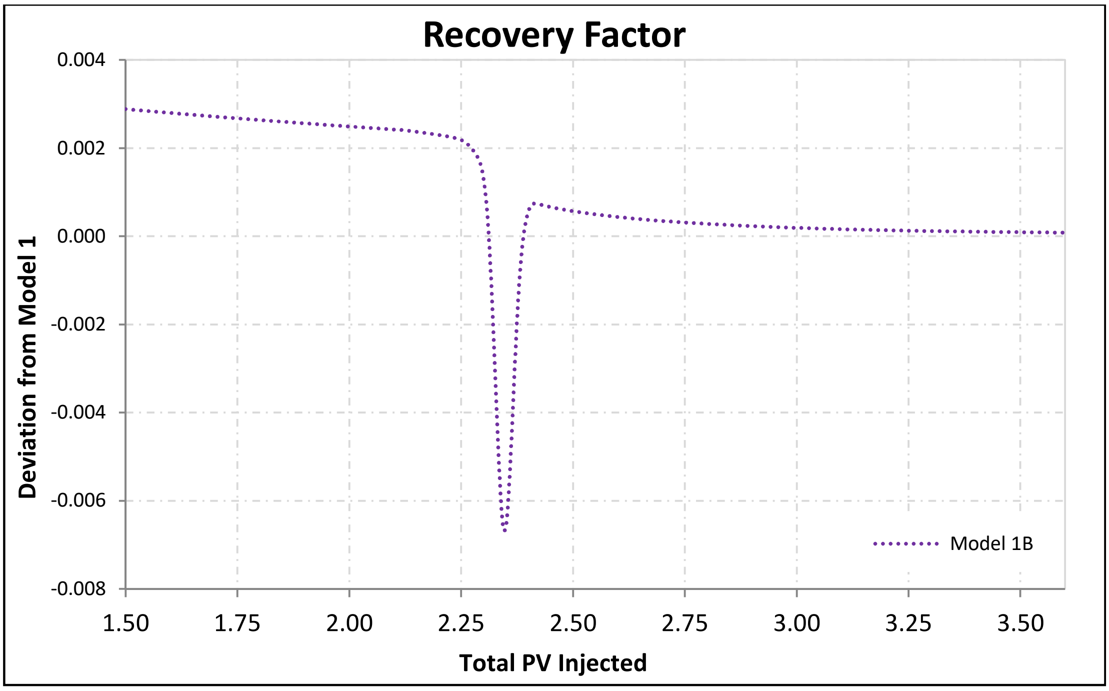

Figure 5-36: Effect of grid orientation on recovery factor (polymer flood)

5.4.3 Effect of Grid Orientation on the Alkali-Polymer Flood

A visible effect caused by an alteration of the grid orientation occurs shortly after the start of the AP flood. Initially, the shape of the propagation front is identical but alters its orientation in accordance with the grid.

As the displacement proceeds, it can be observed that similar to a polymer flood, the propagation front caused by an AP flood is not entirely circular. This is caused by the higher viscosity due to injected polymers and formed surfactants that reduce the effectiveness of the driving force towards the production wells and leads the front to propagate preferably along the grid. Rotation of the grid by 45° generates the same shape, only the orientation differs according to the grid orientation. The shorter flow path of a favorable grid orientation leads to an earlier arrival of the oil ring at the production well, whereby the difference stays in the end of months. The change of the propagation front to a more rectangular shape is caused by boundary effects.

Opposing the variations in grid cell size, different grid orientations produce different saturation patterns, even after a long injection period. At the End of the EOR treatment, the water saturation along the flow path between injection well and production wells is clearly higher than in the other areas of the reservoir model. Even boarder effects are still easily recognizable.

Comparison of the water saturation at the chosen points in time displays, that an examination of the reservoir as a total leads to a significantly smaller deviation range (0.06% to 0.34%) than the examination of individual points (0.01% to 14.82%) for the investigated set. The difference in deviation between the saturation of the entire reservoir and of individual points has a similar range of 0.14% to 14.76%. Comparison of this outcome with the effects of grid cell size demonstrates, that regarding the chosen point of observation, variations in grid orientation have a smaller impact on the simulation results than grid cell size, although the difference is not as significant as the one observed at the water flood and more similar to the one observed at the polymer flood (factor 6 at the water flood and factor 1.8 for the polymer flood compared with factor 3.3 for the AP flood) (Tbl. D.3-5 and Tbl. D.3-6).

The deviation of the water saturation curve of Model 1B from Model 1 performs analogous to the deviation caused by increasing grid cell size. The first additional oil arrives at the production wells, after approximately 1.9 PV were injected. The maximum deviation occurs after approximately 2.07 PV injected and has a magnitude 1.44% and is significantly lower than the maximum deviation caused by varying grid cell sizes. The final water saturation decreases with changing grid orientation, although the difference is only a quarter of the difference due to an increase in grid cell size. The deviation regarding cumulative water production is 1.1% and the deviation regarding recovery factor is in per mill range (Fig. D.3-18 to Fig. D.3-20, Appendix D). Figure 5-37 and Figure 5-38 show the difference plots of the cumulative water production and the recovery factor of the water flood.

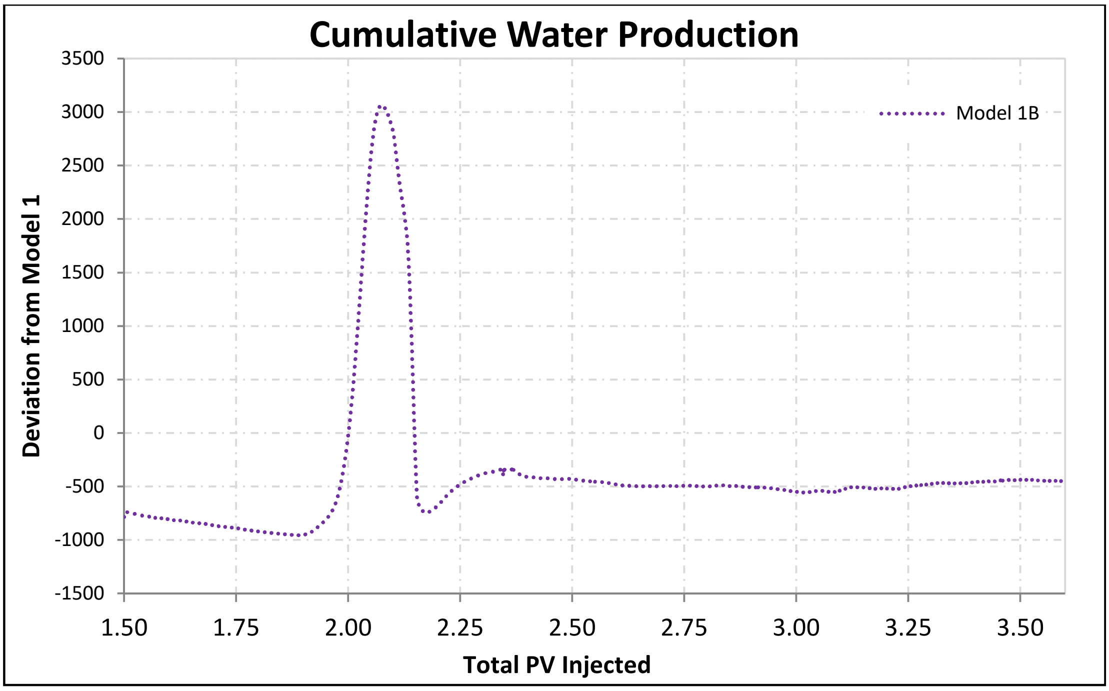

Figure 5-37: Effect of grid orientation on cumulative water production (AP flood 'Match 1')

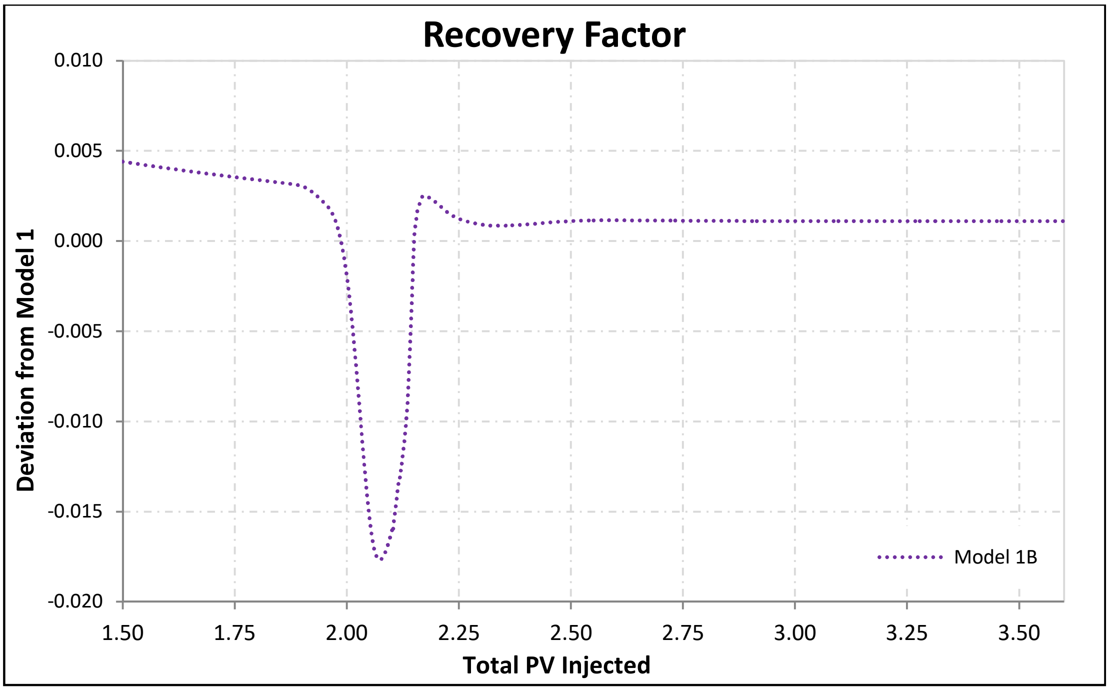

Figure 5-38: Effect of grid orientation on recovery factor (AP flood 'Match 1')

Chapter 6

Conclusion

The results of the executed core flood simulations prove that numerical dispersivity can be utilized to mimic physical dispersivity in a black oil simulation. It was also shown that a black oil simulator can deliver satisfactory results matching chemical treatments. The key perceptions can be summarized as:

1. In long-term applications like chemical EOR treatments, the grid cell size can be further increased without experiencing appreciable loss in accuracy, where AP flood simulations react more sensitive to a further enlargement than polymer flood simulations.
2. The artificially high dispersion and dilution of alkali and polymer concentrations occurring at models with increased grid cell size are the key parameters affecting simulation accuracy, although due to the high injection volume, the final water saturations were almost identical.
3. Generally, the effect of grid cell size is significantly larger than the effect of grid orientation, although exceptions exist for the observation of specific points of the reservoir model. The polymer injection simulation reacts somewhat less sensitive than the water injection simulation, whereas the AP injection simulation is clearly most receptive to variations in grid orientation. It is remarkable that regarding the ‘AP flood simulations, even the comparably small impact of grid orientation is larger than the difference between the two investigated matches.
4. Variation of endpoint relative permeabilities has hardly any impact of the water saturation, but on the pressure differential. As the latter was used as a control parameter, this offers an option for additional matches. Assuming nearly miscible flow instead of miscible flow has a comparable effect, although the impact is less.
5. The impact on the required memory for the field scale simulations is significant; the increase of the grid cell size by a factor 4 from Model 1 to Model 2 reduces the necessary memory by a factor 3.2 from 12,744 MB to 3,950 MB and nonetheless delivers satisfactory results.

Chapter 7

References

Adepoju, O. and Lake, L. (2012). *Investigation of Anisotropic Mixing in Miscible Displacements.* SPE 159557.

Ahl, J. (2004). *Salt diffusion in brick structures. Part II: The effect of temperature, concentration and salt.* In*: Journal of Materials Science 39 (2004) 4247-4254*.

Arzmüller, G., Buchta, S., Ralbovsky, E. and Wessely, G. (2006). *The Vienna Basin.* In: *The Carpathians and their foreland: Geology and hydrocarbon resources: AAPG Memoir 84*. J. Golonka and F. J Picha, eds., pp. 191-204.

Fanchi, J. (1983). *Multidimensional Numerical Dispersion.* SPE 9018-PA, 1983.

Flury, M. and Gimmi, T. (2002). *Solute diffusion.* In: *Methods of Soil Analysis- Physical Methods.* Dabe, J., Tropp, G. (ed.) Wschington, USA

Garmeh, G., Johns, R. and Lake, L. (2007). *Pore-Scale Simulation of Dispersion in Porous Media.* SPE 110228, 2007.

Giden, I., Kometer, B., Toth, P., Geier, H. and Florian, T. (2016). *Technology Driven Rejuvenation of a Mature Field by Doubling the Gross Production Rate.* SPE-181892-MS.

Haajizadeh, M., Fayers, F., Cockin, A., Roffey, M. and Bond, D.(1999). *On the Importance of Dispersion and Heterogeneity in the Compositional Simulation of Miscible Gas Processes.* SPE 57264.

HOT Microfluidics GmbH (2017). CEOR CORE FLOODING FIG

Kienberger, G., and Fuchs, R.(2006). *Case History of the Matzen Field/Matzen Sand (16th TH): A Story of Success - Where is the End?* SPE 100329.

Lantz, R. (1971). *Quantitative Evaluation of Numerical Diffusion (Truncation Error).* SPE 2811-PA.

Li, C., Amador, C. and Ding. Y. (2016). *An Investigation of Dissolution Kinetics of Single Sodium Carbonate Particle with Image Analysis Method.* Chinese Journal of Chemical Engineering, 24. (10). Pp. 1487-1496.

Lüftenegger, M., and Clemens, T. (2017). *Chromatography Effects in Alkali Surfactant Polymer Flooding.* SPE-185793-MS.

OMV Exploration & Production GmbH (2018).

Parakh, H. and Johns, R. (2004). *Use of Stripping Ratios to Identify Dispersion Levels and Displacement Mechanisms in Miscible Gas Floods.* SPE 90854.

Peksa, A., Wolf, K.-H. Pacelli, L. (2015). *Bentheimer sandstone revisited for experimental purposes.* In: *Marine and Petroleum Geology*, no. 67, pp 701-719.

Pereira, L., de Souza, R., Orlande, H. and Cotta, R. (1999). *Estimation of the apparent mass diffusion coefficient by using inverse analysis and radiation measurement techniques.* 3rd Int. Conference on Inverse Problems in Engineering. Port Ludlow, WA, USA.

Schlumberger, 2017. *ECLIPSE Technical Description*

Sheng, J. (2011). *Modern Chemical Enhanced Oil Recovery.* Oxford: Elsevier Inc.

SNF. *FLOPAAM™ For Enhance Oil Recovery Brochure.*

Solano, R., Johns, R. and Lake, L. (2000). *Impact of Reservoir Mixing on Recovery in Enriched-Gas Drives Above the Minimum Miscibility Enrichment.* SPE 59339.

Veedu, F., Delshad; M. and Pope, G. (2010). *Scaleup Methodology for Chemical Flooding.* SPE 135543.

Yuan, C., Delshad, M. and Wheeler, M. (2010*). Parallel Simulations of Commercial-Scale Polymer Floods.* SPE 132441-MS.

Appendix A

Literature Review

A.1 Polymer

Tbl. A.1-1: Properties of Flopaam™ 3630 S (SNF)

Manufacturer	Hydrolysis mol%	Approximate molecular weight 10^6 Da
SNF HC	20-30	20

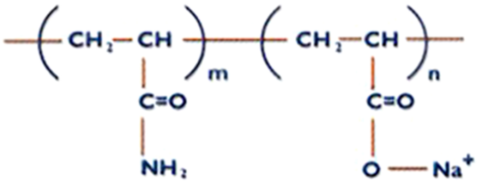

Fig. A.1-1: Chemical Structure of HPAM (SNF)

A.2 Alkaline

Dissociation of sodium carbonate:

$$Na_2CO_3 \rightarrow 2Na + CO_3^{2-} \tag{13}$$

Hydrolysis of carbonate ion:

$$CO_3^{2-} + H_2O \rightarrow HCO_3^- + OH^- \tag{14}$$

A.3 ECLIPSE 100 Polymer Option

Water equation (Schlumberger, 2017):

$$\frac{d}{dt}\left(\frac{VS_w}{B_rB_w}\right) = \sum\left[\frac{Tk_{rw}}{B_w\mu_{w,eff}F_{kr}}(\delta P_w - \rho_w g D_z)\right] + Q_w \tag{15}$$

Polymer equation (Schlumberger, 2017):

$$\frac{d}{dt}\left(\frac{V^*S_wC_p}{B_rB_w}\right) + \frac{d}{dt}\left(V\rho_r C_p^{\alpha}\frac{1-\varphi}{\varphi}\right) = \sum\left[\frac{Tk_{rw}}{B_w\mu_{p,eff}F_{kr}}(\delta P_w - \rho_w g D_z)\right]C_p + Q_wC_p \tag{16}$$

$$V^* = V\left(1 - S_{dpv}\right) \tag{17}$$

V	block pore volume [m³]
S_w	water saturation [ ]
B_r	rock formation volume factor [ ]
B_w	water formation volume factor [ ]
T	transmissibility [m mD]
k_{rw}	water relative permeability [ ]
$\mu_{w,eff}$	effective water viscosity [cP]
F_{kr}	permeability reduction factor [ ]
P_w	water pressure [bar]
ρ_w	water density [kg/m³]
g	gravity constant [m/s²]
D_z	cell center depth [m]
Q_w	water production rate [m³/h]
C_p	polymer concentration [kg/m³]
ρ_r	rock mass density [kg/m³]
C_p^{α}	adsorbed polymer concentration [kg/kg]
φ	porosity [ ]
$\mu_{p,eff}$	effective polymer viscosity [cP]
S_{dpv}	dead pore space within each grid cell [ ]

Effective polymer viscosity (Schlumberger, 2017):

$$\mu_{p,eff} = \left(\mu_m\left(C_p\right)\right)^{\omega}\mu_p^{1-\omega} \tag{18}$$

μ_m	viscosity of fully mixed polymer solution [cP]
μ_p	polymer viscosity at maximum polymer concentration [cP]
ω	Todd-Longstaff mixing parameter [ ]

Permeability reduction (Schlumberger, 2017):

$$F_{kr} = 1.0 + (RRF - 1.0)\frac{C_p^{\alpha}}{C_p^{\alpha max}} \qquad (19)$$

RRF	residual resistance factor [ ]
$C_p^{\alpha max}$	maximum adsorbed polymer concentration [kg/kg]

Weighting factor (Schlumberger, 2017):

$$F = F_{kr}(\log N_c) \qquad (20)$$

F	weighting function [ ]
F_{kr}	defined interpolation parameter [ ]
N_c	Capillary Number [ ]

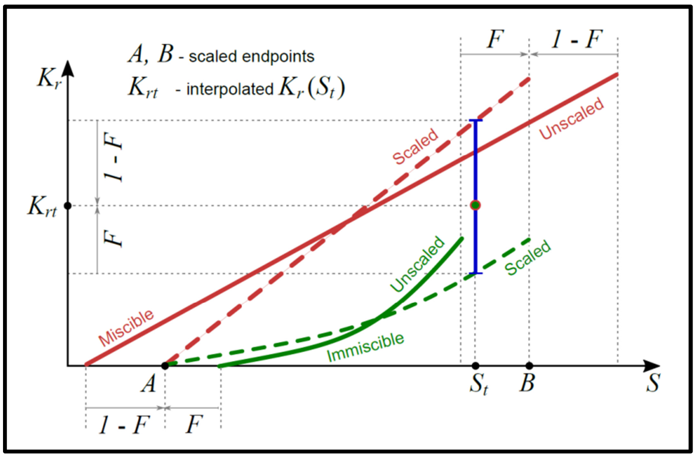

Fig. A.3-1: Interpolation between immiscible and miscible relative permeability curves (Schlumberger, 2017)

Capillary pressure multiplier (Schlumberger, 2017):

$$F_{cp} = \frac{\sigma_{ow}(C_{surf})}{\sigma_{ow}(0)} \qquad (21)$$

Capillary pressure (Schlumberger, 2017):

$$P_{cow} = F_{cp} P_{cow}(S_w) \qquad (22)$$

F_{cp}	capillary pressure multiplier [ ]
$\sigma_{ow}(C_{surf})$	surface tension at the present surfactant concentration [kg/s²]
$\sigma_{ow}(0)$	surface tension at zero concentration [kg/s²]
P_{cow}	water oil capillary pressure [Pa]
$P_{cow}(S_w)$	capillary pressure from the immiscible curves initially scaled to the interpolated end-points calculated in the relative permeability model [Pa]

Viscosity of water-surfactant mixture (Schlumberger, 2017):

$$\mu_{ws}\left(C_{surf}, P\right) = \mu_w(P)\,\frac{\mu_S\left(C_{surf}\right)}{\mu_w\left(P_{ref}\right)} \tag{23}$$

μ_{ws}	viscosity of the water-surfactant mixture [cP]
C_{surf}	surfactant concentration [kg/kg]
P	pressure [Pa]
μ_w	water viscosity [cP]
μ_S	viscosity at the present surfactant concentration [cP]
P_{ref}	reference pressure [Pa]

Surfactant adsorption (Schlumberger, 2017):

$$Mass\ of\ adsorbed\ surfactant = PORV\,\frac{1-\varphi}{\varphi}\,MDCA\left(C_{surf}\right) \tag{24}$$

PORV	pore volume of the cell [m³]
φ	porosity [ ]
MD	mass density of the rock [kg/m³]
CA(C_{surf})	adsorption isotherm as a function of local surfactant concentration in solution [kg/m³]

Appendix B

Data and Methodology

Tbl. A.3-1: Properties of 'Testwasser 1' (OMV Exploration & Production GmbH, 2018)

Property	Value	Unit
Content NaCl	18.96	g/l
Content $NaHCO_3$	1.85	g/l
Shear stress	0.05016	Pa
Shear rate	100	s^{-1}
Shear viscosity	0.5016	mPa s

Tbl. A.3-2: Properties of tracer solution (OMV Exploration & Production GmbH, 2018)

Property	Value	Unit
Content NaCl	18.96	g/l
Content $NaHCO_3$	1.85	g/l
Content KBr	1	g/l
Shear stress	0.04933	Pa
Shear rate	100	s^{-1}
Shear viscosity	0.4933	mPa s

Tbl. A.3-3: Properties of alkaline solution (OMV Exploration & Production GmbH, 2018)

Property	Value	Unit
Content NaCl	18.96	g/l
Content $NaHCO_3$	1.85	g/l
Content Na_2CO_3	7	g/l

Tbl. A.3-4: Properties of chemical slug used within polymer flood (OMV Exploration & Production GmbH, 2018)

Property	Value	Unit
Content NaCl	18.96	g/l
Content $NaHCO_3$	1.85	g/l
Content Flopaam 3630 S	2	g/l

Tbl. A.3-5: Properties of chemical slug used within AP flood (OMV Exploration & Production GmbH, 2018)

Property	Value	Unit
Content NaCl	18.96	g/l
Content $NaHCO_3$	1.85	g/l
Content Na_2CO_3	7	g/l
Content Flopaam 3630 S	2	g/l

Tbl. A.3-6: Rheology of Crude oil - cyclohexane – mixture (OMV Exploration & Production GmbH, 2018)

Shear stress [Pa]	Shear rate [s^{-1}]	Shear viscosity [mPa s]
0.05932	10	5.932
0.3012	50.12	6.01
0.6064	100	6.063

Tbl. A.3-7: Rheology of chemical slug used within Polymer flood (OMV Exploration & Production GmbH, 2018)

Shear stress [Pa]	Shear rate [s^{-1}]	Shear viscosity [mPa s]
0.2003	10	20.03
0.5224	50.12	10.42
0.8181	100	8.18

Tbl. A.3-8: Rheology of chemical slug used within AP flood (OMV Exploration & Production GmbH, 2018)

Shear stress [Pa]	Shear rate [s^{-1}]	Shear viscosity [mPa s]
0.2172	10	21.72
0.5787	50.12	11.55
0.8928	100	8.928

Appendix C

Core Flood Tests

C.1 History Match

Modified Brooks-Corey model:

$$k_{rw} = k_{rw,max}\left(\frac{S_w - S_{wc}}{1 - S_{or} - S_{wc}}\right)^{n_w} \tag{25}$$

$$k_{ro} = k_{ro,max}\left(\frac{S_o - S_{or}}{1 - S_{or} - S_{wc}}\right)^{n_o} \tag{26}$$

k_{rw}	relative water permeability
$k_{rw,max}$	maximum relative water permeability
S_w	water saturation
S_{wc}	connate water saturation
S_{or}	residual oil saturation
n_w	Corey water exponent
k_{ro}	relative water permeability
$k_{ro,max}$	maximum relative water permeability
S_o	oil saturation
n_o	Corey oil exponent

C.2 Grid Size Sensitivity

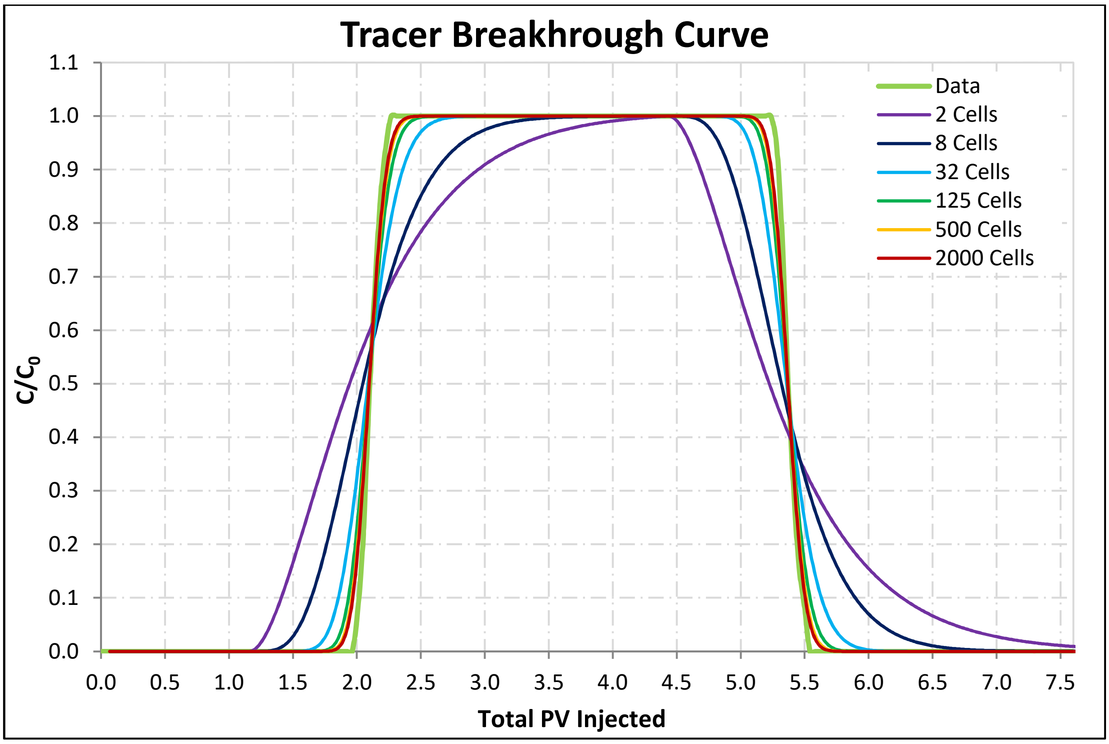

Fig. C.2-1: Grid size sensitivity (Tracer Test 1)

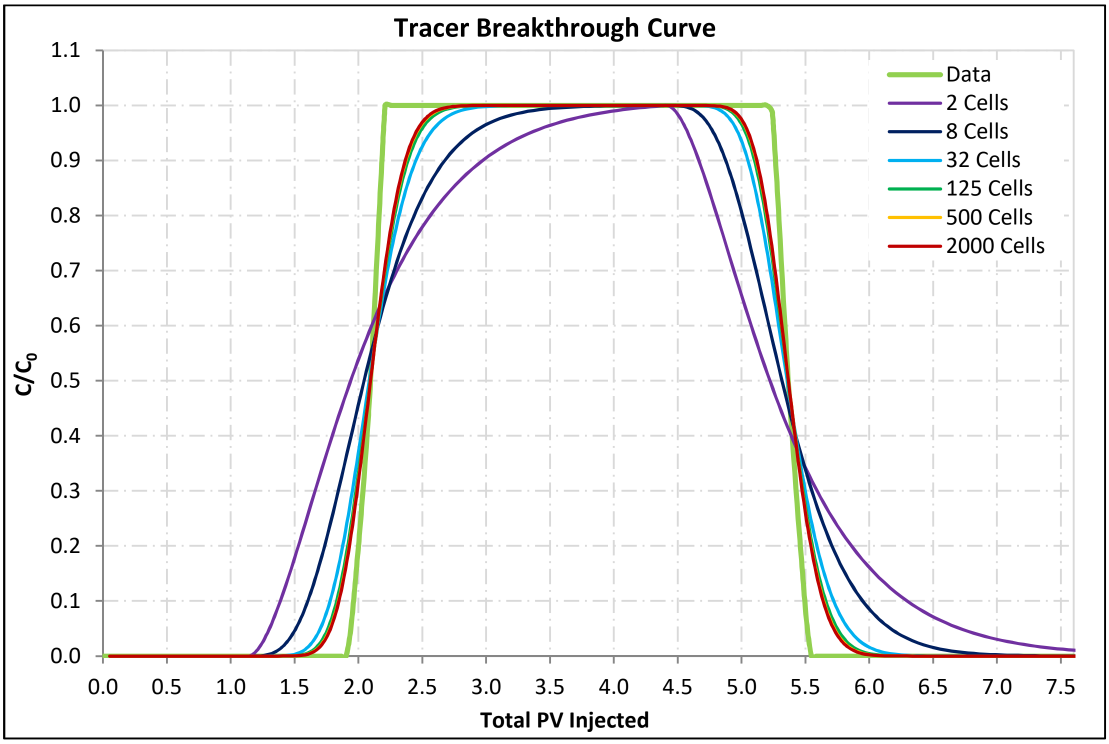

Fig. C.2-2: Grid size sensitivity (Tracer Test 2)

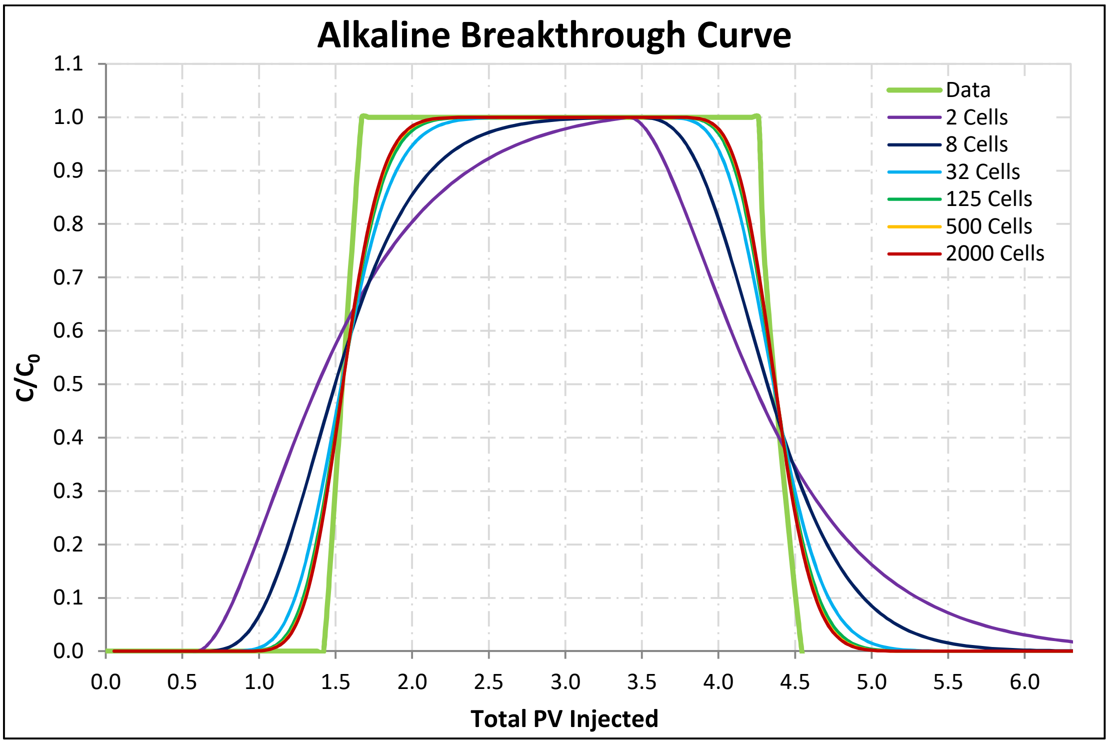

Fig. C.2-3: Grid size sensitivity (Alkaline Test)

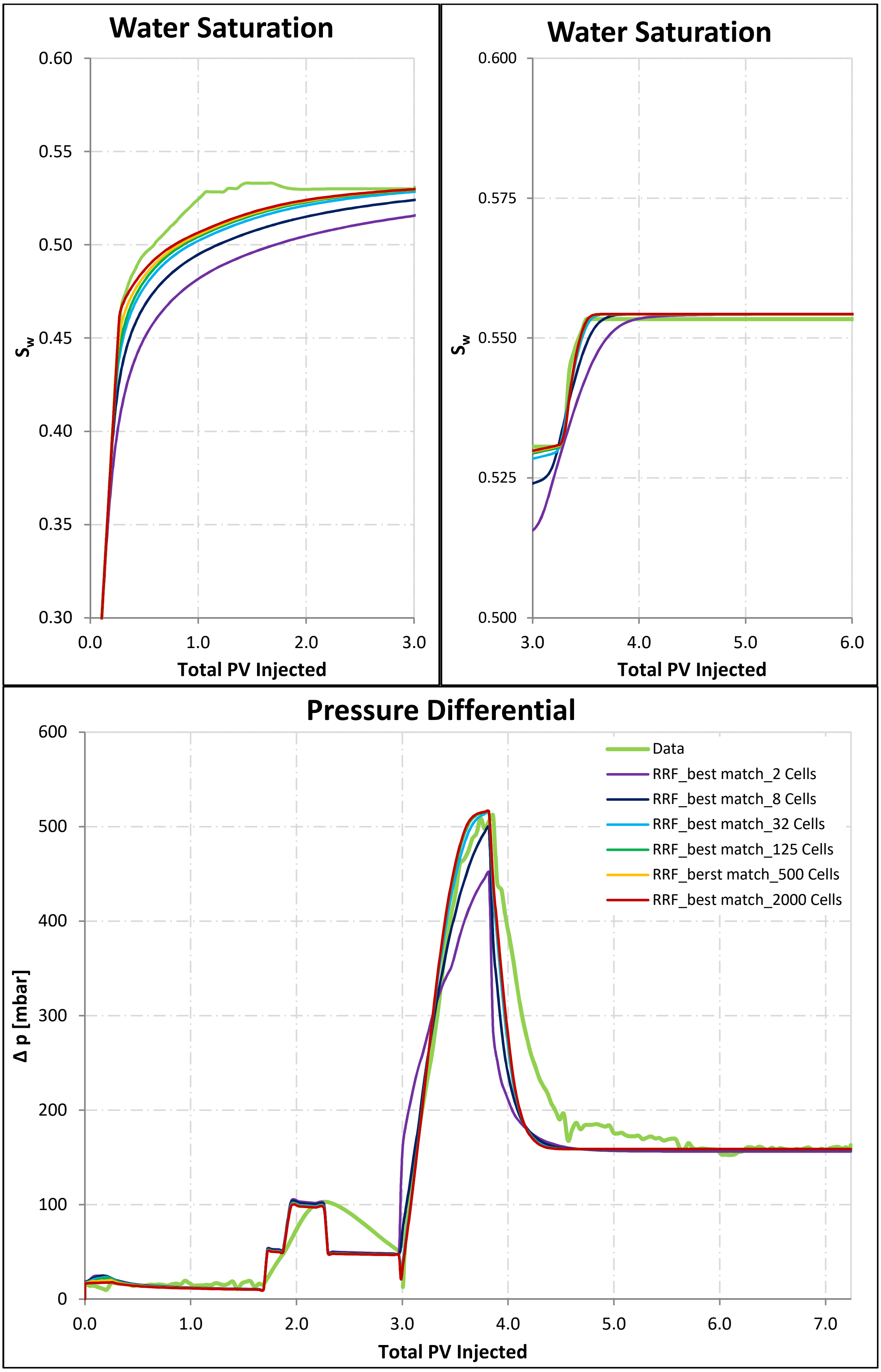

Fig. C.2-4: Grid size sensitivity ('RRF_best match')

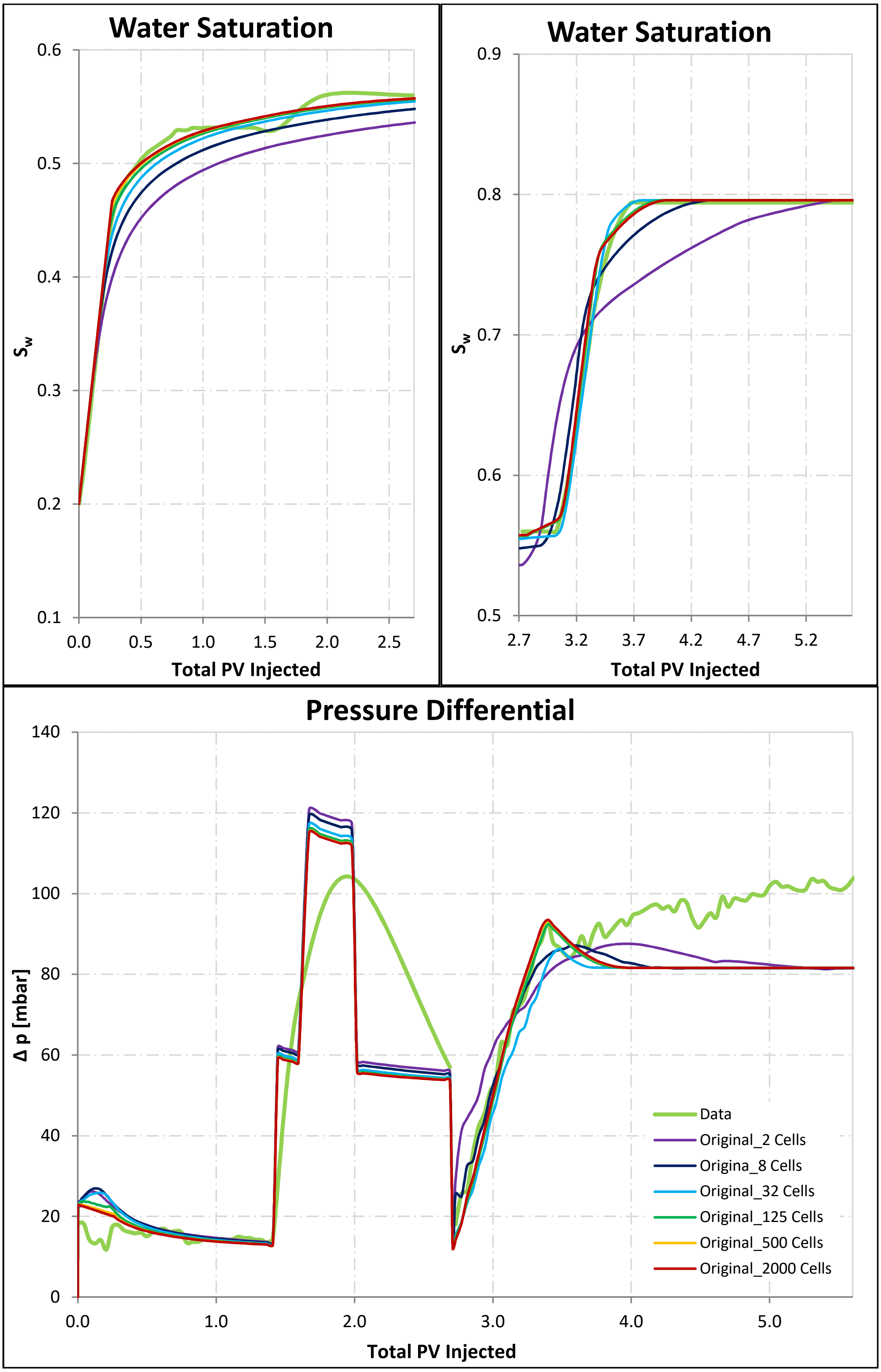

Fig. C.2-5: Grid size sensitivity ('Original')

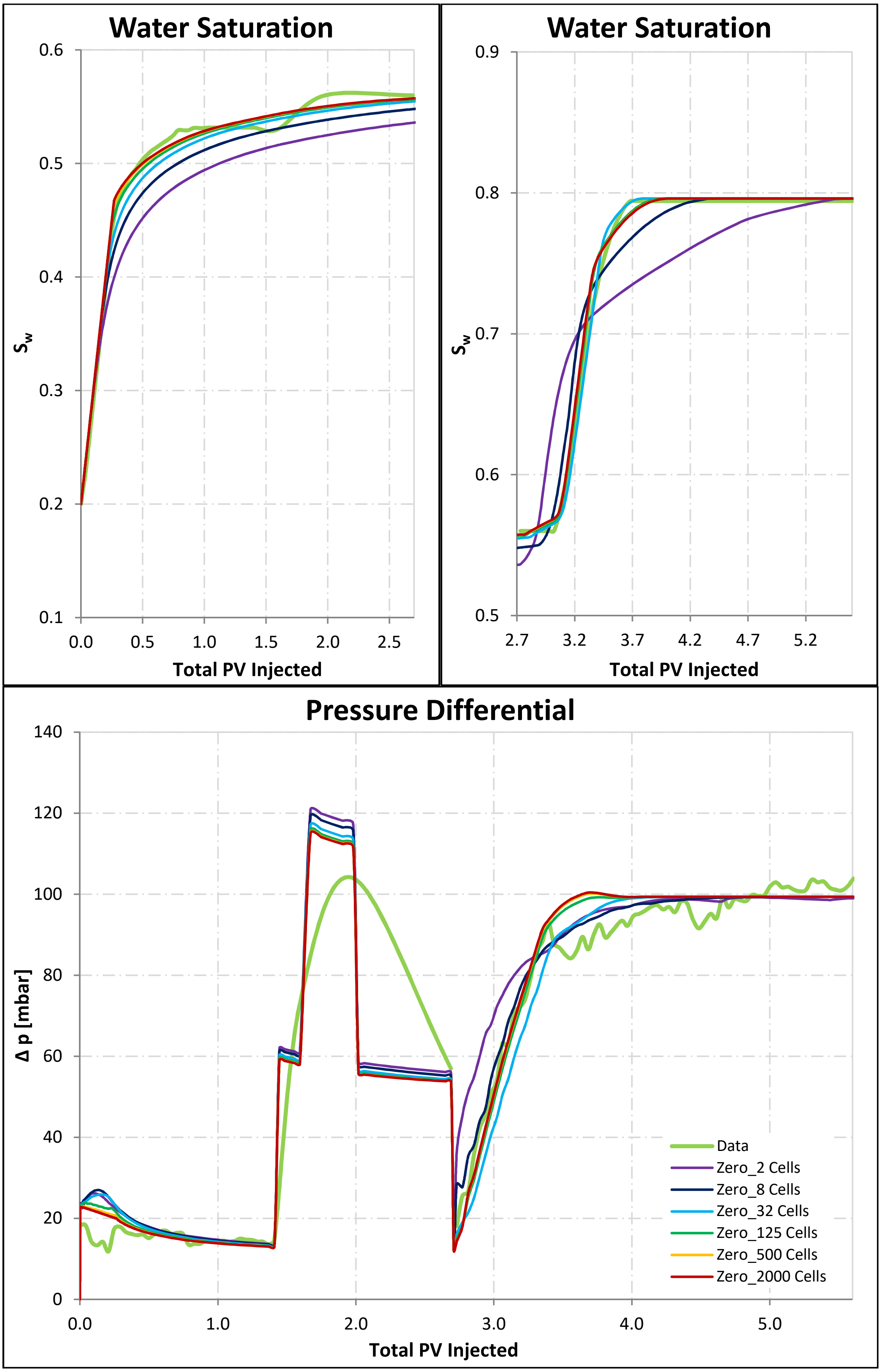

Fig. C.2-6: Grid size analysis ('Zero')

Appendix D

Field Scale Simulation

D.1 Flow Simulation

Tbl. D.1-1: Difference between AP flood 'Match 1' and 'Match 2' regarding S_w (Model 1)

		Water Saturation			
Region	**Match**	**1 week**	**0.5 years**	**5 years**	**End of EOR**
Injector					
	Match 1	0.6248	0.6431	0.6431	0.6431
	Match 2	0.6262	0.6446	0.6446	0.6446
	Deviation	-0.0014	-0.0015	-0.0015	-0.0015
Producer					
	Match 1	0.2001	0.2004	0.3101	0.6262
	Match 2	0.3641	0.3710	0.4104	0.7294
	Deviation	-0.164	-0.1706	-0.1003	-0.1032
Center of Margins	Match 1	0.2001	0.2004	0.3101	0.6262
	Match 2	0.2001	0.2003	0.2001	0.6313
	Deviation	0.0	0.0001	0.11	-0.0051

Tbl. D.1-2: Difference between AP flood 'Match 1' and 'Match 2' regarding S_w (Model 1, entire reservoir)

	Water Saturation			
Match	**1 week**	**0.5 years**	**5 years**	**End of EOR**
Match 1	0.5873	0.5877	0.5919	0.6756
Match 2	0.5872	0.5876	0.5901	0.6783
Deviation	0.0001	0.001	0.0018	-0.0027

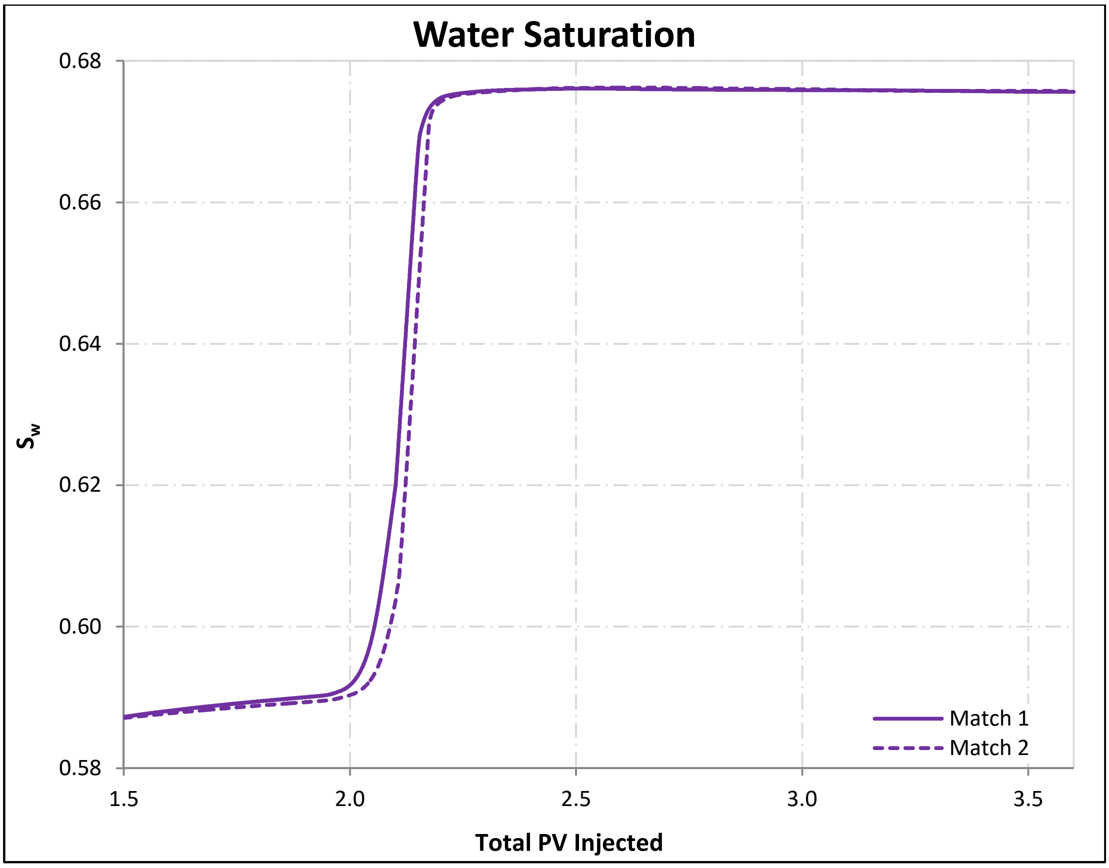

Fig. D.1-1: Difference between AP flood 'Match 1' and 'Match 2' regarding S_w *(Model 1, entire reservoir)*

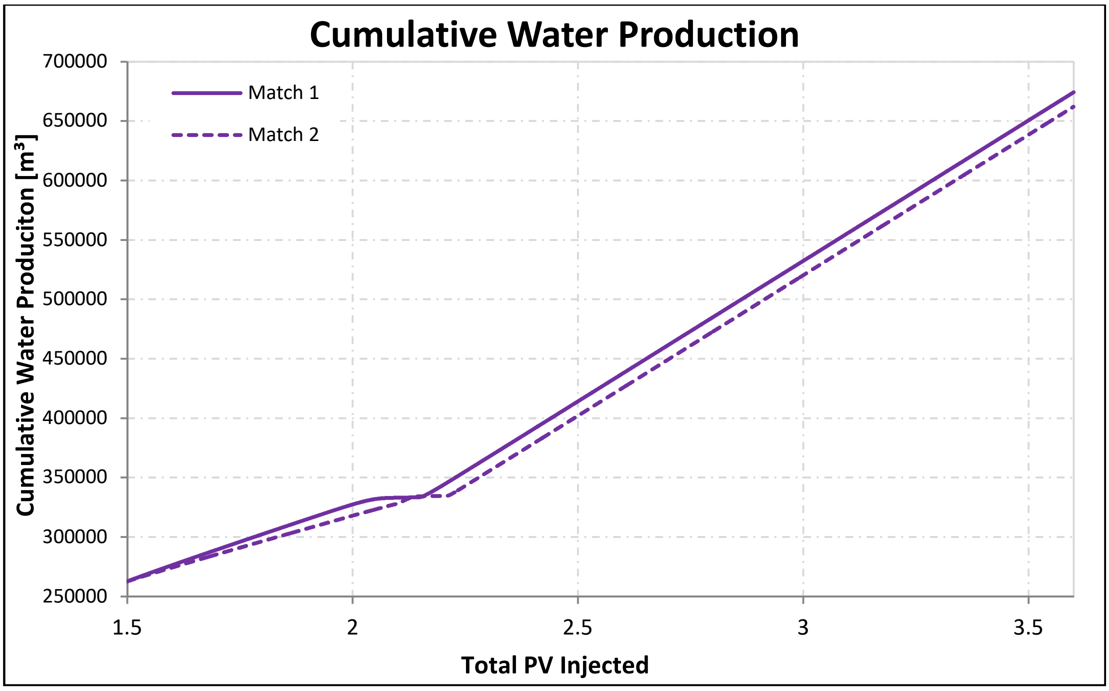

Fig. D.1-2: Difference between AP flood 'Match 1' and 'Match 2' regarding cumulative water production (Model 1, entire reservoir)

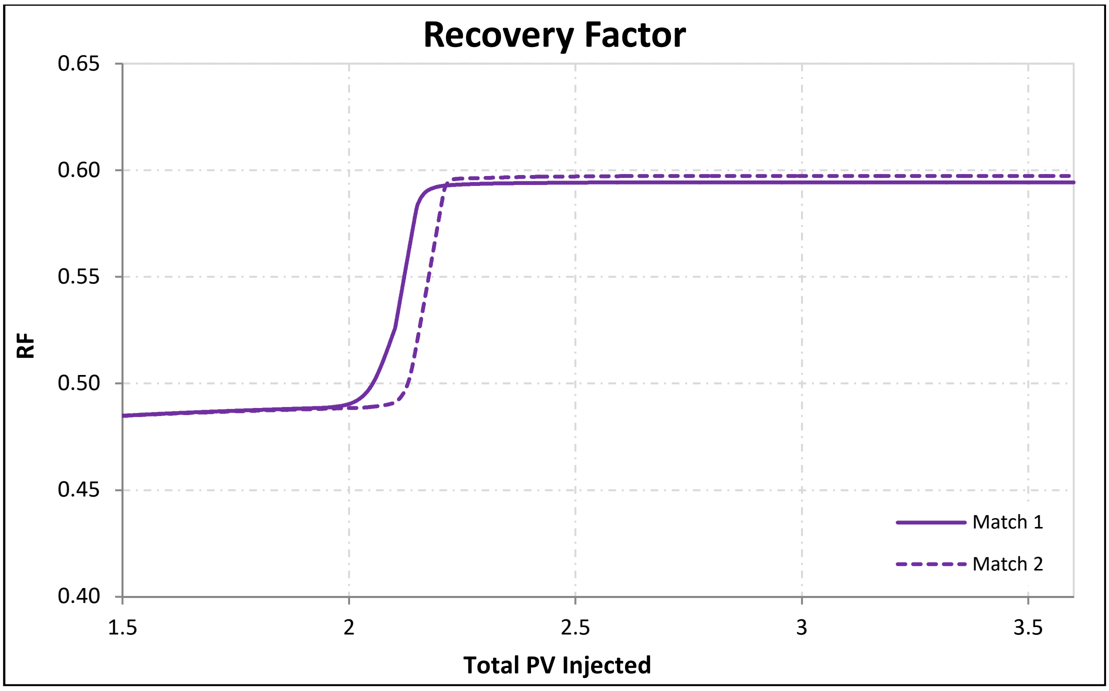

Fig. D.1-3: Difference between AP flood 'Match 1' and 'Match 2' regarding RF (Model 1, entire reservoir)

D.2 Grid Resolution Effects

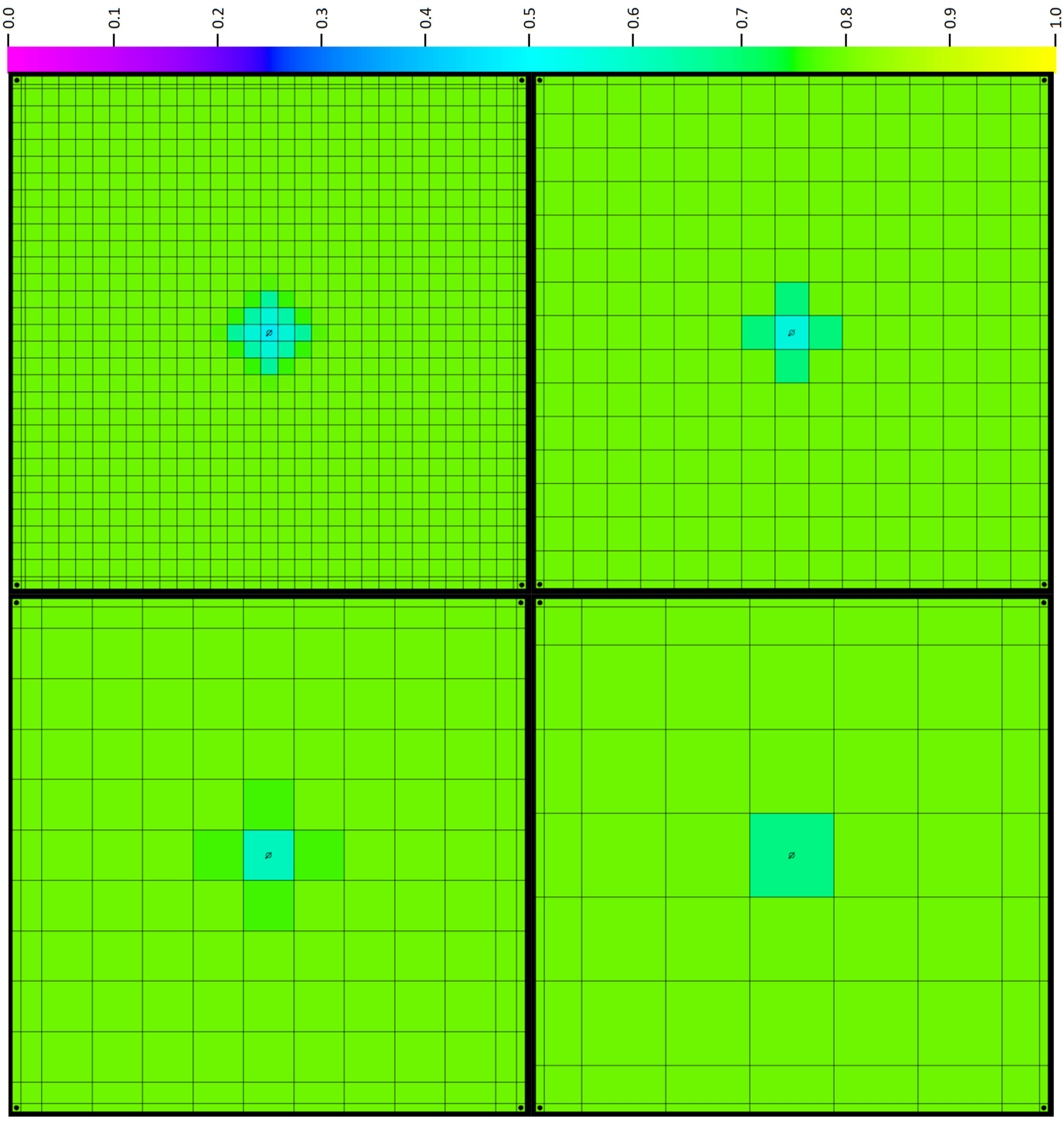

Fig. D.2-1: Effect of increasing grid size on the water propagation after 2 weeks

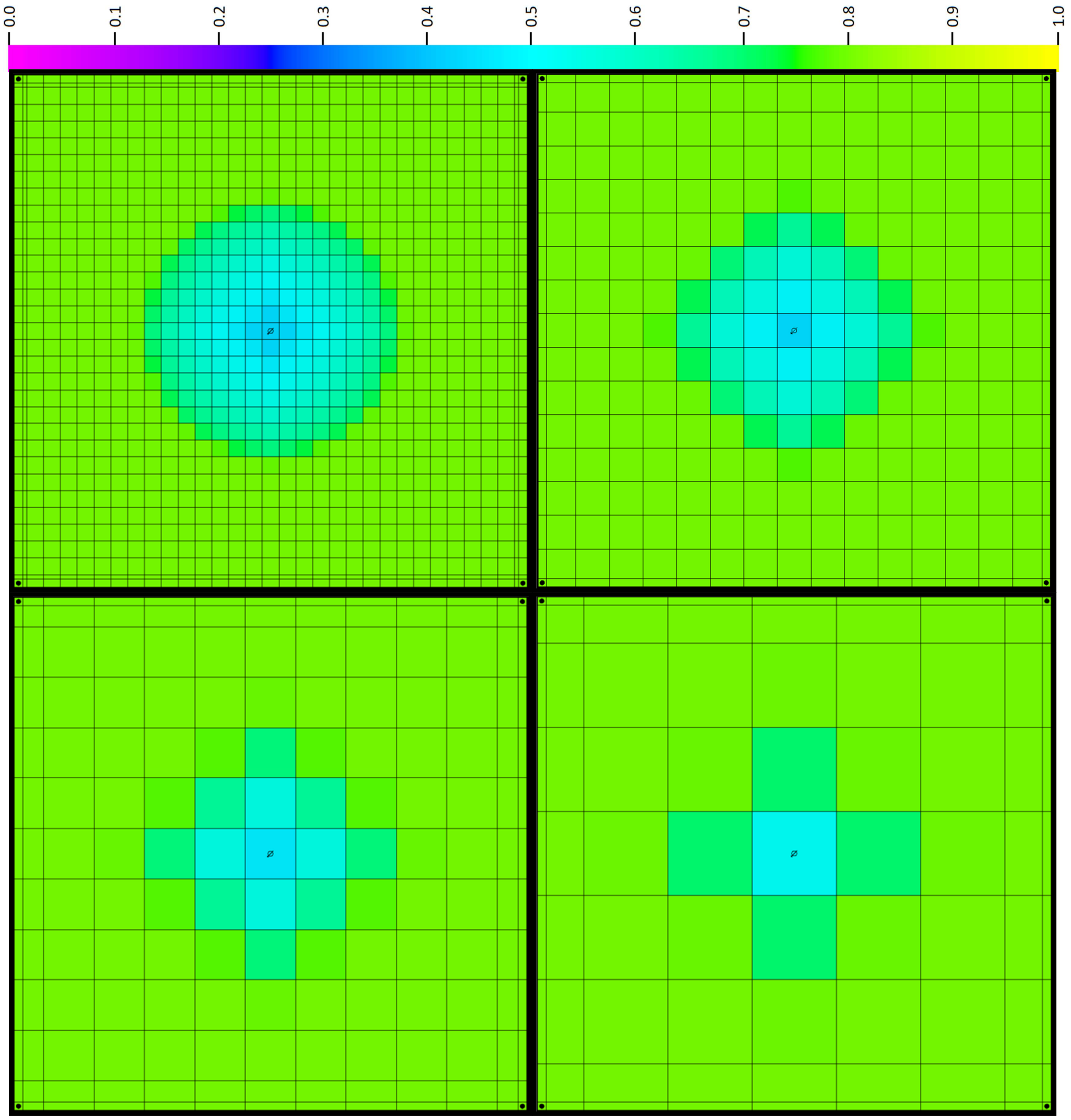

Fig. D.2-2: Effect of increasing grid size on the water propagation after 2 years

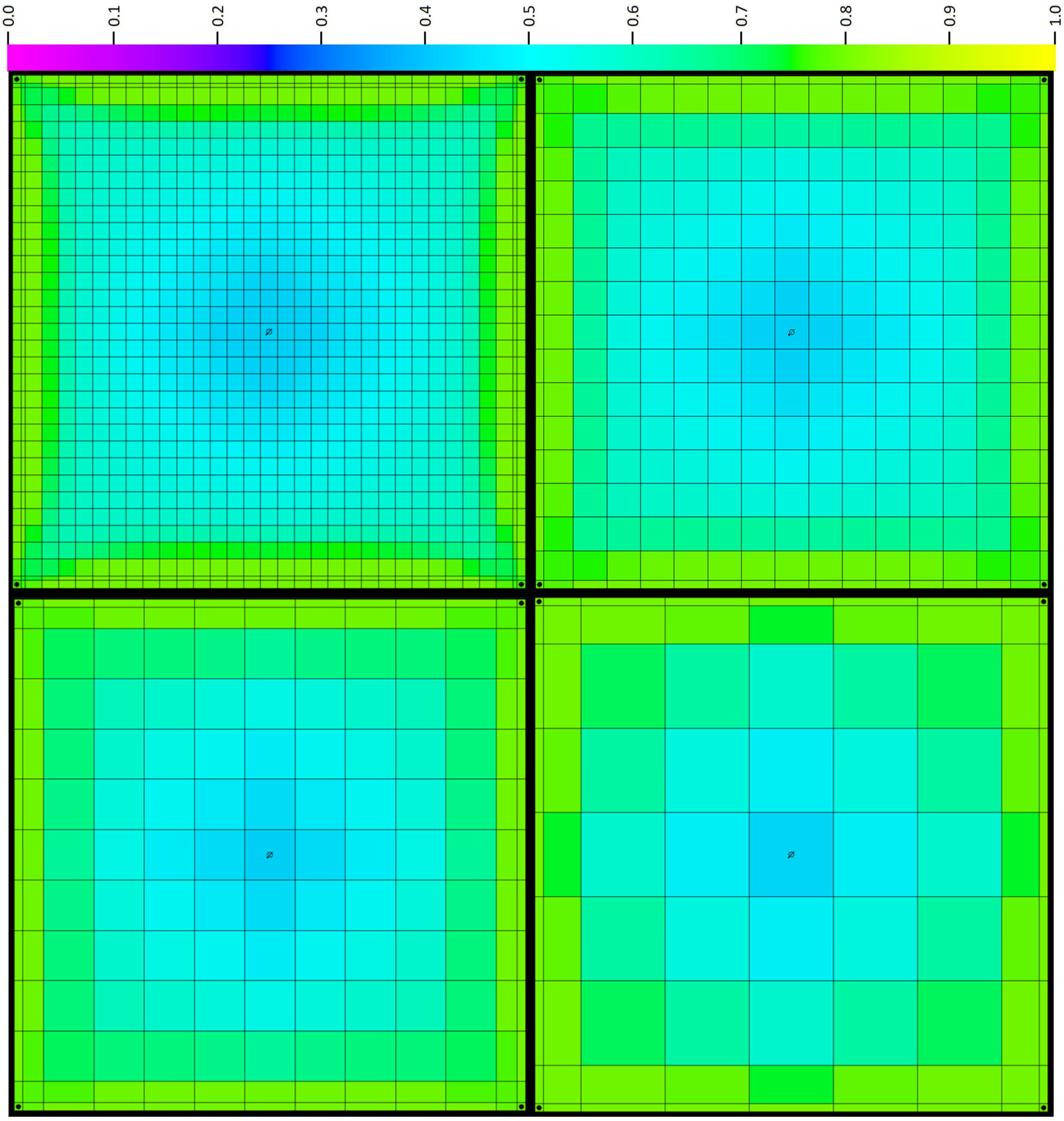

Fig. D.2-3: Effect of increasing grid size on the water propagation after 10 years

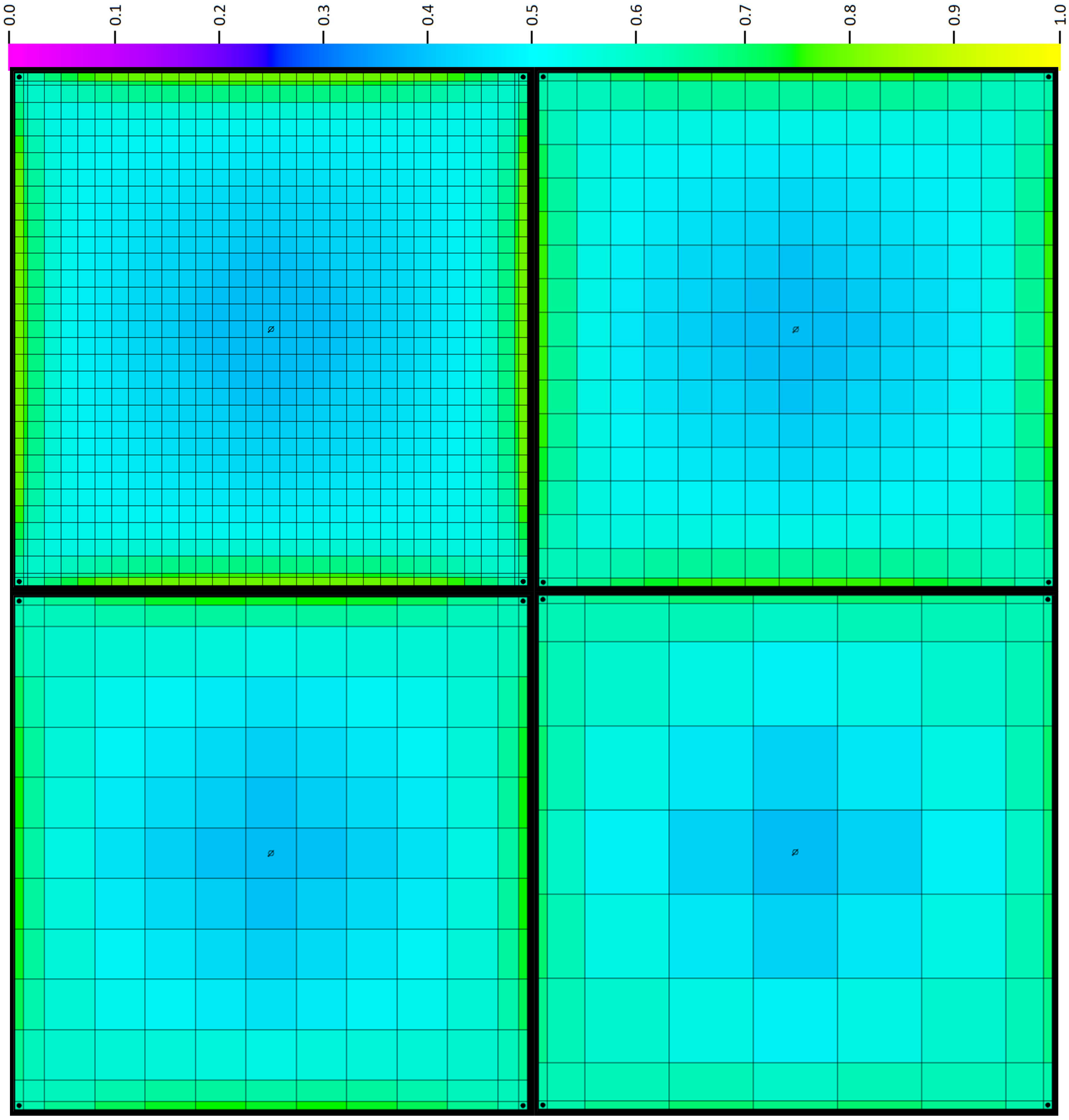

Fig. D.2-4: Effect of increasing grid size at the end of the water flood

Tbl. D.2-1: Effect of the grid cell size on the S_w (water flood)

		Water Saturation			
Region	**Model**	**2 weeks**	**2 years**	**10 years**	**End of water flood**
Injector					
	Model 1	0.5487	0.5700	0.5700	0.5700
	Model 2	0.5140	0.5700	0.5700	0.5700
	Deviation	0.0347	0.0	0.0	0.0
	Model 3	0.4517	0.4633	0.5700	0.5700
	Deviation	0.097	0.1067	0.0	0.0
	Model 4	0.4005	0.5329	0.5699	0.5700
	Deviation	0.1482	0.0371	0.0001	0.0
	Model 5	0.3203	0.4852	0.5596	0.5675
	Deviation	0.2284	0.0848	0.0004	0.0025
Producer					
	Model 1	0.1999	0.1943	0.2357	0.3813
	Model 2	0.1999	0.1943	0.2302	0.3815
	Deviation	0.0	0.0	0.0055	-0.0002
	Model 3	0.1999	0.1943	0.2211	0.3814
	Deviation	0.0	0.0	0.0146	-0.0001
	Model 4	0.1999	0.1943	0.2082	0.3835
	Deviation	0.0	0.0	0.0275	-0.0022
	Model 5	0.1999	0.1943	0.1930	0.3809
	Deviation	0.0	0.0	0.0427	0.0004
Center of Margins	Model 1	0.1999	0.1943	0.1930	0.2307
	Model 2	0.1999	0.1943	0.1930	0.2429
	Deviation	0.0	0.0	0.0	-0.0122
	Model 3	0.1999	0.1943	0.1930	0.2823
	Deviation	0.0	0.0	0.0	-0.0516
	Model 4	0.1999	0.1943	0.1930	0.2957
	Deviation	0.0	0.0	0.0	-0.065
	Model 5	0.1999	0.1943	0.1931	0.3424
	Deviation	0.0	0.0	-0.0001	0.1117

Tbl. D.2-2: Effect of the grid cell size on the S_w of the entire reservoir (water flood)

Model	**Water Saturation** **2 weeks**	**2 years**	**10 years**	**End of water flood**
Model 1	0.2038	0.3964	0.5482	0.5592
Model 2	0.2038	0.3948	0.5481	0.5591
Deviation	0.0	0.0016	0.0001	0.0001
Model 3	0.2038	0.3928	0.5474	0.5583
Deviation	0.0	0.0036	0.0008	0.0009
Model 4	0.2038	0.3907	0.5471	0.5581
Deviation	0.0	0.0057	0.0011	0.0011
Model 5	0.2038	0.3872	0.5451	0.5574
Deviation	0.0	0.0092	0.0031	0.0018

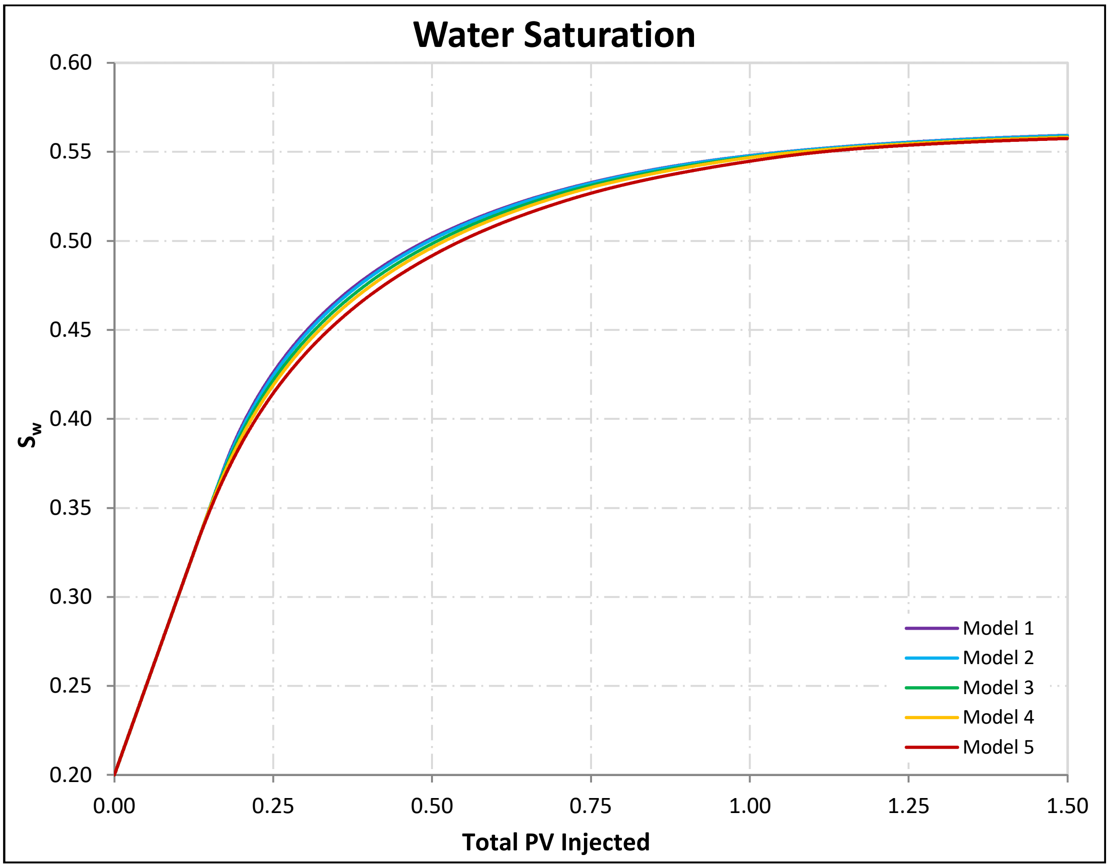

Fig. D.2-5: Effect of the grid cell size on the S_w of the entire reservoir (water flood)

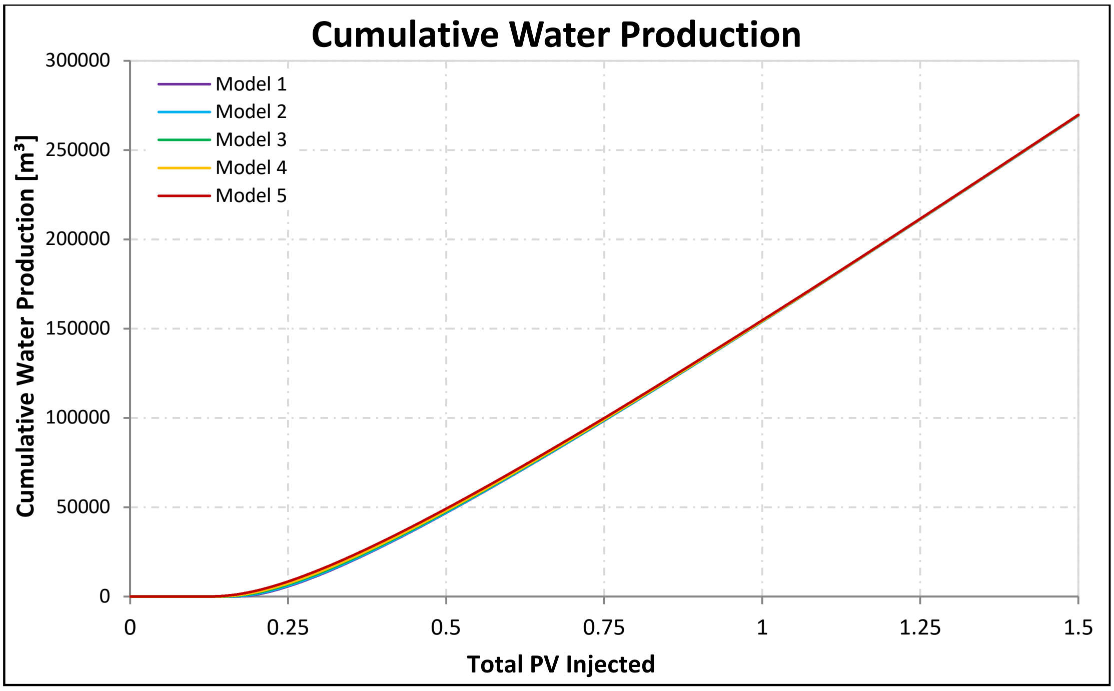

Fig. D.2-6: Effect of the grid cell size on the cumulative water production of the entire reservoir (water flood)

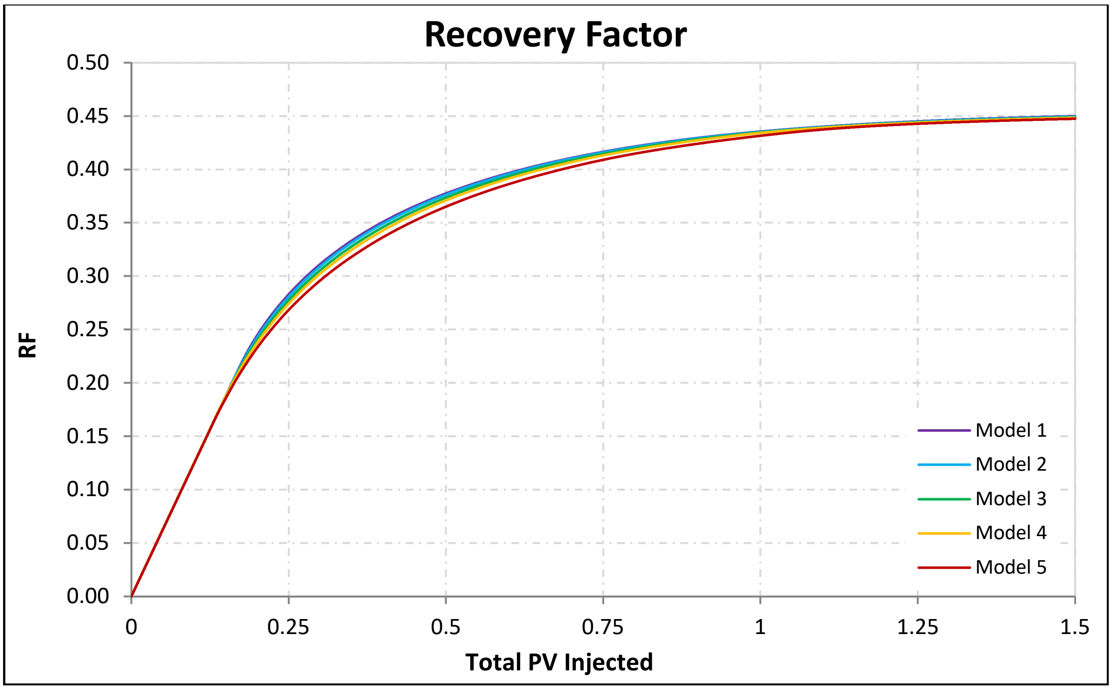

Fig. D.2-7: Effect of the grid cell size on the recovery factor of the entire reservoir (water flood)

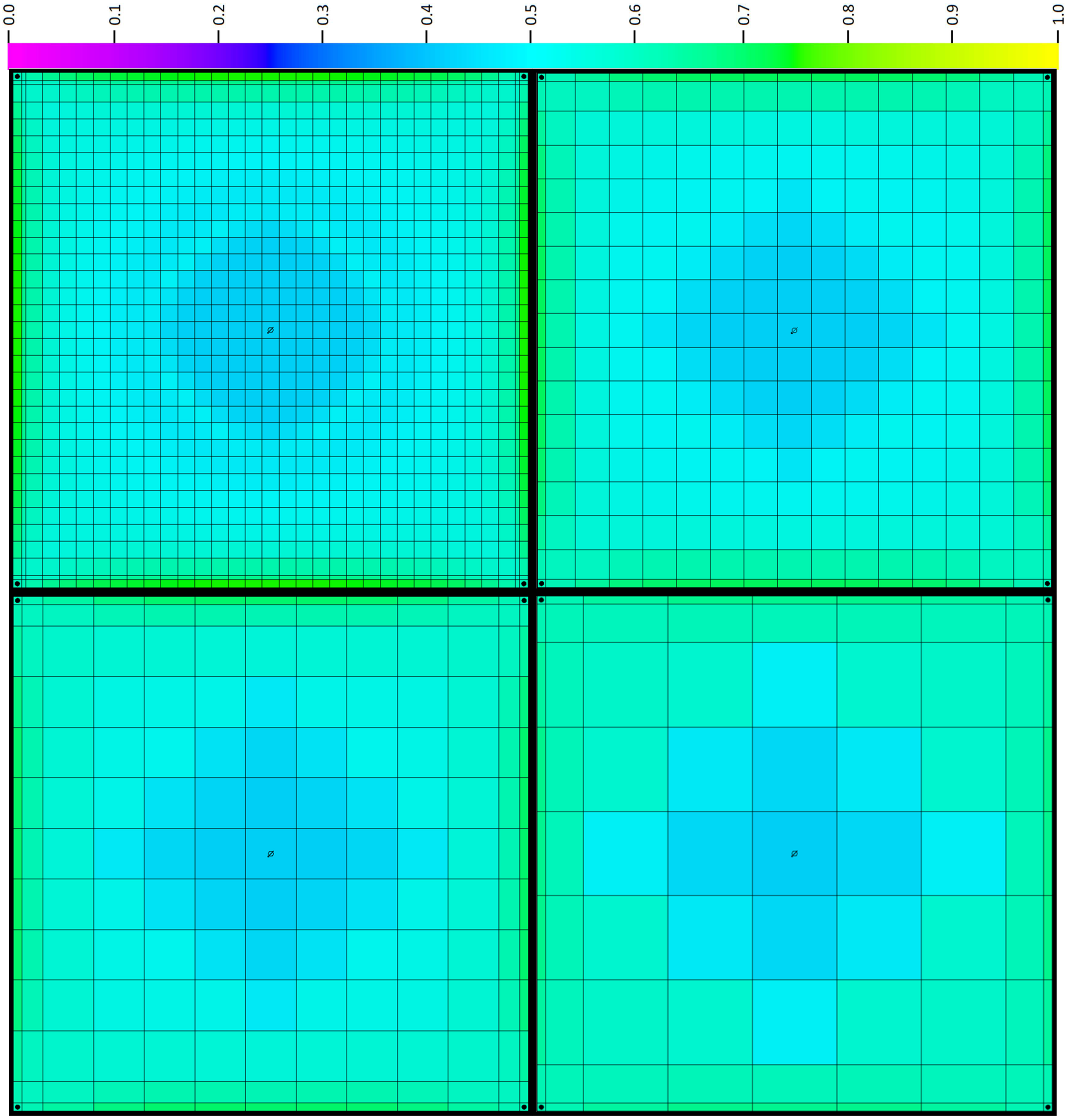

Fig. D.2-8: Effect of increasing grid size on the oil displacement after 0.8 years (polymer flood)

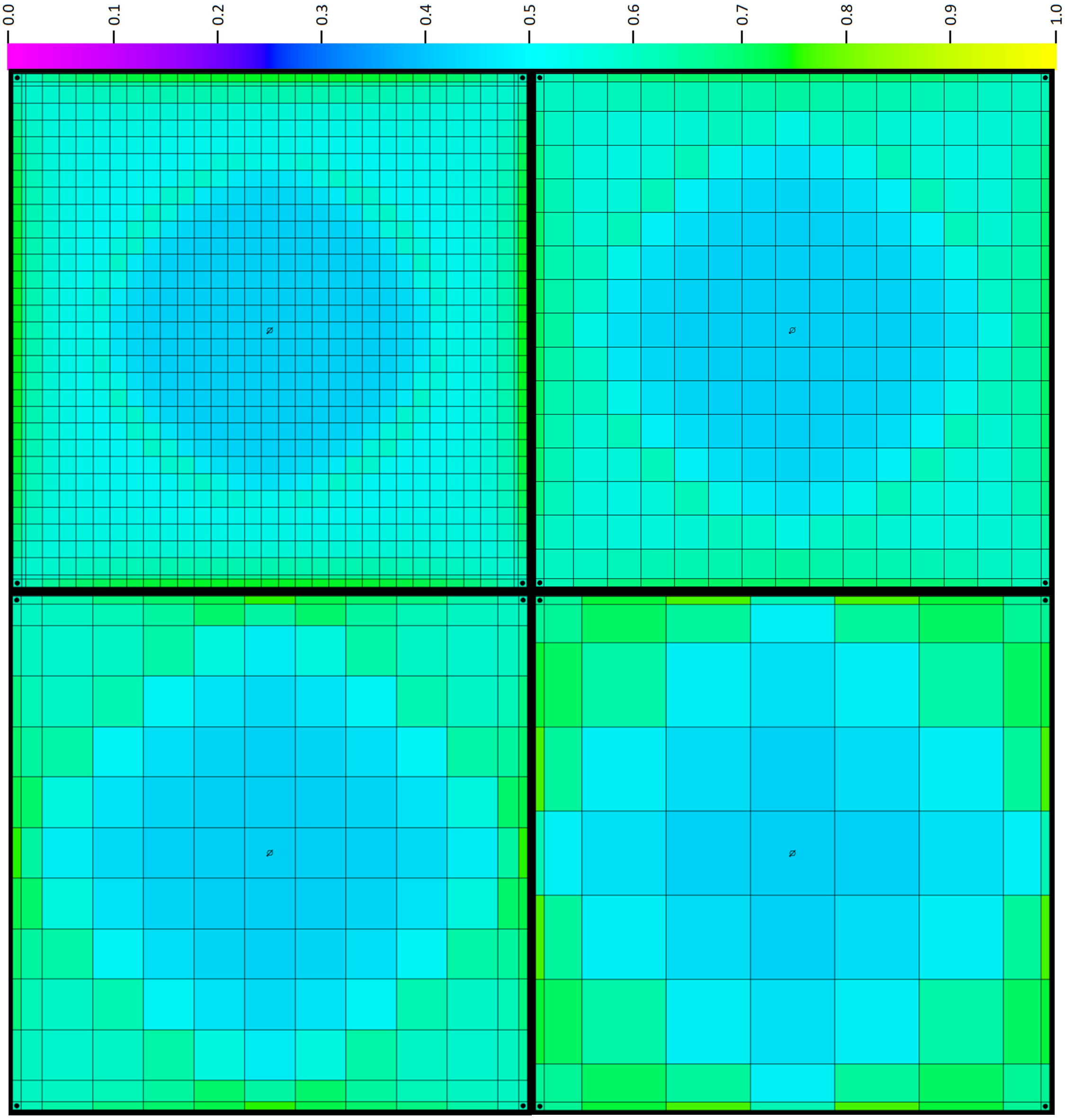

Fig. D.2-9: Effect of increasing grid size on the oil displacement after 2 years (polymer flood)

Tbl. D.2-3: Effect of the grid cell size on the S_w (polymer flood)

		Water Saturation			
Region	**Model**	**0.8 years**	**2 years**	**7.5 years**	**End of EOR**
Injector					
	Model 1	0.5701	0.5702	0.5702	0.5703
	Model 2	0.5701	0.5701	0.5702	0.5702
	Deviation	0.0	0.0001	0.0	0.0001
	Model 3	0.5701		0.5703	0.5703
	Deviation	0.0		-0.0001	0.0
	Model 4	0.5701	0.5701	0.5702	0.5703
	Deviation	0.0	0.0001	0.0	0.0
	Model 5	0.5699	0.5700	0.5701	0.5702
	Deviation	0.0002	0.0002	0.0001	0.0001
Producer					
	Model 1	0.3850	0.3903	0.4059	0.5700
	Model 2	0.3850	0.3901	0.2303	0.5700
	Deviation	0.0	0.0002	0.1756	0.0
	Model 3	0.3844		0.5313	0.5699
	Deviation	0.0006		-0.1254	0.0001
	Model 4	0.3866	0.3904	0.5365	0.5699
	Deviation	-0.0016	-0.0001	-0.1306	0.0001
	Model 5	0.3832	0.3499	0.5389	0.5696
	Deviation	0.0018	0.0404	-0.133	0.0004
Center of Margins	Model 1	0.2361	0.2441	0.5027	0.5693
	Model 2	0.2482	0.2557	0.5320	0.5695
	Deviation	-0.0121	-0.0116	-0.0291	-0.0002
	Model 3	0.2866		0.5369	0.5692
	Deviation	-0.0505		-0.034	0.0001
	Model 4	0.2993	0.2436	0.5359	0.5691
	Deviation	-0.0632	0.0005	-0.033	0.0002
	Model 5	0.3366	0.3845	0.5381	0.5686
	Deviation	-0.1005	-0.1404	-0.0352	0.0007

Tbl. D.2-4: Effect of the grid cell size on the S_w of the entire reservoir (polymer flood)

	Water Saturation			
Model	**0.8 years**	**2 years**	**7.5 years**	**End of EOR**
Model 1	0.5594	0.5596	0.5612	0.5711
Model 2	0.5592	0.5595	0.5626	0.5714
Deviation	0.0002	0.0001	-0.0014	-0.0003
Model 3	0.5585	0.5588	0.5701	0.5714
Deviation	0.0009	0.0008	-0.0089	-0.0003
Model 4	0.5583	0.5586	0.5694	0.5714
Deviation	0.0011	0.001	-0.0082	-0.0003
Model 5	0.5576	0.558	0.5692	0.5714
Deviation	0.0018	0.0016	-0.008	-0.0003

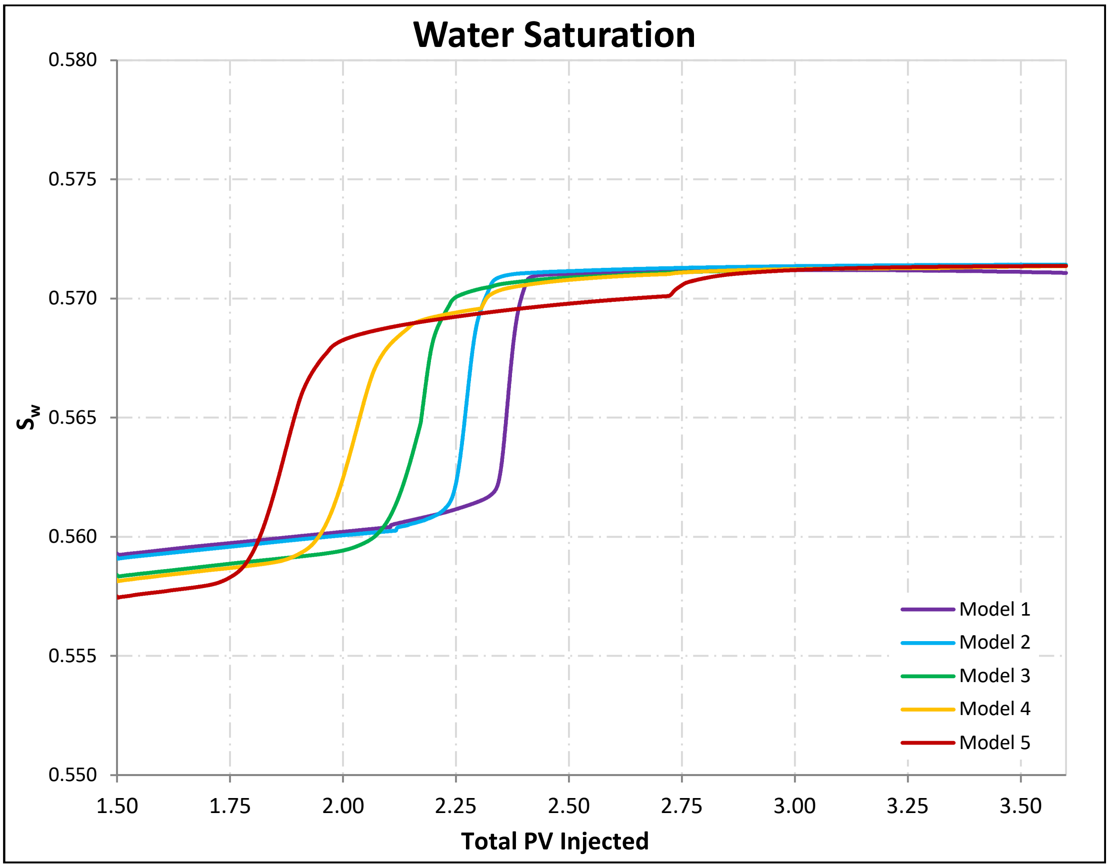

Fig. D.2-10: Effect of the grid cell size on the S_w of the entire reservoir (polymer flood)

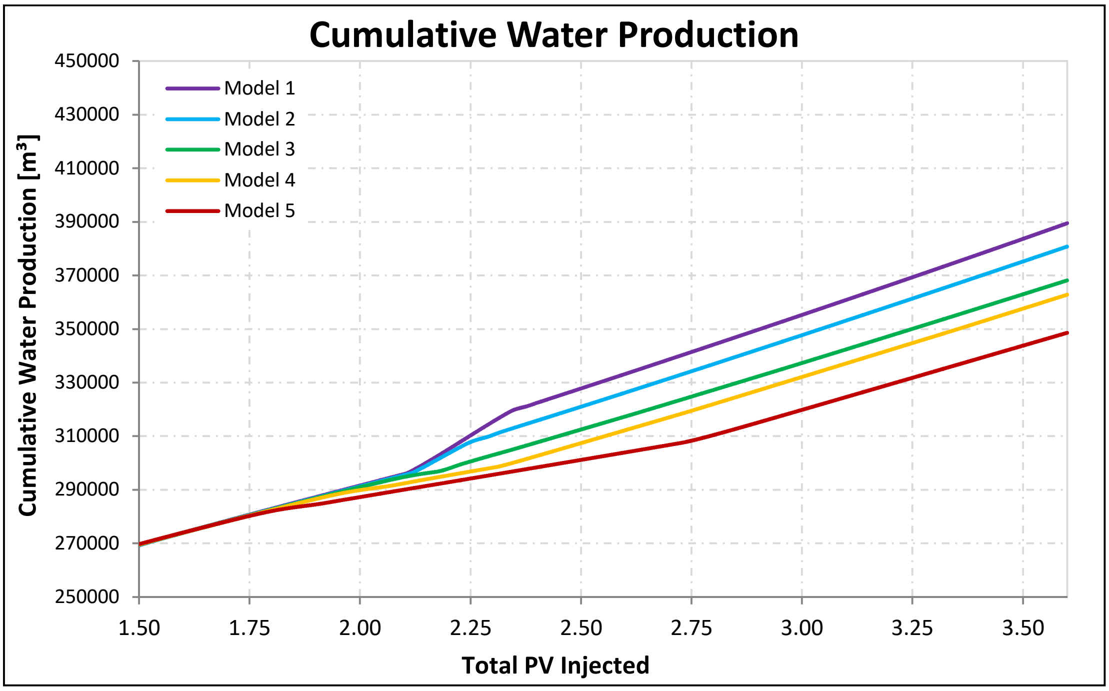

Fig. D.2-11: Effect of the grid cell size on the cumulative water production of the entire reservoir (polymer flood)

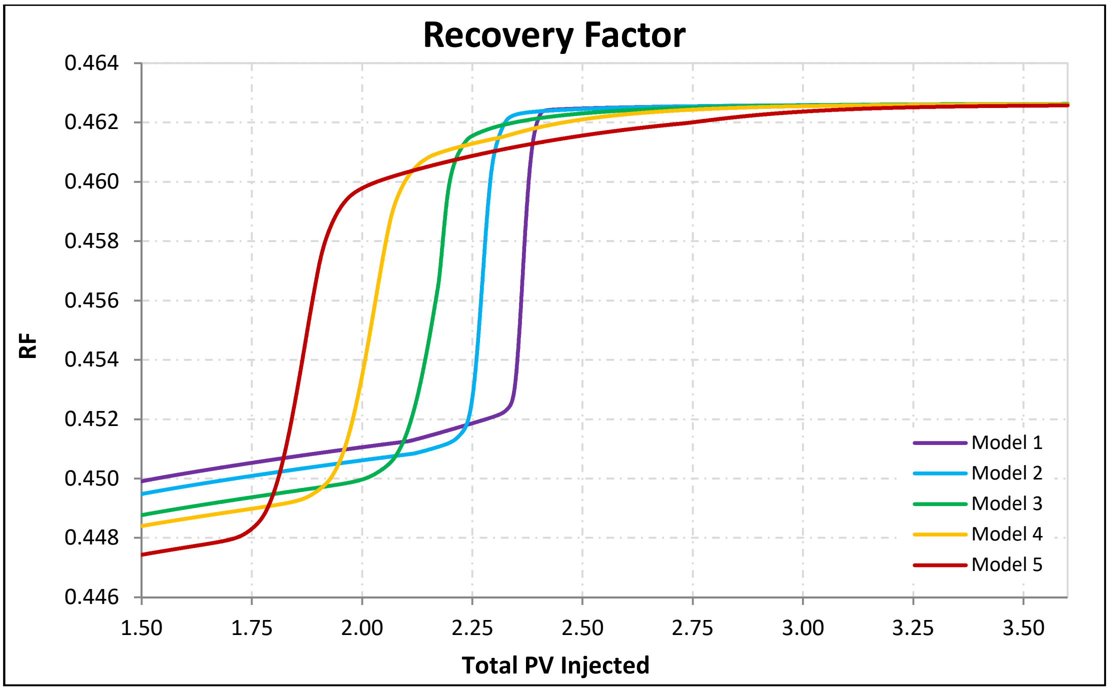

Fig. D.2-12: Effect of the grid cell size on the recovery factor of the entire reservoir (polymer flood)

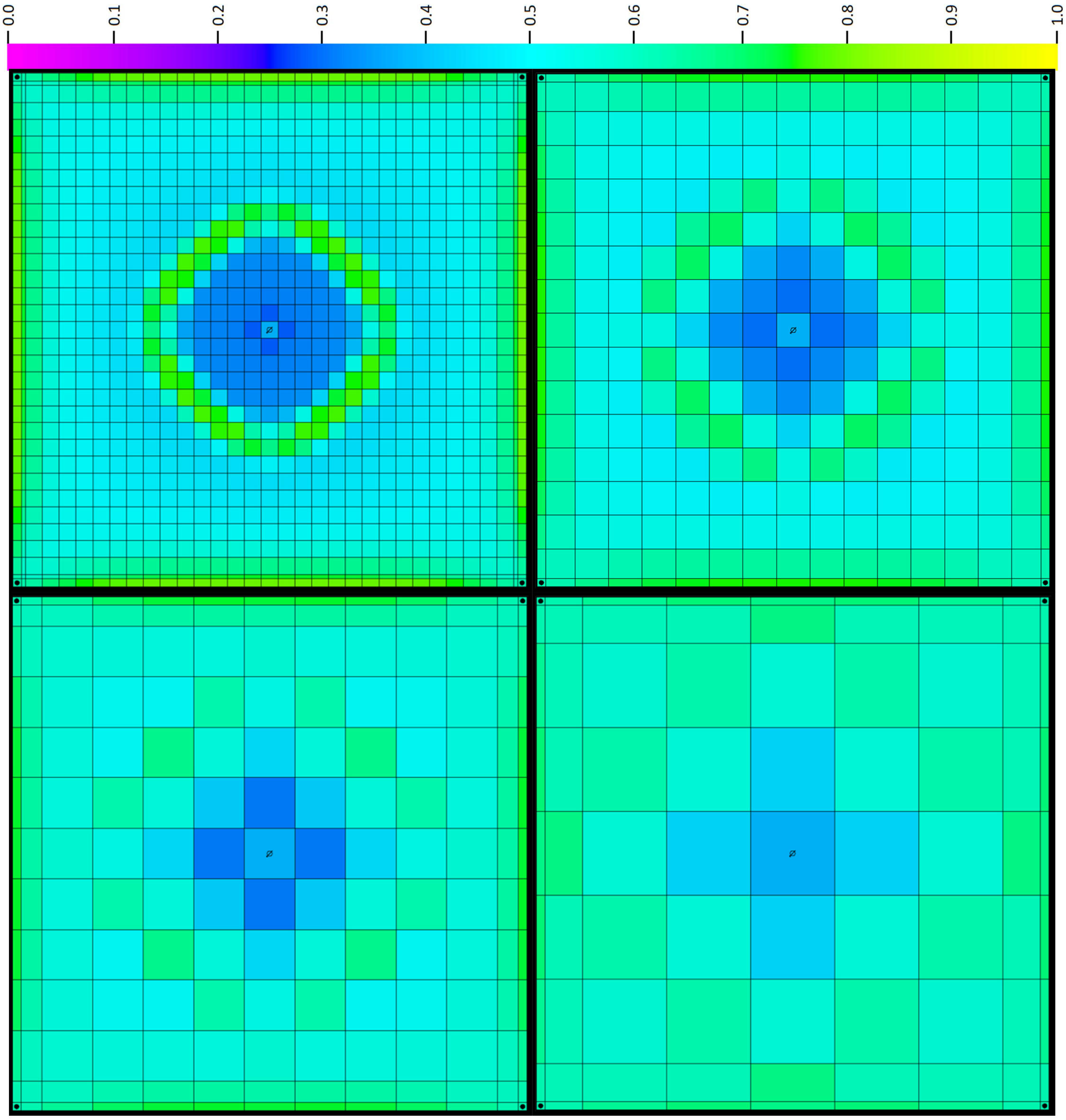

Fig. D.2-13: Effect of increasing grid size on the oil displacement after 0.5 years (AP flood 'Match 1')

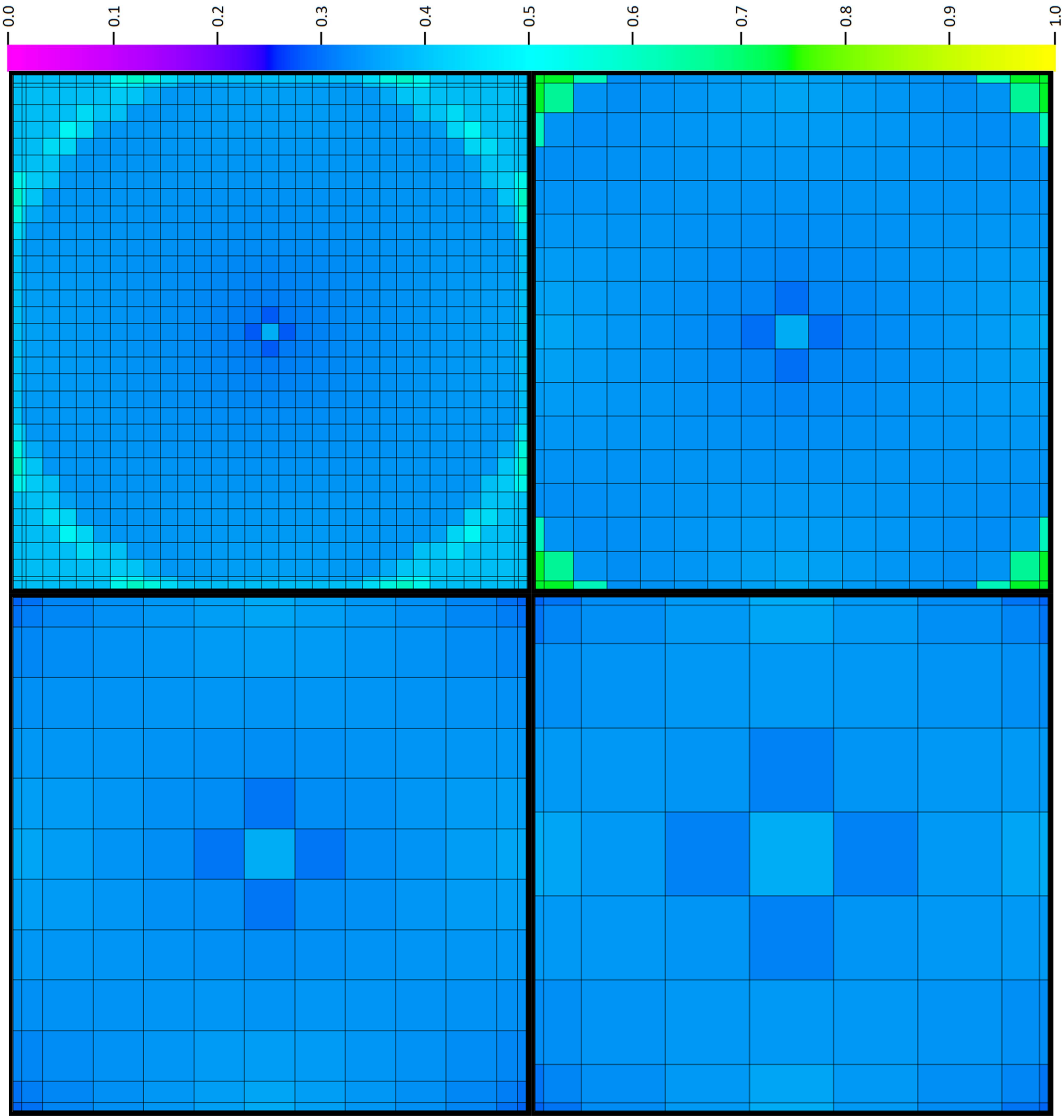

Fig. D.2-14: Effect of increasing grid size on the lower part of the reservoir after 5.6 years (AP flood 'Match 1')

Tbl. D.2-5: Effect of the grid cell size on the S_w (AP flood 'Match 1')

		Water Saturation			
Region	**Model**	**1 week**	**0.5 years**	**5 years**	**End of EOR**
Injector					
	Model 1	0.6248	0.6431	0.6431	0.6431
	Model 2	0.6188	0.6237	0.6240	0.6283
	Deviation	0.006	0.0194	0.0191	0.0148
	Model 3	0.6130	0.6226	0.6245	0.6261
	Deviation	0.0118	0.0205	0.0186	0.017
	Model 4	0.6069	0.6214	0.6248	0.6263
	Deviation	0.0179	0.0217	0.0183	0.0168
	Model 5	0.6007	0.6211	0.6218	0.6218
	Deviation	0.0241	0.022	0.0213	0.0213
Producer					
	Model 1	0.3641	0.3723	0.2021	0.7287
	Model 2	0.3666	0.3728	0.2069	0.7289
	Deviation	-0.0025	-0.0005	-0.0048	-0.0002
	Model 3	0.3717	0.3773	0.2000	0.7294
	Deviation	-0.0076	-0.005	0.0021	-0.0007
	Model 4	0.3747	0.3799	0.2003	0.7293
	Deviation	-0.0106	-0.0076	0.0018	-0.0006
	Model 5	0.3718	0.3771	0.6831	0.7296
	Deviation	-0.0077	-0.0048	-0.481	-0.0009
Center of Margins					
	Model 1	0.2001	0.2004	0.3101	0.6262
	Model 2	0.2006	0.2020	0.2922	0.6825
	Deviation	-0.0005	-0.0016	0.0179	-0.0563
	Model 3	0.2409	0.2483	0.5705	0.6266
	Deviation	-0.0493	-0.0479	-0.2604	-0.0004
	Model 4	0.2561	0.2625	0.5852	0.6273
	Deviation	-0.056	-0.0621	-0.2751	-0.0011
	Model 5	0.3234	0.3247	0.5934	0.6267
	Deviation	-0.1233	-0.1243	-0.2833	-0.0005

Tbl. D.2-6: Effect of the grid cell size on the S_w of the entire reservoir (AP flood 'Match 1')

	Water Saturation			
Model	**1 week**	**0.5 years**	**5 years**	**End of EOR**
Model 1	0.5873	0.5877	0.5919	0.6756
Model 2	0.5871	0.5874	0.5904	0.6758
Deviation	0.0002	0.0003	0.0015	-0.0002
Model 3	0.5863	0.5867	0.6146	0.6748
Deviation	0.001	0.001	-0.0227	0.0008
Model 4	0.5862	0.5865	0.6435	0.6744
Deviation	0.0011	0.0012	-0.0516	0.0012
Model 5	0.5855	0.5858	0.6565	0.6731
Deviation	0.0018	0.0019	-0.0646	0.0025

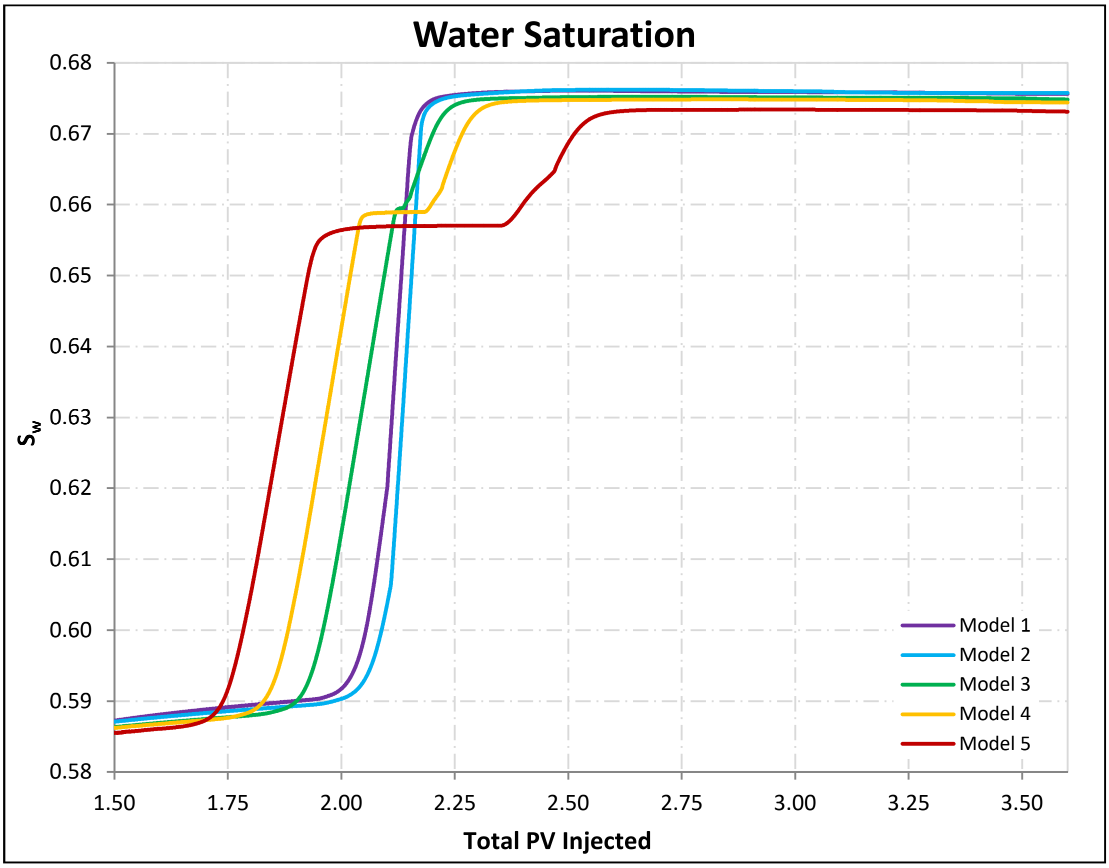

Fig. D.2-15: Effect of the grid cell size on the S_w of the entire reservoir (AP flood 'Match 1')

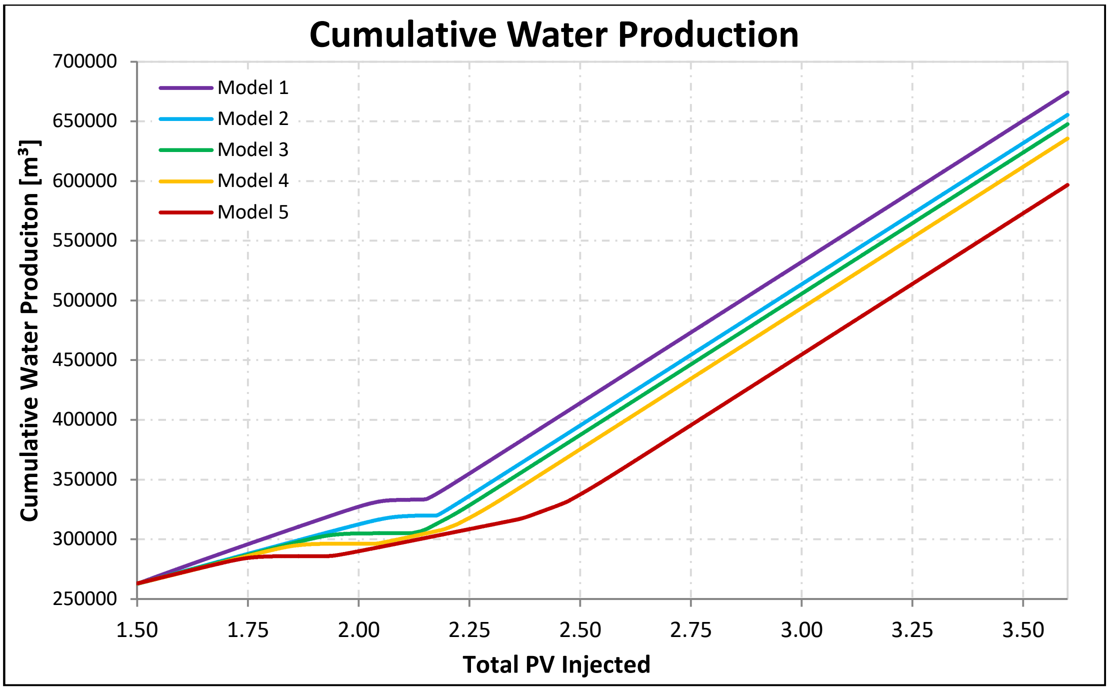

Fig. D.2-16: Effect of the grid cell size on the cumulative water production of the entire reservoir (AP flood 'Match 1')

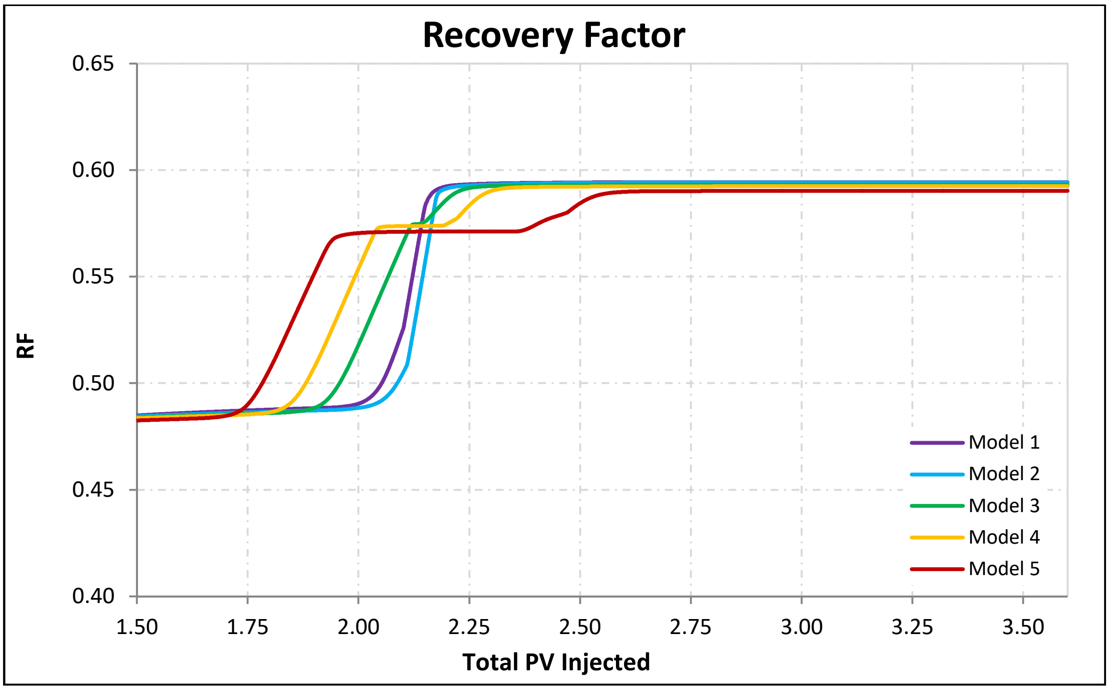

Fig. D.2-17: Effect of the grid cell size on the recovery factor of the entire reservoir (AP flood 'Match 1')

D.3 Grid Orientation Effects

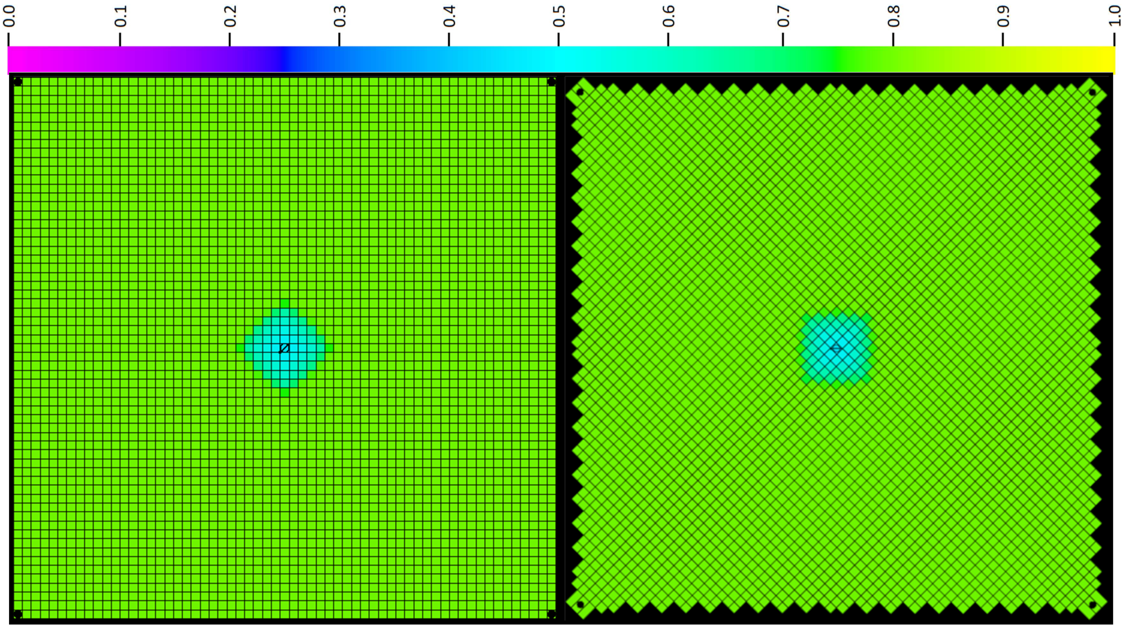

Fig. D.3-1: Effect of the grid orientation on the water propagation after 2 weeks

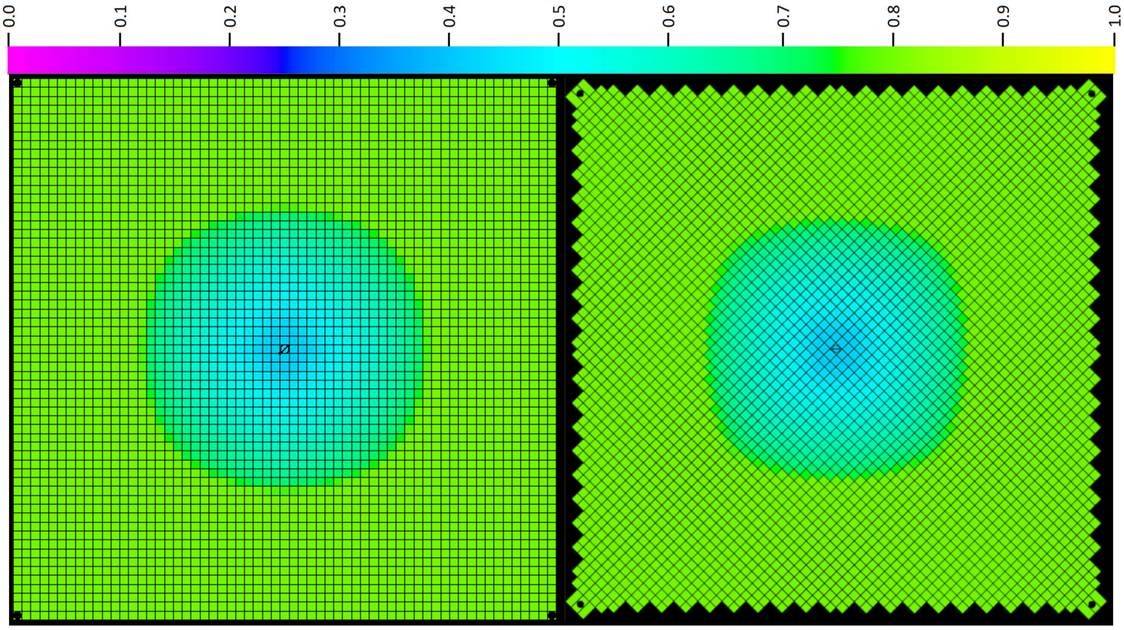

Fig. D.3-2: Effect of the grid orientation on the water propagation after 2 years

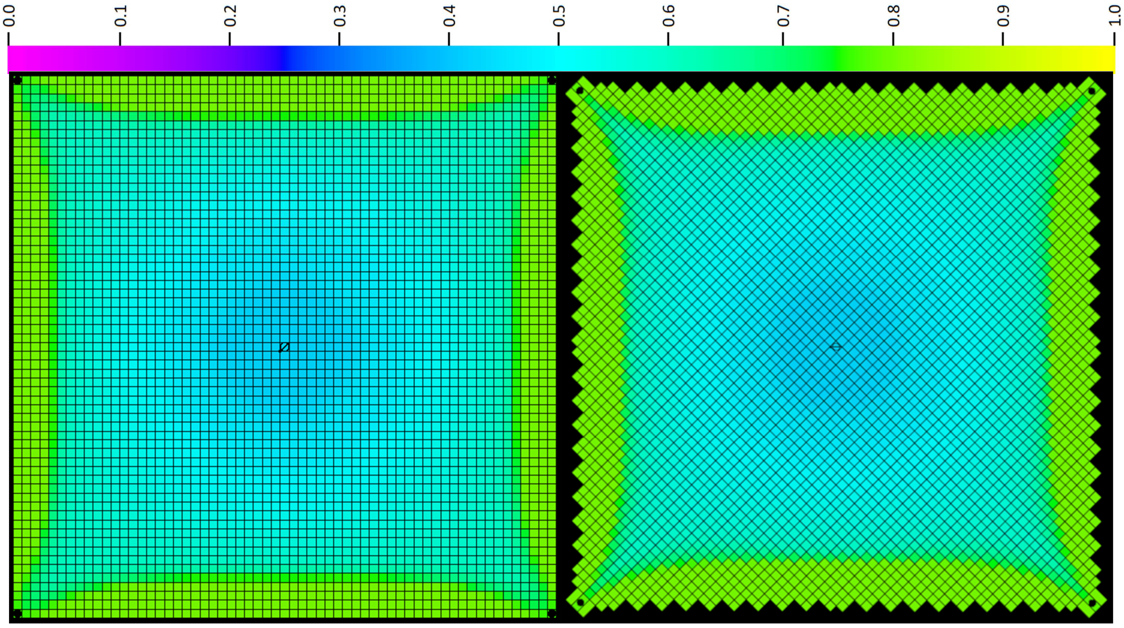

Fig. D.3-3: Effect of the grid orientation on the water propagation after 10 years

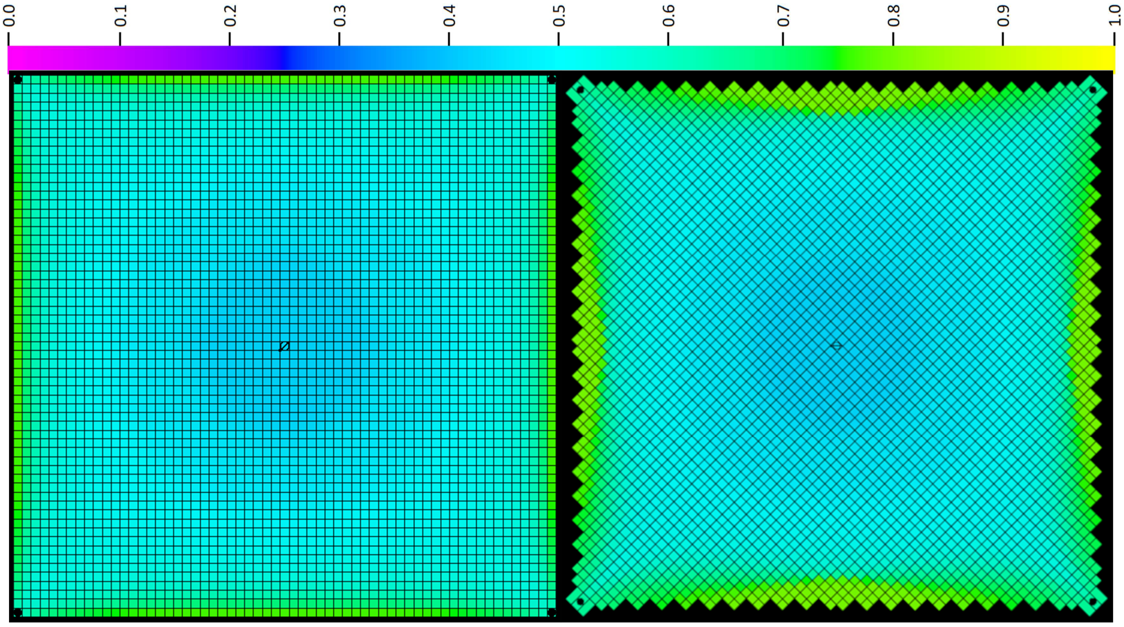

Fig. D.3-4: Effect of the grid orientation on the water propagation at the end of the water flood

Tbl. D.3-1: Effect of the grid orientation on the S_w (water flood)

Region	Model	Water Saturation 2 weeks	2 years	10 years	End of water flood
Injector					
	Model 1	0.5487	0.5700	0.5700	0.5700
	Model 1B	0.5464	0.5700	0.5700	0.5700
	Deviation	0.0023	0.0	0.0	0.0
Producer					
	Model 1	0.1999	0.1943	0.2357	0.3813
	Model 1B	0.1999	0.1944	0.2179	0.3558
	Deviation	0.0	-0.0001	0.0178	0.0255
Center of Margins	Model 1	0.1999	0.1943	0.1930	0.2307
	Model 1B	0.1999	0.1944	0.1930	0.1930
	Deviation	0.0	-0.0001	0.0	0.0377

Tbl. D.3-2: Effect of the grid orientation on the S_w of the entire reservoir (water flood)

Model	Water Saturation 2 weeks	2 years	10 years	End of EOR
Model 1	0.2038	0.3964	0.5482	0.5592
Model 1B	0.2038	0.3915	0.5435	0.5572
Deviation	0.0	0.0049	0.0047	0.002

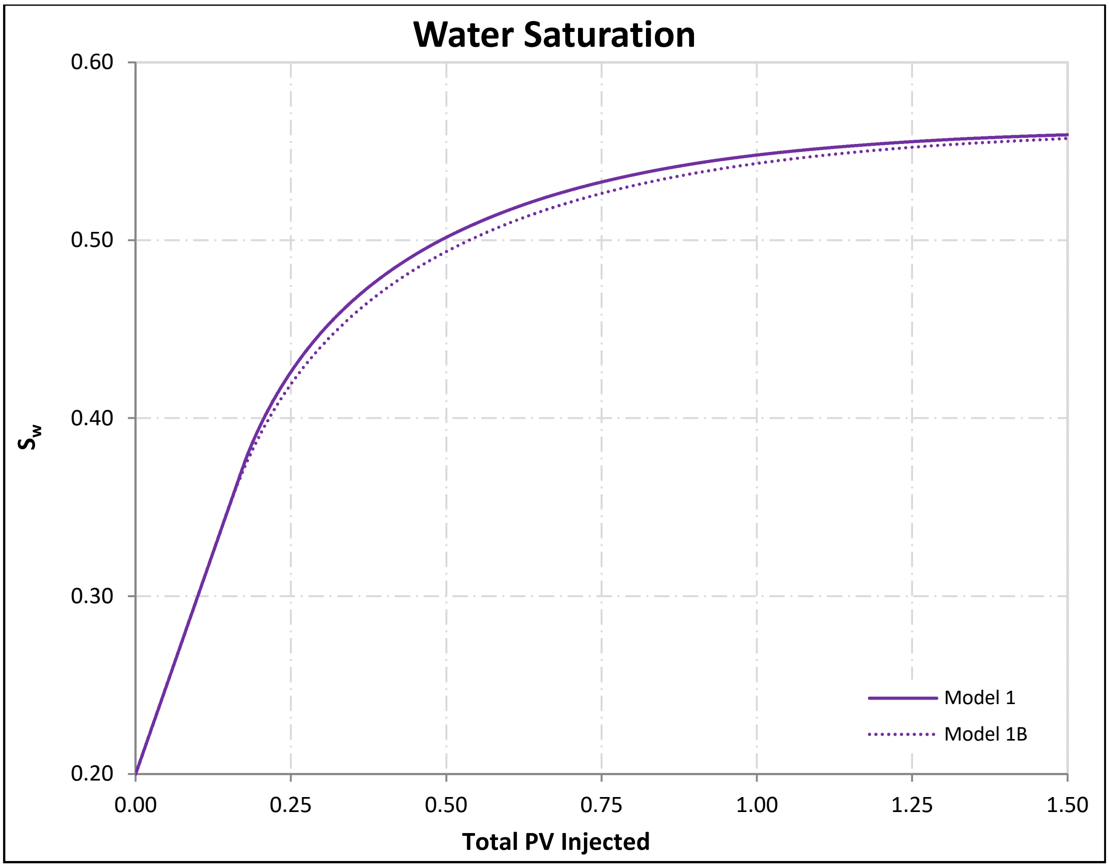

Fig. D.3-5: Effect of the grid orientation on the S_w of the entire reservoir (water flood)

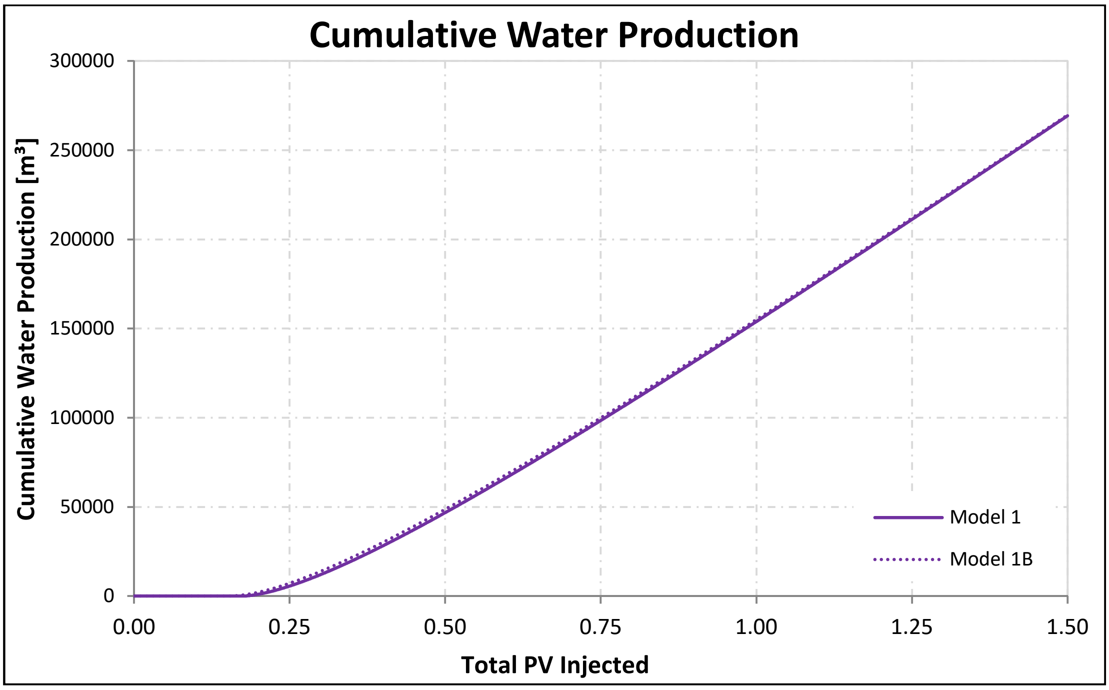

Fig. D.3-6: Effect of the grid orientation on the cumulative water production of the entire reservoir (water flood)

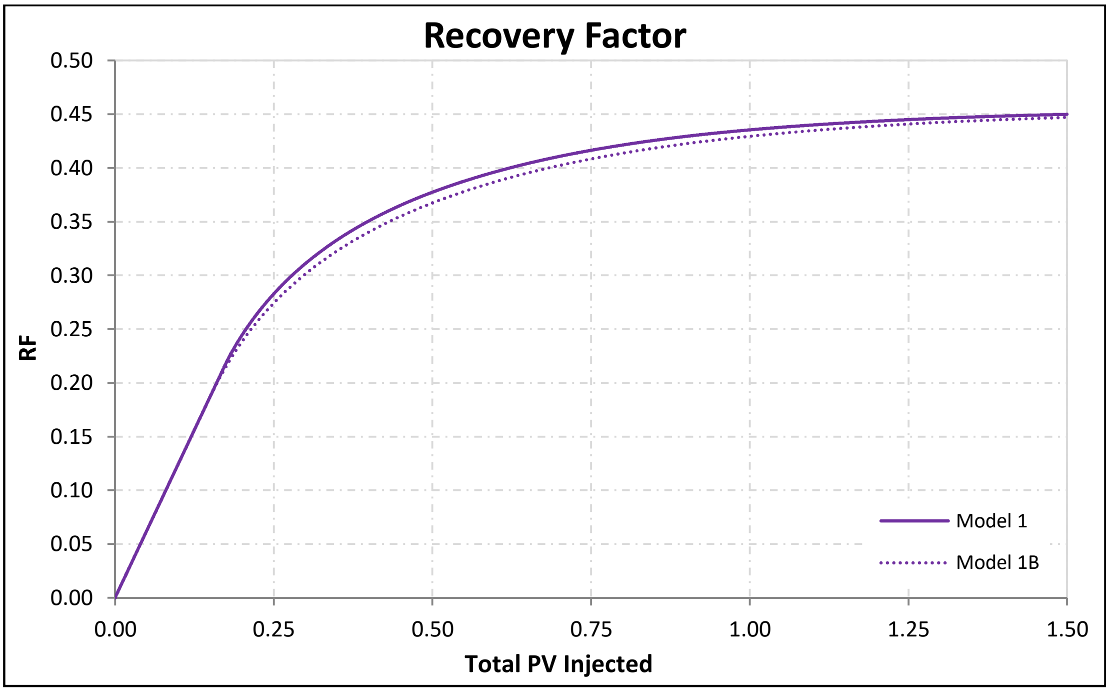

Fig. D.3-7: Effect of the grid orientation on the recovery factor of the entire reservoir (water flood)

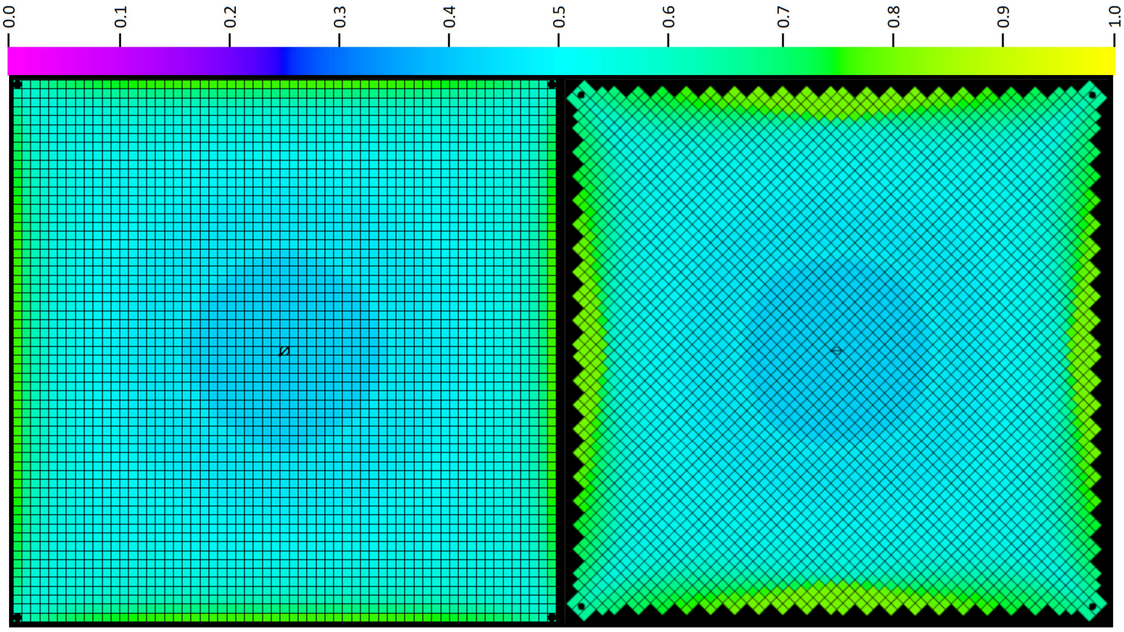

Fig. D.3-8: Effect of the grid orientation on oil displacement after 0.8 years (polymer flood)

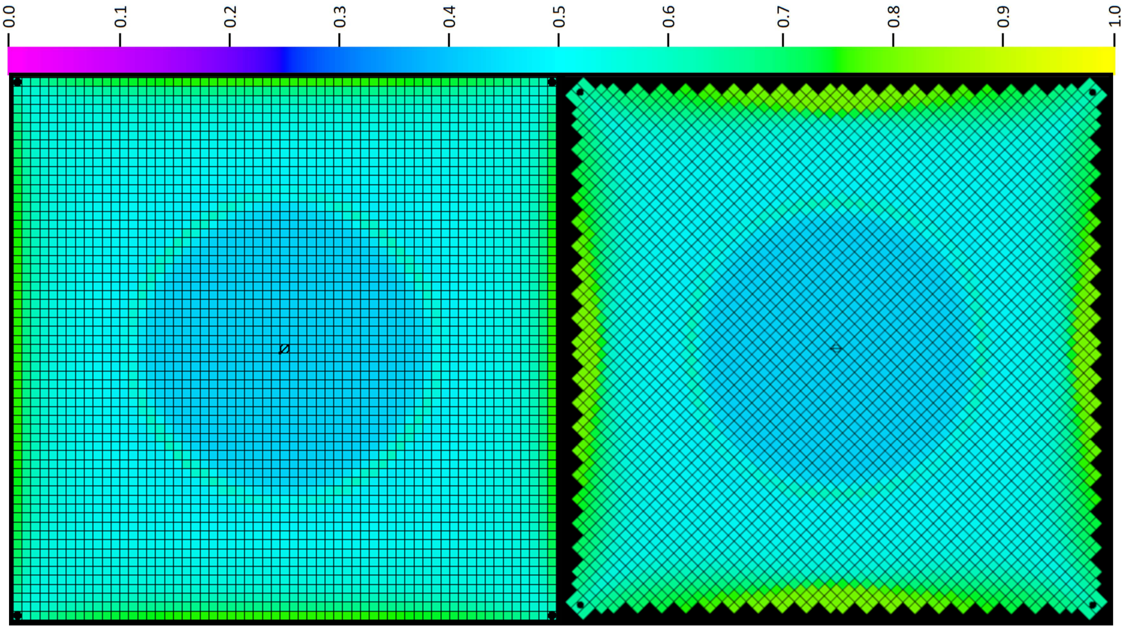

Fig. D.3-9: Effect of the grid orientation on oil displacement after 2 years (polymer flood)

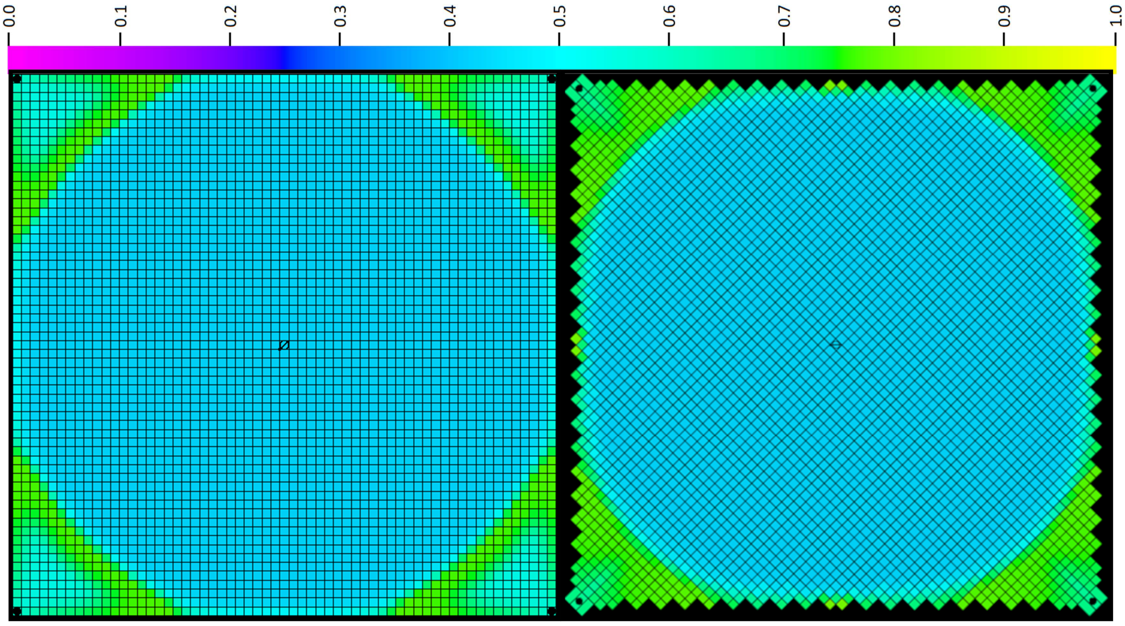

Fig. D.3-10: Effect of the grid orientation on oil displacement after 7.5 years (polymer flood)

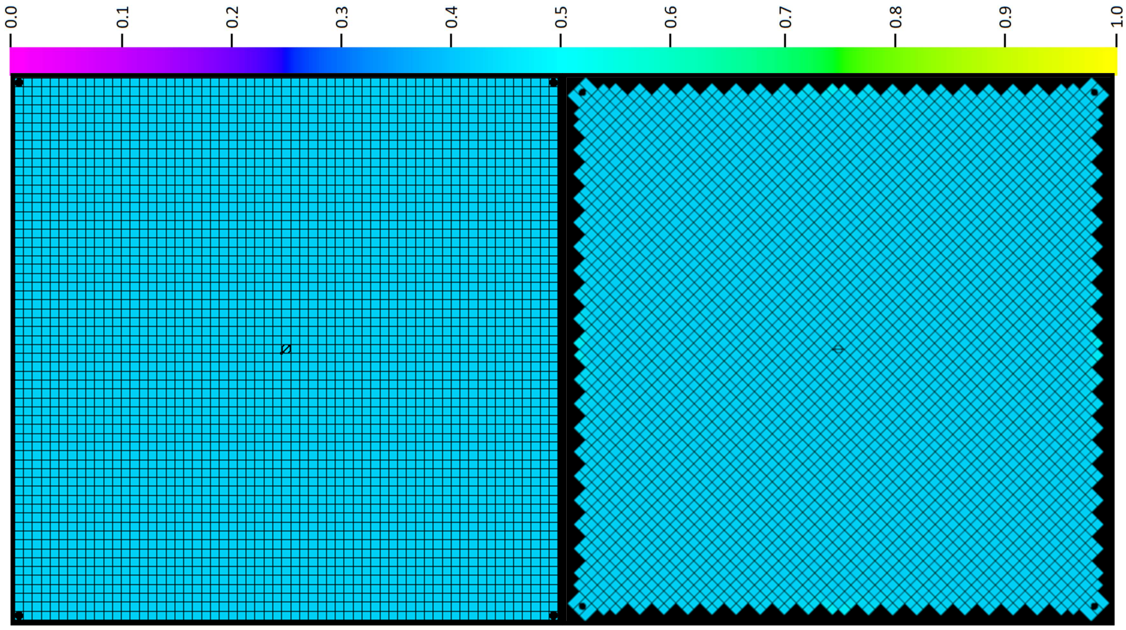

Fig. D.3-11: Effect of the grid orientation on oil displacement at the end of EOR (polymer flood)

Tbl. D.3-3: Effect of the grid orientation on the S_w (polymer flood)

		Water Saturation			
Region	**Model**	**0.8 years**	**2 years**	**7.5 years**	**End of EOR**
Injector					
	Model 1	0.5701	0.5702	0.5702	0.5703
	Model 1B	0.5701	0.5702	0.5702	0.5703
	Deviation	0.0	0.0	0.0	0.0
Producer					
	Model 1	0.3850	0.3903	0.4059	0.5700
	Model 1B	0.3593	0.3645	0.3374	0.5696
	Deviation	0.0257	0.0258	0.0685	0.0004
Center of Margins	Model 1	0.2361	0.2441	0.5027	0.5693
	Model 1B	0.1930	0.1930	0.1935	0.5254
	Deviation	0.0431	0.0511	0.3092	0.0439

Tbl. D.3-4: Effect of the grid orientation on the S_w of the entire reservoir (polymer flood)

	Water Saturation			
Model	**0.8 years**	**2 years**	**7.5 years**	**End of EOR**
Model 1	0.5594	0.5596	0.5612	0.5711
Model 1B	0.5574	0.5577	0.5597	0.5713
Deviation	0.002	0.0019	0.0015	-0.0002

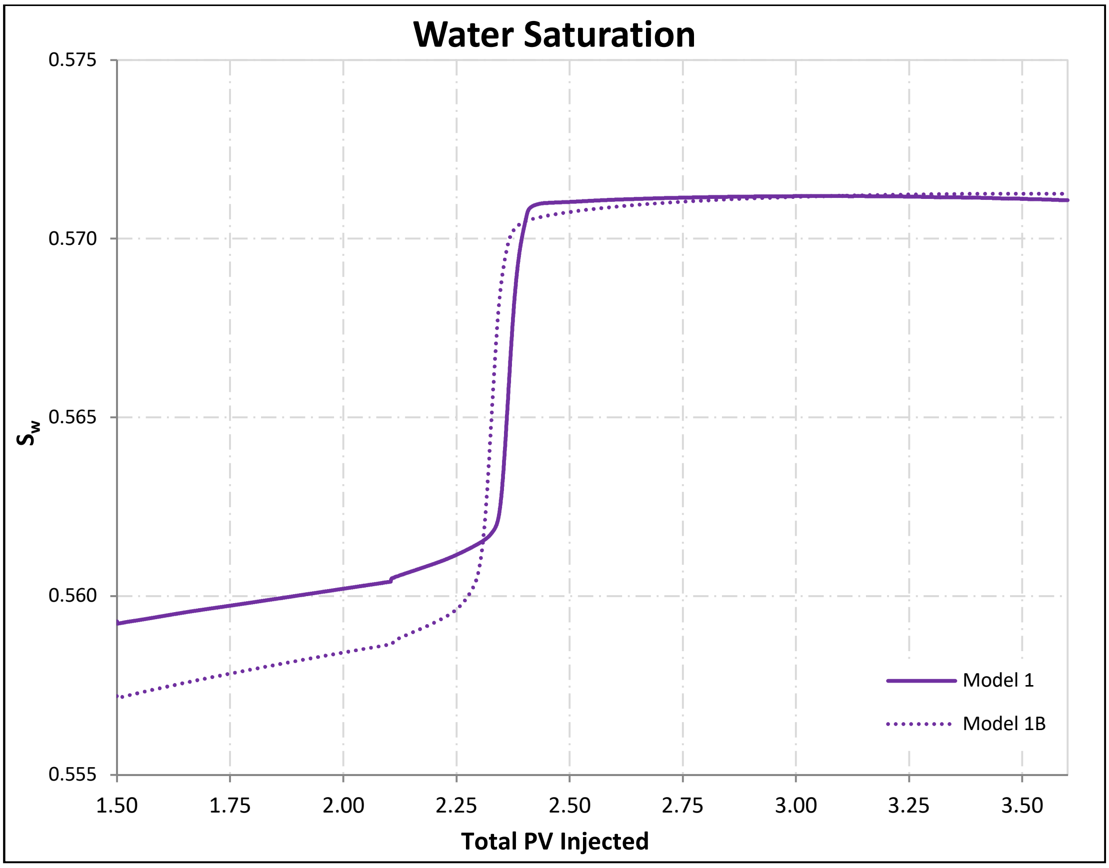

Fig. D.3-12: Effect of the grid orientation on the S_w of the entire reservoir (polymer flood)

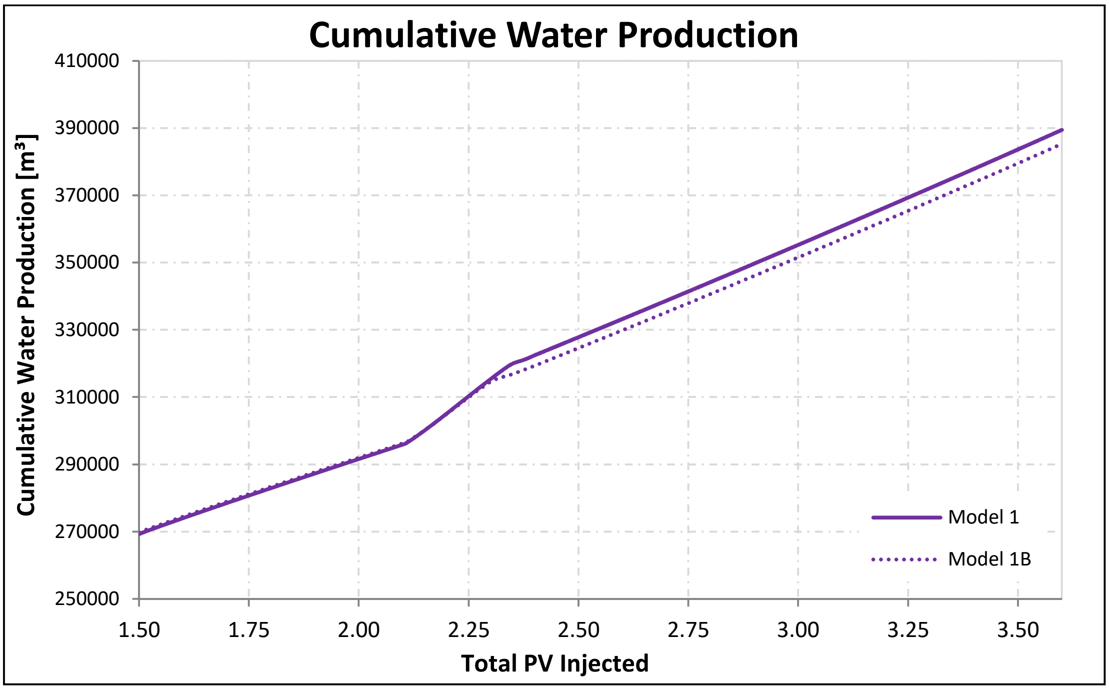

Fig. D.3-13: Effect of the grid orientation on the cumulative water production of the entire reservoir (polymer flood)

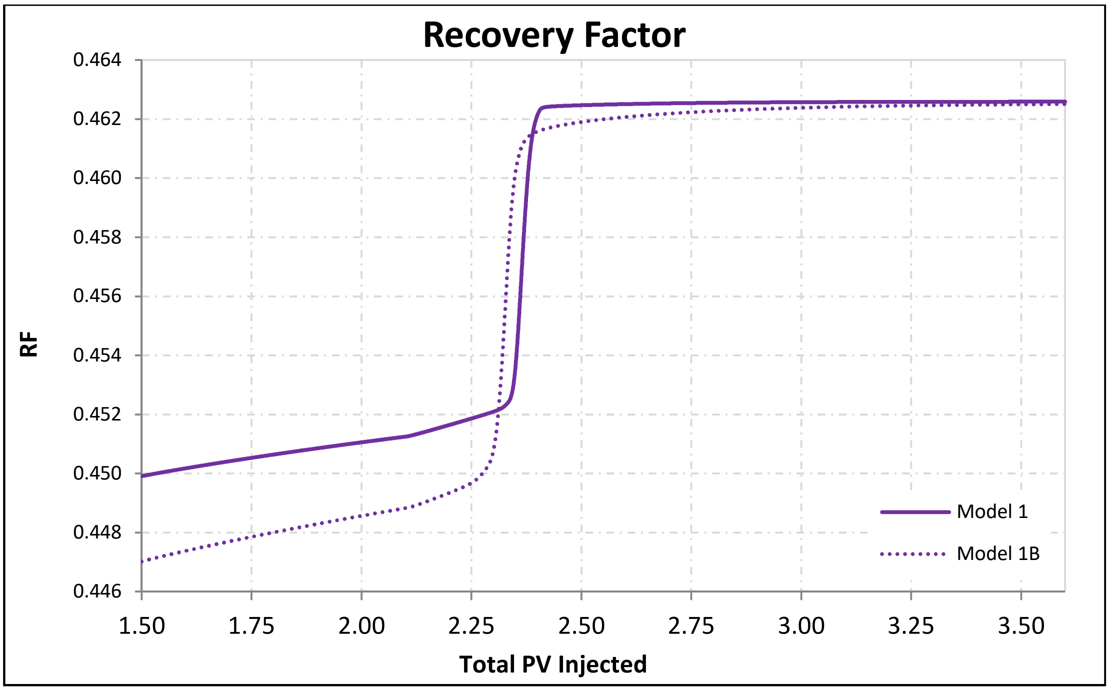

Fig. D.3-14: Effect of the grid orientation on the recovery factor of the entire reservoir (polymer flood)

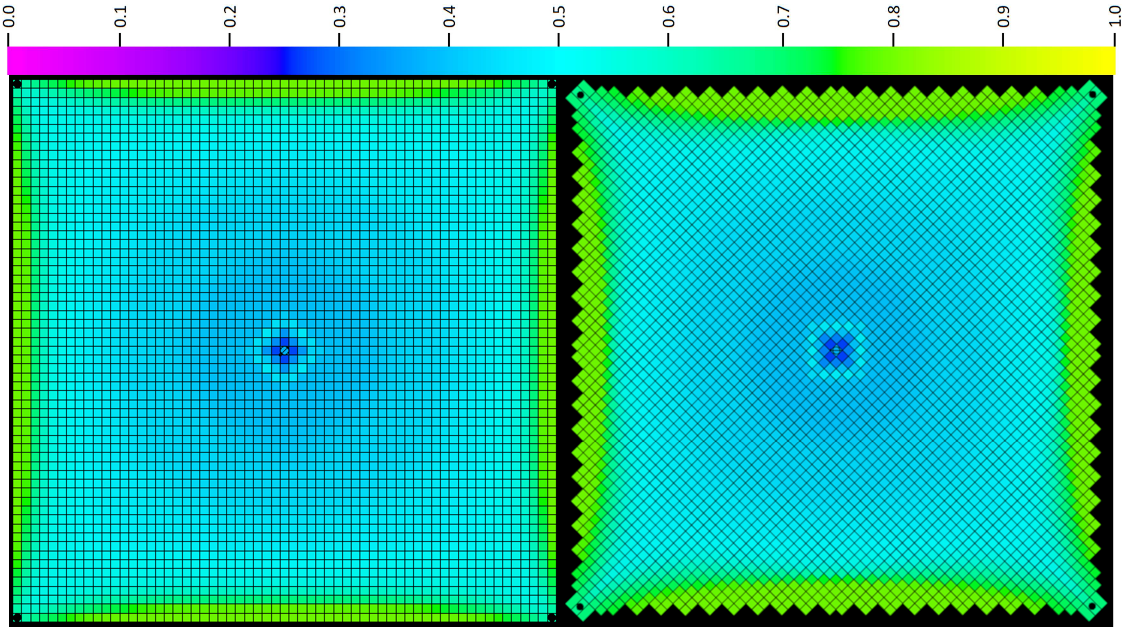

Fig. D.3-15: Effect of the grid orientation on oil displacement after 1 week (AP flood 'Match 1')

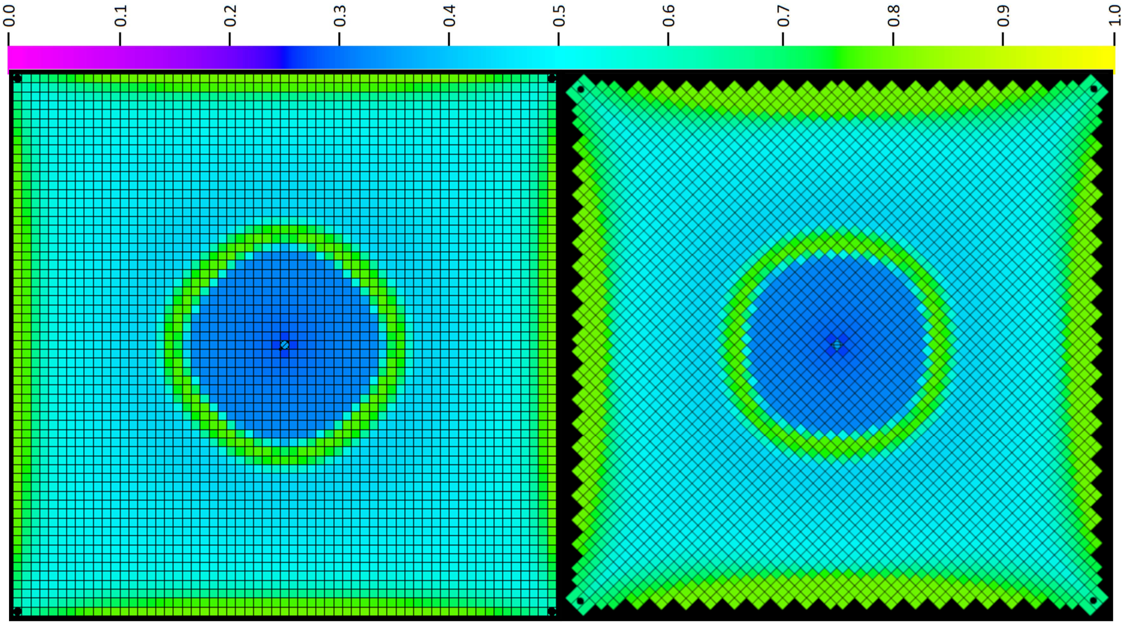

Fig. D.3-16: Effect of the grid orientation on oil displacement after 0.5 years (AP flood 'Match 1')

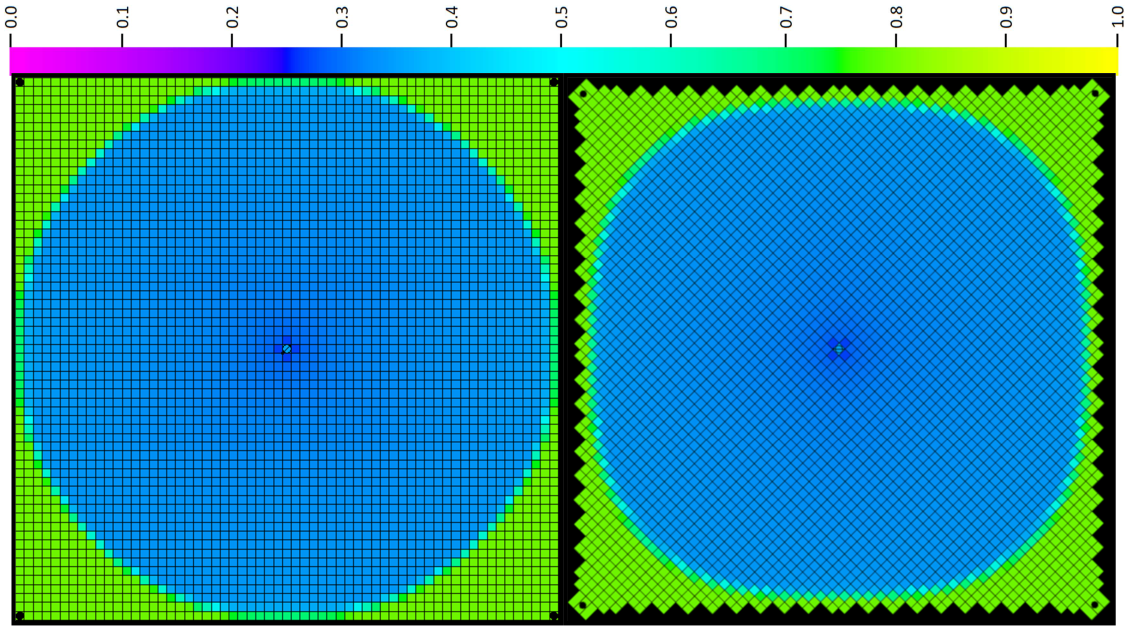

Fig. D.3-17: Effect of the grid orientation on oil displacement after 5 years (AP flood 'Match 1')

Tbl. D.3-5: Effect of the grid orientation on the S_w *(AP flood 'Match 1')*

		Water Saturation			
Region	**Model**	**1 week**	**0.5 years**	**5 years**	**End of EOR**
Injector	Model 1	0.6248	0.6431	0.6431	0.6431
	Model 1B	0.6247	0.6439	0.6439	0.6439
	Deviation	0.0001	-0.0008	-0.0008	-0.0008
Producer	Model 1	0.2001	0.2004	0.3101	0.6262
	Model 1B	0.3310	0.3394	0.2001	0.7209
	Deviation	-0.1309	-0.139	0.11	-0.0947
Center of Margins	Model 1	0.2001	0.2004	0.3101	0.6262
	Model 1B	0.2000	0.2000	0.2000	0.4780
	Deviation	0.0001	0.0004	0.1101	0.1482

Tbl. D.3-6: Effect of the grid orientation on the S_w of the entire reservoir (AP flood 'Match 1')

	Water Saturation			
Model	**1 week**	**0.5 years**	**5 years**	**End of EOR**
Model 1	0.5873	0.5877	0.5919	0.6756
Model 1B	0.5839	0.5846	0.5941	0.6750
Deviation	0.0034	0.0031	-0.0022	0.0006

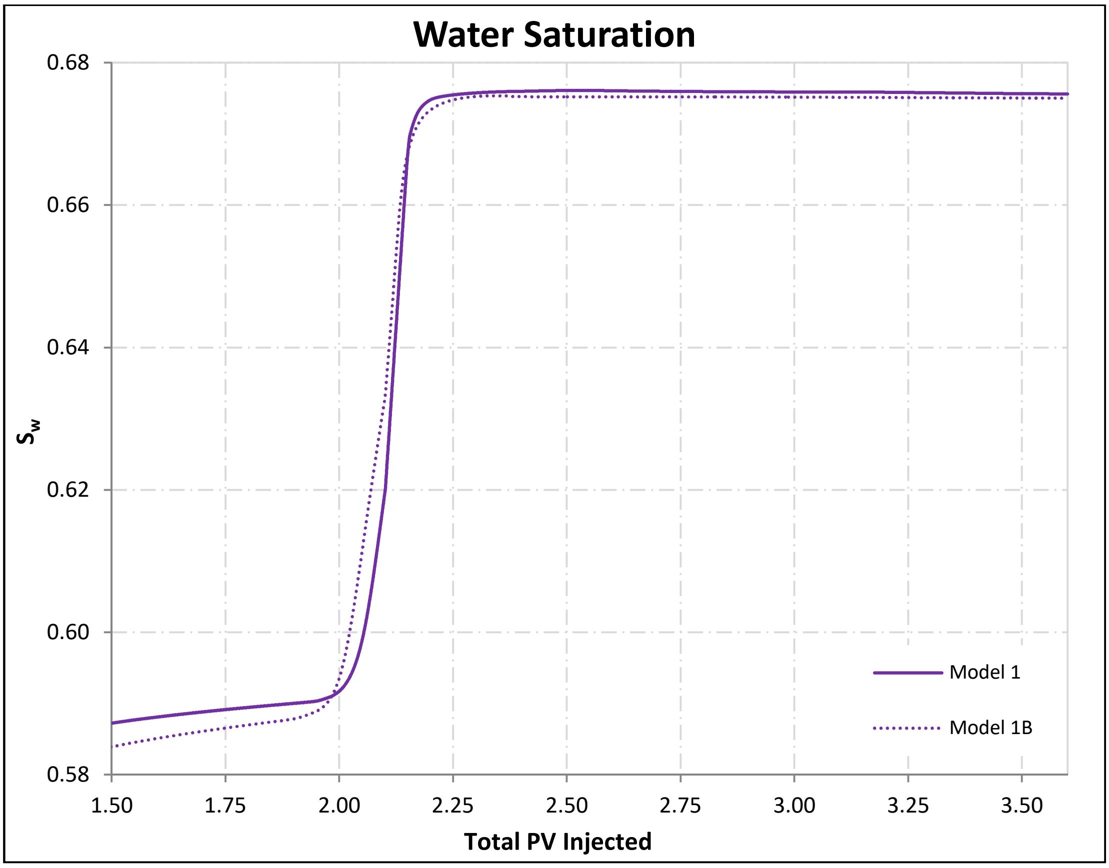

Fig. D.3-18: Effect of the grid orientation on the S_w of the entire reservoir (AP flood 'Match1')

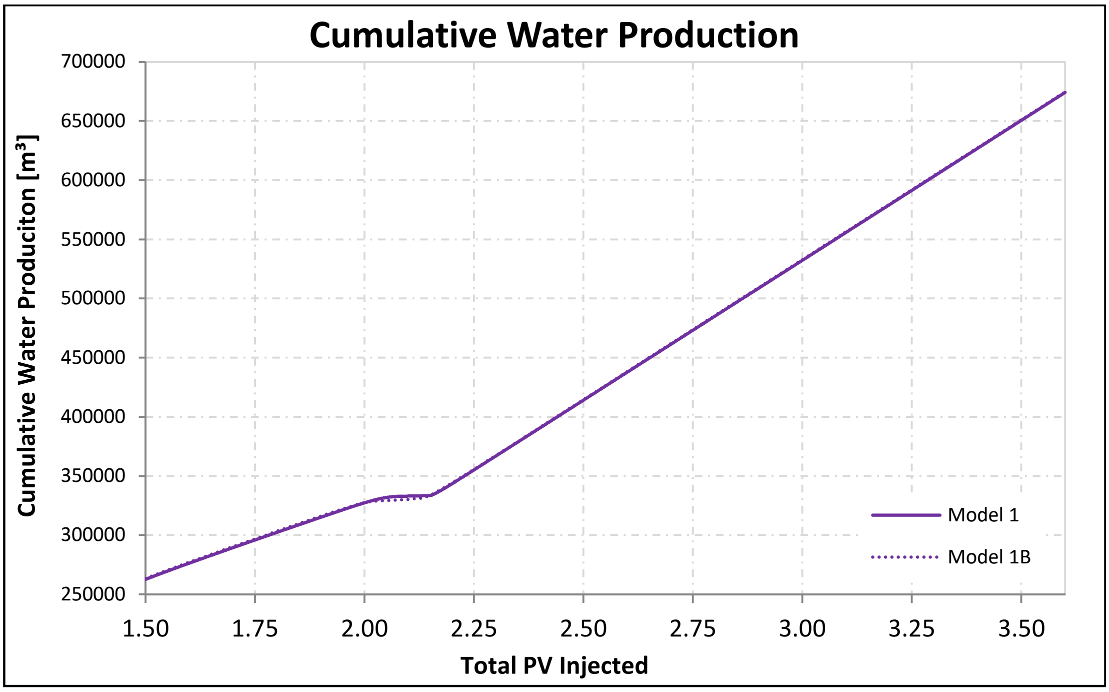

Fig. D.3-19: Effect of the grid orientation on the cumulative water saturation of the entire reservoir (AP flood 'Match1')

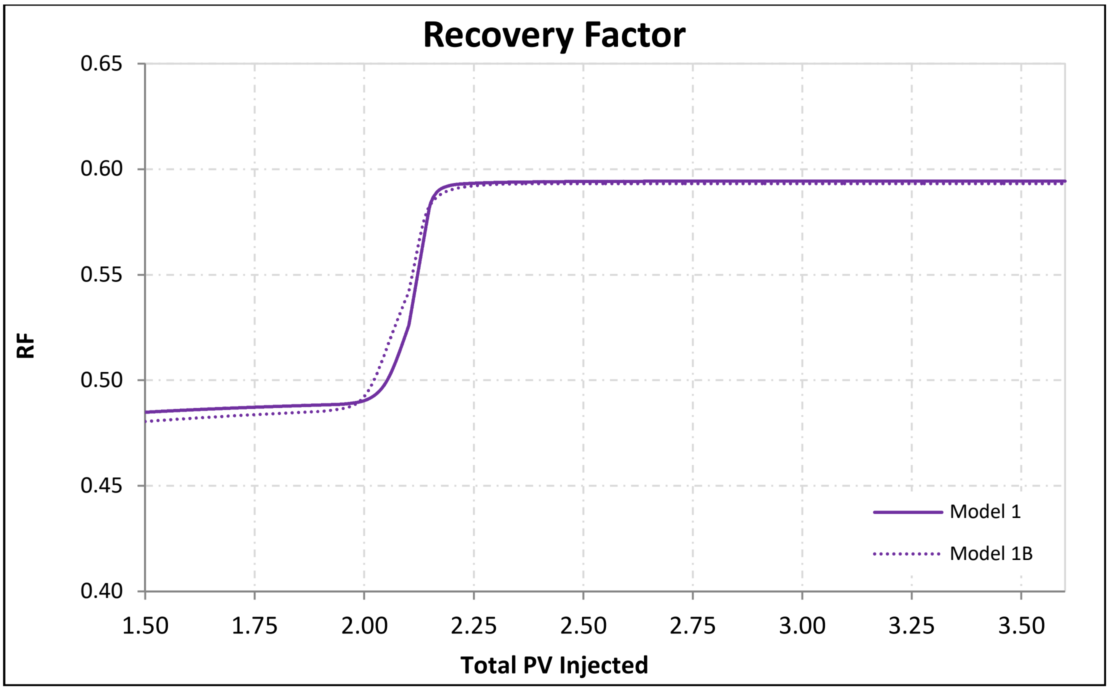

Fig. D.3-20: Effect of the grid orientation on the recovery factor of the entire reservoir (AP flood 'Match1')